Biophysical Investigations into Membrane-Active Peptides and Proteins

Daniel J. Yin

The Queen's College

University of Oxford

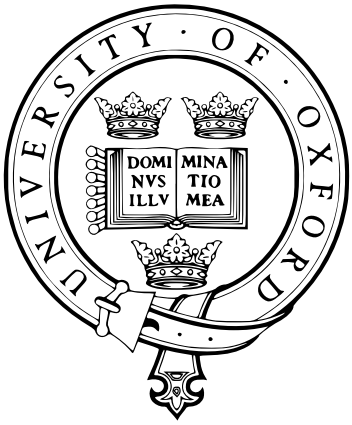

Thesis submitted to the Board of the Medical Sciences Division in partial fulfilment

of the requirements for the degree of Doctor of Philosophy

Oxford, 28 December 2016

Abstract

Biophysical Investigations into Membrane-Active Peptides and Proteins

Daniel J. Yin, The Queen's College, University of Oxford

DPhil Thesis, Trinity Term 2016

The inexorable spread of antibiotic or antimicrobial resistance is a global problem, described by the UK Chief Medical Officer to be "as big a threat as terrorism". Due to uncontrolled, unnecessary overuse of antibiotics in medicine and agriculture, bacterial resistance has evolved to even the antibiotics of last resort. Antimicrobial peptides (AMPs) are a promising class of organic molecule that have been proposed to exert a potent antimicrobial effect, which, directly or indirectly, involve complex interactions with cell membranes. Three broad mechanisms have been proposed for AMPs: carpet, barrel-stave and toroidal pore. However, the molecular basis for the mode of action of AMPs, and the relationship between primary structure and antimicrobial activity, remains poorly understood.

In this thesis, interactions of membrane-active peptides and proteins with model lipid membranes are studied, to understand better the peptide-lipid interactions of two *de novo* AMPs and a functionally related protein puroindoline-b (pinB), which is implicated in antimicrobial plant defence. Quartz crystal microbalance (QCM), solid-state nuclear magnetic resonance (ssNMR), electron paramagnetic resonance (EPR) and neutron reflectivity (NR) are used to achieve this.

The two AMPs were designed rationally with their primary structure predicted to display specific peptide-lipid interactions. Tilamin (tilted antimicrobial insert) was designed by modifying amhelin (antimicrobial insert), a pore-forming AMP. The modified peptide was predicted to disrupt model membranes mimicking bacterial membranes *via* a different mode of action to transmembrane barrel stave pore formation. Chom (chopped cecropin mutant) was designed by shortening the length of a natural AMP, cecropin-B, and was predicted to operate *via* a carpet mechanism.

To model the biophysical properties such as morphology, thickness and charge of native membranes, simplified phospholipid liposomes were used to better understand the membrane-perturbing influence of the AMPs, and whether this was correlated with antimicrobial activity. In the presence of anionic model membranes (mimicking Gram-negative inner membranes and Gram-positive membranes), tilamin and chom adopt amphipathic alpha helix conformations as determined by circular dichroism, while remaining unstructured in solution and in the presence of zwitterionic model membranes mimicking mammalian model membranes. Adoption of a folded conformation appears to be important for the lytic effect of the AMPs. Calcein leakage experiments performed show that the AMPs induce leakage of calcein from the interior of anionic liposomes, consistent with the proposal that membrane permeabilisation is important for antimicrobial activity.

The peptide-lipid interactions of the AMPs were then probed using QCM and ssNMR, giving mechanistic evidence that chom operates *via* the carpet mechanism as predicted. The nature of the mode of action of tilamin remained uncertain. From order parameters of lipids in bilayers, obtained using ssNMR upon interaction with tilamin, a toroidal pore mechanism was proposed, along with a new mode of action that caused monoleaflet poration, though it was not possible to resolve the two mechanism based on data obtained from symmetrical vesicles alone.

Adapting a newly established protocol to control the leaflet distribution of lipids in model membranes, an asymmetrically distributed nitroxide probe reveals for the first time leaflet-specific peptide-lipid interactions using cw-EPR. Tilamin shows changes in bilayer lipid order parameters that do not match those seen for either an all-surface or transmembrane control peptide, indicating more complex interactions. Unique QCM data, heterogeneous changes in order parameter profiles observed with acyl-chain ^{2}H ssNMR, as well as a lack of interaction with the inner leaflets of anionic model membranes seen by cw-EPR taken in combination suggest tilamin operates *via* a more complicated mechanism. Supported by tilt angles obtained by geometric analysis of labelled alanines (GALA) of deuterium-labelled tilamin and atomic force microscopy (AFM) imaging performed with collaborators, the results are consistent with a new mechanism; monolayer poration.

The puroindolines are also studied, due to their potential role as antimicrobial proteins in food safety, and in controlling wheat endosperm texture. The mode of insertion of wild-type puroindoline-B (pinB+) and a single-point mutant (pinBs) into bacterial model bilayers was probed for the first time with ssNMR, EPR and NR. In contrast to previous work on monolayers, pinBs does not cause changes in bilayer lipid order in the gel phase, while pinB+ forms a protein layer on the surface of a membrane. The results suggest that in more native-like model membranes, the tryptophan rich domain (TRD) of pinBs and pinB+ greatly affects the membrane binding properties, with implications for the role of the proteins *in vivo*.

Table of Contents

Abstract ii

List of Tables vi

List of Figures vii

Acknowledgements viii

Publications, Poster Presentations and Other Awards xi

Abbreviations xiii

1 Introduction 1

1.1 Motivation . . . 1
1.2 The cell membrane . . . 2
1.2.1 Membrane lipids . . . 3
1.2.2 Asymmetry in membranes . . . 9
1.3 Antimicrobial peptides . . . 11
1.3.1 History . . . 11
1.3.2 Structure . . . 12
1.3.3 Mode of action . . . 15
1.3.4 Resistance . . . 19
1.4 Experimental techniques used in this thesis . . . 20
1.4.1 Quartz crystal microbalance with dissipation monitoring . . . 20
1.4.2 Solid-state nuclear magnetic resonance (ssNMR) . . . 24
1.4.3 Electron paramagnetic resonance . . . 34
1.4.4 Neutron reflectometry . . . 40
1.4.5 Dynamic light scattering . . . 46
1.4.6 Circular dichroism . . . 48
1.5 Aims of thesis . . . 49

2 Biophysical Investigations of *De Novo* Antimicrobial Peptides 51

2.1 Introduction . . . 51

2.1.1 Principles of peptide design . . . 51
2.1.2 Aims of chapter . . . 53
2.2 Materials and methods . . . 54
2.2.1 Lipids . . . 54
2.2.2 Peptide synthesis . . . 55
2.2.3 Minimum inhibitory concentration . . . 58
2.2.4 Calcein leakage . . . 58
2.2.5 Circular dichroism . . . 59
2.2.6 Quartz crystal microbalance . . . 60
2.3 Results . . . 61
2.3.1 Antimicrobial design strategy . . . 61
2.3.2 Peptide synthesis . . . 64
2.3.3 Minimum inhibitory concentration . . . 65
2.3.4 Calcein leakage . . . 67
2.3.5 Circular dichroism . . . 68
2.3.6 Quartz crystal microbalance . . . 70
2.4 Discussion . . . 78

3 Solid-State NMR Investigations into Tilamin, Chom and Qaela 82
3.1 Introduction . . . 82
3.1.1 Headgroup-deuterated lipid synthetic considerations . . . 82
3.1.2 Aims of chapter . . . 83
3.2 Materials and methods . . . 84
3.2.1 ^{2}H-labelled lipid synthesis . . . 84
3.2.2 Solid-state NMR . . . 84
3.2.3 Dynamic light scattering . . . 85
3.3 Results . . . 85
3.3.1 ^{2}H-labelled lipid synthesis . . . 85
3.3.2 Depaking of ^{2}H ssNMR spectra . . . 88
3.3.3 Changes induced in the headgroup region probed by ^{2}H ssNMR . 90
3.3.4 Changes induced in the acyl region as probed by ^{2}H ssNMR 94
3.3.5 Dynamic light scattering . . . 102
3.4 Discussion . . . 105

4 Investigations into Asymmetric Model Membranes 112
4.1 Introduction . . . 112
4.1.1 Cyclodextrin mediates lipid exchanges between vesicles . . . 112
4.1.2 Analysis of EPR spectra to determine lipid dynamics . . . 115

4.1.3 Mimicry of bacterial cell membranes . . . 117
4.1.4 Aims of chapter . . . 119
4.2 Materials and methods . . . 120
4.2.1 Lipids . . . 120
4.2.2 Buffers for fluoresence quenching . . . 120
4.2.3 Peptides . . . 120
4.2.4 Dynamic light scattering . . . 121
4.2.5 Calcein leakage . . . 121
4.2.6 Fluorescence measurements . . . 121
4.2.7 Asymmetric vesicle Formation . . . 122
4.2.8 Fluorescence measurements . . . 124
4.2.9 EPR . . . 124
4.3 Results . . . 127
4.3.1 Separation of donor vesicles from acceptor vesicles . . . 127
4.3.2 Determination of phospholipid yield . . . 128
4.3.3 Fluorescence-based determination of label distribution in leaflets 128
4.3.4 Fluorescence experiments on asymmetric model membranes . . . 130
4.3.5 Towards a Gram-negative model membrane . . . 133
4.3.6 EPR studies on asymmetric peptide-lipid interactions . . . 137
4.4 Discussion . . . 148

5 Biophysical Investigations into Puroindoline-b 152
5.1 Introduction . . . 152
5.1.1 The puroindolines . . . 152
5.1.2 Aims of chapter . . . 155
5.2 Materials and methods . . . 155
5.2.1 Extraction and purification of pinB+ and pinBs . . . 155
5.2.2 Solid-state NMR . . . 157
5.2.3 TEMPO Partitioning . . . 157
5.2.4 Neutron reflectivity . . . 158
5.3 Results . . . 162
5.3.1 Purification of pinB+ and pinBs . . . 162
5.3.2 ssNMR investigations into lipid-protein interactions . . . 163
5.3.3 EPR to determine changes in membrane fluidity . . . 166
5.3.4 Neutron reflectivity . . . 169
5.4 Discussion . . . 175

6 Conclusions and Future Work **178**

6.1 Conclusions 178

6.2 Future work 185

References **190**

A ^{2}H-Labelled Phospholipid Synthesis **224**

B Full Sequence of PinA, PinB+ and PinBs **234**

List of Tables

1.1 Typical representative lipid compositions of mammalian and bacterial membranes 5
1.2 The acyl chain length and saturation distribution of lipid headgroup types for mammalian and bacterial membranes studied in this thesis . . 6
1.3 Table of flip-flop rates ($t_{\frac{1}{2}}$) for different lipid species 10
1.4 A selected timeline of AMP discovery 13
1.5 Table showing the properties of magnetic nuclei used extensively in biological systems 26

2.1 Minimum inhibitory concentrations for tilamin, chom and qaela compared to conventional antibiotics 66
2.2 Penetration depth of different harmonics calculated for an SLB 80

3.1 Table summarising the changes in quadrupolar splittings of headgroup-deuterated MLVs in the absence and presence of tilamin 90
3.2 Table summarising the changes in quadrupolar splittings of headgroup-deuterated MLVs in the absence and presence of qaela 92
3.3 Dynamic light scattering size measurements, showing size changes of MLVs in the presence and absence of tilamin and chom 104

4.1 The various properties of different cyclodextrins 113
4.2 Table summarising the changes in fluorescence intensity of symmetric POPC (1% rhodamine-PE) LUVs due to quenching 130
4.3 Table summarising the changes in fluorescence intensity of asymmetric POPC (1% rhodamine-PE) LUVs due to quenching 132
4.4 Table showing the peptides, and molecular properties thereof, used in asymmetric cw-EPR experiments 138
4.5 EPR order parameters for asymmetric LUVs in the absence and presence of Helix-8 peptide (P:L 1:10) 142
4.6 EPR order parameters for asymmetric LUVs in the absence and presence of WALP-23 (P:L 1:25) 144

4.7 EPR order parameters for asymmetric LUVs in the absence and presence of tilamin and chom (P:L 1:25) 147
4.8 The lipid composition of brain polar lipid 149

5.1 Lipid composition and solvent contrast conditions for the NR experiments performed. 161
5.2 Summary of scattering length densities for the components studied and the solution subphases 161
5.3 Table summarising changes in TEMPO partitioning of model membranes caused by pinB+ and pinBs 168
5.4 Structural parameters obtained for an asymmetrically deposited bilayer in the absence and presence of pinB+ 171
5.5 Structural parameters obtained for an asymmetrically deposited bilayer in the absence and presence of pinBs 172

List of Figures

1.1 The danger posed by antibiotic resistance 1
1.2 The biological membranes of different cellular species 3
1.3 The structures of commonly occurring membrane lipids 4
1.4 The polymorphic forms of various lipids. 7
1.5 The asymmetric lipid distribution of phospholipids between the outer and inner leaflets of different cell membranes 9
1.6 Number of AMPs discovered since 1970 11
1.7 Collated properties of all known AMPs 14
1.8 Schematic showing the generally accepted mechanisms by which the lytic effect of AMPs with cell membranes is exerted 16
1.9 Schematic showing bilayer deposition on a QCM chip 21
1.10 Δf-ΔD plots for the interaction of two AMPs with a DMPC SLB 22
1.11 Zeeman splitting for a spin $I = 1$ nucleus 25
1.12 Schematic showing detection of NMR signal and relaxation 27
1.13 A schematic showing the effect of quadrupolar coupling on the energy levels and resulting NMR spectrum for a quadrupolar nucleus 31
1.14 Examples of ^{2}H ssNMR in understanding peptide-lipid interactions . . . 33
1.15 Hyperfine splitting in a nitroxide EPR spectrum 35
1.16 Examples of commercially available EPR probes 36
1.17 Schematic showing acquisition of an EPR spectrum 37
1.18 Principal hyperfine splittings of a nitroxide-labelled phospholipid 39
1.19 Experimental setup for time-of-flight neutron reflectivity 42
1.20 Typical neutron reflectivity and scattering length density profiles 43
1.21 Schematic of an adsorbed lipid bilayer and use of contrast matching . . . 45
1.22 Relationship of particle size to autocorrelation function 47
1.23 Characteristic CD spectra of peptides of different secondary structure . . 49

2.1 An archetypal alpha-helix 52
2.2 The primary sequences of tilamin, amhelin and qaela compared 61
2.3 Helical wheel projections for tilamin and qaela 62
2.4 Helical wheel projections for cecB and chom 63

2.5 The analytical hplc traces and mass spectra for tilamin and chom 65
2.6 Minimum inhibitory concentrations for tilamin, chom and qaela 65
2.7 The fluorescence spectrum of POPC:PG LUVs in the presence of tilamin . 67
2.8 Permeation of model membranes by tilamin and chom, as monitored by calcein fluoresence 68
2.9 CD spectra of tilamin, qaela and chom 69
2.10 A typical QCM experiment 71
2.11 Net f and D changes upon chom addition to different SLBs 72
2.12 Net f and D changes upon tilamin addition to different SLBs 73
2.13 Δf-ΔD plots for chom 75
2.14 Δf-ΔD plots for tilamin 77

3.1 Retrosynthetic analysis to synthesise biologically relevant lipids 82
3.2 Migration of a 1,2-diacylglycerol to the thermodynamically more stable 1,3-isomer can be acid- or base-catalysed. 83
3.3 Formation of intermediary diol **2-2** 85
3.4 Formation of protected diacylglycerols **2-4**,**2-5** and **2-6** 86
3.5 Strategies to form diacylglycerols **2-7** and **2-8** 86
3.6 Formation of ^{2}H-labelled headgroups 87
3.7 Formation of POPG-d_2, DMPG-d_2, POPE-d_4 and DMPE-d_4 88
3.8 Spectra showing pake spectra of MLV dispersions, and resultant depaked spectra 89
3.9 Depaked ^{2}H ssNMR spectra of POPC:POPG-d_2 (3:1) and POPC:POPE-d_4 (3:1) MLVs in presence and absence of tilamin 91
3.10 Depaked ^{2}H ssNMR spectra of POPC:POPG-d_2 (3:1) and POPC:POPE-d_4 (3:1) MLVs in presence and absence of qaela 92
3.11 Depaked ^{2}H ssNMR spectra of POPC:POPG-d_2 (3:1) and POPC:POPE-d_4 (3:1) MLVs in presence and absence of chom 93
3.12 Depaked ^{2}H ssNMR spectra of POPC-d_{31} (3:1), POPC-d_{31}:POPG (3:1) and POPC:POPG-d_{31} (3:1) MLVs in presence and absence of tilamin 94
3.13 Order parameter profile for POPC-d_{31}, POPC-d_{31}:POPG (3:1) and POPC:POPG-d_{31} (3:1) in the presence and absence of tilamin 96
3.14 Depaked ^{2}H ssNMR spectra of POPC-d_{31} (3:1), POPC-d_{31}:POPG (3:1) and POPC:POPG-d_{31} (3:1) MLVs in presence and absence of qaela 97
3.15 Order parameter profile for POPC-d_{31}, POPC-d_{31}:POPG (3:1) and POPC:POPG-d_{31} (3:1) in the presence and absence of qaela 98
3.16 Depaked ^{2}H ssNMR spectra of POPC-d_{31} (3:1), POPC-d_{31}:POPG (3:1) and POPC:POPG-d_{31} (3:1) MLVs in presence and absence of chom 99

3.17 Order parameter profile for POPC-d_{31}, POPC-d_{31}:POPG (3:1) and POPC:POPG-d_{31} (3:1) in the presence and absence of chom 100
3.18 ^{2}H NMR spectra of POPC-d_{31} MLVs in the presence of tilamin P:L 1:25, in the presence of unlabelled POPC:POPG 3:1 MLVs 101
3.19 Size distribution, as determined by DLS, of MLV dispersions in the absence and presence of tilamin and chom at P:L 1:100 and 1:25 102
3.20 The primary sequences and predicted helical structure of tilamin, qaela and chom. 105
3.21 Fluorescence micrographs of anionic GUVs treated with tilamin and chom 107
3.22 Cartoon of the proposed mechanism of action of chom and cecB 108
3.23 Cartoon of the proposed mechanism of action of qaela 109
3.24 Cartoon of the proposed mechanism of action of tilamin 110

4.1 Molecular structures of α-, β- and γ-cyclodextrin 113
4.2 Schematic showing the methodology to produce asymmetric vesicles . . 114
4.3 EPR spectra of DPPC lipid bilayers, at 46°C, labelled at different positions along the *sn*-2 acyl chain 116
4.4 Typical structure of lipopolysaccharides 119
4.5 Scheme to form asymmetric vesicles 127
4.6 A phosphorus concentration assay showing the amount of phospholipid and fluorescence spectra before and after outer leaflet exchange 128
4.7 Fluorescence spectra showing leaflet-specific quenching rhodamine-PE in an LUV and SUV 129
4.8 Fluorescence spectra showing the quenching by I^- of rhodamine-PE specifically incorporated into the outer leaflet of a POPC LUV 131
4.9 Fluorescence spectra showing the quenching by I^- of rhodamine-PE specifically incorporated into the inner leaflet of a POPC LUV 132
4.10 Fluorescence spectra showing the quenching by I^- of rhodamine-labelled LPS specifically incorporated into the outer leaflet of a POPC LUV 133
4.11 Dynamic light scattering profile showing the donor POPC MLVs and the acceptor, asymmetric POPC LUVs with LPS selectively incorporated into the outer leaflet 134
4.12 Permeation of model membranes by tilamin, chom, and gramD, as monitored by calcein fluoresence. 135
4.13 The structure of Gramicidin D 136
4.14 Circular dichroism spectrum of h8 peptide in the presence of different liposomes 138
4.15 Helical wheel projections of h8p, WALP-23, chom and tilamin 139

4.16 Reaction scheme for reduction of TEMPO-DPPC 140
4.17 EPR spectra of symmetrically- and asymmetrically- labelled POPC LUVs (1.5% spin-label), with and without h8p (P:L 1:5) 141
4.18 Intrinsic fluorescence of tryptophan in the presence of POPC LUVs 143
4.19 EPR spectra of symmetrically- and asymmetrically- labelled POPC LUVs (1.5% spin-label), with and without WALP-23 (P:L 1:25) 144
4.20 Intrinsic fluorescence of tryptophan 145
4.21 EPR spectra of symmetrically- and asymmetrically- labelled POPC LUVs (1.5% spin-label), with and without tilamin and chom (P:L 1:25) 146
4.22 AFM images and peptide tilt angles obtained for tilamin on model membranes 150
4.23 Summary of biophysical characterisation of tilamin, which taken in combination suggest a new mode of action 151

5.1 The primary sequences of the cysteine-enclosed tryptophan loop of pinA and pinB 153
5.2 Schematic showing the different binding characteristics of pinB and pinBs on different lipid monolayers 154
5.3 TEMPO EPR spectrum in a DMPE:DMPG (3:2) MLV dispersion 158
5.4 Purification of pinBs and pinB+ 163
5.5 The effect of temperature (and lipid phase) on the ^{2}H ssNMR spectra of DMPE:DMPG-d_2 MLVs 164
5.6 ^{2}H ssNMR spectra of headgroup-labelled membranes in the absence and presence of pinBs and pinB+ 165
5.7 Changes in TEMPO partitioning in DPPG:DPPE (3:2) MLVs induced by pinB+ and pinBs 166
5.8 Changes in TEMPO partitioning in DPPG MLVs induced by pinB+ and pinBs 168
5.9 Neutron reflectivity profiles and scattering length density profiles for SLB before and after pinB+ addition 170
5.10 Neutron reflectivity profiles and scattering length density profiles for SLB before and after pinBs addition 173
5.11 Neutron reflectivity profiles and scattering length density profiles for SLBs interacting with pinBs and pinB+ for one contrast 174

6.1 Rationally altering the primary sequence of cecB to chom predictably changes the mode of action 181
6.2 Rationally altering the primary sequence of amhelin to tilamin predictably changes the mode of action 182

6.3 New approaches to modelling natural bacterial membranes 187
6.4 Schematic depiction of formation of SMA lipodisqs 188

Acknowledgements

living is easy with eyes closed
misunderstanding all you see

Strawberry Fields Forever
Lennon-McCartney

I am immensely grateful to so many people on whose vertiginous shoulders I stand.

Professor Anthony Watts has been an incredible supervisor and I have enjoyed my time in the Watts group greatly. His scientific knowledge and advice, generosity of time, boundless energy and sense of humour have been invaluable these last four years. I'll always look back fondly on my time spent under his supervision, and hope he continues to inspire young scientists.

Sous-supervisor Dr Peter Judge has been a constant source of support and wide- ranging scientific knowledge. Peter really made my jump into biochemistry an enjoyable one; he's a great scientist, teacher and friend. I will never know if his regular slip into double entendre is deliberate or not.

My industrial supervisor Dr Max Ryadnov (National Physical Laboratory) has also been a great mentor, with brilliant ideas for projects and always willing to lend a hand whenever I needed it.

My thanks also go to Dr Luke Clifton (Rutherford Appleton Laboratory) who was a huge source of help over the course of our collaboration on the puroindoline project. Thank you for all the help both on and off the neutron beam, and the fun discussions. I look forward to publishing our work on tissue box-attenuated neutron reflectivity.

Keeping me sane was fellow AMP ally "unlucky" Marc-Phillip Pfeil, who was, is and will be an incredible friend. Thanks for all the antimicrobial, NMR, EPR and non-scientific ruminations. It will be equal parts sad and almost certainly good for us that we won't be spending every second together any more.

The Watts group, former, current (and seemingly forever) has been a fantastic group to work in, I've enjoyed my time here greatly. Thank you to Garrick, Javier, "computer" Juan, "swiss" Juan, Paty, Ros, Rosana and hell's angel Pete Fisher, it's been a blast. In particular, thanks to nocturnal Juan "classic" and diurnal Dylan aficionado Patricia for introducing me to all things EPR and twenty four hour support. Thanks also to Steve Lavington for proof reading a very many number of chapters. He is by far the second best guitarist in the lab, and also a good egg and very good scientist, he'll go far.

My formative PhD years were spent back at the chemistry bench in the Hamilton Group across the road at the Chemistry Research Laboratory. Professor Andy Hamilton, and Doctors Madu Jayatunga, Pete Knipe, Hannah Lingard, James Luccarelli, Hayden Peacock, Melanie O'Sulogan and Sam Thompson were a largely superb group of people to be around. The S6 family inspired me to do a PhD in the first place, and their constant support will always be appreciated. In particular, I have to thank Hayden for endlessly interesting conversations, musical and scientific percipience and advice, and proof reading prowess helping me break up clumsy sentences, and James. The hand grenade was a large part of my appointment as a PhD student in the Watts group, I'll always be grateful. I'm looking forward to reassembling the Hamilton task force across the Atlantic. I'd also like to thank Dr Martin Smith, who has been a great mentor during my eight years in Oxford. You've helped me every step of the way more than you probably know.

For my year away from sleepy Oxford in the bustling metropolis of Teddington at the National Physical Laboratory, I'd like to thank Dr Angelo Bella, Baptiste Lamarre, Dr Jascindra Ravi, Nilofar Faruqui and Dr James Noble for being so helpful during my stay. Many thanks also to James and Katherine Heath (and Alice, Henry and Bertie) who put a roof over my head by housing me in their attic during my time in TW11. They are superb and I can't thank them enough for their hospitality. I'll always appreciate the kindness they showed me and the memories of Bushy Park.

Thanks to Dr David Staunton (Department of Biochemistry), Dr Will Myers (CAESR) and Professor Tim Claridge (Department of Chemistry) for support on the biophysical characterisation, EPR and NMR performed during this thesis. Thanks also to Professor Richard Frazier and Dr Becky Green (University of Reading) for their helpful discussions on the puroindoline project.

I am grateful to the Medical Research Council for funding my study, and the Queen's college and Department of Biochemistry for the various conference and travel opportunities during my PhD.

Thank you also to my proof reading fairies Carys Roberts, not-Ivo Graham, Jack Iain Skelly, James Snowden, Lauren Bradley, Matt Beer, Matt Young, Mike Holmes, Dr Owen Osborne and Sophie Rimington-Pounder for all the i's dotted, t's crossed, ramblings unrambled and desultories resultoried. On top of that you've been bloody legends.

This PhD would have been a lot greyer without Dr Natalie Tillack. It's been bloody einsame spitze, you're a gem. Looking forward to stealing horses with you in the future.

I would be nowhere without the love and support of my family, Mum, Dad and Jenny (and Utti!), thank you for absolutely everything.

To Greg, never forgotten.

Publications, Poster Presentations and Other Awards

Publications

A. Pyne, M. P Pfeil, I. Bennett, J. Ravi, P. Iavicoli, B. Lamarre, A. Roethke, S. Ray, H.Jiang, A. Bella, B. Reisinger, **D. Yin**, B. Little, J. Munoz-Garcia, E. Cerasoli, P. Judge, N.Faruqui, L. Calzolai, A. Henrion, G. Martyna, C. Grovenor, J. Crain, B. Hogenboom,A. Watts, and M. Ryadnov, "Engineering monolayer poration for rapid exfoliation of microbial membranes", Chem. Sci., 2016 (in press).

In preparation

D. Yin, M. R Sanders, L. Clifton, P. J. Judge, M. P. Pfeil, A Watts, R. A. Frazier, and R.J. Green, "The Interaction of tryptophan-rich puroindoline-b wild-type and mutant proteins with liposome models of biological membranes".
P. M. Dijkman, J. Munoz-Garcia, S. Lavington, P. S Kumagai, R. I dos Reis, **D. Yin**, P.J. Stansfeld, A. J. Costa-Filho, and A. Watts, "Stability of a G protein-coupled receptor helix 8 in lipid membranes".

Poster presentations

D. Yin, P. J Judge, S. Thompson, A. Watts, "Synthesis of ^{2}H-labelled phospholipids for solid-state NMR studies of membrane-active peptides", poster at American Chemical Society 246th National Meeting, 2013.

D. Yin, M. P Pfeil, P. J Judge, J. H Bolivar, L. A Clifton, A. D Graham, S. Thompson, R. J Green, R. A Frazier, A. Watts, "Spectroscopic studies on the antimicrobial activity of puroindoline B from wheat", poster at 9th European Biophysics Congress, Lisbon, Portugal, 2013.

D. Yin, P. J Judge, S. Thompson, M. Ryadnov, A. Watts, "Characterisation of the antimicrobial activity of *de novo* designed peptides: a functional study by ssNMR and QCM, poster at British Biophysical Society Biennial Meeting, Warwick, 2014.

D. Yin, P. J Judge, M. Ryadnov, A. Watts, "Characterisation of the lipid interactions with membrane-active peptides: a functional study by ssNMR, EPR and QCM, poster at British Biophysical Society Biennial Meeting, Liverpool, 2016.

Other awards

Max Perutz Science Writing Award -
"The War on the War on the War on Bacteria"

Peter Beaconsfield Award -
"The Fight Against the Fight Against the Fight Against Bacteria"

Abbreviations

5/12/14/16-PCSL	1-palmitoyl-2-stearoyl-(5/12/14/16-doxyl)-sn-glycero-3-phosphocholine
ACN	Acetonitrile
AFM	Atomic force microscopy
AMP	Antimicrobial peptide
BPL	Brain polar lipid
cecB	Cecropin B
CFU	Colony forming unit
CHO	Chinese hamster ovary
ChoC	N-terminal 21 amino acids of cecB
ChoM	ChoC with G14I G20K
CL	Cardiolipin
CMC	Critical micelle concentration
CPP	Cell-penetrating peptides
CSA	Chemical shift anisotropy
CW	Continous wave
cwEPR	Continous wave EPR
DAA	Direct acting antiviral
DCM	Dichloromethane
DHB	2,5-Dihydroxybenzoic acid matrix
DHPC	1,2-Dihexanoyl-sn-glycero-3-phosphocholine
DIPEA	N,N-Diisopropylethylamine"
DLPC	1,2-dilauroyl-sn-glycero-3-phosphocholine
DLPG	1,2-Dilauroyl-sn-glycero-3-phosphoglycerol
DLS	Dynamic light scattering
DMF	Dimethylformamide
DMF	N,N-dimethylformamide
DMPC	1,2-dimyristoyl-sn-glycero-3-phosphocholine
DMPG	1,2-dimyristoyl-sn- glycero-3-phosphoglycerol
DMSO	Dimethyl sulfoxide
DNA	Deoxyribonucleic acid
EDT	1,2-Ethanedithiol
EDTA	Ethylenediaminetetraacetic acid
EM	Electron microscope
EPR	Electron paramagnetic resonance
ERG	Ergosterol
ESR	Electron spin resonance
FID	Free induction decay
FRET	Forster resonance energy transfer
FT	Fourier transform
FTIR	Fourier-transform infra-red
GALA	Geometric analysis of labelled alanine
GPCR	G-protein coupled receptor
GUV	Giant unilamellar vesicle
HBTU	3-[Bis(dimethylamino)methyliumyl]-3H-benzotriazol-1-oxide hexafluorophosphate
HCl	Hydrogen chloride
HEPES	4-(2-Hydroxyethyl)piperazine-1-ethanesulfonic acid
HG	Headgroup
HPLC	High Performance Liquid Chromatography
IR	Infra-red
KI	Potassium Iodide

L:P	Lipid-to-protein ratio
LPC	Lysyl-phosphatidylcholine
LPG	Lysyl-phosphatidylglycerol
LPS	Lipopolysaccharide
LUV	Large unilamellar vesicle
MALDI	Matrix-assisted laser desorption/ionisation
MAS	Magic angle spinning
MBHA	4-Methylbenzhydrylamine hydrochloride
MD	Molecular dynamics
MD	Molecular dynamics
MEM	2-Methoxyethoxymethyl
MIC	Minimal inhibitory concentration
MLV	Multilamellar vesicle
MR	Molar Ratio
MS	Mass spectrometry
MSP	Membrane scaffold protein
MWCO	Molecular weight cut-off
NBD	4-Chloro-7-nitrobenz-2-oxa-1,3-diazole
NHS	N-Hydroxysuccinimide
NMR	Nuclear magnetic resonance
NR	Neutron reflectivity
OM	Outer membrane
PA	Phosphatidic acid
PBS	Phosphate buffered saline
PC	Phosphatidylcholine
PDB	Protein data bank
PE	Phosphatidylethanolamine
PEK	Phosphate EDTA Potassium (as part of buffer)
PG	Phosphatidylglycerol
PI	Phosphatidylinositol
pI	Isoelectric point
POPC	1-palmitoyl-2-oleoyl-sn-glycero-3-phosphocholine
POPE	1-Palmitoyl-2-oleoyl-sn- glycero-3-phosphoethanolamine
POPG	1-palmitoyl-2-oleoyl-sn-glycero-3-phosphoglycerol
ppm	Part per million
PS	phosphatidylserine
QCM	Quartz crystal microbalance
RMSD	Root-mean-square deviation
RNA	Ribonucleic acid
RP-HPLC	Reversed phase HPLC
RPM	Revolutions per minute
SDS	Sodium dodecyl sulfate
SDS-PAGE	Sodium dodecyl sulfate polyacrylamide gel electrophoresis
Seff	Effective order parameter
SLB	Supported lipid bilayer
SM	Sphingomyelin
SMA	Styrene maleic acid
sNMR	Solution NMR
SPR	Surface plasmon resonance
Sseg	Segmental order parameter

ssNMR	Solid-state NMR
SUV	Small unilamellar vesicle
SW	Sweep width
T1	Spin-lattace relaxation
T2	Spin-spin relaxation
TEM	Transmission electron microscopy
TEMPO	4-Hydroxy-2,2,6,6-tetramethylpiperidine 1-oxyl
TFA	Trifluoroacetic acid
TFE	Tetrafluoroethylene
TFE	Trifluoroethanol
Tis	Triisopropylsilane
TLC	Thin-layer chromatography
Tm	Transition temperature (bilayer)
TOF	Time- of-flight
TRD	Tryptophan rich domain
TRIS	Trisaminomethane
UV	Ultra-violet
v/v	volume-to-volume ratio
w/v	weight-to-volume ratio
wt/wt	weight-to-weight ratio

Chapter 1

Introduction

1.1 Motivation

The inexorable spread of antibiotic or antimicrobial resistance is a global problem, described by the UK Chief Medical Officer to be "as big a threat as terrorism" [1]. Due to uncontrolled, unnecessary overuse of antibiotics in medicine and agriculture, through adaptation and genetic selection, bacterial resistance has emerged to even the antibiotics of last resort [2]. A recent UK Government report estimated the number of deaths attributable to antibiotic resistance every year globally to stand at 700,000, and to increase to 10 million by 2050, potentially outnumbering deaths attributable to cancer (Figure 1.1 A) [3]. Despite efforts to financially incentivise drug companies to produce novel antibiotics, fewer new classes are being created each year (Figure 1.1 B) [4]. Antimicrobial peptides (AMPs) are a promising class of molecule

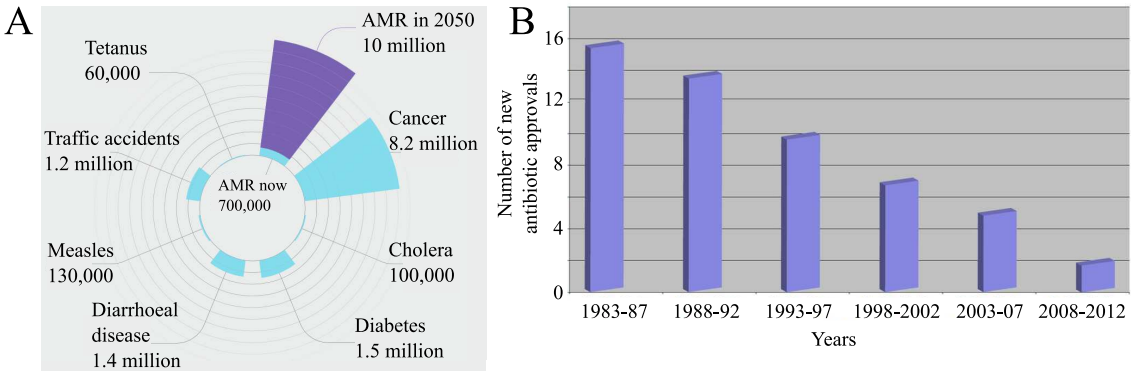

Figure 1.1 The danger posed by antimicrobial resistance (AMR). ***A:*** The estimated number of deaths attributed to AMR, and its projected impact by 2050 [5]. ***B:*** Graph showing the year-on-year decrease of new FDA-approved antibiotics [6].

that have been proposed to exert a potent antimicrobial effect, which, directly or indirectly, involve complex interactions with cell membranes [7]. The exact mode of

action of these molecules and the basis of their selectivity has yet to be fully established, and adding to this knowledge base is the focus of this thesis.

1.2 The cell membrane

Across all living cells, the biological membrane is a crucial component that allows interactions with the outside world. Amongst many functions, it regulates influx and efflux of nutrients and toxins, provides structural rigidity to maintain or permit changes in cell morphology, maintains electrochemical ion currents, and is a ubiquitous interface for signalling processes that allow a cell to communicate with its surroundings.

The biological membrane is a hydrophobic barrier which is formed in part by lipids; amphipathic molecules that contain a hydrophobic "tail" and hydrophilic "head". In aqueous media, lipids self associate (*via* the entropically driven hydrophobic effect to form a membrane which segregates the hydrophobic tails from bulk water), thus forming a semi-permeable membrane. The importance of lipids as constituents of the cell membrane (as well as other processes such as energy storage [8] and signalling [9]), is evidenced by the fact that 5% of all eukaryotic genes code for lipids biosynthesis [10]. Also present in a biological membrane are a diverse range of membrane proteins, which can be embedded in the membrane and/or extend out into solution. The lipids, proteins and other species that constitute a biological membrane are incredibly diverse, and composition, morphology and function of different membranes across species varies widely. A simplified model, the fluid mosaic model [11], defines the membrane as a two-dimensional bilayer of lipids, in which proteins and other species diffuse laterally, with some species performing both structural and functional roles. Some predominant features of prokaryotic and eukaryotic membranes are given in Figure 1.2.

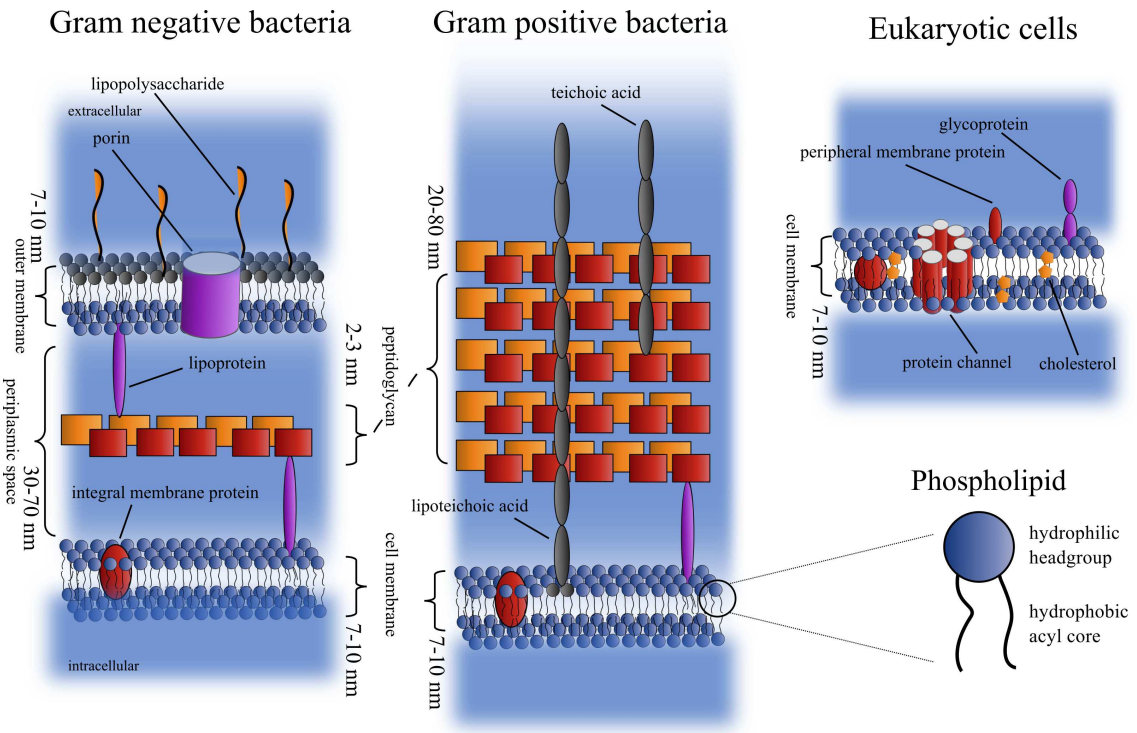

Figure 1.2 The biological membranes of different cellular species. Lipid bilayers contain a very many number of different molecular species, with the predominant and common structures shown. The quoted thicknesses are an estimate and can very greatly between species and also depend on the technique used to measure thickness (such as transmission electron microscopy and X-ray diffraction). Figures adapted from [12, 13].

1.2.1 Membrane lipids

Over 40,000 lipids, classified according to the chemical identity of the hydrophobic and hydrophilic portions of the molecule, have been isolated [14], and a quarter of these are glycerophospholipids [15]. Glycerophospholipids comprise a glycerol esterified with two fatty acids (the hydrophobic "tail"), which is esterified to a phosphate at the *sn*-3 position.* The phosphate is condensed with a hydrophilic headgroup to furnish the amphipathic lipid. The headgroup varies in size and charge, and these properties affect the physical behaviour of the bulk membrane they constitute. For example, phosphatidylcholine (PC) and phosphatidylethanolamine (PE)

*sn stands for stereospecific numbering. This nomenclature for lipids is conventional used, allowing the spatial conformation of the molecule to be intuited quickly [16].

lipids are zwitterionic (the cationic choline and 1° amino group respectively balancing the charge of the anionic phosphate), while phosphatidylglycerol (PG), phosphatidylserine (PS) and phosphatidylinositol (PI) lipids bear an overall negative charge at physiological pH. Additionally, the size of the headgroups influences the conformation they adopt in lipid bilayers [17]. The acyl chains also vary in length and degree of unsaturation. Common phospholipids found in biological membranes are summarised in Figure 1.3.

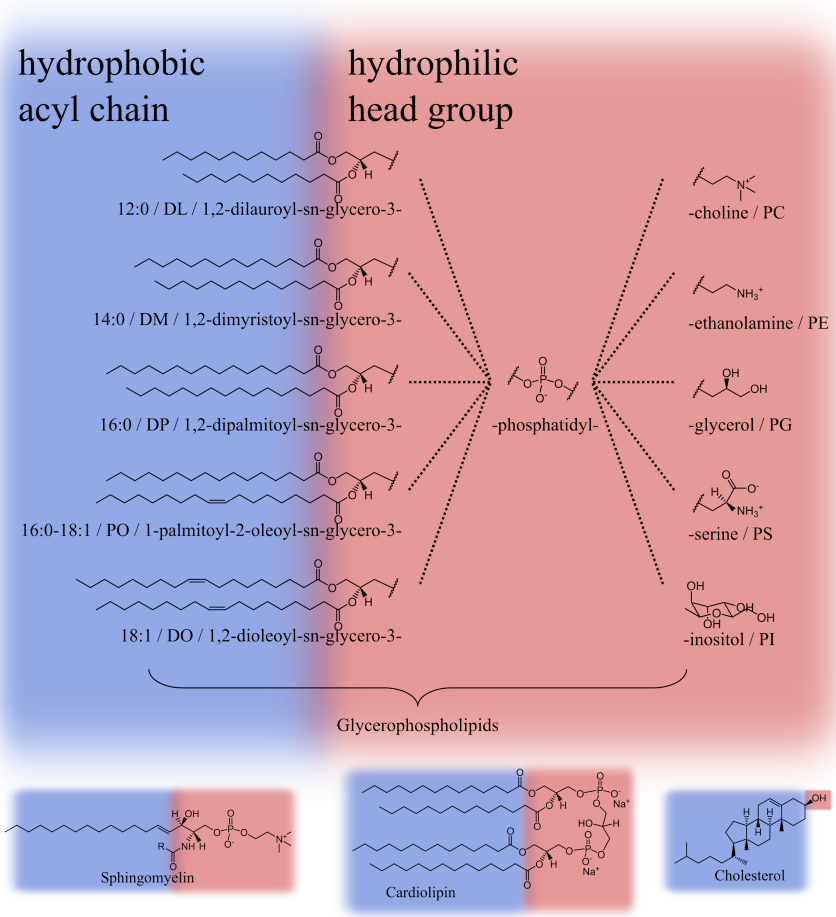

Figure 1.3 The structures of commonly occurring membrane lipids. Glycerophospholipids are composed of an hydrophobic diacyl "tail", and a hydrophilic phosphatidyl "head". The acyl chain length (first number of shorthand notation), degree of saturation (second number of shorthand notation), and headgroup identity varies greatly between cell membranes. Sphingomyelin is closely related to the glycerophospholipids and the R group can be any of the acyl chains associated with glycerophospholipids. Cholesterol consists of a hydrophilic hydroxyl group bonded to a hydrophobic sterol core.

The biological membranes of the organelles of all species have differing compositions of lipids. Headgroup identity varies across species, and are even absent in some; for example 15% of Gram-negative bacterial membranes are devoid of phosphatidylcholine [18]. The distribution of different headgroups amongst different cell membranes is given in Table 1.1; models for mammalian cell membranes, and those of Gram-negative and Gram-positive bacteria will be studied extensively in this thesis.

	Lipid composition (molar %)							
Organism	PC	PE	PI	PS	PG	SM	CL	CLT
E. coli (inner membrane)	-	70 – 80	-	-	15 – 20	-	5	-
S. aureus	-	20	-	-	50	-	30	-
Mammalian Cell (Rat brain)	40	34	3.4	11.5		6.4	30	21.5(w/w)

Table 1.1 Typical representative lipid compositions of the biological membranes of a gram negative bacterial inner membrane (*top*)[19], a gram positive bacterial membrane (*middle*)[20], and a mammalian plasma membrane (*bottom*)[21].

In addition, the acyl chain length and degree of saturation also varies greatly (and have also been shown to be genetically controlled and induced by bacteria in response to external pressures such as temperature [22]); thin-layer chromatography and mass spectrometry to compare lipids isolated from a cell membrane to lipid standards has been carried out for membranes across many species and tissue types [23]. The differences in lipid headgroup and acyl chain identity are the basis for the selectivity of many processes affecting specific cell types, such as the toxicity of antimicrobial peptides for bacteria [24], marking PS-rich membranes for apoptosis [25], and the identification of cancerous cells from their abnormal lipid profile [26]. The variation in acyl chains across cell membranes of different eukaryotes and prokaryotes organisms are given in Table 1.2; commonly occurring acyl lengths across many species are DM- and PO- lipids, and are used extensively in forming model membranes.

Membrane	Lipid	Acyl length and saturation												
type	headgroup	14:0	15:0	16:0	16:1	17:0	17:1*cpr*	18:0	18:1	18.2	19:1*cpr*	20:1	20:4	22:6
Rat brain														
	-PC [27]	0.3	-	45.0	1.4	-	-	13.8	32.5	-	-	0.4	5.1	0.5
	-PE [28]	-	-	7.1	1.7	-	-	34.3	35.2	-	-	3.8	9.9	7.6
	-PS [29]	0.9	0.6	22.8	2.2	0.8	-	15.3	15.0	30.9	-	-	7.6	0.3
E. coli														
	-PE [30]	8	-	47	23	-	10	-	11	-	-	-	-	-
	-PG [30]	2	-	43	20	-	7	-	26	-	-	-	-	-
	-CL [30]	2	-	42	20	-	4	-	30	-	-	-	-	-
S. faecalis														
	-PG [31]	5.6	2.3	38.1	6.8	-	-	1.9	17.3	-	31.5	-	-	-
S. lactis														
	-CL [32]	11.6	-	22.5	15.6	-	-	-	48.9	-	-	-	-	-

Table 1.2 The acyl chain length and saturation distribution of different lipid headgroup types for a eukaryotic cell membrane (*top*), a Gram-negative bacterial inner membrane (*middle*), and a family of closely related Gram-positive bacterial membranes, which are studied in this thesis. $X:X$ refers to acyl length : number of unsaturated bonds in the acyl chain. cpr=*cis*-11,12-methyleneoctadecanoyl.

Mesotropic behaviour and morphology of lipidic structures

Phospholipids in aqueous dispersions spontaneously self associate to form a variety of morphologically distinct macroscopic structures, depending on the lipid type/mixture and environmental factors (Figure 1.4).

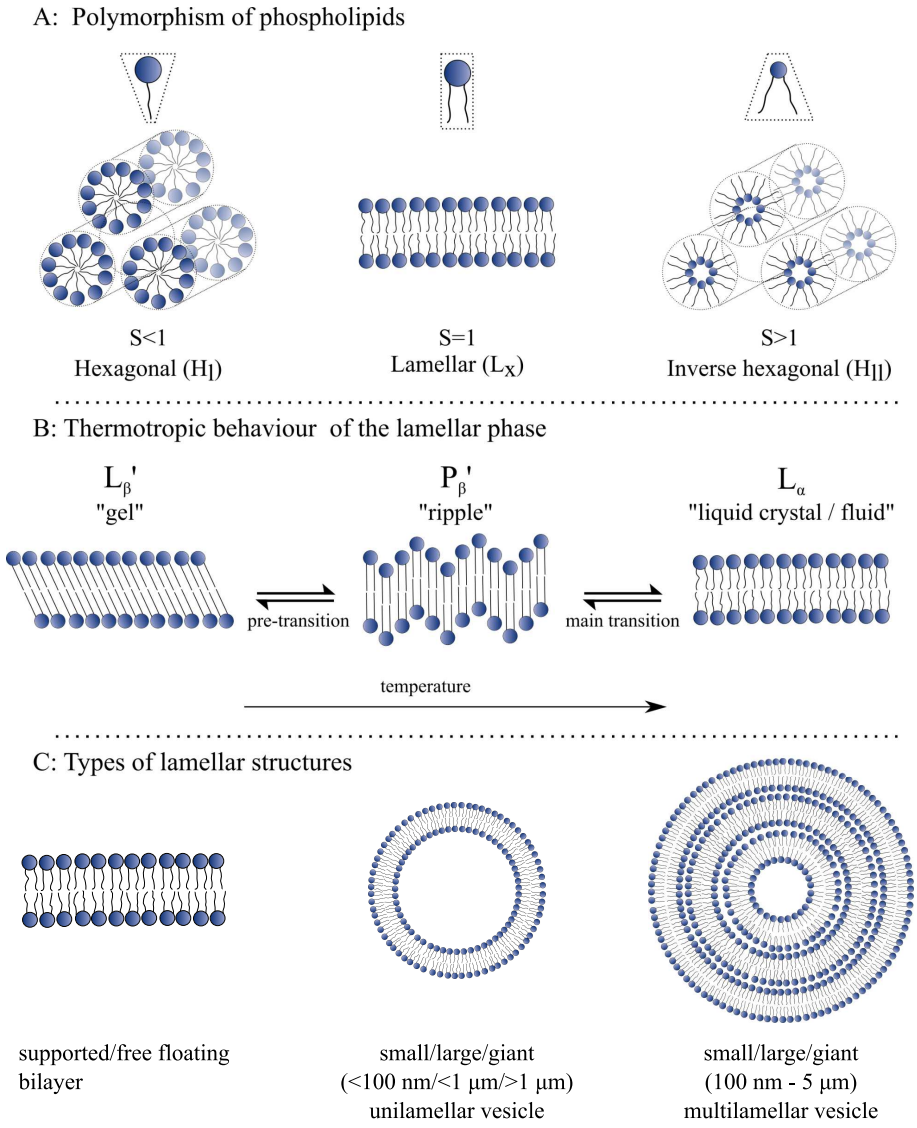

Figure 1.4 The polymorphic forms of various lipids.

The nature of the headgroup and number of acyl chains of a lipid dictate the steric shape of the molecule. It can be described by the shape parameter $S = \frac{V}{l_c a_o}$ [33], where a_o is the optimum area per lipid, V is the volume per lipid and l_c is the fully extended (all-*trans*) length of the acyl chain. For $S < 1$, lipids are cone shaped, and form micelles and the rod-shaped hexagonal H_I phase. For $S = 1$, lipids (such as -PC)

are cylindrical, and form lamellar phases and organise into bilayers. For $S > 1$, lipids (such as -PE) are wedge shaped and form inverse micelles and the rod-shaped hexagonal H_{II} phase (Figure 1.4 A). Phases can also interconvert with temperature and pH [34].

The lamellar phase shares many characteristics of native membranes, in terms of curvature, bilayer structure and fluidity. Within the lamellar phase, several thermotropic subphases exist. The gel phase (L_{β}') describes where the acyl chains are tightly packed together due to van der Waals interactions, with little lateral movement $\backsim$ 5 μm s^{-1} [35]). The intermediary ripple phase (P_{β}') maintains this lack of lateral motion but the planar bilayer experiences corrugated undulations [36]. After a certain temperature the van der Waals interactions are, cooperatively, partially overcome. The hydrophobic core becomes more fluid, with greater lateral movement ($\backsim$ 25 μm s^{-1}), and the lipids enter the liquid crystal (L_{α}) phase (Figure 1.4 B). The temperature at which this transition occurs depends on the length of the lipid acyl chains (and hence degree of van der Waals interactions) and the ability of the headgroup to hydrogen-bond between neighbouring headgroups.

The phase of the lipid membrane is physiologically important; a study on the antimicrobial peptide microcin J25 by FT-IR showed that the AMP preferentially interacts with gel-phase lipids [37]. In addition, it is believed that in mammalian membranes there is a coexistence of laterally separated lipid domains of different phases, sometimes called lipid rafts [38].

The lamellar structures can also vary in their global macromolecular organisation (Figure 1.4 C); vesicles of varying sizes and number of layers can be formed by mechanical extrusion and sonication, to form small unilamellar vesicles (SUVs, $r < 50$ nm), large unilamellar vesicles (LUVs, $50 < r < 400$ nm) or multilamellar vesicles (MLVs, $r < 500$ nm), where r is the radius of the vesicles. The addition of polymers and membrane scaffold protein allows ($\backsim$ 10 nm) size bilayers to be formed [39, 40].

It is clear the choice of lipids to mimic specific cell membranes must be accompanied by considerations of the phase behaviour of the lipids, and the polymorphic phase formed, if it is to be amenable to the methodology used to interrogate molecular interactions.

1.2.2 Asymmetry in membranes

Membrane lipids do not only vary between cellular species; the distribution of lipids between the two leaflets of the lipid bilayer has also been shown to be asymmetrically distributed. Methods of chemically altering the outer leaflet of a membrane have revealed the asymmetric distribution of lipids, for example by reaction of nucleophilic PE lipids with a radioactive reporter (Figure 1.5) [41].

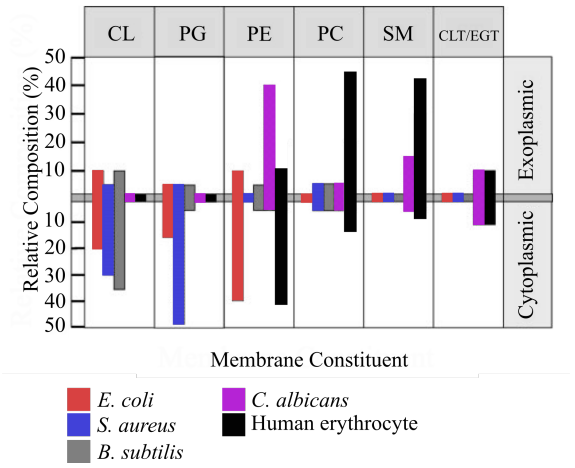

Figure 1.5 The asymmetric lipid distribution of phospholipids between the outer and inner leaflets of different cell membranes. **CL:** Cardiolipin **PG:** Phosphatiydlclycerol **PE:** Phosphatidylethanolamine **PC:** Phosphatidylcholine **SM:** Sphingomyelin **CLT/EGT:** Cholesterol (mammalian membranes) / ergesterol (Fungal membranes). Data reproduced from [20].

Asymmetry has important implications for biological function; for example in normal red blood cells, approximately 76% of total zwitterionic PC lipids are located on the outer leaflet of the cell membrane, while around 80% of total PE lipid and all PS lipids are located on the inner leaflet [42], creating charge separation between the two leaflets. The collapse of this asymmetry in humans has been found to contribute to anemia [43].

Lipid asymmetry is thermodynamically unfavourable and is actively maintained in biological membranes by enzymes that "flip" lipids from the outer leaflet to the inner leaflet (flippases [44]), or "flop" lipids in the other direction (floppases [45]). Scramblases also exist which indiscriminately flip and flop lipids, which are thought to destroy asymmetry in membranes [46]. In the absence of such enzymes, lipids can also spontaneously "flip" and "flop" to re-equilibrate lipid distribution. The lifetime of the asymmetry, or converserely the rate of re-equilibration of a membrane lipid distribution by flip flop, has been measured by EPR [47], fluoresence [48] and small angle neutron scattering [49]. Table 1.3 displays the time taken for flip-flop ($t_{\frac{1}{2}}$) for different lipids.

Lipid type	Lipid host	Vesicle type	T (°C)	$t_{\frac{1}{2}}$ (h)	ref
14 : 0 PC	14 : 0 PC	SUV	23	16	[50]
			30	10	[50]
		LUV	30	$\leqslant 9$	[51]
			50	$\leqslant 0.7$	[51]
16 : 0 PC	18 : 1 PC	SUV	30	> 48	[52]
16 : 0 – 18 : 1 PC	16 : 0 – 18 : 1 PC	LUV	37	1000	[53]
egg PG (10%)	16 : 0 PC	-	45	11.2	[54]
	18 : 1 PC	-	50	13	[54]

Table 1.3 Table of flip-flop rates ($t_{\frac{1}{2}}$) for different lipid species. A compendium of flip flop rates can be here [23].

$t_{\frac{1}{2}}$ strongly increases with acyl chain length and hence the hydrophobic thickness of the bilayer. It also increases at higher temperatures, increasing unsaturation in(and hence more fluid) acyl chains, and with larger, charged headgroups.

Although the importance of asymmetry in natural membranes was highlighted at the same time that the fluid-mosaic model was proposed [11, 33, 55], recreation of this in model membrane systems has not greatly explored. Methods of achieving asymmetry in model membranes are covered in Chapter 3.

1.3 Antimicrobial peptides

1.3.1 History

Antimicrobial peptides (AMPs), or host defence peptides, are a class of molecule that have a broad spectrum toxicity against eukaryotic and prokaryotic species. First discovered in 1939 [56], AMPs have been isolated in virtually every species screened for this activity (Table 1.4). Fruit flies that were genetically modified to not produce AMPs are susceptible to infections from fungi such as *M. anisopliae*, providing the first direct evidence for the role of AMPs in the innate immune system [57, 58]. Since the association of cathelicidin AMPs with mammalian host defence [59] in 1994, there has been a vast increase in AMPs discovered every year, and to date over 2,500 AMPs have been deposited in the antimicrobial peptide database (Figure 1.6) [60].

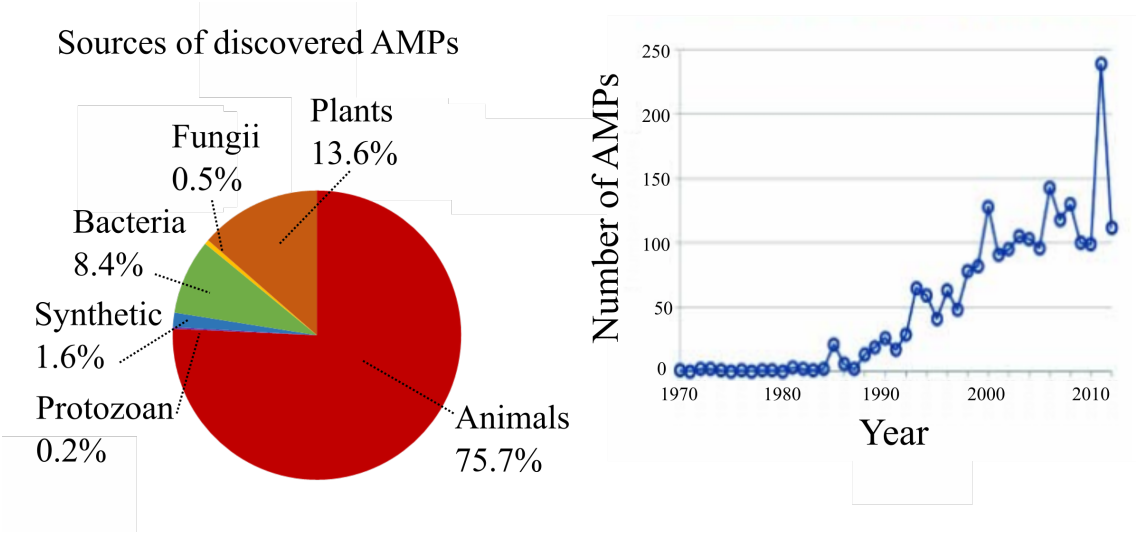

Figure 1.6 (*left:*) The distribution amongst species where AMPs have been discovered. (*right:*) Number of AMPs discovered since 1970. Data reproduced from [61].

1.3.2 Structure

AMPs target a variety of organisms and necessarily vary in their structural features, but share a broad shared set of characteristics. AMPs, generally between 10 and 50 amino acids long, tend to have unstructured extended conformations in solution ([61]). In the presence of a membrane environment, the peptides adopt an amphipathic secondary structure, with a polar, cationic, face that can interact with the polar, anionic or zwitterionic, headgroup of the lipid bilayer in an electrostatic manner, and a hydrophobic face that interacts with the hydrophobic acyl core *via* van der Waals interactions [72].

A large number of AMPs are α-helical in the presence of membranes, including the frog-derived magainins [73] and LL-37 [69]. Other peptides form β-sheets, stabilised by disulfide bonds, such as lactoferrin B and the human defensins [74]. θ-defensins, found in non-human primates [75], consist of a pair of antiparallel β-sheets which are stabilised by three disulphide bonds arranged as a ladder. They have also been shown by NMR to form trimers in a concentration-dependent manner in the presence of detergent micelles [76]. Other AMPs do not adopt any defined secondary structure, even in the presence of lipid membranes, such as the histidine-rich histatin [77]. The secondary structures of AMPs that have been deposited in the antimicrobial peptide database, are a distribution between α-helices, β-sheets, a mixture of conformations, and unknown (14%, 3%, 21% and 62% respectively) [74]. It is important to note that for a very many number of AMPs, there is no clear evidence that there is a single bioactive structure. Due to the small size and dynamic nature of AMPs, and the lack of a specific cellular target, they can sample a variety of secondary structures which do not strictly conform to a single population of α-helices or β-sheets. For example, indolicin, a small 13-residue AMP was shown to sample unordered, β-turn and "wedge" shaped conformations, depending on lipid environment [78].

AMP	Year discovered	Source	Comments
Gramicidin [56]	1939	Soil *Bacillus* strain	First AMP discovered, used clinically against *Neisseria*
Purothionin [62]	1942	Common wheat	First plant derived AMP
PolymixinB [63]	1947	*Paenibacillus polymyxa*	
Melittin [64]	1967	Bee venom	Also used to treat HIV
Bombinin [65]	1970	Fire-bellied toad	
Cecropin [66]	1981	Silk moth	First demonstration of α-helical structure
Defensin [67]	1985	Human skin	First AMP isolated in humans
Mersacidin [68]	1992	*Bacillus* HIL Y-85,54728	
LL-37 [69]	1996	Various mammals	
Thrombocidin [70]	2000	Human blood platelets	Chemokine also functions as AMP
Teixobactin [71]	2015	Uncultured bacteria	First new class of antibiotic action in 30 years

Table 1.4 A selected timeline of AMP discovery [61].

Most AMPs also display a substantial positive charge, with the majority ranging from +2 to +10 (Figure 1.7, left). It is believed the electrostatic attraction to negatively charged PG, PS and CL lipids, as well as LPS and teichoic acids, is the basis for the selective toxicity of the cationic AMPs to microbial membranes [20]. However, the majority of AMPs do not carry a charge greather than +5, as higher charges causes increased hemolytic activity, presumably as a result of indiscriminate binding to all cell membranes. A study on the synthetic peptide L-V13K, where the charge of the charged face of the amphipathic helix was varied between −5 and +10, found that the relationship between charge and hemolysis was not simple, and a drastic increase of 32% hemolytic activity was observed between +8 and +9 charged peptides [79].

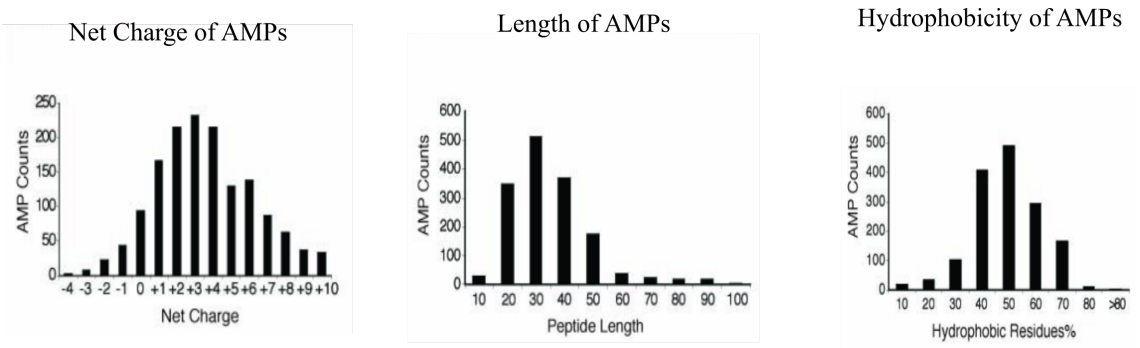

Figure 1.7 Collated properties of all known AMPs. Data reproduced from the antimicrobial peptide database [74].

The hydrophobicity of AMPs also varies between 40% and 70% of hydrophobic residues, such as Leu, Ile, Val, compared to the total. Increases in hydrophobicity are also positively correlated with hemolytic activity (Figure 1.7, right). Another study, again on L-V13K, demonstrated that increasing the hydrophobicity of the peptide caused an increase in hemolytic activity and degree of self-association, which in fact resulted in a decrease in bactericidal activity due the aggregated species being too large to penetrate the bacterial cell wall [80].

AMPs are also produced non-ribosomally by microbes, and examples abound of AMPs containing non-proteinogenic amino acids. The familiy of Gramicidin peptides, for instance, contain a mixture of alternating *D* and *L*-amino acids in the peptide back-

bone [81], and are synthesised by four non-ribosomal peptide synthetases [82]. Alamethicin, an AMP produced by the fungus *Trichoderma viride* that forms ion channels in bacteria, belongs to a family of peptides known as peptaibols [83]. These peptides contain amino acids such as ethylnorvaline, isovaline and hydroxyproline, are acetylated at the N-terminus and hydroxylated at the C-terminus to an alcohol. Synthetic AMPs also exist with β- and γ- peptide backbones, with subsequent stability to hydrolysis [84].

1.3.3 Mode of action

The link between AMP structure, peptide-lipid interactions and subsequent bactericidal mode of action has remained elusive. There is evidence that interactions between AMPs and cells are not receptor mediated; enantiomers containing all D-amino acid analogues of the original primary structure have an identical efficacy and bactericidal effect [85].

The site of action which leads causes the death of the microbe is thought to be the cell membrane, as detailed in many reviews [20, 86, 87]. Disruption or compromising of cell membrane or cell wall integrity would lead to cell death due to collapse of ion gradients and leakage of cellular components. The highly charged and amphipathic AMPs are ideally suited to electrostatic interactions with the (generally) negatively charged lipid membrane headgroup region, and hydrophobic interactions with the acyl core. This relationship also provides a basis for the selectivity of AMPs since the cell membranes of different species differ in their lipid compositions.

The membrane perturbations that lead to cell death are divided into three broad mechanisms of action, summarised in Figure 1.8.

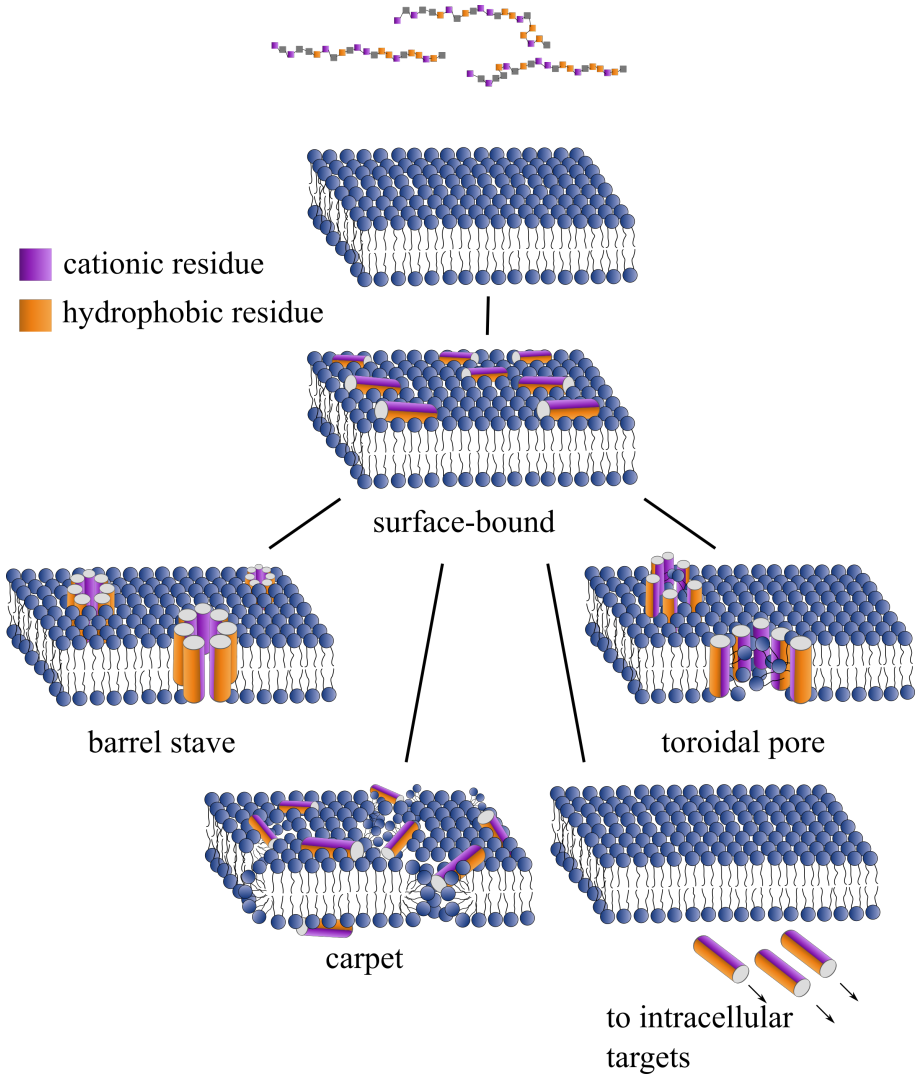

Figure 1.8 Schematic showing the generally accepted mechanisms by which the lytic effect of AMPs with cell membranes is exerted. The peptides are initially generally unstructured in solution (with the exception of peptides stabilised by sulfide bridges). Upon first contact with a bacterial membrane, the peptide folds into a variety of amphipathic secondary structures and associates with outer surface of the cell membrane. Several subsequent independent (but sometimes co-acting) peptide-lipid interactions have been observed which are thought to be the cause of the peptides' bactericidal effect. ***Barrel stave*** After surface binding, the peptides orient across the cell membrane to form pores. ***Carpet*** Above a threshold concentration, the surface-associated peptides cause membrane destabilisation in a detergent-like manner, rupturing the cell membrane into smaller vesicles. ***Internalisation*** Some peptides translocate the cell membrane without compromising its structural integrity, and destroy intracellular targets. ***Toroidal Pore*** Peptides orient transmembrane like the barrel stave, but the pore is lined by lipids, connecting the inner and outer leaflets.

Carpet mechanism

In this process, AMPs bind to the outer leaflet of a microbial membrane. After a threshold concentration on the surface is reached, perturbation of lipid fluidity and membrane thickness cause disruption of membrane integrity due to unfavourable energetics by exposing the acyl core to the aqueous environment. This has been shown to be sufficient for bactericidal effect; indolicin was shown to not penetrate cell membranes by CD, NMR and fluorescence experiments while still causing lysis of bacteria [88]. Peptides need not necessarily act in a cooperative manner, and oligomerisation is not a requisite for this phenomenon. Despite acting in a detergent-like manner, the AMPs still discriminate between different cell membranes. It is thought that the preferential initial interaction of AMPs of this class with more negatively charged bacterial membranes precludes interaction with mammalian membranes that are less highly charged in the outer leaflet.

Barrel stave mechanism

Upon associating with a bacterial membrane, peptides adopt a transmembrane orientation, making contacts with the lipid headgroups of the inner leaflet of the bilayer. By associating with other transmembrane monomers, an aqueous pore can form, causing the collapse of ion gradients. By associating in clusters, the hydrophobic faces of each amphipathic oligomer can project out towards the acyl lipid core, while the hydrophilic face lines the aqueous pore, forming a thermodynamically stable structure. Subsequently, more peptides can associate, expanding the pore. Evidence for this mode of action is provided by solid-state NMR experiments; labelling of the backbone of alamethicin with ^{15}N revealed the AMP was oriented with a 17° tilt to the membrane normal [89]. In addition, conductance measurements confirmed the existence of pores within the membrane, with a conductivity of 180 pS/m [90].

Toroidal pore mechanism

Toroidal pores are adopted by many α-helical peptides such as the magainins and melittin [91]. In a similar manner to barrel stave-forming peptides, AMPs of this class first orient flat on the membrane. Upon reaching a critical threshold concentration, the peptides insert transmembrane and form a peptide-lipid supramolecular complex in which the phospholipid headroups curve inwards, forming a continuum between the inner and outer leaflets. The orientation of the phospholipid headgroups has been confirmed by ^{31}P solid-state nuclear magnetic resonance (ssNMR) on model membranes [91]. The curvature strain induced by the peptides cause disruption of cell membrane integrity, but AMPs have been shown to translocate in this manner to the interior of a cell membrane. Thus, the true targets of some AMPs may be intracellular components, and the transient pores may merely be a means of gaining entry into the cell, which may be mechanistically similar to the related family of non-bacterical cell-penetrating peptides [92].

Non-membrane interactions

AMPs have been demonstrated to target intracellular components of a cell membrane; bacteria can survive extended periods following permeabilisation of the cell membrane, implying factors other than membrane disruption play a role [93]. Indolicin was shown by SPR and fluorescence measurements, to bind to double-stranded DNA with micromolar affinity [78], comparable to the binding of DNA to zinc finger proteins [94], hinting at targets other than the cell membrane, and suggesting the boundary between AMPs and traditional, target-specific antibiotics may be a blurred continuum.

There is also growing evidence that under physiological conditions, membrane interactions may not even play a role in antimicrobial activity, and instead the secreted AMPs modulate the immune system of the host [95]. LL-37 was shown to be less efficacious against *E. coli* in minimum inhibitory concentration (MIC) experiments

with elevated salt concentrations, simulating a more biologically relevant environment. However, they were also found to promote cytokine production and wound healing [96]. In a separate study, cathelicidins injected in the bladders of mice were shown to induce a "second wave" of AMP production from host leukocytes [97].

1.3.4 Resistance

Despite their prevalence, AMPs appear to induce remarkably little resistance in the pathogen they are attacking. The ability of a pathogen to alter lipid make-up of the cell in response to an AMP does not appear to be a mechanism for inducing resistance compared to modification of the gene of a specific intracellular target [20]. The fact that most AMPs are broad spectrum, *ie* toxic to both Gram-negative and Gram-positive bacteria, implies they are exploiting a fundamental property of a range of genetically unrelated bacterial species that is not easily modified. Another explanation is that most AMPs are not constitutively expressed, and are only induced during an pathogenic attack to the host [98]. It could be that the relatively low presence of AMPs in the general biological environment prevents pathogens from accruing an appropriate defence mechanism.

However, examples do exist of resistance being acquired upon treatment with AMPs. *Vibrio cholerae* was demonstrated to alter the outer membrane surface of the Gram-negative bacterium in the presence of polymixin B. Using mass spectrometry, it was observed that modification of lipid A, a component of LPS which makes up a large part of the outer membrane, with glycine and diglycine residues reduced the surface charge of the cells. This results in an associated reduction in susceptibility to the AMP [99]. In another study, *in vivo* and *in vitro* studies showed that *S. flexneri*, another Gram-negative bacterium, dampened host innate immune response by suppressing transcription of AMP peptide genes [100]. It has also been posited that bacteria could express an anionic complimentary helix that can form coiled coils with an AMP, nullifying its activity [101, 102]. The reported mechanisms by which bacteria may acquire

resistance are summarised elsewhere [20].

Summary

It is still far from clear precisely how AMPs interact with lipid membranes, and how this is correlated to bactericidal activity. A single mechanism or multiple co-acting or independent processes may be occurring. Due to their small size and lack of long range order, few examples in the literature exist on crystallised AMP structures [60], and solution NMR on micelles cannot replicate the native morphology and complexity of cell membranes, and hence a great need remains to characterise fully AMPs and their complex peptide-lipid interactions in better model membranes.

1.4 Experimental techniques used in this thesis

1.4.1 Quartz crystal microbalance with dissipation monitoring

General principles

Quartz crystal microbalance (QCM) is an instrument that can be used to measure 3-dimensional changes in mass and structure of a supported lipid bilayer [103].[†] In the course of an experiment, an AC voltage is applied to a piezoelectric quartz chip. This causes the chip to oscillate in shear mode (*ie* parallel to the chip surface) at its fundamental frequency, as well as at harmonics, or overtones, above this. Lipid vesicles can be flowed over the chip, and adsorption to the surface causes them to rupture and form a supported lipid bilayer (Figure 1.9).

The change in resonance frequency of the chip (Δf) is sensitive to addition of material and can be related to the mass adsorbed by the Sauerbrey equation [106]

$$\Delta m = -C\frac{\Delta f_n}{n}, \tag{1.1}$$

[†]As the name suggests, QCM was originally used as an ultrasensitive weighing device [104].

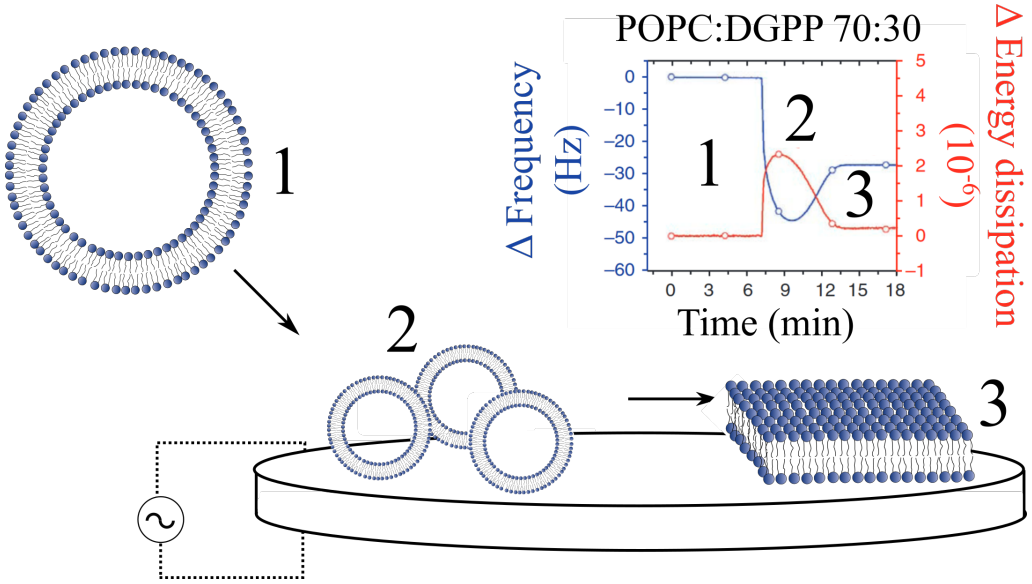

Figure 1.9 Schematic showing bilayer deposition on a QCM chip. (***1***) Vesicles in solution diffuse onto the surface of the chip (***2***), causing a drop in the chip frequency. After a threshold concentration the adsorbed vesicles spontaneously rupture to form a supported lipid bilayer (SLB), with an associated increase in frequency as water is lost from the surface. The inserted QCM trace of Δ frequency and Δ dissipation energy against time show the formation of a stable POPC:DPGG 70:30 SLB. QCM trace reproduced from [105].

where n is the overtone number and C is a sensor dependent mass sensitivity constant, which for standard 14 mm 5 Hz chips routinely used is 17.7 ng/cm^{2}Hz [107]. It should be noted that the Sauerbrey equation only strictly holds for rigid masses in a vacuum, and thus the mass deposited is normally described in a qualitative manner. This can be further converted to the thickness and viscoelasticity of the film by the Voigt viscoelastic model [108]. By removing the AC voltage periodically it is also possible to measure the energy (E) lost to the surrounding environment. Experimentally this is related to the measured dissipation factor D by [104]

$$D = \frac{E_{dissipated}}{2\pi E_{stored}}. \tag{1.2}$$

High D values imply less rigidty in the material, while low D values suggest structural compactness and rigidity.

The key advantage of QCM to measure changes of bilayer properties upon interaction

with a peptide, is that the different harmonics can supply 3-dimensional information on the supported bilayer [109]. The frequency of a harmonic is inversely proportional to the depth of penetration [110]. Thus, higher frequency harmonics probe near the surface of the chip, with lower harmonics probing structural and mass changes further from the surface. It is hence possible to examine changes as a function of hydrophobic and hydrophobic depth of the supported bilayer.

Δf-ΔD *plots to probe mechanisms of action*

Raw QCM data are typically presented as Δf-Δt and ΔD-Δt plots, showing mass and structural rigidity changes over time. A useful way of interpreting the QCM data is by constructing a Δf-ΔD plot [111], and figure 1.10 shows two typical Δf-ΔD plots, for caerin 1.1 and a related mutant.

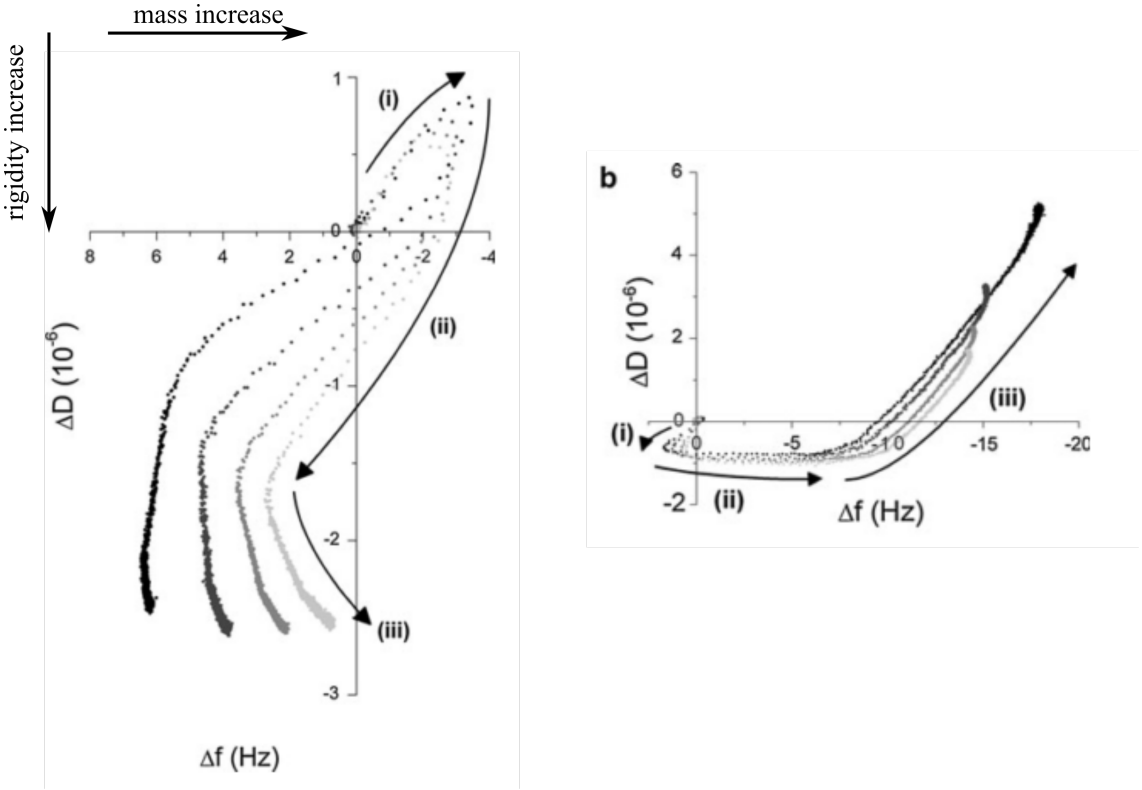

Figure 1.10 Δf-ΔD plots for the interaction of two AMPs with a DMPC SLB. The interaction of caerin 1.1 (***A***) with the SLB is markedly different from a double proline to glycine mutation (***B***). The darkest to lightest traces are for the third to ninth harmonics. Data reproduced from [109].

Each data point is an instantaneous D and f value at a given time, and thus the spacing between points gives an indication of the rate of the molecular events taking place, providing qualitative details for describing mechanism of action and dynamics when an AMP is flowed over the supported lipid bilayer [109, 112]. Sudden changes in direction of the Δf-ΔD plot that show different molecular rearrangements are occurring in the bilayer, and the number of points on the Δf-ΔD plot allows inference of the timescale of the process. In the example above, the two Δf-ΔD plots in Figure 1.10 show the interaction of caerin 1.1, an AMP from the Australian tree frog, and a double proline to glycine mutant of caerin 1.1 [109]. It can be seen that the wild-type peptide has periods of accumulating on the surface (Figure 1.10 A(i)). This is followed by a sudden and fast decrease in mass with an accompanied increase in rigidity of the membrane (Figure 1.10 A(ii)), indicating speculative lipid removal from the SLB. Then, slow mass gain at the lowest harmonics is observed (Figure 1.10 A(iii)), implying these interactions are all occurring at the headgroup region of the SLB. These observations are consistent with the carpet mechanism. The mutant however displays a starkly different Δf-ΔD plot (Figure 1.10 B), showing only gradual accumulation of peptide on the surface of the SLB, implying no disruption is taking place. It can be seen that from the Δf-ΔD plots that in conjunction with complimentary techniques such as NMR and EPR, mechanistic information can be gained and related to the primary structure of the AMPs in question, providing a mechanistic fingerprint which can be compared to other AMPs.

QCM has also been used to examine the presence of different lipid membrane constituents, and the effect they have on AMP interactions. QCM experiments performed with three synthetic arginine-tryptophan (R_xW_y) AMPs, revealed that the positioning of tryptophan residues affected the disrupting ability of the peptides, and that the presence of cholesterol accentuated these differences [112]. This provided evidence for the importance of cholesterol-tryptophan interactions [113], and the significance of cholesterol in protecting mammalian membranes from destruction by AMPs.

1.4.2 Solid-state nuclear magnetic resonance (ssNMR)

General Principles

Magnetic resonance techniques exploit an intrinsic property of many types of particle, namely angular momentum, or more commonly, spin. In nuclear magnetic resonance spectroscopy (NMR) magnetically active nuclei with non-zero spin are the molecular probes that are exquisitely sensitive to the surrounding electronic environment and dynamics. One of the many advantages of NMR is that the probes are non-perturbing (or minimally perturbing magnetically active isotopes) that often are already present in the system of interest.

Nuclear spin is a quantized property, and the magnitude of which ($|\vec{I}|$) is given by equation 1.3:

$$|\vec{I}| = [I(I+1)]^{\frac{1}{2}}\hbar, \tag{1.3}$$

where I, the nuclear spin quantum number, also quantized, can take whole- and half-integer values greater to or equal to 0 (Equation 1.4):

$$I = 0, \frac{1}{2}, 1, \frac{3}{2}, 2, ... \tag{1.4}$$

The constant $\hbar$, the reduced Planck's constant, is related to the Planck's constant by $\hbar = \frac{h}{2\pi}$. Spin is a vector quantity and hence has an associated direction, which is also quantized. The direction component takes $2I+1$ values. The projection of the vector onto an arbitrary axis, conventionally the z-axis, and hence the z component of the angular momentum $\vec{I}_z$ is given by equation 1.5:

$$\vec{I}_z = m\hbar, \tag{1.5}$$

where m is the quantised magnetic quantum number, and can take values between $-I$ and I in integer steps. In the absence of a magnetic field, these orientations are

energetically equal (degenerate). Magnetically active nuclei have an associated magnetic moment parallel to the angular momentum, given by:

$$\vec{\mu} = \gamma \vec{I}, \tag{1.6}$$

where the constant γ is the gyromagnetic ratio. Upon application of a magnetic field of strength $\vec{B}$, the degeneracy of the orientations of angular momentum is lifted, where the energy of each state is given by equation 1.7:

$$E = -\mu_z B = -m\hbar\gamma B. \tag{1.7}$$

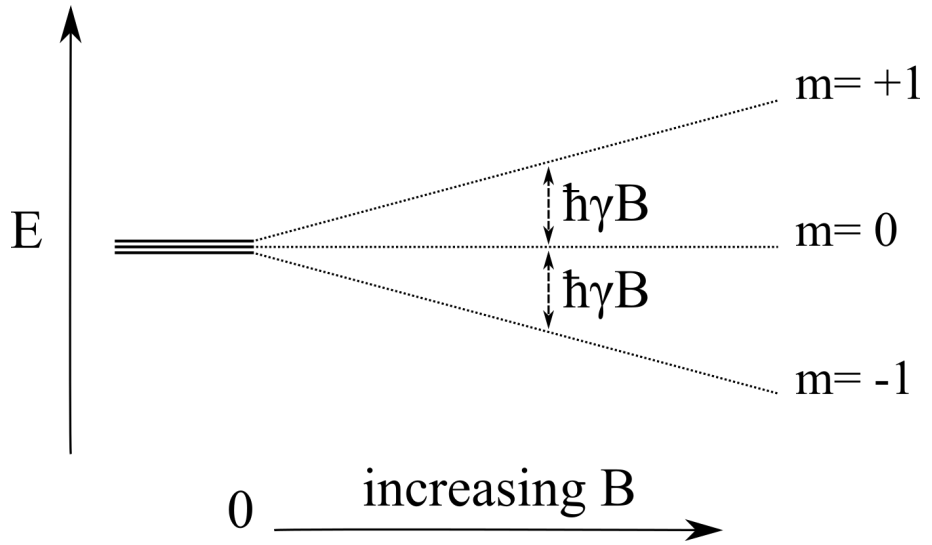

Figure 1.11 Zeeman splitting for a spin $I = 1$ nucleus, such as deuterium. As the magnetic field increases, as does the splitting between energy levels and hence the energy required to induce transitions.

This phenomenon is known as the Zeeman effect and is illustrated in Figure 1.11. To induce a transition between energy levels, the selection rule $\Delta m = \pm 1$ must be obeyed. Substitution of equation 1.7 therefore gives the resonance, or Larmor frequency of an incoming photon to induce a transition (Equation 1.8):

$$\Delta E = h\nu = \hbar\gamma B \implies \nu = \frac{\gamma B}{2\pi}. \tag{1.8}$$

The Larmor frequency of important magnetically active nuclei are summarised in Ta-

Nucleus	Spin quantum nº	Gyromagnetic ratio 10^7 T^{-1} s^{-1}	Resonance frequency MHz	Natural abundance %	Sensitivity relative to ^{13}C
^{1}H	$\frac{1}{2}$	26.75	400	99.985	5670
^{2}H	1	4.11	61.4	0.015	0.0082
^{13}C	$\frac{1}{2}$	6.73	100.6	1.108	1
^{15}N	$\frac{1}{2}$	−2.71	40.5	0.37	0.022
^{19}F	$\frac{1}{2}$	25.19	376.5	100	4370
^{31}P	$\frac{1}{2}$	10.84	162.1	100	40.48

Table 1.5 Table showing the spin quantum number, gyromagnetic ratio, resonance frequency (in a 9.4 T magnetic field), natural abundance and sensitivity relative to ^{13}C, of various magnetic nuclei used extensively in biological systems. Adapted from Rattle and Hore [114, 115].

ble 1.5. The Larmor frequency ν is not solely related to the intrinsic property of a nucleus; extrinsic factors such as the presence, concentration, distance, and relative orientation of other magnetic active nuclei can affect the magnetic field experienced by a nucleus, which gives a wealth of valuable structural and dynamic information on the molecular system.

Sensitivity

The distribution of nuclear spins amongst their energy levels is governed by the Boltzmann distribution. Taking a spin $I = \frac{1}{2}$ nuclear system, the ratio of the two populations can be represented in Equation 1.9:

$$\frac{n_{upper}}{n_{lower}} = e^{-\frac{\Delta E}{kT}}, \tag{1.9}$$

where k is the Boltzmann constant, T is the temperature, and $n_{upper/lower}$ refer to the population of the two spin states. ΔE, the difference in energy between spin states, even in a strong magnetic field, is minuscule compared to the thermal energy (roughly estimated at room temperature, using the above equations as 0.02 $Jmol^{-1}$ compared to 24000 $Jmol^{-1}$, respectively). Using the approximation $e^{-x} \approx 1 - x$ (for small x) the population difference can be expressed as:

$$\frac{n_{lower} - n_{upper}}{n_{lower} + n_{upper}} = \frac{\Delta E}{2kT}. \tag{1.10}$$

Therefore, for a proton in a typical 11.7 T magnetic field (more commonly known as a 500 MHz NMR spectrometer) at room temperature, the normalised difference in populations is 4.1×10^{-5}.

The sensitivity of any spectroscopic technique is governed by the net absorption of incident radiation, which in turn is subject to differences in energy level populations. As such, even for the most sensitive nucleus, ^{1}H, NMR is an inherently very insensitive technique, compared with fluoresence and EPR. Therefore, the key drawback of this technique is requiring comparatively large amounts of material, and specific chemical labelling, when looking at nuclei with a low natural abundance such as ^{2}H.

Signal detection and relaxation

In the magnetic field, the slight excess of spins in the lower energy level(s) results in an overall bulk magnetization, M_z. The spins are precessing randomly about this vector at the Larmor frequency, and hence there is no overall magnetization in the $x' - y'$ plane (Figure 1.12 A).

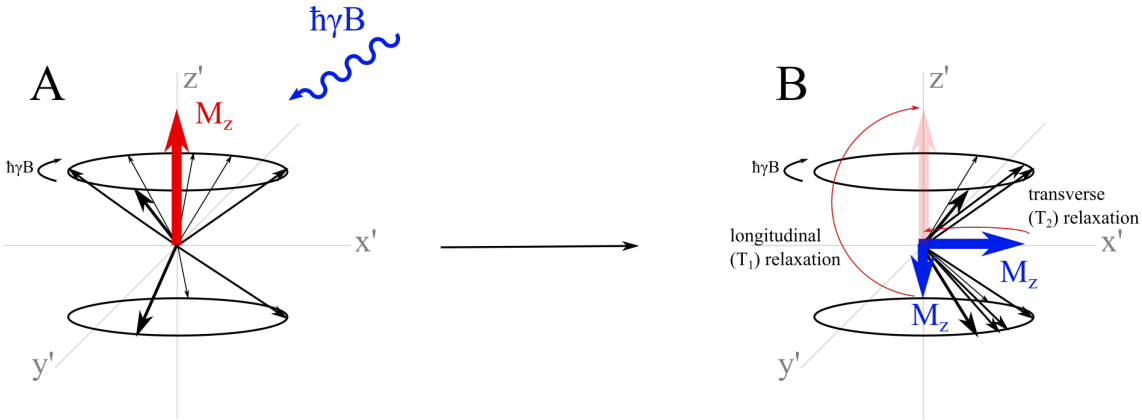

Figure 1.12 Schematic showing how an NMR signal is detected, when viewed in the rotating laboratory frame. **A:** In a stationary field, more spins are aligned with the field, causing a magnetization in the z' axis. The spins are not in phase so there is no magnetisation in the $x' - y'$ plane. **B:** Absorption of a pulse of Larmor frequency radiation causes transitions between energy states (reduction/inversion of M_z) and phase coherence (non-zero M_{xy}). Return to equilibrium state is caused by T_1 (longitudinal, M_z to original value) and T_2 (transverse, M_{xy} returns to 0) relaxation. Adapted from [115].

In a typical NMR experiment, a pulse of radiofrequency radiation at the Larmor frequency causes transitions between energy levels, causing a reduction in M_z. The pulse also causes the spins to precess together (known as phase coherence), resulting in a magnetization in the $x' - y'$ plane (M_{xy}) that precesses about M_z (Figure 1.12 B). A magnetic coil detects this rotating magnetisation which gives rises to the NMR spectrum. To return back to equilibrium population of energy levels, M_z returns back to the value (longitudinal relaxation) with a characteristic time T_1, and M_{xy} returns back to 0 (transverse relaxation) with a characteristic time T_2.

In the solution-state, T_1 and T_2 is mostly affected by spin-lattice relaxation, where instantaneous anisotropic dipolar interactions between a given nucleus and nuclei in the surroundings provide a time-dependent, fluctuating and local magnetic field. The field contains a component oscillating at the Larmor frequency which induces this transition. This relaxation rate depends on the size of the molecule (or collection of molecules) the nucleus is situated in. This in turn is described by a rotational correlation time τ_c, which is the time taken for the root-mean-square deflection of the molecule to be about 1 radian. The correlation time is related to the size (collection of) molecule(s) by equation 1.11:

$$\tau_c = \frac{4\pi\eta r^3}{3kT} \tag{1.11}$$

Where r is the hydrodynamic radius of the (collection of) molecule(s), and η is the viscosity of the solvent.

A second means of relaxation, spin-spin relaxation, is derived from short-range anisotropic interactions of a nucleus with other nuclei through bonds and space, and electrons in bonding orbitals mediated by the magnetic field and electric field gradients. these anisotropic phenomena have an angular dependence and are proportional to $3\cos^2\theta - 1$, where θ is the angle between the vector connecting a pair of spins and the external magnetic field. Since these interactions lead to a "swapping" of energy between

two spins in the system, longitudinal relaxation is not affected, and hence spin-spin relaxation only affects T_2. For molecules rapidly tumbling in solution (*ie* $\tau_c \ll T_1$ and T_2), these anisotropic interactions are averaged to 0 apart from very specialised cases (such as the centre of metal complexes [116]).

The critical difference between solution-state NMR and solid-state NMR is that the anisotropic interactions contributing to T_2 are not averaged out by molecular tumbling, and relaxation of spins is very fast. By the Heisenberg uncertainty principle, $\Delta T \Delta E \leq \frac{\hbar}{2}$, where ΔE and ΔT are uncertainties in energy in energy and time respectively, very short relaxation times cause large uncertainties in the energy of a transition, giving very broad lines in the NMR spectrum. These broadening effects can be suppressed by spinning a sample at the "magic angle", in which the sample is macroscopically aligned relative to the magnetic field at an angle which cancels the $3\cos^2\theta - 1$ term when spun sufficiently fast (magic angle spinning). However, within these broad spectra lie a wealth of orientational, angular and dynamic information which can describe the changes occurring in lipid membranes during interactions with peptides and proteins which can give valuable mechanistic information on these interactions.

It can therefore be seen that to study peptide-lipid interactions in a native-like environment, model membrane bilayers, with a t_c on the 10^{-6} timescale, must be studied in the solid state, and consideration of relaxation mechanisms leads to line broadening, but also important structural information, explained below.

^{2}*H ssNMR*

NMR-active nuclei present in model membranes experience interdependent anisotropic interactions, although interpreting the resulting NMR spectrum becomes difficult, with a very many number of broad overlapping resonances preventing deconvolution. In this regard, ^{2}H, with its low natural abundance, is an ideal nucleus as a molecular probe. It can be chemically installed at specific location on a membrane,

for example in the acyl or headgoup region of a lipid in a membrane, to allow unambiguous assignment of a resonance. Additionally, dipolar interactions with nearby hydrogens are much reduced, as this interaction is proportional to $\gamma_H\gamma_D$, which is a small term due to the low gyromagnetic ratio of deuterium.

Having a spin quantum number $I = 1$, ^{2}H nuclei have a non-spherical charge distribution, creating an asymmetric electric field within the nucleus and imbuing it with a quadrupole moment. This quadrupole moment can interact with fluctuating electric field gradients in a magnetic field, leading to a quadrupolar splitting. Since this anisotropic phenomenon depends on the orientation of a given C-D bond to the external magnetic field, molecular motion can be detected by observing changes in the spectrum. The quadrupolar interaction is smaller than the Zeeman interaction (hundreds of kilohertz compared with tens of megahertz respectively), and as such can be treated as a perturbation on the Zeeman interaction. Thus, substituting in Equation 1.7, the energy of a given level, to the first order, can be expressed:

$$E_{tot} = E_{Zeeman} + E_{quadrupolar} = -m\hbar\gamma B + \frac{eQ}{4I(2I-I)}V^{(2,0)}[3m^2 - I(I+1)], \qquad (1.12)$$

where e is the charge of an electron, Q is the nuclear quadrupole moment and $V^{(2,0)}$ is largest irreducible component of the electric field gradient tensor. The quadrupolar splitting, on the order of tens of kHz, is about two orders of magnitude greater than the dipolar coupling, scalar coupling and chemical shift anisotropy, which can be ignored. Thus, for ^{2}H the Zeeman-split energy levels are further perturbed by the quadrupolar interaction, and the splitting between these two resonances is given in Equation 1.13:

$$\Delta\nu_Q = \frac{3}{2}\frac{eQ}{h}V^{(2,0)}. \qquad (1.13)$$

For an immobile, frozen solid with the principal axis of the C-D bond vector parallel

to the electric field gradient, $V^{(2,0)} = V_{zz} = eQ$, and the quadrupolar splitting reduces to $\Delta\nu_Q = \frac{3}{2}\frac{e^2qQ}{h}$, a constant known as the static quadrupolar coupling constant. This bond vector can adopt any orientation by rotation about the electric field gradient tensor by an angle θ, followed by a second rotation about the new axis by an angle ϕ. The quadrupolar splitting thus becomes:

$$\Delta\nu_Q(\theta,\phi) = \frac{3}{2}\frac{e^2qQ}{h}\left(\frac{3\cos^2-1}{2} + \frac{1}{2}\eta\sin^2\theta\cos 2\phi\right) \tag{1.14}$$

where η is known as the asymmetry parameter. For a C–D bond in an alkyl chain, $\eta = 0$ (axial symmetry) and hence the expression for the relationship between a C–D bond vector and the quadrupolar splitting emerges in Equation 1.15:

$$\Delta\nu_Q(\theta) = \frac{3}{2}\frac{e^2qQ}{h}\left(\frac{3\cos^2\theta-1}{2}\right). \tag{1.15}$$

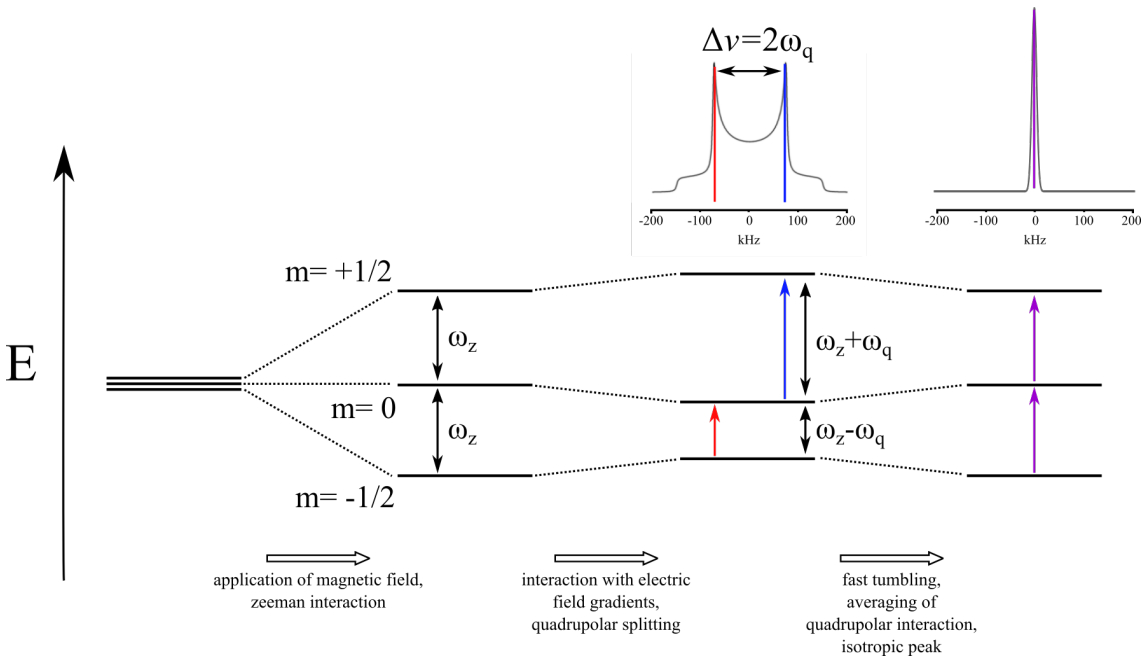

Figure 1.13 A schematic showing the effect of quadrupolar coupling on the energy levels and resulting NMR spectrum for a quadrupolar nucleus ($I = 1$). The Zeeman contribution $-\hbar\gamma B$ is collected at ω_z and quadrupolar contribution $\frac{3}{4}eQV^{(2,0)}$ collected as ω_q.

This perturbing effect is summarised in Figure 1.13. Equation 1.15 yields useful structural and dynamic information for a given C-D bond on a lipid in a membrane; the

time averaged orientation of the bond about a director axis, typically taken to be perpendicular to the membrane normal, can be represented by an order parameter S_{CD} for the entire CD_2 segment as

$$\Delta\nu_Q = \frac{3}{4}\frac{e^2qQ}{h}\left(\frac{\overline{3\cos^2\theta - 1}}{2}\right) = \frac{3}{4}\frac{eQ}{h}S_{CD}, \tag{1.16}$$

where the extra factor of two accounts for the two axially symmetric C−D bonds of a CD_2 segment. For an aligned sample, the time-averaged orientation, read directly from quadrupolar splittings, gives the conformational freedom of a CD_2 bond, while measurements of relaxation times give the rates of these motions.

^{2}*H ssNMR to study biological membranes*

The segmental order parameter S_{CD} can describe many structural features of a lipid membrane. By selectively labelling different segments of an acyl chain, order parameter profiles can be obtained, and the relationship between motional freedom and hydrophobic depth can be obtained. Figure 1.14 A (overleaf) shows that in general, tight hydrogen-bond- mediated packing of lipid headgroups restricts rotational freedom close to the interfacial region, with diminishing effects closer to the hydrophobic core and S_{CD} therefore decreases towards the end of the acyl chain. These segments are sensitive to addition of biological molecules to the membrane; the addition of membrane active peptides and proteins have been previously explored: for example, ampullosporin A and alamethicin, two widely studied AMPs, and were shown to cause a lipid-disordering effect in model membranes, but the greatest effect was observed with anionic membranes, giving some explanation of selectivity and activity (1.14 A) [117].

Membrane-active peptides and proteins can also induce macroscopic changes in a membrane; by looking at the average changes of S_{CD} across the acyl region, it was shown that the channel-forming AMP gramicidin A causes membrane thinning to accommodate the peptide [118]. In addition, if a peptide causes rupture of a membrane

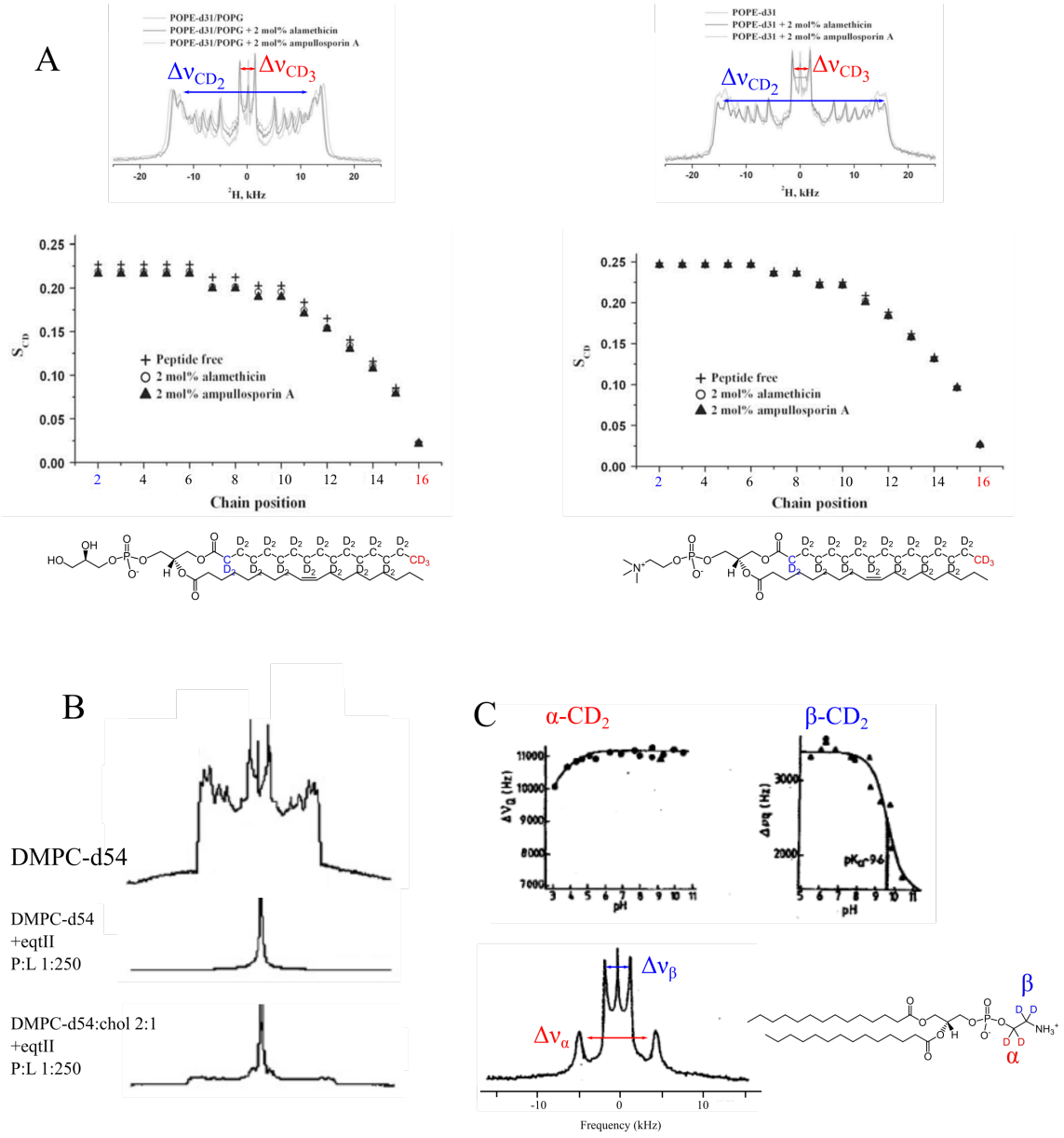

Figure 1.14 Examples of ^{2}H ssNMR in understanding peptide-lipid interactions. ***A:*** The magnitude of disorder induced along an acyl core by two AMPs changes depends on lipid composition. Greater disordering is observed in anionic (*left*) POPE:PG-d_{31} membranes compared to (*right*) POPC-d_{31} membranes, revealing lipid specificity [118]. ***B:*** The addition of an antibacterial protein equinatoxin II (eqtII) causes collapse of quadrupolar splittings (*centre*) compared to a lipid only control (*top*), indicating formation of small isotropic vesicles. The addition of cholesterol (*bottom*) partially prevents this [119]. ***C:*** The quadrupolar splittings of two CD_2 segments in the headgroup of DMPE-d_4 are sensitive to pH, which causes a concomitant change in headgroup conformation [120].

into small, rapidly tumbling vesicles ($\tau_c < 10^{-6}$ s) then the quadrupolar interaction will be averaged, resulting in a single isotropic peak, as observed for the antibacterial protein equinatoxin II (1.14 B) [119]. It was also found that the presence of cholesterol partially prevents isotropic vesicle formation, suggesting a role for sterols in eukaryotic membranes in protecting against AMP toxicity. The timescale of ^{2}H ssNMR is around 10^{-6} s. Therefore, any particles tumbling faster than this will average the quadrupolar splittings, leading to an isotropic line (Figure 1.13 B). From equation 1.11, the τ_c for a 100 nm LUV is 1.2 µs, whereas that for a 1000 nm MLV is 0.2 ms. Larger MLVs therefore permit measurement of quadrupolar splittings, but by measuring changes in the splitting (or collapse to an isotropic line) one can infer changes to macroscopic structure upon addition of an AMP.

Strategic labelling of a phospholipid headgroup can also determine changes in headgroup tilt and conformational freedom; ^{2}H-labelled phosphatidylethanolomine lipids have previously been used as "molecular voltmeters" sensitive to changes in ionic strength (1.14C) [120].

Parameters obtained by ssNMR can thus be used to build a comprehensive picture on how lipid membranes are affected by AMPs, and contribute a great deal of mechanistic data to help understand mechanisms of action.

1.4.3 Electron paramagnetic resonance

General principles

Electron paramagnetic resonance, or electron spin resonance (EPR/ESR), probes membrane structure and dynamics using the unpaired electrons of a nitroxide moiety as the molecular probe. An electron has a spin quantum number $S = \frac{1}{2}$ (S is analogous to I) and hence an associated spin, and can be treated in a very similar way to nuclei in NMR. Here, electronic transitions are observed rather than nuclear transitions. In continuous wave (CW)-EPR, continuous microwave (10^9 Hz) radiation is applied to

the sample in a magnetic field, and the first derivative of the absorption spectrum is recorded (Figure 1.15).

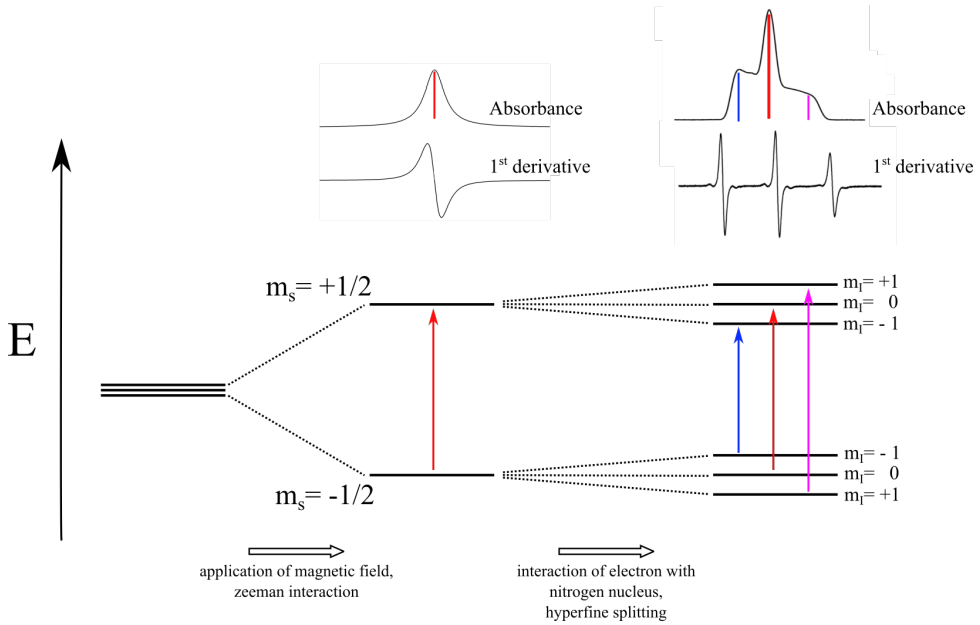

Figure 1.15 Hyperfine splitting in a nitroxide EPR spectrum. The single allowed Zeeman transition is split further into three allowed transitions due to hyperfine coupling to the nitrogen nucleus. The first derivative of the absorbance spectrum is typical of a nitroxide spin label, with the shape and splitting dependent on the spin probe's mobility and orientation.

The difference in energy levels permits investigation of membrane structure on dynamics on a 10^{-9} s timescale, compared to ^{2}H ssNMR which occurs on a 10^{-6} s timescale. In the vast majority of cases, an unpaired electron is not available in a biological system, and has to be strategically introduced; a range of lipids, labelled with a nitroxide spin probe at different positions, are commercially available (Figure 1.16). The TEMPO and DOXYL spin labels contain a N$-$O$\cdot$ bond which is the reporter system analogous to a C$-$D bond in ssNMR. Similar to NMR, an electron can exist in $2S+1=2$ degenerate states or orientations. Upon application of a magnetic field, this degeneracy is lifted and the energy of each state is given in Equation 1.17:

$$E = g\mu_B m_S B, \tag{1.17}$$

where the constant μ_B is the Bohr magneton, B the magnetic field strength, m_S the

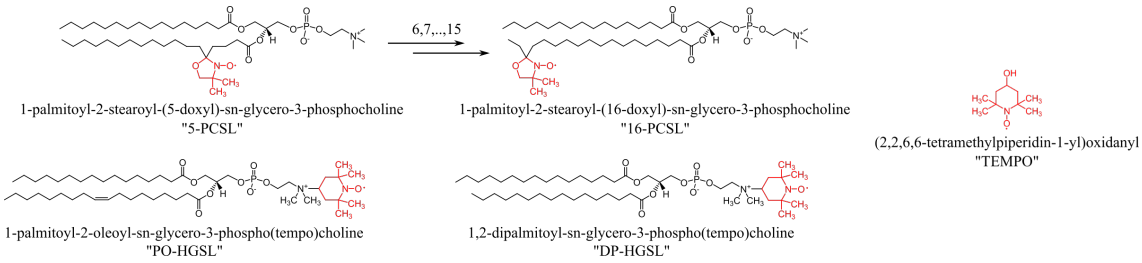

Figure 1.16 Examples of commercially available EPR probes.

magnetic quantum number and g the g tensor of the electron. In accordance with the selection rule $\Delta m_S = \pm 1$, the resonance frequency of a transition is given by equation 1.18:

$$\Delta E = h\nu = g\mu_B B. \tag{1.18}$$

In a 0.3 T field, $\Delta E \approx 9$ GHz, which falls within the microwave region in the electromagnetic spectrum. Typical CW-EPR experiment use a small window of excitation radiation known as an X-Band[‡] (frequency window around 9.6 GHz).

In contrast to NMR, an ESR spectrum is typically presented as the first derivative of the absorbance spectrum; this is done to increase the signal to noise ratio. As a spectrum is acquired, the external magnetic field is modulated sinusoidally at around 100 kHz. If an EPR transition is encountered over this range, the reflected microwaves are amplitude modulated, while any random noise is suppressed in this process. For any part of the EPR signal that is approximately linear over the modulation range, the resultant signal approximates to the slope of that line, leading to a spectrum that is essentially the first derivative of the absorption spectrum (Figure 1.17) [121].

[‡]The term X-band originates from military radio communication during World War II and is technically defined by the difficulty in producing wavelength tunable microwave sources. More recent microwave sources higher frequency frequency windows such as Q band (35 GHz) and W Band (95 GHz)

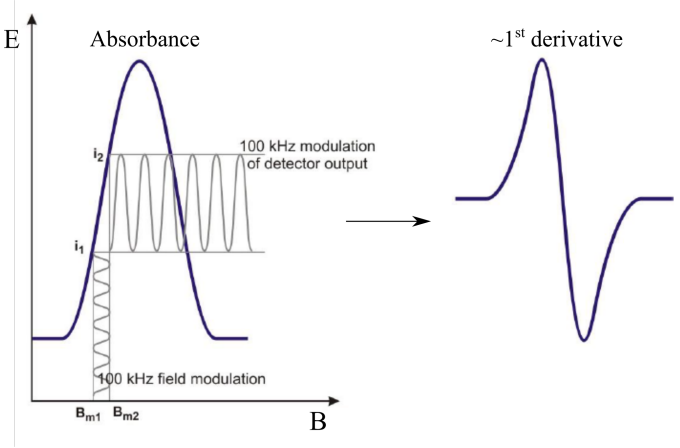

Figure 1.17 Schematic showing acquisition of an EPR spectrum. Along the EPR signal,the main field is oscillated around 100 kHz. Moving from field B_{m1} to B_{m2} the change in amplitude is modulated and the resulting peak to peak value of the wave is approximately the slope of the signal between B_{m1} and B_{m2}. Noise is suppresed as the slope is approximately 0 over the modulation. Adapted from [122].

Sensitivity

Due to the higher frequency of radiation required to cause transitions between energy levels for EPR compared to ssNMR(300 – 1000 MHz and 500 GHz, respectively) EPR spectroscopy enjoys a subsequent increase in sensitivity (around 200 times [123]), hence requiring less sample. However, as a consequence dipolar couplings, within a 15 Å limit, have a perturbing effect on EPR transitions, and spin label concentrations above 5% of the lipid total in a membrane cause line broadening and make interpretation of spectra more difficult [124]. Dipolar interactions between spin labels (H_{ee}) are stronger between electrons than nuclei (H_{xy}), as from consideration of the terms for dipolar coupling between nuclei and electrons (Equations 1.19 and 1.20 respectively):

$$H_{xy}/Hz = \frac{\mu_0}{4\pi}(3\cos^2\theta - 1)\frac{\hbar\gamma_A\gamma_X}{r_{AX}^3} \tag{1.19}$$

$$H_{ee}/Hz = \frac{\mu_0}{4\pi}(3\cos^2\theta - 1)\frac{\hbar\mu_B^2}{r_{AX}^3}. \tag{1.20}$$

Coupling between electrons is about 10^6 times stronger due to the larger Bohr magneton.

Hyperfine splittings

The energy levels of an electron in a magnetic field are not only perturbed by the Zeeman effect. In the presence of other electrons and magnetic nuclei, further perturbations to the energy levels can be introduced as perturbations of the total spin Hamiltonian $\vec{H}_0$ in Equation 1.21:

$$\hat{H}_0 = \hat{H}_{Zee} + \hat{H}_{ZFS} + \hat{H}_{HF} + \hat{H}_{nucZee} + \hat{H}_{NQ} + \hat{H}_{NN} \tag{1.21}$$

where $\hat{H}_{Zee}$ is the Zeeman interaction, $\hat{H}_{ZFS}$ the zero field splitting, $\hat{H}_{HF}$ the hyperfine interaction between the electron spin and the spins of other nuclei (^{14}N for nitroxide labels), $\hat{H}_{nucZee}$ the nuclear Zeeman interaction, $\hat{H}_{NQ}$ the angular quadrupole interaction (not present for spins with $I < 1$), and $\hat{H}_{NN}$ dipolar interactions between nuclear spins. For nitroxide labels, in dilute systems, only the Zeeman and hyperfine interactions need to be considered, and thus the Hamiltonian reduces to equation 1.22:

$$H = \mu_B g \vec{B} \hat{S} + \hat{I} A \hat{S}, \tag{1.22}$$

where $\hat{I}$ is the nuclear spin operator, A is the hyperfine tensor, and $\hat{S}$ is the nuclear spin operator. Analagous to the quadrupolar interaction, the hyperfine splitting is much smaller than the Zeeman interaction, and hence can be considered a perturbation to the system. In the case of nitroxide spin labels, the interaction is with the nitrogen nucleus of the N−O· bond. The unpaired electron can exist in three orientations of the p_z orbital of the ^{14}N atom. Hence, each Zeeman-split energy level is further split into three energy levels, and, obeying the selection rules $\Delta m_s = \pm 1$, $\Delta m_I = 0$ three allowed transitions are possible, as shown previously in Figure 1.15. This hyper-

fine splitting is sensitive to the gross structure and dynamics of the surrounding spin label environment.

Continuous wave electron paramagnetic resonance to study biological membranes

A DOXYL spin label on the acyl chain of a phospholipid undergoes fast long axis rotation and wobbling within a defined cone around the long axis. This anisotropic motion in a lipid bilayer characterises the amplitude (order) and dynamics of the whole bilayer. The appearance of the EPR spectrum can be understood by considering the nitroxide label relative to the molecular axes of the spin-labelled lipid (Figure 1.18 A).

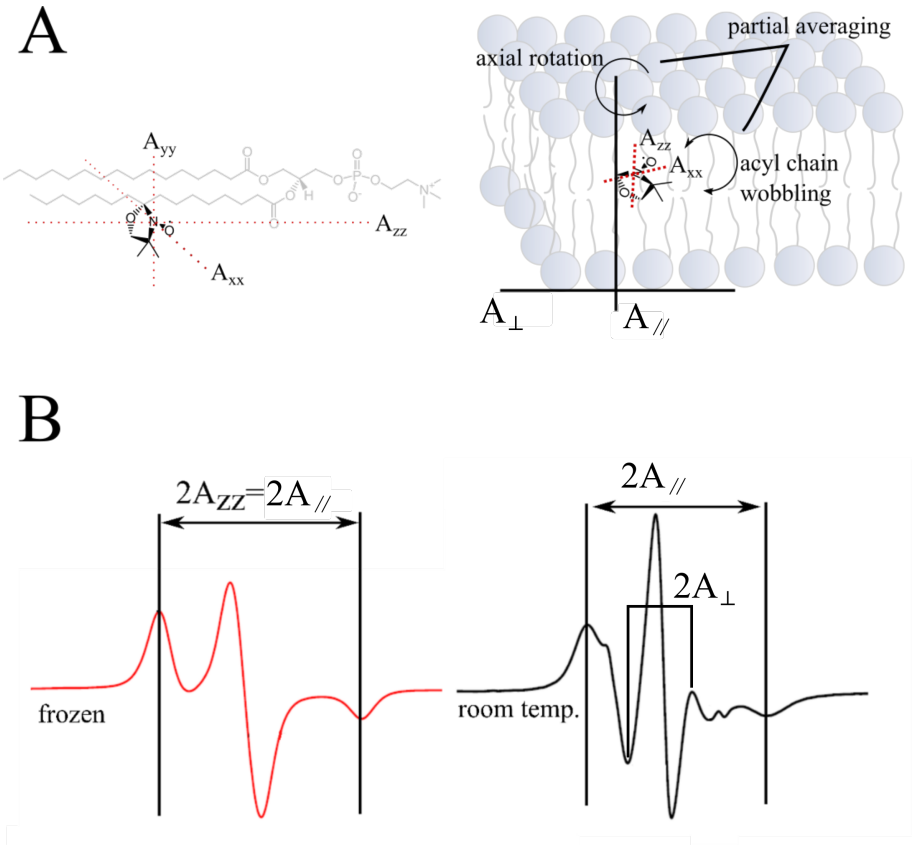

Figure 1.18 Principal hyperfine splittings of a nitroxide-labelled phospholipid. ***A:*** The principal axes, A_{zz}, A_{xx} and A_{yy} of a nitroxide-labelled phospholipid. The A_{zz} axis is parallel to the molecular long axis. In a phospholipid bilayer axial rotations and trans-gauche isomerisations cause partial averaging compared to the maximum splittings, $A_\parallel$ and $A_\perp$. ***B:*** In rigid frozen samples no averaging occurs and the principal splittings can be directly measured. At higher temperatures a normalised order parameter S_{eff} can be calculated as in Equation 1.23. Figure adapted from Marsh and Watts [47].

The principal z-axis, A_{zz} of the nitroxide spin label lies parallel to the long axis of the lipid, and is therefore oriented parallel to the membrane normal (the principal axes A_{xx} and A_{yy} are orthogonal to this). The maximum hyperfine splitting consequently occurs when the magnetic field is aligned parallel to the membrane normal, and the minimum where it is perpendicular. In reality, the parallel hyperfine splitting, $A_{\parallel}$, is smaller than A_{zz} due to trans-gauche isomerisations in the acyl chain segments, and rapid axial rotation, causing partial averaging. Similarly the perpendicular hyperfine splitting $A_{\perp}$ is slightly larger than A_{xx} due to the same effect. The extent of averaging, and hence the measure of spin-label mobility, can be quantified and normalized by the spin label order parameter S_{eff} in Equation 1.23, where A_{zz} and A_{xx} can be measured directly from the hyperfine splittings of a frozen oriented sample where no averaging occurs (Figure 1.18 B):

$$S_{eff} = \frac{A_{\parallel} - A_{\perp}}{A_{zz} - A_{xx}} \tag{1.23}$$

Complimentary to ^{2}H ssNMR, EPR order parameter profiles can be obtained, and the response of bilayer order parameters to the presence of other membrane constituents such as cholesterol [125] and lipid domains [99] have been investigated. It is common for ordering effects (increases in S_{eff}) to be observed in EPR, while disordering effects, increases in amplitude of lipid mobility, are seen in ssNMR [126]. This is due to molecular motions being probed at different timescales (10^9 for EPR, $10^4 - 10^6$ for ssNMR). In addition, the non-native nitroxide spin label may affect motions in the acyl core due to less efficient lipid packing.

1.4.4 Neutron reflectometry

Neutron reflectometry (NR), a type of neutron scattering technique, allows investigation of the structure and dynamics of biological interfaces. Compared to X-ray techniques, NR suffers from a poorer signal-to-noise ratio and hence poorer resolution ($\backsim$ 0.3 nm compared to 2 nm for X-ray diffraction and NR respectively [127]) due to the neutron flux. However, due to greater penetrating ability of neutrons compared

to X-rays, NR allows the study of the bulk properties below the surface of an interface [128]. In addition, separate components of a system, such as lipids and proteins, can be independently studied using isotope labelling and contrast matching, as explained below.

General principles

Neutrons are spin $\frac{1}{2}$ sub-atomic particles, that interact with nuclei *via* the strong force resulting in nuclear scattering,[§] and the strength of this interaction is quantified by the neutron scattering cross section σ:

$$\sigma = 4\pi b^2 \tag{1.24}$$

Where b is the isotope-specific neutron scattering length. The sign of b is arbitrary (conventionally positive values of b are for a repulsive interaction with the nucleus). This expression can be extended to an interface containing many nuclei, by defining the neutron scattering length density, p_z as in equation 1.25:

$$\rho_z = \sum_{i=1} b_i n_i \tag{1.25}$$

where n_i is the number density of a given nucleus. The scattering length density profile gives the scattering length density as a function of distance from the surface of the scattering, and can be measured by reflectivity experiments.

In a typical experiment, neutrons produced by a spallation source[‖] are filtered by beam choppers, producing a band of neutrons with a narrow distribution of wavelengths. The refractive index of most materials for neutrons is close to that for a vacuum, so the critical angle for reflection of the beam is very small [129]. To ensure that the incident radiation is below this angle, a collimator focuses the beam of neutrons

[§]Interactions can also occur with unpaired electrons, resulting in magnetic scattering.

[‖]Whereby neutrons are ejected from the an on-site particle accelerator. Other neutron sources can be found at https://en.wikipedia.org/wiki/Neutronsource.

before interacting with the sample. The neutrons then undergo specular reflection upon hitting the sample, and are detected. Figure 1.19 summarises the general outline of a time-of-flight neutron reflectivity experiment to study liquid interfaces [127].

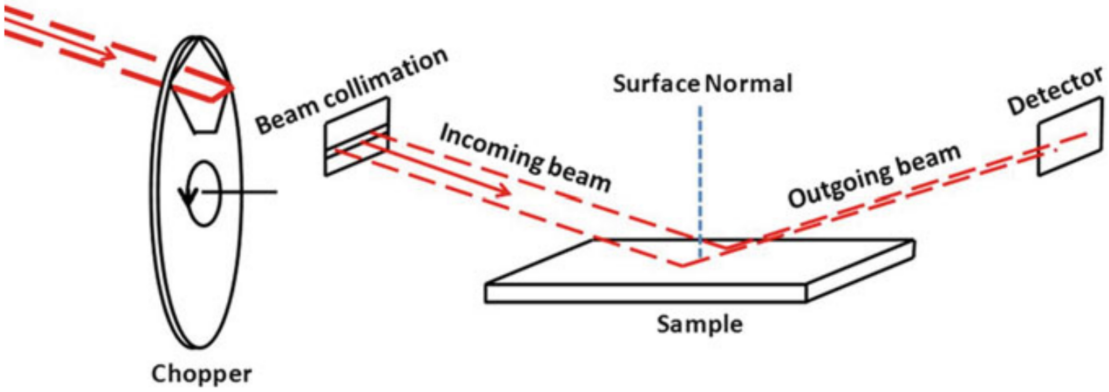

Figure 1.19 Experimental setup for time-of-flight neutron reflectivity. Reproduced from [130].

.

The ratio of reflected intensity to the initial incident intensity, which is the reflectivity, is measured as a function of the momentum transfer vector, given in Equation 1.26:

$$Q_z = \frac{4\pi}{\lambda} \sin\Theta, \tag{1.26}$$

where Θ is the angle of specular reflection from the surface. The momentum transfer vector is a measure of the change of momentum of the neutron due to reflection from the sample. The wavelengths of the neutrons are determined by calculating the time (t) taken for them to travel between the beam collimator and the detector (Equation 1.27):

$$\lambda = \frac{h}{mL} t, \tag{1.27}$$

where m is the neutron mass, and L is the distance between the collimator and detector [129]. The resulting reflectivity is related to the composition of the interface, or profile of interfaces, normal to the surface. A typical profile is given in Figure 1.20 A.

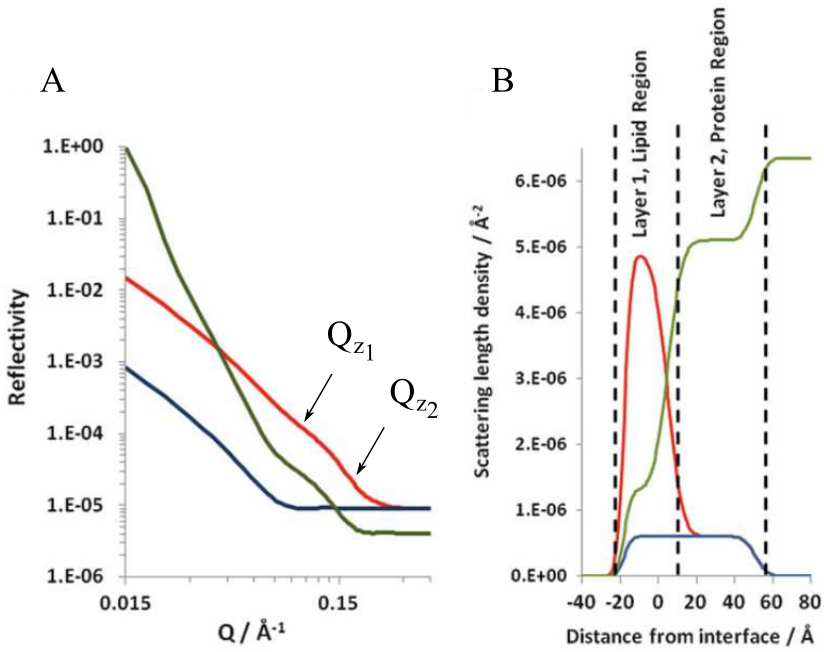

Figure 1.20 ***A*** Typical neutron reflectivity and ***B*** scattering length density profiles for a lipid monolayer. The three profiles are of the same monolayer, with different degrees of solvent contrast matching and isotopic substitution, explained below. From the multiple conditions (hydrogenated lipid, hydrogenated protein in D_2O (green), deuterated lipid, hydrogenated protein in null-reflective water (red) and hydrogenated lipid, hydrogenated protein in null-reflective water (blue)) the depth of insertion of the protein into the monolayer can be calculated. Figure adapted from [130]. $Q_{z_{1/2}}$ refer to fringes in the interference pattern.

The fringes of the profile occur due to interference between neutrons reflected from top and bottom of the interfacial layer. The spacings of the interference fringes are related to the thickness (D nm) of the layer by

$$Q_{z_2} - Q_{z_1} = \frac{2\pi}{D}. \tag{1.28}$$

Assuming scattering from the surface is negligible (the Born approximation [131]), the neutron reflectivity profiles are further converted into real-space scattering length density profiles (defined in Equation 1.24), as a function of distance of the interface from the surface. The scattering length density profiles can then give molecular information on the interfaces (Figure 1.20 B). For each layer on the surface (for example, the head region and lipid tails), the scattering length density is the summation of all

the components of the system:

$$\rho_{layer} = \rho_{lipid}\phi_{lipid} + \rho_{peptide}\phi_{peptide} + \rho_{solvent}\phi_{solvent} \tag{1.29}$$

where ρ_x and ϕ_x are the scattering length density and volume fraction, respectively, of a component at an interface. Thus, the contributions from each component to the interfacial structure can be determined.

Contrast matching

The main advantage of NR over X-ray diffraction is the ability to exploit the different neutron scattering lengths of different nuclei; for ^{1}H and ^{2}H, $b = -3.74 \times 10^{-5}$ Å and $+6.64 \times 10^{-5}$, respectively. Despite near chemical identity,[¶] components of a sample with different levels of deuteration will have large effects on the scattering length density profiles (Figure 1.21).

For example, a 8 : 92 mix (by volume) of D_2O and H_2O in the experiment solvent results in a scattering length density of 0, rendering the solvent "invisible" (known as null reflective water) to the neutrons, meaning all elastic scattering can be attributed to the lipid and protein components. By altering the levels of deuteration in lipid, protein and solvent, different contrasts can isolate different contributions to neutron scattering lengths. Thus, unique models can be fitted to the data to allow greater accuracy in describing the interfacial system.

Neutron reflectivity to study antimicrobial peptide-lipid interactions

The structural information obtained from NR can help elucidate mechanisms of action for AMPs. A recent study investigated the effect of two AMPs on monolayers of differing lipid composition [134]. Melittin is an AMP thought to act *via* a toroidal pore or barrel stave mechanism [135], while magainin has previously shown to disrupt

[¶]Deuterated lipids do have slightly lower transition temperatures due to the weaker van der Waal interactions between deuterated acyl chains [132] and deuterated proteins can also display different denaturation temperatures [133].

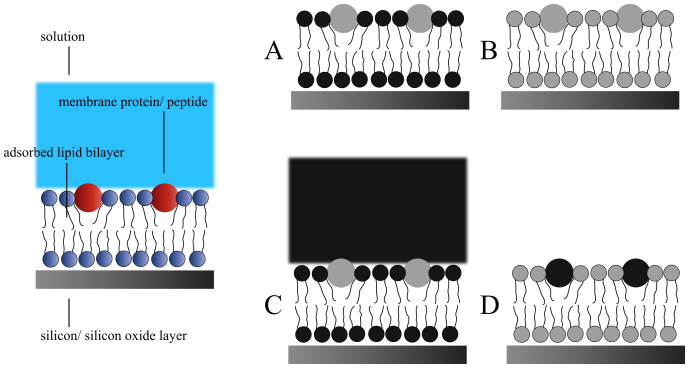

Figure 1.21 Schematic of an adsorbed lipid bilayer. Exploiting the different neutron scattering lengths of ^{1}H and ^{2}H, contrast matching allows contributions to reflectivity to come from different components of the water/protein/lipid system. ***A:*** ^{2}H-labelled lipid and ^{1}H-labelled protein in null reflective water - lipid component dominates. ***B***: ^{1}H-labelled lipid and ^{1}H-labelled protein in null reflective water - protein component dominates. ***C***: ^{2}H-labelled lipid and ^{1}H-labelled protein in D_2O - solution and protein components dominates. ***D***: ^{1}H-labelled lipid and ^{2}H-labelled protein in null reflective water - protein component dominates. The baseline value at high Q corresponds to background neutron scattering occurring due to inelastic scattering of neutrons by the interface. Figure adapted from [130].

model membranes in a carpet-like manner [136]. NR reflectivity profiles for monolayers of DPPG and DPPC, showed that melittin caused significant concentration-dependent reductions in density and increases in thickness in the acyl region of the interface upon addition of melittin. These data, in combination with complimentary FTIR and surface pressure measurements, suggests the peptide first associates with the headgroup region of the monolayer, and above a threshold concentration inserts into the monolayer, acting in a toroidal pore-like fashion. Similar effects for both zwitterionic and anionic monolayers confirmed that the AMP is not selective in its permeabilising ability. Similar experiments with magainin revealed no insertion into the acyl region of the interface [134], giving further evidence that the AMP does not penetrate a cell membrane but rather solubilises it by accumulation on the surface.

In another study the effect of maculatin, an AMP isolated from the Australian tree frog [137], on DMPC and DMPG:DMPC (1:4) bilayers was investigated with NR [138]. Significant changes in solvent penetration into the acyl region suggested that macu-

latin was forming pores. In addition, the thickness of the headgroup region was reduced, which suggested a rearrangement headgroup conformation upon interaction with the peptide. The lack of change in neutral bilayers in comparison also suggested the peptide showed specificity for bacterial membranes.

Greater control of forming free-floating bilayers has allowed more sophisticated model membranes to be investigated by NR. Gram-negative bacteria possess an inner and outer membrane, with varying lipid compositions between the leaflets of these two membranes [139]. It was demonstrated that it was possible to form an asymmetric floating bilayer mimicking a Gram-negative outer membrane, with LPS incorporated into the outer leaflet, and phospholipids incorporated into the inner leaflet of a floating bilayer, with the surface-bound phospholipids mimicking the inner membrane [130]. NR allowed resolution of all components, confirming the asymmetry of the system, and allowing measurement of time taken to lose the symmetry. In another study utilised these advanced model membranes, it was shown the binding of an antimicrobial protein was ablated by the presence of uncharged sugar groups in the outer region of LPS preventing access to the negatively charged phosphate groups [140]. This study highlighted the importance of LPS in the defence of some bacteria to AMPs, and of the need for creating more native-like model membranes to gain further insights into the mechanism of AMPs.

1.4.5 Dynamic light scattering

General principles

It is important to be able to determine the size of the liposomal model membranes being used in ssNMR and EPR, amongst other techniques. Dynamic light scattering (DLS), or photon correlation spectroscopy, allows measurement of particle size at a resolution of up to 1 nm in diameter. DLS measures Brownian motion of a sample, and relates this to the size and heterogeneity of the sample. Brownian motion is the random motion of a sample of particles in a fluid, due to buffeting by solvent molecules.

The rate of Brownian motion depends on the size of the particles, temperature and the viscosity of the solvent, according to equation 1.30:

$$d(H) = \frac{kT}{3\pi\eta D}, \tag{1.30}$$

where $d(H)$ is the hydrodynamic diameter of the particles, T the temperature, η the viscosity of the solvent, and D is the experimentally determined translational diffusion coefficient. The rate of Brownian motion affects the rate of fluctuation of scattered light intensity, which is detected in DLS (summarised in Figure 1.22).

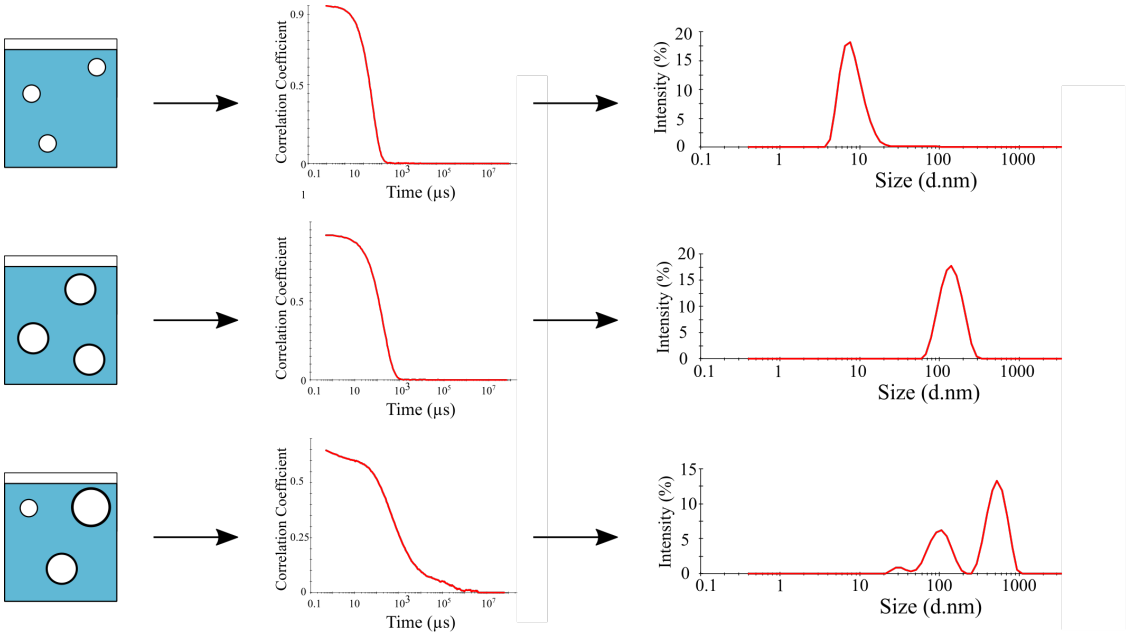

Figure 1.22 Relationship of particle size to autocorrelation function. Small particles cause a quick loss of correlation of intensity fluctuation relative to time t=0 (*top*), and slower loss of correlation for larger particles (*middle*). The steepness of the autocorrelation correlation depends on the polydispersity of the sample, with a shallower gradient for polydisperse samples (bottom) [312].

Measurement of particle size

The autocorrelator in DLS measures the fluctuation as a function of time, relative (or correlated) to the starting intensity. The correlation (and hence correlation coefficient) will persist for longer for larger, slower moving particles, and *vice versa*. The

steepness of the correlation function gives a measure of the polydispersity of the sample. The correlation function is based on either cumulant analysis, or non-negative least-squares fitting, given in Equation 1.31 and 1.32 respectively:

$$G(t) = A(1 + Be^{-2\Gamma_t}) \tag{1.31}$$

$$G(t) = A(1 + Bg_n(t)) \tag{1.32}$$

where A is the baseline autocorrelation function, B the intercept, $g_n(t)$ the sum of exponential functions in Equation 1.31. Γ_t is related to the translation diffusion constant by equation 1.33:

$$D = \frac{\Gamma_t}{q^2} \tag{1.33}$$

$$q = (\frac{4\pi n}{\lambda_0}) \sin(\frac{\theta}{2}), \tag{1.34}$$

where n is the refractive index of the dispersant, λ_0 the incident wavelength of scattered light, and θ the scattering angle. Hence, the hydrodynamic radius can be determined according to equation 1.30.

1.4.6 Circular dichroism

UV Circular dichroism (CD), is a widely used technique to determine the secondary structure of peptides, proteins and other macromolecules. Depending on their environment, certain electronic transitions cause differential absorption of circularly polarised light. In peptides, the amide bond gives rise to absorptions in the far-UV ($180-250$ nm) region. Two amide transitions, $n-\pi^*$ and $\pi-\pi^*$, absorb UV radiation at 190 nm and 220 nm respectively, and are responsible for the two absorbance of the CD spectrum in this wavelength range(Figure 1.23). The intensity and precise wavelength of these transitions are dependent on the torsion angles within the peptide

backbone, and hence are sensitive to differences in secondary structure. Freely available software is available to deconvolute more complicated spectra which a mixture of populations of differing secondary structures exist [141]. CD is therefore a useful

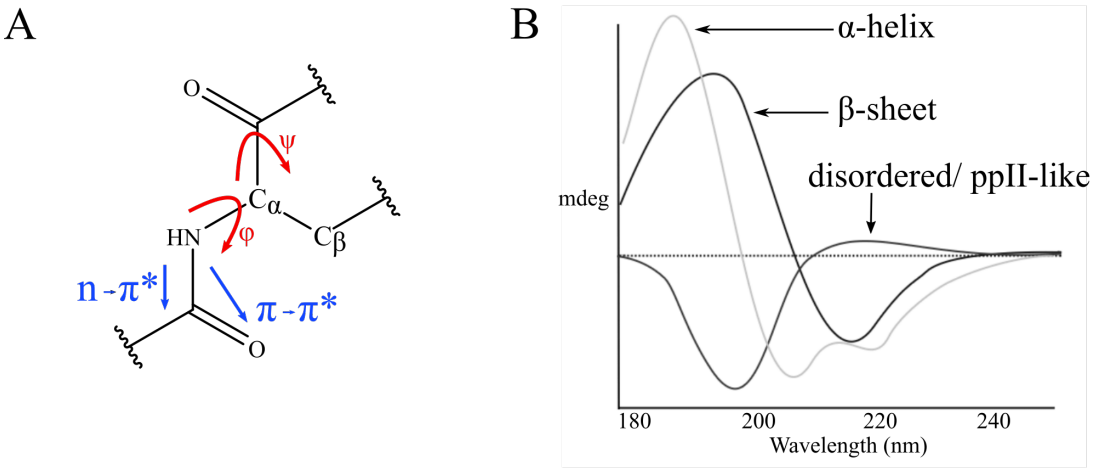

Figure 1.23 ***A:*** The electronic transitions that give rise to the main spectral features, $n-\pi^*$ and $\pi-\pi^*$, depend on the torsion angles, ϕ and ω, which depend on the secondary structure adopted by the peptide. ***B:*** Characteristic CD spectra of peptides of different secondary structure

technique to measure changes in peptide structure in the presence of lipid membranes, which plays a major role determining specificity for different membranes [142, 143].

1.5 Aims of thesis

The molecular basis for the mode of action of AMPs, and the relationship between primary structure and antimicrobial activity remains poorly understood. This thesis uses a variety of model membranes to study the peptide-lipid interactions of membrane active peptides and proteins of interest, and to improve upon existing models to extract more physiologically relevant information.

Two *de novo* synthetic AMPs are extensively studied, with their primary structure rationally designed to display specific peptide-lipid interactions. The link between the

primary structure, the secondary structure and behaviour in the presence of model membranes using QCM, and the antimicrobial activity of the AMPs is the basis for the work in Chapter 2.

The mechanisms of action of the two AMPs is explored in greater detail using ^{2}H ssNMR of acyl chain-deuterated membranes in Chapter 3. The interactions of peptides with lipids deuterated in the headgroup region has been underexplored as lipids of this type are not commercially available. The synthesis of a variety of a headgroup deuterated lipids and their interactions with the AMPs is also discussed.

The interactions of AMPs with asymmetric model membranes have to date not been previously investigated. Using novel asymmetric liposome formation protocols [144], leaflet-specific peptide-lipid interactions of the two *de novo* AMPs as well as other membrane-active peptides are probed for the first time in Chapter 4, using cw-EPR. Using the same protocol, a liposomal Gram-negative outer membrane mimic is attempted, and the biophysical properties of this system are studied.

The biophysical properties of the membrane protein puroindoline B [145], with a membrane interacting region structurally related to antimicrobial peptides, will be explored with QCM, ssNMR, EPR and NR in Chapter 5, in an attempt to understand its biological function.

The conclusions from the work in this thesis within the context of the literature, as well as a comment on the future direction for this work, forms the basis of chapter 6.

Chapter 2

Biophysical Investigations of *De Novo* Antimicrobial Peptides

2.1 Introduction

2.1.1 Principles of peptide design

The challenge of forming a desired secondary structure from a *de novo* sequence has been deemed the "inverse folding problem" [146]; *i.e.*, instead of predicting a structure from a given primary structure, a target secondary or tertiary structure is the input, while the required primary structure to achieve this is the experimental output [147].

Peptide design does not suffer the drawbacks from protein design such as consideration of global molecular ordering between secondary structural elements to form complicated tertiary or quaternary structures, but certain challenges remain, especially in the area of AMP design. In the absence of such long-range global interactions, short range order can be more difficult to achieve. For example, the RGD (Arg-Gly-Asp) sequence is an epitopic loop structure found in many unrelated proteins which binds to integrin and is important for many cell-cell interactions [148]. However, the isolated peptide bearing the sequence is less active [149], highlighting the importance of higher order interactions in dictating secondary structure.

For AMPs, the requirements of a desired peptide are the ability to selectively form a bioactive amphipathic structure in the presence of pathogenic membranes, while remaining inactive in the presence of mammalian membranes [150]. Alpha-helices

are attractive candidates to provide this role, as they fold into predictable structures that obey empirical rules for their formation, as shown in Figure 2.1.

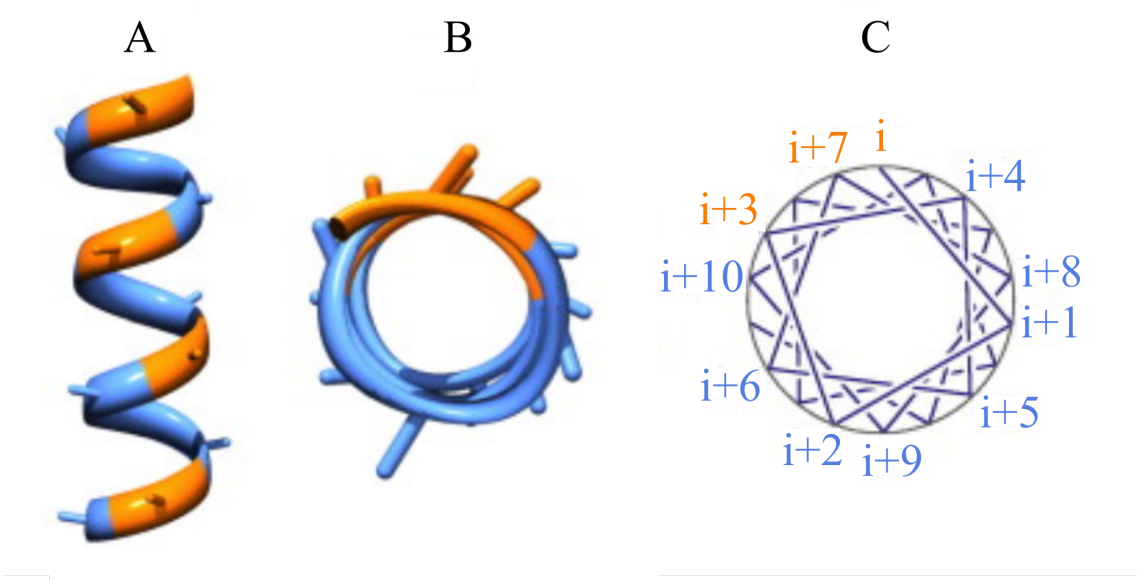

Figure 2.1 An archetypal alpha-helix, viewed **A:** side-on and **B:** top-down, with the i, $i+3$ and $i+7$ residues on the same face. **C:** A typical helical plot showing the distribution of residues around the helical "cylinder". Figure adapted from [151].

Peptides with a repeating sequence $(HPPHPPP)_n$, where H and P are hydrophobic and polar residues respectively, have been shown experimentally to form alpha helices [152].* The identity of the amino acids in the peptide chain have also been calculated to display propensities for beta-sheet and alpha-helix formation [153, 154]. The hydrophobic residues can affect peptide oligomerisation, with larger residues favouring tetramers and high-order oligomers [155]. By virtue of the helix structure, i, $i+3$ and $i+7$ residues lie above each other, which conveniently allows for amphipathic helices with in-built separation of polar and hydrophobic residues on different faces [101, 156]. These properties thus render *de novo* alpha-helices attractive candidates for new AMPs.

*It has also been shown empirically that $(HP)_n$ sequences bias beta-sheet structures [149].

2.1.2 Aims of chapter

The aim of the work described in this chapter is to use inverse peptide design principles to synthesise two *de novo* antimicrobial peptides that display broad-spectrum activity against Gram-negative and Gram-positive bacteria, while being non-toxic to mammalian cells. An attempt will then be made to establish a link between antimicrobial activity and molecular interactions between the AMPs and lipid membranes. Minimum inhibitory concentrations (MICs) for the peptides to cause bacteriostasis in Gram-negative and Gram-positive bacteria will be carried out first to establish the activity and selectivity of the designed AMPs. To mitigate the inherent complexity of natural cell membranes, model membranes designed to mimic the properties of mammalian and bacterial cells will then be used to study AMP-lipid interactions using circular dichroism (CD), calcein leakage, and quartz crystal microbalance (QCM) experiments.

The first approach is to adapt the primary structure from a peptide previously studied in the group. Amhelin (antimicrobial helix insert) has been found to form laterally expanding pores of $\backsim 3.2$ nm in supported lipid bilayers, as determined by atomic force microscopy [155] (Figure 2.2). It was shown that pore formation could be stabilised and equilibrated, and could cause membrane integrity to persist. In addition, unless the length of the peptide is well matched to the thickness of the bilayer, hydrophobic mismatch may result in reduced or abrogated activity [157]. Therefore, amhelin will be rationally modified to tilamin (tilted antimicrobial insert) in an attempt to make the mechanism of action less specific for certain bilayer thicknesses, while maintaining a low cytotoxicity to mammalian cells.

The second approach is to alter the structure of a naturally occurring peptide, cecropin B (cecB), to improve antimicrobial activity. CecB is an AMP from the larger family of cecropin peptides, isolated from the hemolymphs of *Hyalophora cecropia* [158, 159]. CecB is 35 amino acids long and is selective for Gram-negative bacte-

ria [160], with modified sequences also showing potent anticancer activity [161]. The peptide consists of two alpha helices; the N-terminal helix is amphipathic and thought to favour surface binding to membranes [162], and the C-terminal helix is hydrophobic, favouring insertion into membranes (Figure 2.4). The mechanism of action of cecB is debated, with different groups proposing often contradictory modes of action. ATR-FTIR showed that cecropin B oriented parallel to the membrane normal [163] and that NBD-labelled cecB existed as monomers from binding isotherms [164, 165], consistent with a carpet mechanism. Conversely, pores of $\backsim$ 4.2 nm were observed in *E. coli* membranes treated with cecB as seen by electron microscopy [160], implicating pore formation in antimicrobial activity. The cecB sequence will be modified to chom (chopped cecropin mutant) as outlined in the design rationale below, to retain or improve the activity of the native peptide, but be simplified in order to better understand the mode of action, and determine if the full sequence is necessary.

2.2 Materials and methods

The thesis makes continuous references to lipid:lipid and peptide:lipid molar ratios, which will be given as (X:X). Non-molar ratios will be explicitly stated when used.

2.2.1 Lipids

POPC, POPG, DMPC and DMPG were purchased from Avanti Polar Lipids (Alabaster, AL). Lipids were dissolved to a concentration of 25 mg mL^{-1} in $CHCl_3$ ($CHCl_3$:MeOH (3:1 *v/v*) for anionic lipids) and stored at −20 °C until use, for up to six months. LPS (extracted from *E. coli* serotype O26:B6) was purchased from Sigma Aldrich.

Below is a general protocol describing the preparation of large unilamellar vesicles (LUVs), small unilamellar vesicles (SUVs) and multilamellar vesicles (MLVs), which were used extensively in the entire thesis. Also explained is the lipid concentration determination protocol, which was also regularly used throughout the thesis.

The requisite lipid composition was mixed from stocks, dried under a stream of nitrogen, then *in vacuo* for at least 1 h. The lipid film was then suspended in the desired buffer and the lipid film left to hydrate for 1 h above the transition temperature of the lipid mixture.

Small unilamellar vesicle formation

The lipid suspension was sonicated in a Jencons-PLS bath sonicator (Leicestershire, UK) for 30 min, after which the cloudy lipid suspension turned clear. The size of the particles varied between batches and experiments but were typically 20 – 30 nm, as determined by DLS.

Multilamellar vesicle formation

The lipid suspension already contained a heterogeneous mixture of differently sized MLVs; to narrow the size distribution and equilibrate the buffer between lamellae the MLVs were subjected to five freeze thaw cycles between liquid N_2 and a temperature above the transition temperature of the lipid bilayers.

Large unilamellar vesicle formation

MLVs were subjected to extrusion to downsize the MLVs into a monodisperse population of large unilamellar vesicles according to an established procedure [166]. The lipid suspension was passed 11 times through an Avanti mini-extruder (Avanti Polar Lipids, Alabaster, AL) containing a polycarbonate filter (Whatman, Maidstone, UK) with a pore size of 100 nm. The resultant LUVs had a mean diameter of 120 – 140 nm, depending on exact lipid composition.

2.2.2 Peptide synthesis

All chemicals used in the synthesis of the peptide were analytical grade. Rink amide MBHA resin and all N-terminus Fmoc protected amino acids were purchased from

Novaniochem (Darmstadt, Germany). N,N-dimethylformamide (DMF), dichloromethane (DCM), N,N-diisopropylethylamine (DIPEA), O-benzotriazole-N,N,N',N'-tetramethyluronium-hexafluoro-phosphate (HBTU), piperidine, trifluoroacetic acid (TFA), triisopropyl silane (TIS), 1,2-ethanedithiol (EDT), diethyl ether, 2,5-dihydroxybenzoic acid (DHB) matrix and acetonitrile (ACN) were purchased from Sigma Aldrich (USA).

The procedure to synthesise both tilamin (KARLAKLRARLYRLKARLARL-NH_2) and chom (KWKVFKKIEKMIRNIRNKIVK-NH_2) was identical. The peptide was synthesised using solid-phase synthesis [167], on a Liberty microwave peptide synthesiser (CEM Inc., Matthews, NC, USA), on a 100 µM scale each time. Any amino acids with reactive side chains were purchased with acid-labile Boc (*tert*-butyloxycarbonyl) protecting groups orthogonal to the base-labile Fmoc (Fluorenylmethyloxycarbonyl) group. Rink amide MBHA resin was used with 0.65 mmol/g substitution. Piperidine (20% v/v in DMF) was used for deprotection of the growing peptide chain. HBTU (0.5 M and DIPEA (1.0 M) were used for amino acid coupling as activator and activator base, respectively.

After N-terminal deprotection, the peptide was transferred to a microwave reactor (CEM Inc., Matthews, NC, USA) for acylation of the N-terminus. The peptide was suspended in a 5 mL solution containing (v/v) 90% DMF, 5% acetic anhydride and 5% pyridine, at 75 ℃ for 10 min, followed by a washing step in DMF (5 mL). This process was repeated at least twice, or until disappearance of the starting material was detected by MALDI mass spectrometry (by hydrolysing a small aliquot of the mixture in TFA).

The peptide was cleaved from the resin, and the side chains deprotected, by incubating the peptide overnight at room temperature in a 50 mL solution of (v/v) 95% TFA, 2.5% TIS, 2.5% H_2O. The suspension was filtered under vacuum, with the peptide contained in the filtrate. The filtered resin was washed with DMF 5 mL twice, and the filtrates combined. The crude peptide was precipitated in cold Et_2O (100 mL), and

centrifuged at 3,500 RPM for 1 h at 4 ℃. The Et_2O was removed, the pelleted peptide dissolved in H_2O (20 mL), and lyophilised overnight.

Purification

The crude peptide was redissolved in H_2O (12 mg mL^{-1}) and purified by high performance chromatography (RP-HPLC) on a Jasco HPLC (Great Dunmow, UK) using a Vydac C18 semi-preparative column (Grace, Dearfield, IL, USA) with a linear gradient of H_2O and AcCN (gradient from 10% v/v to 60% v/v of solution B in solution A - solution A: 95% v/v H_2O, 5% v/v AcCN, 0.1% v/v TFA; solution B: 95% v/v ACN, 5% v/v H_2O, 0.1% v/v TFA).

The identity of each peptide was confirmed by matrix-assisted laser desorption/ionisation time of flight (MALDI-ToF) mass spectrometry on an Autoflex III (Bruker, Germany) in reflectron positive mode using a 2,5-dihydrobenzoic acid (DHB) matrix solution (10 mg mL^{-1} DHB in 50% v/v H_2O, 50% v/v ACN, 0.1% TFA). The purity of the peptide was determined by RP-HPLC on a Jasco HPLC using a Vydac C18 analytical column (Grace, Dearfield, IL, USA) with a linear gradient of H_2O and ACN (gradient from 0% v/v to 90% v/v of solution B in solution A, which were the same mixtures as above). The purified peptides were freeze dried and stored at −80 ℃ until use.

Peptide stocks

Lyophilised peptides were in H_2O at an approximate concentration of 15 mg mL^{-1}. The precise concentration, c (M), of the stock was determined according to the Beer-Lambert Law [168]:

$$c = \frac{A_{280}}{\epsilon_{280} \times l} \tag{2.1}$$

where A_{280} is the absorbance at 280 nm (arising from the aromatic tyrosine and tryptophan residues of tilamin and chom, respectively), l the path length (cm), and ϵ_{280} is

the extinction coefficient of the peptide at 280 nm (M^{-1} cm^{-1}), calculated according to a literature procedure [169]. The stock solution was aliquoted and stored at −20 ℃.

2.2.3 Minimum inhibitory concentration

Minimum inhibitory concentrations (MICs) were deduced by broth microdilution on Gram-negative bacteria (*E. coli* (K12) and *P. aeroginosa* (ATCC 27853)) and Gram-positive bacteria (*S. aureus*), according to the Clinical and Laboratory standards institute [170]). Typically, 100 µL of 4×10^6 CFU mL^{-1} of each bacterium in Mueller Hinton media broth (Oxoid) was incubated in a 96-well microtiter plate with 100 µL of serial twofold dilutions of tilamin and chom, from 200 − 0 µM, at 37 ℃ on a 3D orbital shaker overnight. The plates were then read at 600 nm using a Victor 2 plate reader (Perkin-Elmer). The MIC was defined as the lowest peptide concentration that resulted in no absorbance at 600 nm. All experiments were repeated in triplicate and the results averaged.

2.2.4 Calcein leakage

Calcein entrapped LUV preparation

Large unilamellar vesicles were prepared as outlined above. The vesicles were suspended in self-quenching calcein solution (Calcein (70 mM), TRIS-HCL (10 mM, pH 7.4) to a concentration of 10 mM, and extruded to form 100 nm LUVs. To remove un-entrapped calcein, the LUVs were passed through a size exclusion column (5 mL HiTrap Desalt column (GE Healthcare)), at a flow rate of 2 mL/min and pressure of 0.45 MPa. The faintly yellow LUVs eluted at 1.5 mL, while all strongly-yellow coloured, excess calcein eluted separately after 3 mL. The final concentration of the liposome samples was determined by the lipid concentration assay.

Fluorescence measurements

Fluorescence measurements were performed on a Perkin-Elmer LS-50B fluorimeter (slit width 5 mm). After blanking, samples were excited at 490 nm, and spectra read between 500 nm and 530 nm. LUV samples were diluted to a concentration of 10μM. Peptides were added to make final lipid:peptide ratios of 1 : 0 (lipid only), 500 : 1, 250 : 1, 100 : 1 and 50 : 1. Fluorescence spectra were then taken again 5 min after addition. After 5 min Triton X-100 (10% v/v in H_2O, 5 µL) was added to the cuvette, and a final fluoresence measurement made to obtain the maximal leakage result. The calcein leakage (%L) was determined, by a standard protocol [171] according to

$$\%L = \frac{F - F_o}{F_T - F_o} \times 100, \tag{2.2}$$

where F is the fluoresence maximum at 520 nm of the sample after peptide is added to the LUV suspension, F_o is the initial fluoresence maximum before peptide addition, and F_T is the fluoresence after addition of Triton-X100 (maximum fluoresence). All measurements were repeated in triplicate, and plotted as the average with the standard deviation shown.

2.2.5 Circular dichroism

CD spectra were recorded on a JASCO J-815 spectropolarimeter fitted with a Peltier temperature controller. POPC and POPC:POPG (3:1) LUVs were prepared as described in Section 2.2.1, in sodium phosphate buffer (10 mM, pH 7.4) at a concentration of 3 mM. Tilamin, chom and qaela were made up as 3 mM solutions in phosphate buffer (10 mM, pH 7.4), and diluted to 3 µM for CD measurements, to give a peptide:lipid ratio of 1:100. Spectra were obtained between 190 and 260 nm using a 1 mm quartz cuvette, at a scan rate of 20 nms^{-1}. All spectra were background corrected by appropriate control subtraction. Experimentally measured ellipticities (θ), were converted to molar ellipticities Θ according to $\Theta = \frac{\theta}{cl}$ where c is the peptide concentration and l is the cuvette path length.

2.2.6 Quartz crystal microbalance

QCM experiments were carried out on an E4 QCM-D system from Q-sense AB (Västra Frölunda, Sweden), on 5 MHz SiO_2 QCM-D chips, also from Q-sense AB. To ensure reproducible results the QCM chips were cleaned between readings by immersion in 2% SDS for 30 min, rinsing with H_2O and subjecting the chips to ozone for 10 min.

LUVs of POPC, POPC:POPG (3:1) and POPC:POPG (3:1) w/LPS[†] at a concentration of 5 mg mL^{-1}. LUVs were prepared from lipid films by suspension in HEPES (10 mM) with NaCl (150 mM) and $MgCl_2$ (5 mM, pH 7.4) above the transition temperature of the lipid mixture.

After flowing 2 mL buffer over the QCM chips at a flow rate of 250 µLmin^{-1}, setting the desired temperature, and ascertaining a stable f and D reading across all harmonics, the LUV suspension was diluted to 0.1 mg mL^{-1} and flowed across the chips at a flow rate of 100 µL for 20 min or until a stable SLB had formed as determined by a constant f and d value. Buffer was then flowed across the chips for 1 min at 100 µLmin^{-1} to remove any unbound lipid.

Tilamin and chom were flowed over the chips at 0.2 µM, 2 µM, 5 µM and 10 µM at a flow rate of 250 µLmin^{-1}. After 10 min, the flow was stopped for 15 min, after which time 2% SDS, EtOH and H_2O were sequentially flowed over the chip at a flow rate of 1 mLmin^{-1} to remove peptide and bound lipid from the surface of the chip.

Data was analysed using the Qtools software package [‡].

[†]Due to heterogeneity between different LPS sources it is very difficult to ascertain a molecular weight, and conventionally lipid:LPS ratios of 1 µmol:20 µg are used [172]. "For simplicity 3 µmol:1 µmol:60 µg" will whenceforth be described as "3:1 POPC:POPG w/LPS".

[‡]www.biolinscientific.com/q-sense/

2.3 Results

2.3.1 Antimicrobial design strategy

Tilamin and qaela

The primary sequence of tilamin (tilted antimicrobial insert) was adapted from a peptide previously researched by collaborators; amhelin (antimicrobial helical insert) [155]. The primary structure of tilamin, its relationship to amhelin and a non-functional control peptide (described below) is shown in Figure 2.2.

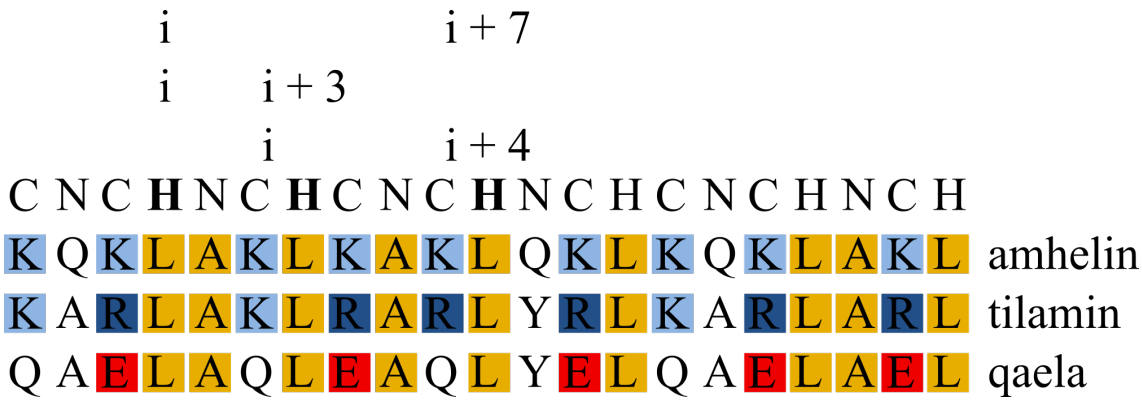

Figure 2.2 The primary sequences of tilamin, amhelin and qaela compared. i, $i+3$ and $i+7$ spacings are shown on the N residues. Cationic lysines and arginines and highlighted in light and dark blue respectively. Absolute sequence identities are displayed in orange.

Both peptides conform to the heptdad repeat strategy [149] of three $CHNCHCN$ stretches, where C,N and H are cationic, neutral polar and hydrophobic residues respectively. This motif has been shown to allow formation of alpha helices [152] of 3.15 nm. All residues were selected due their high propensity for alpha-helix formation [173]. The placement of hydrophobic residues at i, $i+3$ and $i+7$ on the helix allowed, due to geometric constraints imposed by the alpha-helix, amphipathicity with segregation of leucines onto one hydrophobic seam. A non-functional control, qaela (named after the first five residues in the sequence), was also synthesised, with all cationic lysines substituted for glutamine, and all but one arginine substituted for anionic glutamic acid (one was converted to glutamine to aid purification). This peptide

was predicted to have similar structural properties to tilamin but be inactive due to electrostatic repulsion with anionic membranes. The helical wheel projection of tilamin, and the non-functional control qaela is shown in Figure 2.3. The ratio of 1 : 1.5 hydrophobic and cationic residues, and breaking the hydrophobic face of leucines and alanines with cationic residues was to prevent hemolysis associated with broad hydrophobic faces [174].

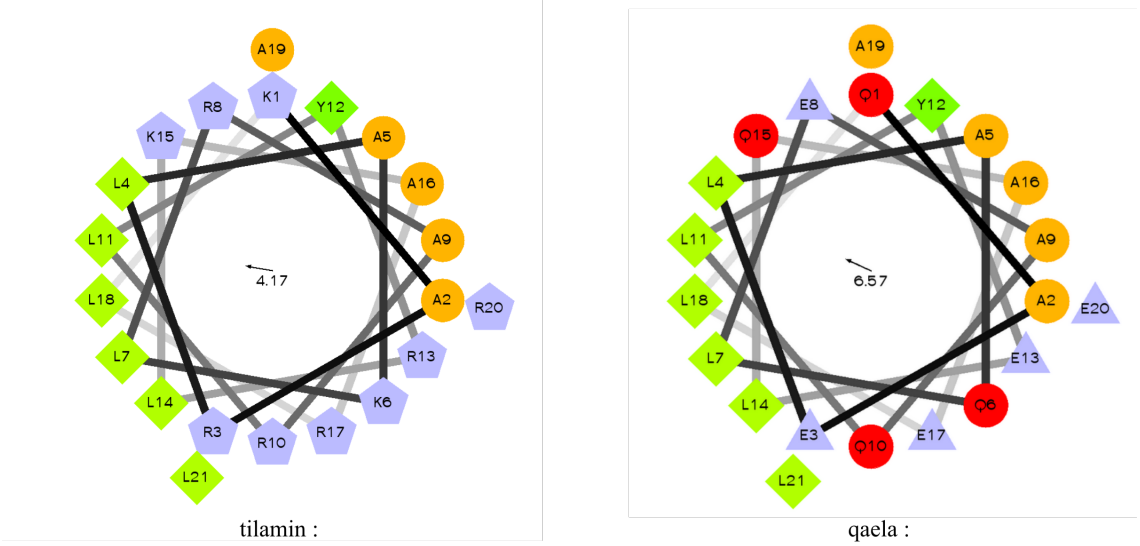

tilamin :
KARLAKLRARLYRLKARLARL-NH_2
molecular weight: 2578.2
charge at pH 7.2: +10
isoelectric point: 12.81

qaela :
QAELAQLEAQLYELQAELAEL-NH_2
molecular weight: 2414.66
charge at pH 7.2: -4
isoelectric point: 3.55

Figure 2.3 Helical wheel projections for tilamin and qaela. Blue pentagons/triangles correspond to (potentially) cationic/anionic residues, green diamonds are hydrophilic residues, and orange/red circles are hydrophilic residues, with red being the most hydrophilic. The arrows denote the hydrophobic moment of the peptides when folded as an alpha helix [175]. Helical projections created using an online resource [176].

Three major modifications were made to amhelin to form tilamin. Two glutamines were substituted for alanines, to prevent excess peptide aggregation associated with glutamine-rich peptides [177]. The central glutamine residue was substituted with tyrosine to break the helicity of the peptide, to allow more flexibility to accommodate to changing membrane architecture during deformation. The hydrophobic residues were also predicted to interact favourably with the acyl core of the bilayer. Finally, six lysines were substituted with arginine. Arginyl residues can form five hydrogen-

bonds with water and stabilise forming phosphate clusters [178], which should enhance interfacial binding. Three lysines were kept in the sequence due their greater ability to traverse the bilayer in their unprotonated form compared to arginine [178], allowing interaction with the inner leaflet headgroups (known sometimes as snorkelling [179]).

Chom

The primary structure of chom (chopped cecropin mutant) was initially based on the sequence of naturally occurring AMP cecropinB. The primary structures of both peptides are shown in Figure 2.4 A, and their linear primary sequences in Figure 2.4.

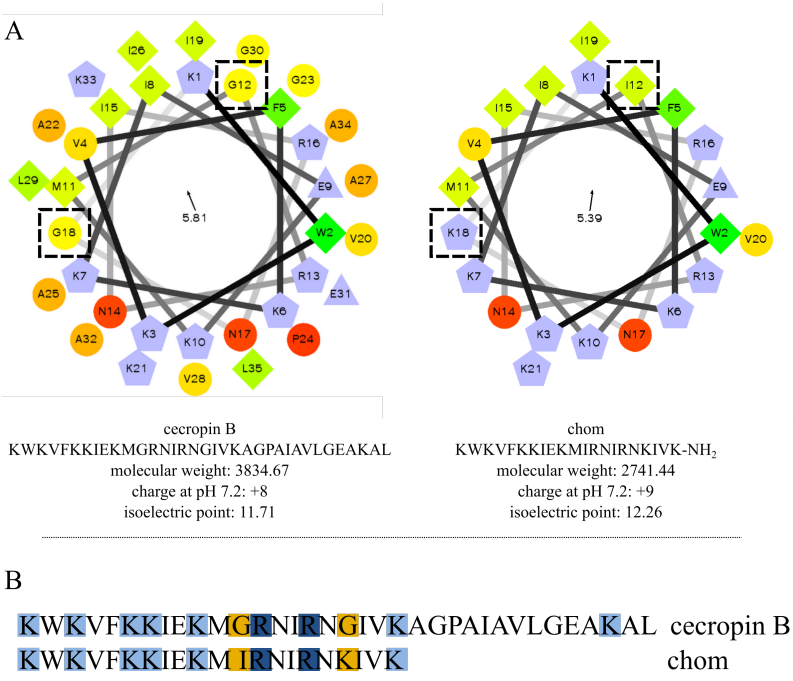

Figure 2.4 A: Helical wheel projections for cecB and chom. Blue pentagons/triangles correspond to (potentially) cationic/anionic residues, green diamonds are hydrophilic residues, and orange/red circles are hydrophilic residues, with red being the most hydrophilic. Helical projections created using an online resource [176]. Point residue changes are highlighted. **B:** The primary sequences of chom and cecB compared. Cationic lysines and arginines and highlighted in light and dark blue respectively. Modifications from the original cecB sequence, other than chopping of the peptide, are displayed in orange.

The cecB peptide was "chopped" in half for several reasons; the amphipathic N-terminal helix is highly conserved between cecA and cecB [162], and it has been further shown that the hydrophobic C-terminal half is dispensable in cytotoxicity against cancer cells [180]. Further modification included removing the glycine zipper $G(X)_nG$ motif. Glycine zippers have been demonstrated to aid helix packing of peptide oligomers [181], and stabilise toroidal pores for shorter peptides similar in length to chom [182]. However, the polar glycine residues on the hydrophobic face can inhibit interfacial structure in the acyl region of membranes and affect pore-formation kinetics [183]. Therefore, the glycines were replaced with lysine and isoleucine to increase migration dynamics, and enhance imperfect amphipathicity in the helix, which also has been shown to aid pore formation [184].

The modifications to both peptides were then tested to see if antimicrobial activity was retained or improved, and if the mechanism of interaction could be elucidated further.

2.3.2 Peptide synthesis

Tilamin and chom were synthesised using solid-phase peptide synthesis. Their identity and purity were determined using MALDI-ToF and analytical HPLC, respectively. Figure 2.5 shows the mass spectra and analytical HPLC traces for tilamin and chom.

Both peptides were synthesised at a purity of > 98%, as judged by integration of the analytical HPLC traces. Qaela, the proposed non-functional AMP, was synthesised by M.Pfeil (University of Oxford).

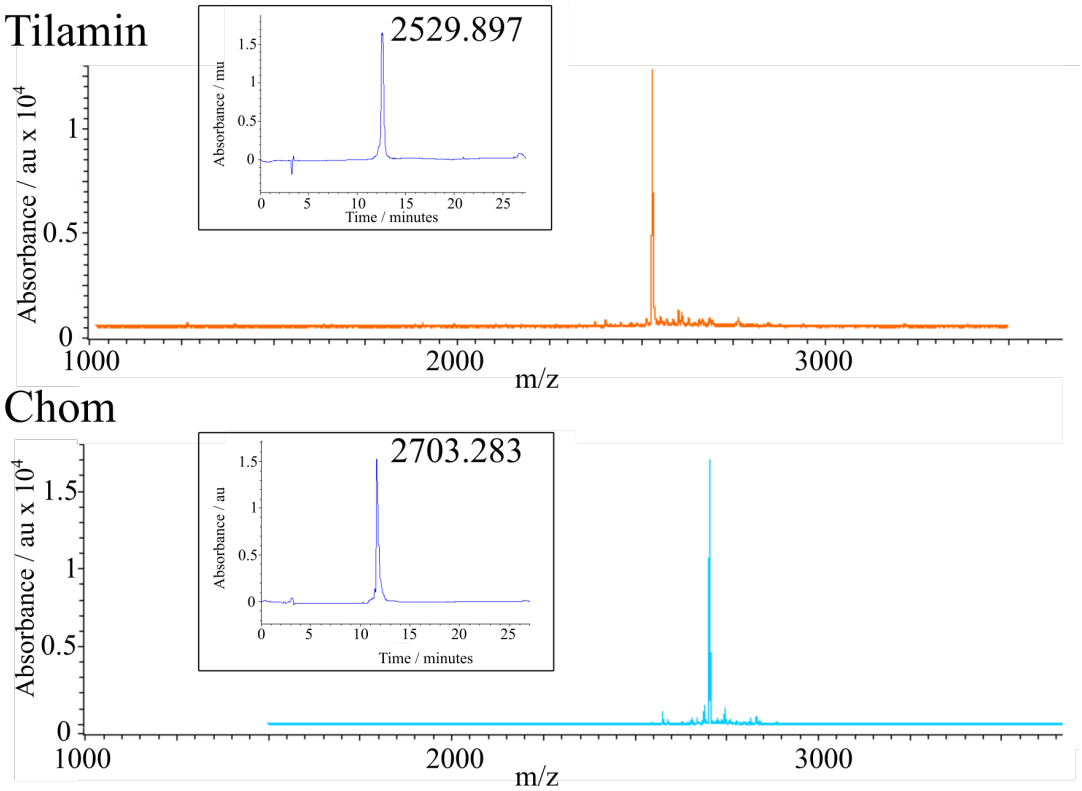

Figure 2.5 The mass spectra and analytical hplc traces (inset) for tilamin (*top*) and chom (*bottom*).

2.3.3 Minimum inhibitory concentration

Figure 2.6 shows the inhibition of overnight growth of Gram-negative (*E. coli* and *P. aeruginosa*) and Gram-positive (*S. aureus*) bacteria by tilamin, the negative control qaela, and chom.

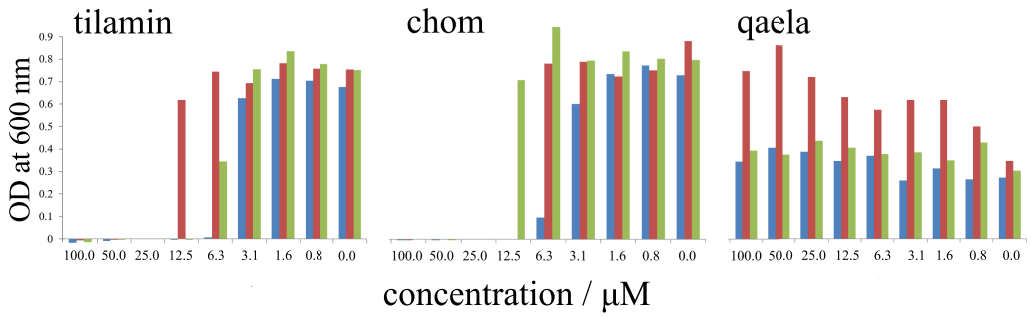

Figure 2.6 Minimum inhibitory concentrations for tilamin, chom and qaela, against Gram-negative (*E. coli* and *P. aeruginosa*) and Gram-positive (*S. aureus*) bacteria. All MIC determinations were the average of at least three independent measurements.

The MICs of the tilamin, chom and qaela were compared to those obtained for conventional antibiotic agents cecropin B and daptomycin, and the 50% lethal concentration (LC_{50}) against human erythrocytes, in Table 2.1.

	MIC of Peptide					
	tilamin	chom	qaela	cecropin B	amhelin	daptomycin
E. coli	3.125	6.25	> 100	< 1	3.125	> 100
S. aureus	25	3.125	> 100	> 100	50 >	7.7
P. aeruginosa	6.25	6.25	> 100	1.6	12	> 100
Human erythrocytes*	> 500	> 500	> 500	> 500	>> 500	> 500

Table 2.1 Minimum inhibitory concentrations (measured in μM) for tilamin, chom and qaela compared to conventional antibiotics. * Instead of MIC, 50% lethal concentration (LC_{50}) was determined for human erythrocytes. LC_{50} and cecropin B, amhelin and daptomycin MICs were evaluated by B. Lamarre (National Physical Laboratory, Teddington, UK).

The MIC experiment indicated that chom and tilamin display potent broad-spectrum bacteriostatic activity against Gram-negative and Gram-positive bacteria. Despite sharing many structural features with tilamin, the anionic negative control qaela was not active against any of the bacterial strains tested, suggesting electrostatic interactions played a large role in antimicrobial activity. The greater absorbance for *S. aureus* samples was possibly due to sedimentation of the bacteria in the wells. The observation that the LC_{50} of the two active peptides were over 20 times greater than the highest MIC (of tilamin against *S. aureus*) suggests that they are non-toxic while being broad-spectrum. The MICs of tilamin and chom were not similar in magnitude or bacterial selectivity to cecB, which acts by accumulating at the outer membrane of Gram-negative bacteria [185], or daptomycin, which was been shown to form pores and also interact with intracellular targets [186]. In addition, while being similarly active against both Gram-negative bacteria tested, chom was much more active against Gram-positive *S. aureus* compared with cecB, as was tilamin compared to amhelin, suggesting the primary sequence modifications resulted in more active peptides. The data were consistent with a different mechanism of action to the control peptides.

2.3.4 Calcein leakage

To determine if the AMPs caused leakage of model membranes, calcein leakage experiments were carried out over a range of P:L ratios. Calcein is a fluorescent small molecule (622 Da) that is dianionic at neutral pH, and has been used to investigate leakage of lipid vesicles induced by AMPs [187, 188]. Calcein self-quenches at high concentrations (above 70 mM) when inside vesicles. As the vesicle leaks, whether spontaneously over time or upon addition of an AMP that disrupts the membrane, calcein is released and there is an increase in fluorescence due to reduced self-quenching. At the end of the experiment Triton-X100 detergent is added, and the resulting fluorescence corresponded to complete leakage (Figure 2.7).

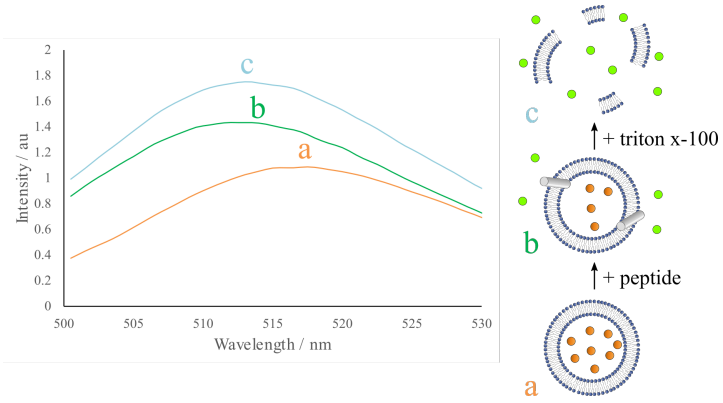

Figure 2.7 The fluorescence spectrum of calcein, entrapped in POPC:PG (3:1). *Orange:* Lipid only sample. *Green:* + tilamin (peptide:lipid 1:100). *Blue:* + Triton X-100(10% v/v in H_2O, 5 µL).

The blue shift upon membrane leakage was due to the leaked calcein experiencing a changing polarity from the highly concentrated vesicle interior to the bulk solution. The ability of chom and tilamin to induce leakage in POPC LUVs, mimicking mammalian membranes, and POPC:PG (3:1) LUVs, mimicking bacterial membranes, was investigated at different peptide:lipid ratios, as shown in Figure 2.8 (overleaf).

Generally, an increase in calcein leakage was observed as the peptide:lipid ratio was increased, as the greater concentration of AMP caused disruption of the LUVs, which resulted in calcein leakage, suggesting that peptide-lipid interactions, specifically mem-

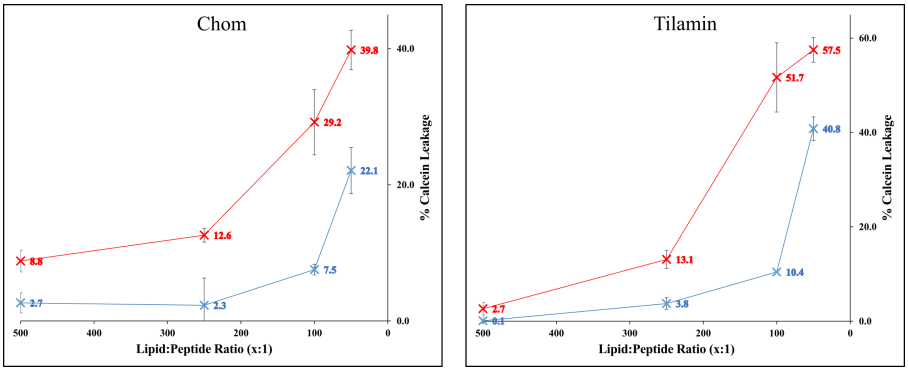

Figure 2.8 Permeation of model membranes by tilamin (*right*) and chom (*left*), as monitored by calcein fluoresence. X-POPC:PG(3:1), X-POPC. Each point is the average of 3 measurements, with the standard deviation shown.

brane leakage, could play a role in the mechanism of both AMPs. The induced leakage was less for zwitterionic POPC LUVs compared to anionic POPC:PG (3:1) LUVs for both peptides. This suggested that the AMPs displayed some preference for anionic membranes, presumably on the basis of electrostatic interactions. Tilamin displayed a sharp increase in membrane leakage between peptide:lipid molar ratios of 1:250 and 1:100, while a more gradual increase was observed for chom, implying that at a certain threshold concentration between, tilamin underwent a rearrangement at the membrane, perhaps adopting a conformation in the bilayer that caused greater leakage of calcein over the time course of the experiment. Conversely, the more gradual increase observed for chom suggested that the leakage from the model membrane was caused by a single concentration dependent mechanism.

2.3.5 Circular dichroism

To determine if the selective leakage induced by the AMPs was a result of their secondary structure, CD experiments were performed. The secondary structure of tilamin, qaela and chom was assessed in the absence of any liposomes, and in the presence of POPC and POPC:POPG (3:1) 100 nm LUVs, at a peptide:lipid molar ratio of 1 : 100, as shown in Figure 2.9.

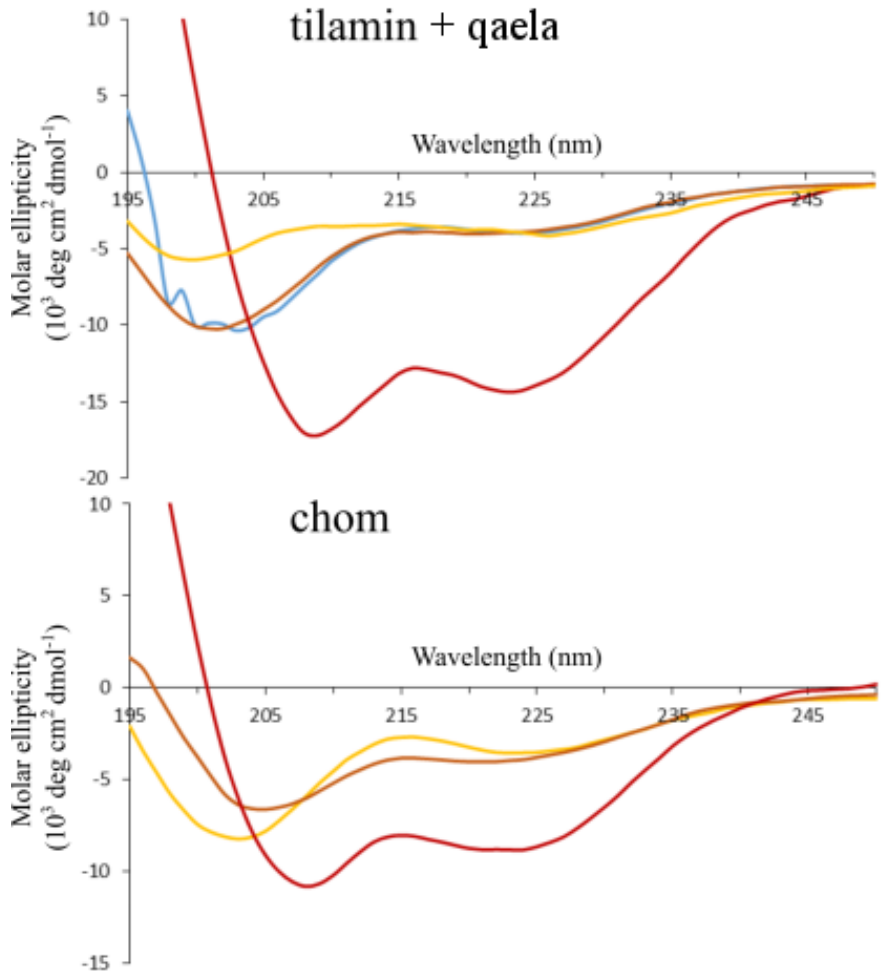

Figure 2.9 CD spectra of tilamin and chom in the absence (yellow) and presence of POPC (orange) and POPC:POPG (3:1) (red) 100 nm diameter LUVs. The CD spectrum of qaela in the presence of POPC:POPG (3:1) LUVs is shown in blue. Peptide/LUV concentration was 0.03/0.3 mM.

The trends in Figure 2.9 were the same for both functional AMPs. In solution, and in the presence of zwitterionic POPC LUVs (P:L 1:100), tilamin and chom remained unstructured, with CD spectra showing random coil conformations, with a broad maximum around 200 nm. In the presence of anionic POPC:PG (3:1) LUVs, both peptides adopted an alpha-helix conformation, evidenced by two minima in the CD spectra of 222 and 207 nm. The non-functional control qaela remained unstructured in the presence of POPC:PG LUVs, which was likely due to electrostatic repulsion between the peptide and the liposomes. The results indicated that in the presence of anionic LUVs, the two functional AMPs were able to form amphipathic alpha helices, which

were stabilised by interactions between the acyl region of the LUV bilayer and the hydrophobic face, and the phospholipid headgroup/water interface and the hydrophilic face. Qaela did not display any secondary structure in the presence of anionic membranes, presumably due to repulsive electrostatic forces.

2.3.6 Quartz crystal microbalance

To assess how the peptides disrupted membrane structure, and the rates of these processes, QCM experiments were performed with the peptides interacting with a variety of supported lipid bilayers; POPC to mimic mammalian cell membranes, POPC:POPG (3:1) to mimic anionic bacterial membranes, and POPC:POPG (3:1) w/LPS to more accurately mimic the outer membrane of a Gram-negative bacterial membrane.

SLB formation

Figure 2.10 (overleaf) shows a typical QCM experiment. SUVs were first flowed over the chip, and after rupture of the adsorbed vesicles an SLB was formed for POPC, POPC:POPG (3:1) and POPC:POPG:LPS (3:1:80 μg).

The large initial decrease/increase in $\Delta f/\Delta D$ at around 10 min was caused by intact LUVs adsorbing on the surface of the chip, and after collapse to form SLBs, $\Delta f/\Delta D$ values of $\backsim 26$ Hz/$\approx 0.5 \times 10^{-6}$ were obtained, consistent with previous literature values [189]. It was not possible to form DMPC or DMPC:DMPG 3:1 SLBs; the QCM trace showed a continuous gradual decrease/increase of $\Delta f/\Delta D$ to $\backsim 67$ Hz/6×10^{-6}, indicating the adsorbed LUVs were not rupturing. This could have been due to the phase behaviour of the DM- lipids; DMPC and DMPG have gel-liquid crystal T_m values of 23 °C, compared with −2 °C for POPC and POPG [190], and being at the transition temperature at room temperature may have hindered vesicle rupture. Despite examples in the literature of SLB formation for DM- lipids [191], changing temperature and divalent cation concentration (previously shown to aid vesicle rupture [192]) did not affect the QCM traces, and hence DM- length lipids were not investigated further.

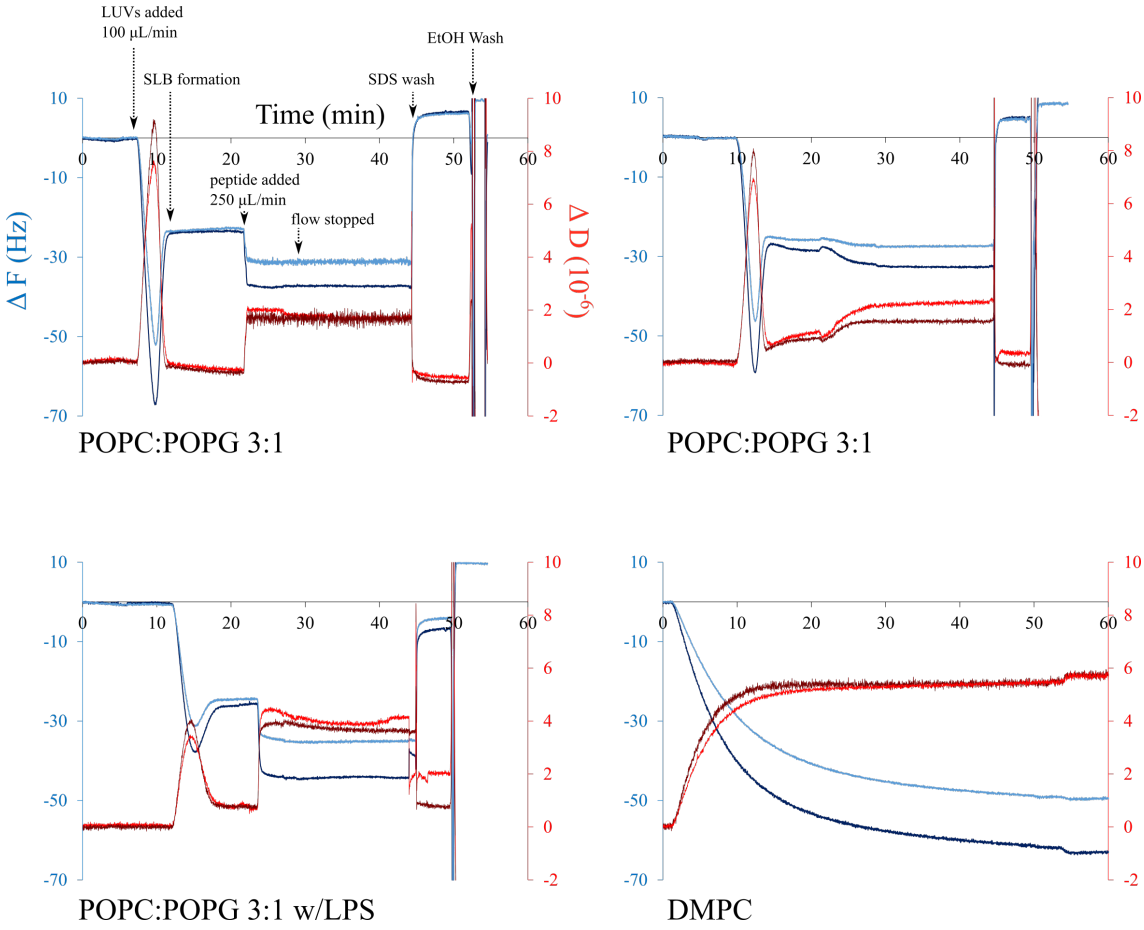

Figure 2.10 A typical QCM experiment, showing SLB formation for POPC, POPC:POPG (3:1) and POPC:POPG:LPS (3:1:80 ug), and the failed SLB formation for DMPC. SUVs were first flowed over the chip, and after rupture of the adsorbed vesicles an SLB was formed. Peptide was then flowed across the cell, after which time flow was stopped for fifteen minutes to allow the system to equilibrate. f and D measurements were made for overtones 3-11; shown are the frequency/dissipation values for overtone 3 (dark blue/dark red) and 11 (light blue/light red).

The formation of SLBs with POPC:POPG (3:1) w/LPS, not previously attempted, differed from SLBs containing only glycerophospholipids. A more modest decrease in $\Delta f/\Delta D$ was observed upon LUV adsorption ($\backsim -35$ Hz compared with $\backsim -70$ Hz for POPC/POPC:POPG 3:1) before formation of the SLB. This suggested that the presence of the highly charged LPS destabilised the LUVs to permit rupture before a critical threshold amount of adsorbed LUVs was reached.

After SLB formation, an AMP was then flowed across the cell, after which time flow was stopped for fifteen minutes to allow the system to equilibrate. f and D measure-

ments were made for overtones 3-11; the fundamental frequency f_1 was not measured at it was prone to instabilities [192].

Net changes in $\Delta f/\Delta D$ due to peptide interactions

Tilamin and chom were flowed across the SLBs at varying concentrations. The net changes in frequency, corresponding to mass deposition/removal, and dissipation energy, corresponding to structural rigidity, as a function of overtone were calculated from the QCM traces. Figure 2.11 shows the net changes in f and D for chom. Chom

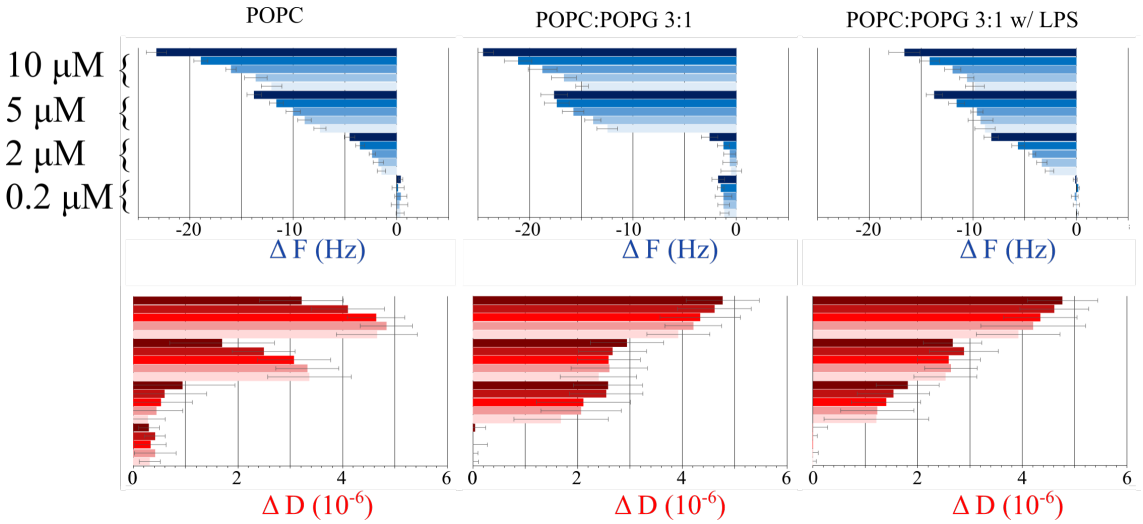

Figure 2.11 Net f and D changes upon chom addition to POPC,POPC/POPG and POPC/POPG/LPS SLBs, at different concentrations. Blue/red bars indicate changes in frequency/dissipation, with dark-to-light bars corresponding to harmonics 3-11.

displayed a concentration dependent decrease in frequency, indicating an increase in mass due to peptide binding. The greatest increase in mass was, for all SLB lipid types, observed at harmonic 3, *ie* furthest from the chip surface, meaning the peptide was mainly binding to the headgroup region of the SLB. In addition, for all SLB lipid types a concurrent increase in dissipation energy was observed, indicating a loss of structural rigidity, which was similar across all harmonics. This observation could be due to the peptide disrupting the SLB, causing influx of water to the chip surface and increasing bilayer fluidity. Above 2 µM, there was no significant difference between POPC and POPC:PG (3:1) SLBs in terms of Δf or ΔD, at any harmonics. This may

have been due to chom saturating the SLB to such an extent that initial electrostatic interactions were not discriminatory, and membrane disordering was mainly driven by hydrophobic interactions with the bilayer. The results indicated chom could be exerting its antimicrobial effect *via* a carpet-like mechanism (Figure 1.8 in introduction). Smaller changes in frequency and dissipation energy were observed for SLBs containing LPS, suggesting the presence of the polysaccharide headgroup of LPS prevented interaction of chom with the SLB.

A different mode of interaction was observed for tilamin (Figure 2.12). At 0.2 µM and 2 µM an *increase* of frequency was observed, suggesting lipid removal as a result of partial peptide insertion into the bilayer, similar to caerin 1.1, another AMP studied by QCM [103]. A corresponding decrease of dissipation of energy was also recorded, indicating the SLB was becoming more rigid, which may be due to peptide binding, but in a different mode to chom, causing a reduction in lipid mobility. From 2 µM and 5 µM an abrupt change in peptide-lipid interactions was seen, manifested by a small increase in mass across all harmonics, as well as a decrease in SLB rigidity. This effect was also observed, but with no greater intensity, at 10 µM. These results

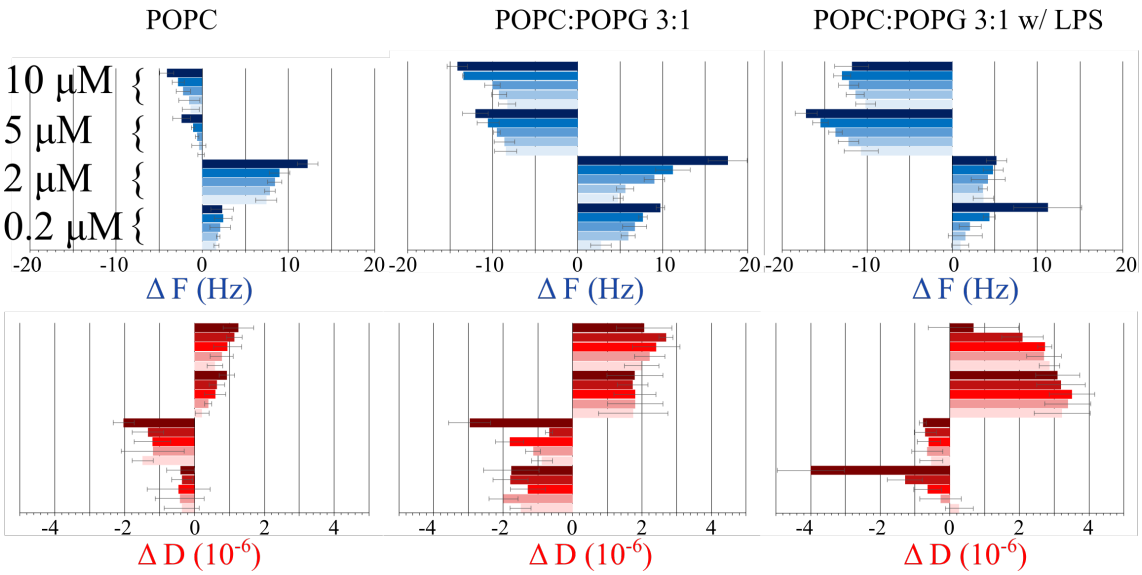

Figure 2.12 Net f and D changes upon tilamin addition to POPC,POPC/POPG and POPC/POPG/LPS SLBs, at different concentrations. Blue/red bars indicate changes in frequency/dissipation, with dark-to-light bars corresponding to harmonics 3-11.

were consistent with a model where tilamin first inserts into a membrane, perhaps as monomers, at the headgroup region, displacing lipids. Once a threshold concentration is reached, a structural reorganisation takes place, where an increase in mass is observed. The change in structural arrangement could be due to oligomerisation of tilamin when a sufficient amount binds to the membrane, and the increase of mass could be a result of water influx to replace the displaced lipids. Greater changes were observed for POPC:POPG (3:1) SLBs with and without LPS compared to POPC, suggesting electrostatic interaction of tilamin with the anionic headgroups was necessary for the membrane interactions.

To obtain a qualitative description of how the AMPs interacted with the SLBs, and the timescales for such interactions, Δf-ΔD were next plotted.

Δf-ΔD plot of peptide-lipid interaction - chom

Figure 2.13 shows the Δf-ΔD plots for chom interacting with different SLBs at different concentrations. For clarity, only the 3rd, 7th and 11th harmonics were plotted. Each point on the plot corresponded to a time point, and hence the further the spacing between points, the faster the SLB reorganisation causing the change in Δf and ΔD. For all concentrations of chom, broadly the same plot was obtained, where the trace moves in a north-east direction, indicating an increase in mass on the SLB and a loss of structural rigidity. In every trace, the 3rd harmonic experiences the greatest changes, suggesting the peptide was residing furthers from the chip surface, at the headgroup region of the SLB. In addition, the *difference* between harmonic 3 and the other harmonics was greatest for SLBs containing LPS. This suggested that most of the peptide was interacting with the LPS outer core, and less able to reach the lipid bilayer closer to the surface. So, while LPS interacted with chom allowing binding to the SLB, it may also have simultaneously prevented further interactions deeper into the bilayer due to strong electrostatic interactions with the AMP.

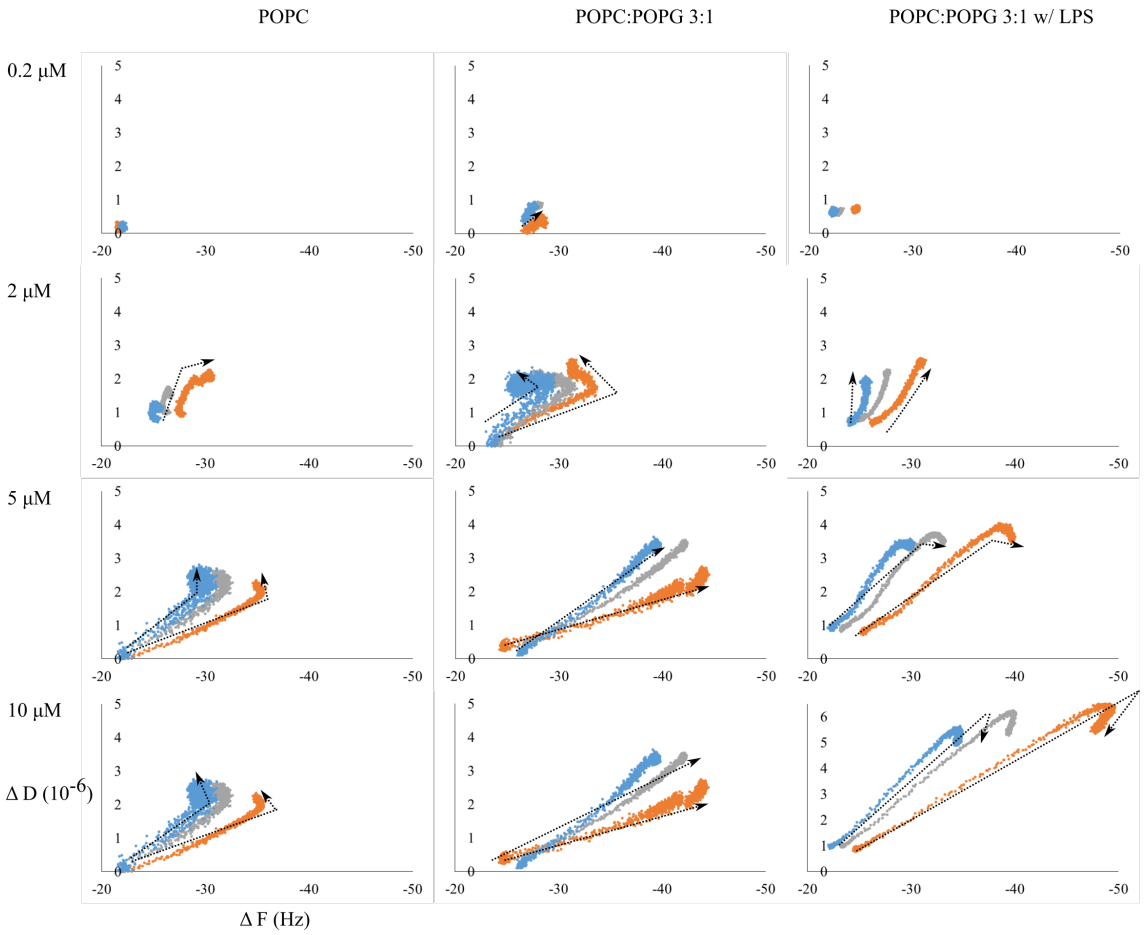

Figure 2.13 ΔF-ΔD plots for chom with POPC,POPC/POPG and POPC/POPG/LPS SLBs, at varying concentrations. Δf is plotted in reverse order, so that changes from left-to-right correspond to increases in mass, while increases in dissipation energy correspond to decreases in structural rigidity. For clarity, only the 3rd (orange), 7th (grey) and 11th (blue) harmonics are plotted. Arrows indicate the evolution of the QCM trace over time.

At 2 µM, the fastest response to the chom addition was from POPC:POPG SLBs, and more gradual for POPC and POPC/POPG/LPS, suggesting electrostatic interactions contributed to fast binding (less than two minutes), which was less fast with pure POPC SLBs and SLBs containing LPS. The decrease in structural rigidity could be explained by the peptide interrupting the packing of the fluid membrane, increasing *trans-gauche* isomerisations in the acyl chains and hydrogen-bond networks in the headgroups, which may allow water to enter the bilayer, which would further increase the mass measured [193].

Above 2 μM all changes in mass deposition occurred within two minutes, implying above a threshold concentration the interaction of chom with an SLB is not selective for lipid headgroup identity. For POPC and POPC/POPG SLBs, after fast peptide addition, a slow increase of dissipation energy was observed, which could be due to water penetrating the bilayer. For POPC/POPG/LPS, a slow *decrease* was measured, which might imply a more complex structural rearrangement of the LPS occurring to accommodate the bound peptide.

Δf-ΔD plot of peptide-lipid interaction - tilamin

Figure 2.14 shows the Δf-ΔD plots for tilamin interacting with different SLBs at different concentrations.

A more complicated picture emerges for tilamin compared to chom. At 0.2 μM and 2 μM, a general decrease of mass was observed, with an increase in structural rigidity. This suggested tilamin was displacing lipids in the SLB, and decreasing the fluidity of the membrane, perhaps in a cholesterol-like manner [194]. A very large decrease in mass and increase in rigidity was measured for the third harmonic for POPC/POPG/LPS; suggesting that tilamin was bound mainly to the LPS outer core. At 2 μM for POPC/POPG, and 5 μM for POPC/POPG/LPS, a very complicated Δf-ΔD plot was generated. This was difficult to ascribe to a specific mechanism of interaction with the SLB, and was probably due to a mixture of processes occurring simultaneously; a population of monomers may be disrupting the headgroup region of the SLB in a carpet-like fashion, while others are aggregating and forming transmembrane pores (Figure 1.8 of introduction). These AMP-lipid interactions would not be separable using QCM alone. At 10 μM, all Δf-ΔD plots resembled the situation for chom, suggesting at this concentration the mode of membrane interaction was the same.

For both peptides, the QCM data indicated that most interactions with the SLBs were located near the headgroup region of the SLB, and, as changes were not equal between harmonics, the AMPs were not inserting transmembrane into the SLBs in a

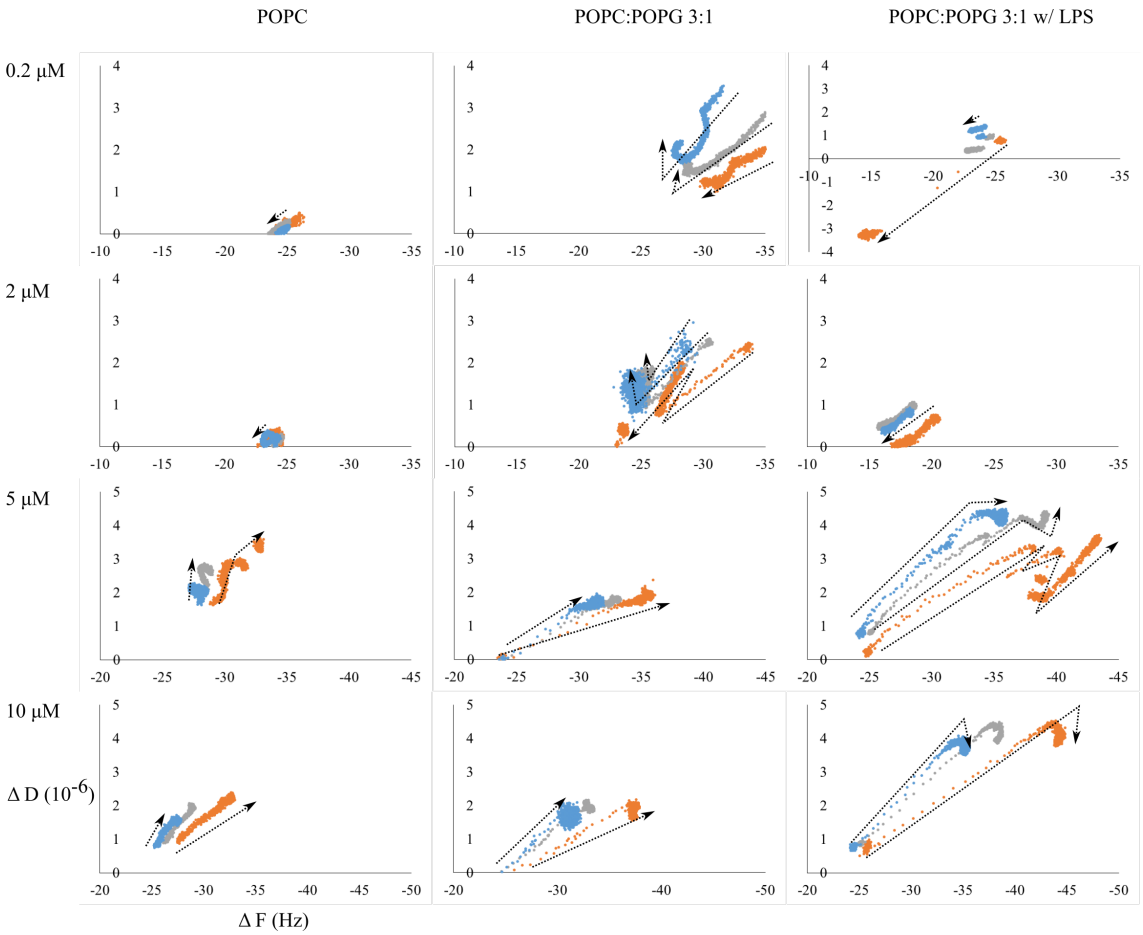

Figure 2.14 Δf-ΔD plots for tilamin with POPC,POPC/POPG and POPC/POPG/LPS SLBs, at varying concentrations.Δf is plotted in reverse order, so that changes from left-to-right correspond to increases in mass, while increases in dissipation energy correspond to decreases in structural rigidity. For clarity, only the 3rd (orange), 7th (grey) and 11th (blue) harmonics are plotted. Arrows indicate the evolution of the QCM trace over time.

barrel stave mechanism. However, a toroidal pore mechanism could not be precluded: lipid loss from the headgroups of both leaflets would also lead to heterogeneous changes across harmonics. The fact that chom was less discriminate towards POPC and POPC/POPG SLBs may be a result of the peptide being less charged; chom has an overall charge of +9 compared to +10 for tilamin.

2.4 Discussion

The aim of this chapter was to synthesise two *de novo* AMPs, sequences of which were based on a previous synthetic and a natural AMP, amhelin and cecropin B, respectively [155, 195]. The modifications, which were implemented to improve antibacterial activity and further elucidate AMP modes of action, were shown by MIC experiments to retain antimicrobial activity (Table 2.1). Indeed, tilamin and chom both showed improved activity against Gram-positive *S. aureus* compared with amhelin and cecB, respectively. None of the peptides showed displayed any haemolytic activity against human erythrocytes, suggesting they could be promising future therapies.

Experiments on model membranes mimicking bacterial and mammalian membranes revealed insights into how the peptides exerted their antimicrobial activity. Calcein leakage revealed that both peptides caused concentration-dependent leakage of calcein from the interior of anionic model membranes, with less leakage observed from neutral model membranes (Figure 2.8). Perhaps not surprisingly, this finding implied that, at minimum inhibitory concentrations, membrane disruption was involved in the bactericidal mode of action of both AMPs. However, maximum leakages of 39.8% and 57.5% of chom and tilamin, respectively, are fairly modest compared to other synthetic AMPs that display 100% leakage at the same concentration and lipid composition [171]. Indeed, cecropin B, at the same peptide:lipid ratio, caused > 95% leakage in PC:PA vesicles [196]. The contrast in leakage efficiency underpins the importance of the lipid composition of model membranes. Phosphatidic acid does not have a headgroup compared to phosphatidyl lipids, and may not be a suitable model for bacterial membranes. The utility of calcein leakage experiments could be improved with lipid compositions more accurately resembling real cell membranes. In addition, in light of other AMPs, these findings also suggest that membrane leakage may not be the sole mechanism of action of both peptides, or that partial leakage is sufficient to compromise cell membrane integrity and to kill bacterial cells. In spite of this, the timescales for calcein leakage and membrane perturbation measured using

QCM ($\backsim$ 5 min) correlate well with the rates of killing of cells by AMPs [197], suggesting that membrane pertubation are intimately linked to bactericidal effect.

Circular dichroism revealed that both peptides folded into desired alpha helices in the presence of anionic model membranes, while remaining unstructured in solution and in the presence of neutral membranes (Figure 2.9). This implies that initial electrostatic attraction to anionic membranes permits amphipathic helix formation, stabilised by interactions with the bilayer, which is precluded in neutral membranes. It also suggests that secondary structure of both peptides is a prerequisite for antimicrobial activity and helps explain the bactericidal activity of both peptides, without causing hemolysis. However, it was not possible to determine the absolute amount of secondary structure *per* peptide; the peptides could be an equilibrium mixture of alpha-helical in contact with the membrane and disordered in solution, with the proportion depending on the partitioning ability of the peptide, or, once at the membrane, could be interconverting between alpha helical and disordered. Indeed, previous studies have showed that different AMPs, while displaying the same CD spectrum, or amount of helical content, can either be stable alpha helices in a model membrane, or rapidly interconverting between coiled and disordered, as deduced from computer modelling[313].

Finally, QCM experiments revealed chom and tilamin disrupted membranes primarily *via* interactions with the headgroup of the bilayer (Figures 2.14,2.13). SLBs of different lipid composition were differentially affected, underpinning the importance of lipid specificity in the AMPs mode of action. Abrupt changes in peptide-lipid interactions were observed with tilamin at a threshold concentration, indicating that the peptide may be operating *via* a two-step process.

QCM is a useful qualitative technique to evaluate AMP mechanisms of action; the ability to probe different harmonics of the sensor chip allows the changes in structure as a function of bilayer depth to be examined upon peptide binding. However, QCM

measurements alone are not sufficient to quantify or confirm a mode of action; quantitative estimates of mass changes for lipid bilayers from Δf measurements suffer from an inability to accurately model a lipid bilayer on the chip [198]. The Sauerbrey equation, which relates changes in frequency to changes in areal mass on the chip [199], is only valid for rigid solid films. However, a bilayer is non-rigid, and "wet", *i.e.* suspended in an aqueous medium. Calculations of areal mass on the chip based on frequency are underestimated using the Sauerbrey relation [200], and despite other approaches accounting for this (visco-elastic modelling [111]), it is not possible to attain absolute changes in mass (and dissipation) solely from the experimental parameters. In addition, the penetration depth of a given harmonic n (δ_n), where the amplitude of the shear wave has decreased by a factor e at a given overtone, has been calculated for different harmonics for a bilayer, as shown in Table 2.2 [201].

overtone number	3	5	7	9	11
penetration depth in membrane	14.6 nm	11.3 nm	9.5 nm	8.4 nm	7.6 nm

Table 2.2 Penetration depth of different harmonics calculated for an SLB. Table reproduced from [189].

It is clear that the different harmonics contain overlap and are not sensitive to changes in discrete parts of the supported lipid bilayer. In addition, regions beyond the bilayer are probed by lower harmonics, and hence sensitive to bulk solvent properties. QCM should therefore only be used a qualitative guide for AMP mechanisms of action.

In conclusion, the two *de novo* AMPs displayed broad spectrum antimicrobial activity, without mammalian cell toxicity. The secondary structure of both peptides was dependent on lipid environment, with the attainment of alpha-helical structure apparently important for membrane interactions. Both peptides caused cell leakage from model membranes, suggesting that membrane permeabilisation was one contribution to the antimicrobial activity of the peptide. QCM experiments gave a qualitative description of how the AMPs interacted with model membranes, with binding oc-

curring mainly at the headgroup of the SLBs, with tilamin showing a concentration-dependent mode of action.

The preliminary data were not sufficient to definitively outline a mode of action, and hence solid-state NMR experiments were carried out next in order to gain structural information on bilayer changes upon perturbation by the AMPs at greater resolution.

Chapter 3

Solid-State NMR Investigations into Tilamin, Chom and Qaela

3.1 Introduction

3.1.1 Headgroup-deuterated lipid synthetic considerations

To examine the initial binding of a membrane active peptide to the surface of a bilayer, lipids can be labelled with ^{2}H in the hydrophilic headgroup. This requires a flexible convergent chemical synthesis that can be used to form ^{2}H-labelled headgroup lipids with varied acyl chain length and unsaturation, and the stereochemistry of any stereocentres preserved. Eibl showed that PE, PC and PG lipids could be synthesised in this manner from a labelled headgroup of glycerol, ethanolamine or choline, and 1,2-diacylglycerol with different acyl chains (Figure 3.1) [202, 203].

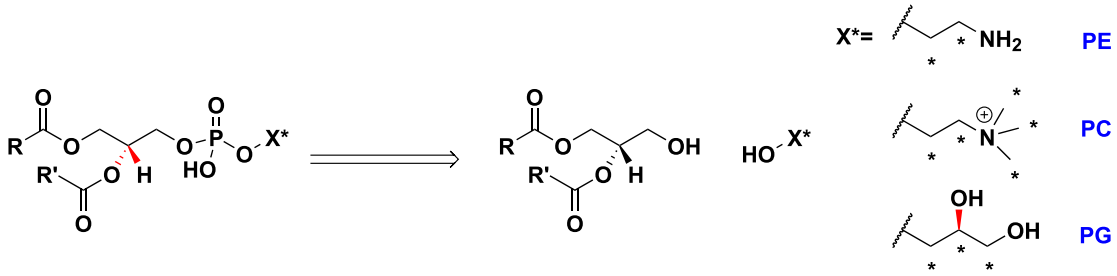

Figure 3.1 Retrosynthetic analysis to access biologically relevant lipids (phosphatidylcholine, -ethanolamine, and -glycerol), with asterisks indicating potential positions of deuteration. Stereocentres shown in red.

Chemically synthesising a variety of lipids with ^{2}H-labelled headgroups allows several interactions with membrane peptides to be examined. Different headgroups with different charge properties allow animal and bacterial membranes to be mimicked with subsequent differences in the interaction with AMPs helping explain natural cell se-

lectivity. Differing degrees of unsaturation in the acyl chain affect the phase properties at a given temperature allowing the disrupting influence of membrane peptides on different lipid phases be studied. Synthetic considerations include preventing epimerization at any stereogenic centres in the molecule, preserving double-bond geometry in any unsaturated bonds in the acyl chains, and avoiding isomerisation of 1,2-diacylglycerol to the thermodynamically more stable 1,3 form (Figure 3.2)[204].

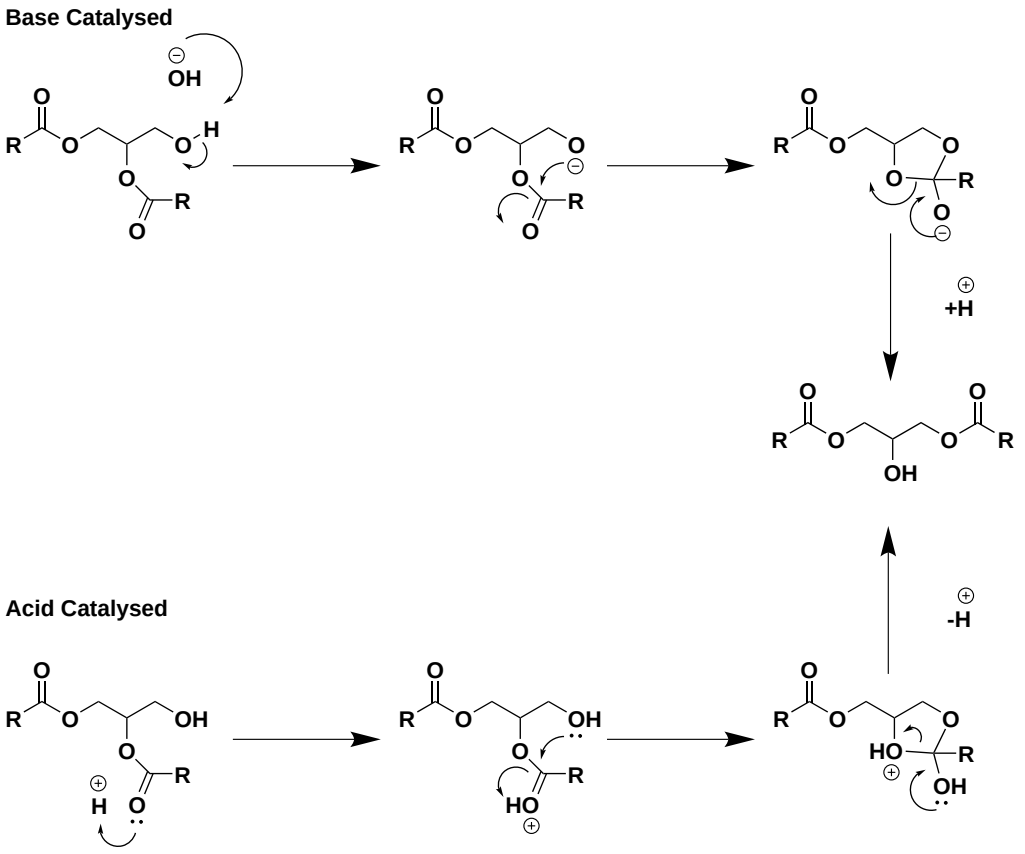

Figure 3.2 Migration of a 1,2-diacylglycerol to the thermodynamically more stable 1,3-isomer can be acid- or base-catalysed.

3.1.2 Aims of chapter

To gain a more quantitative insight into the nature of the AMP-lipid interactions that cause membrane disruption, ^{2}H ssNMR experiments will be formed with model membranes mimicking different cell membranes, containing lipids deuterated in the acyl and headgroup regions. Headgroup-labelled lipids are not commercially available, and will be synthesised using a combination of established and novel methods. DLS

experiments will be performed to evaluate any changes in membrane morphology caused by AMP binding.

3.2 Materials and methods

3.2.1 ^{2}H-labelled lipid synthesis

POPC-d_{31} and POPG-d_{31} were purchased from Avanti Polar Lipids (Alabaster, AL). Lipids were dissolved to a concentration of 25 mg mL^{-1} in $CHCl_3$ ($CHCl_3$:MeOH (3:1 *v/v*) for anionic lipids) and stored at −20 ℃ until use, for up to six months. For the chemically synthesised headgroup-deuterated POPG-d_2, DMPG-d_2, POPE-d_4 and DMPE-d_4, reaction procedures and spectroscopic data confirming the products of reactions are listed in the appendix.

3.2.2 Solid-state NMR

Sample loading

Lipid films were prepared as described in Section 2.2.1. Films were hydrated in 20 µL ^{2}H-depleted HEPES buffer (20 mM, pH 7.0), and freeze-thawed five times to form MLVs. Peptides from a concentrated stock (> 10 mg mL^{-1}) were added directly to the lipid dispersion. Samples were loaded into a 4 mm NMR MAS rotor by centrifugation (2000 RPM, 1 min) through a 1 mL pipette tip.

Instrumentation

Static ssNMR experiments were performed on 800 MHz and 500 MHz Infinity plus wide bore spectrometers, equipped with 4 mm HXY probes at 21 ℃. ^{2}H Spectra were acquired at 122.78 or 77.67 MHz using a quadrupole echo sequence with a 4 µs 90° pulse, a 50 µs refocusing delay and a recycle delay of 0.5 s. The spectra were then left-shifted to the echo maximum and depaked [205]. From the depaked spectra, order parameters (S_{CD}) were calculated according to

$$\Delta\nu_Q = \frac{3}{4}\frac{e^2qQ}{h} \cdot S_{CD} \tag{3.1}$$

where $\frac{e^2qQ}{h}$ is the static quadrupolar coupling constant.

3.2.3 Dynamic light scattering

DLS experiments were carried out on a Zetasizer Nano NS (Malvern Instruments) at 21 ℃. The data represented the average of twenty 10 s experiments. The intensity distribution was generated using OmniSize 3.0.1 software.

3.3 Results

3.3.1 ^{2}H-labelled lipid synthesis

Synthesis of 1,2-diacylglycerols

Adapting a literature procedure [206], diol **2-2** was formed from (*S*)-(+)-solketal in two steps (Figure 3.3). MEM was chosen as a protecting group as it allowed long chain acyl groups to be added to diol **2-2** in a way that preserved stereochemistry, and its removal proceeded in conditions that did not cause complete isomerisation to the 1,3-diacylglycerol.

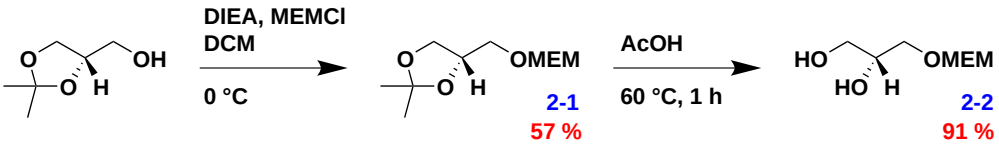

Figure 3.3 Formation of intermediary diol **2-2**

Reaction of diol **2-2** with various acyl chlorides yielded diacyl glycerols of differing chain length (Figure 3.4). For formation of monoacyl glycerol **1-3**, the acyl group had to be installed on the terminal position of the molecule, so the reaction was carried out under kinetic conditions at -10 °C . Disubstitution was disfavoured by

using only 1.3 equivalents of the acyl chloride. Some disubstituted diacylglycerol **2-4** was formed, but could usefully be isolated and taken forward to eventually form dipalmitoyl-based lipids.

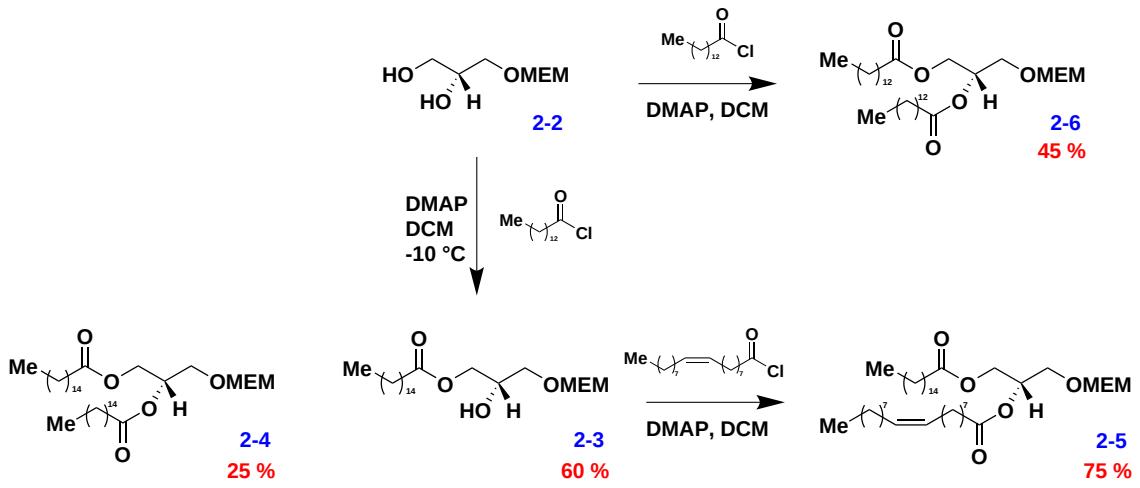

Figure 3.4 Formation of protected diacylglycerols **2-4**,**2-5** and **2-6**

Deprotection according to literature procedures was difficult (Figure 3.5) [207], since during the work up the use of ammonium hydroxide presumably facilitated base-catalysed acyl migration (Figure 3.2).

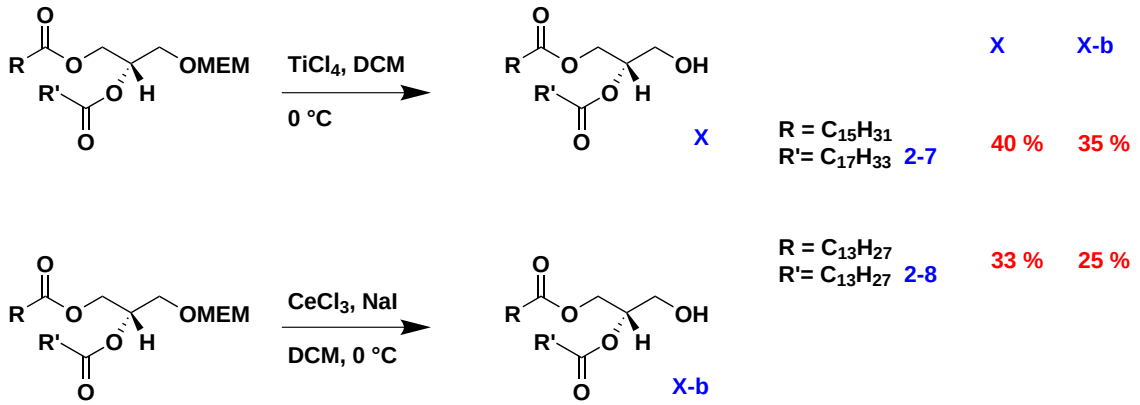

Figure 3.5 Strategies to form diacylglycerols **2-7** and **2-8**

A new, chemically more mild approach was attempted using cerium chloride heptahydrate [208], which required less harsh work up conditions (extraction of the organic phase with ethyl acetate), however the elevated reaction temperature also accelerated migration as monitored by TLC. Comparison of yields led to abandonment

of this new route. Silicic acid impregnated with boric acid has previously been reported to prevent acyl migration during flash column chromatography as silica gel is slightly acidic [209]. However, it was found to be difficult to handle, making inconsistent and poorly packed columns, and eventually a conventional silica gel column was used to obtain the 1,2 diacylglycerols **2-7** and **2-8** in reduced yield.

Synthesis of ^{2}H-labelled headgroups

To form the correct diastereomer of the final lipid, a protected PG headgroup (solketal) had to be synthesised so that only one hydroxyl group was free to react. Installation of deuterium at one position was successful (Figure 3.6). Phosphatdiylethanolamine headgroup was also synthesised by raney nickel-mediated hydrogen-deuterium exchange [210].



Figure 3.6 Treatment of an ester with a deuterated reducing agent forms the deuterated headgroup **2-9**, while raney nickel-mediated hydrogen-deuterium exchange furnishes deuterated PE headgroup **2-10**

Syntheis of headgroup-labelled phospholipids

Reaction with the diacyl glycerols **2-7** and **2-8** with the deuterated headgroups **2-9** and **2-10** yielded POPG-d_2,DMPG-d_2, POPE-d_4, DMPE-d_4 (Figure 3.7). The reduced yield of the PG-d_2 lipids was presumed to be due to the additional purification step in forming the final compound.

The synthesised lipids were then used to investigate AMP interactions with lipid headgroups in model membranes.

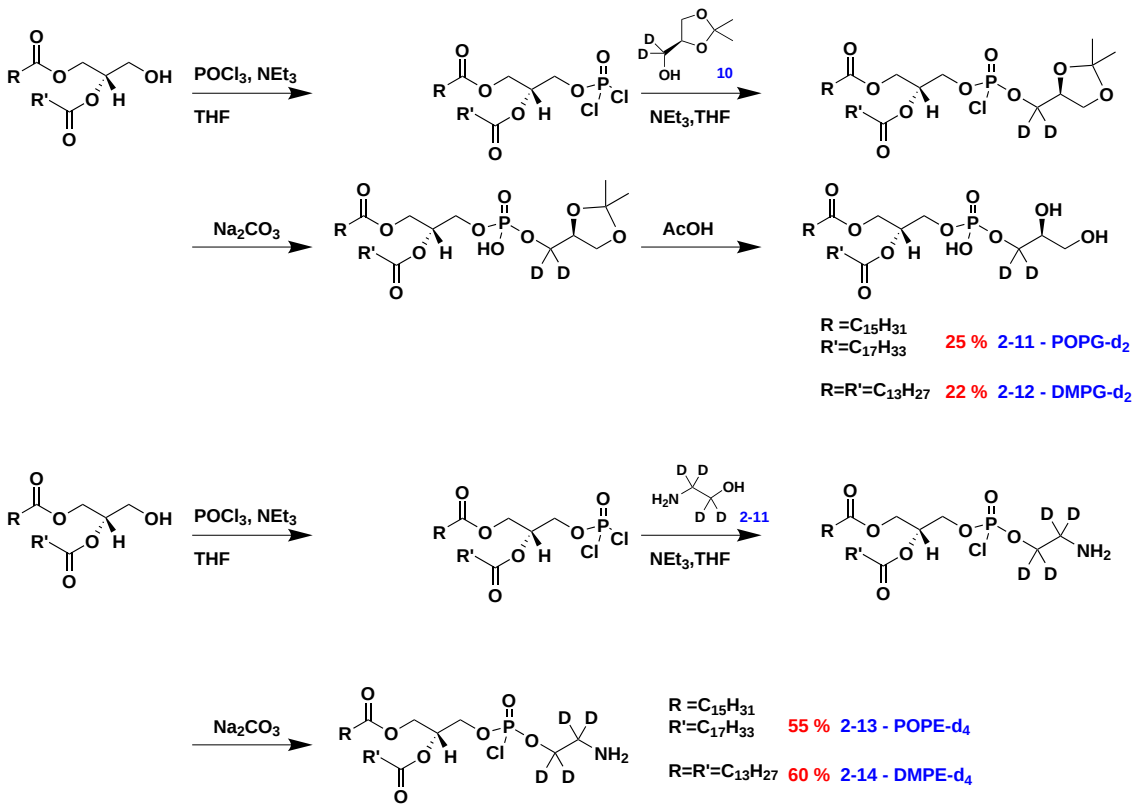

Figure 3.7 Formation of POPG-d_2, DMPG-d_2, POPE-d_4 and DMPE-d_4

3.3.2 Depaking of ^{2}H ssNMR spectra

Unoriented vesicles were used to study peptide interactions with model membranes, as their preparation is much faster than for oriented samples($\backsim$ 30 min for unoriented vesicles compared to $\backsim$ 48 h for oriented samples in a best case scenario, which has $\backsim$ 50% hydration). However, ssNMR experiments carried out on these systems produced spherically averaged Pake powder spectra [211]. They contained contributions from all angles of the bilayer relative to the applied magnetic field, making interpretation of spectra with multiple CD_2 resonances difficult. Figure 3.8 shows the pake powder ^{2}H spectra of unoriented dispersions of headgroup- and acyl-deuterated POPG in a POPC:POPG (3:1) MLV, and the resultant depaked spectra. The headgroup-deuterated POPG-d_2 powder spectrum resulted in a single quadrupolar splitting corresponding to the CD_2 bond on the glycerol headgroup. The central isotropic peak was due to natural abundance ^{2}H in the sample buffer, and small isotropic vesicles formed during MLV formation. The partially allowed $\Delta m = \pm 2$ also gave a contribu-

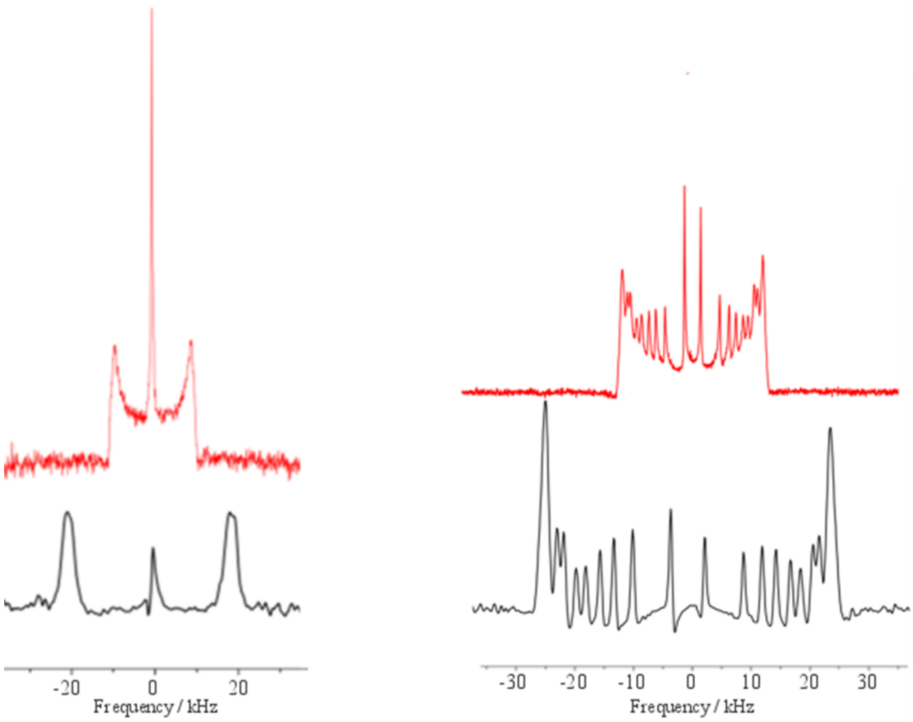

Figure 3.8 ^{2}H ssNMR spectra of unoriented MLV dispersions (*red*) of POPC:POPG-d_2 (3:1) (*left*) and POPC:POPG-d_{31} (*right*). After applying the NMRPipe depaking macro, depaked spectra were produced (*black*)

tion to the central isotropic line [212]. The acyl chain powder spectrum contained multiple splittings, corresponding to a CD_2 segment along the acyl chain, where reductions in the splitting corresponded to reduced motional order on the 10^5 timescale. The splittings of both spectra contained contributions from every angle of the membrane relative to the magnetic field.

The powder spectra were numerically transformed *via* an NMRPipe macro to yield a depaked spectrum [205, 213]. Every simulated splitting corresponded to a CD, CD_2 or CD_3 group, in a membrane oriented with the normal parallel to the magnetic field. By removing the angular contributions to the order parameter S_{CD}, it was possible to calculate it directly from measured quadrupolar splittings.*

For headgroup-deuterated lipids with few quadrupolar splittings, peaks could be unambiguously assigned. With acyl-deuterated spectra, in common with established

*The decrease in signal-to-noise in the depaked window is a consequence of the windowing function part of the depaking macro

practice [214], the smallest resolvable splittings were assigned to the six CD_2 positions closest to the acyl tail. The larger and broader peaks, known as the plateau region, were assigned to the remaining CD_2 segments, assuming a monotonic increase in molecular ordering closer to the headgroup, to give smoothed order parameter profiles [215], as discussed below.

3.3.3 Changes induced in the headgroup region probed by ^{2}H ssNMR

To investigate the effect of AMPs on the headgroup regions of model membranes, POPC:POPG-d_2 (3:1) MLVs mimicking bacterial cell membranes and POPC:POPE-d_4 MLVs mimicking mammalian cell membranes were formed with the chemically synthesised lipids.

Tilamin

Figure 3.9 (overleaf) shows the ^{2}H NMR spectra of both lipid mixtures in the absence and presence of tilamin.

Large changes were observed for tilamin interacting with POPC:POPG-d_2 MLVs; the quadrupolar splitting of the C-D headgroup was reduced by 7.5 ± 2 kHz, suggesting a significant reduction in motional order or a change in conformation of the PG- headgroup (Table 3.1).

	Lipid Only			P:L 1:100		
	$\Delta\nu_Q(\alpha)$/kHz	$\Delta\nu_Q(\beta)$/kHz	$\Delta\nu_Q$: $\Delta\nu_{iso}$	$\Delta\nu_Q(\alpha)$/kHz	$\Delta\nu_Q(\beta)$/kHz	$\Delta\nu_Q$: $\Delta\nu_{iso}$
POPC:POPE-d_4 (3:1)	43.7 ± 2	17.1 ± 2	8 : 1	44.6 ± 2	16.6 ± 2	6 : 1
POPC:POPG-d_2 (3:1)	45.3 ± 2	-	5 : 1	37.7 ± 2	-	1 : 4

Table 3.1 Table summarising the changes in quadrupolar splittings of headgroup-deuterated MLVs in the absence and presence of tilamin (1:100), and changes in the ratio of the quadrupolar splitting to the central isotropic peak.

In addition, the intensity of the splitting was greatly reduced compared with the large isotropic peak, indicating either a large population of the the PG lipids in the MLV were completely disordered, or macroscopic changes induced the MLVs to form small,

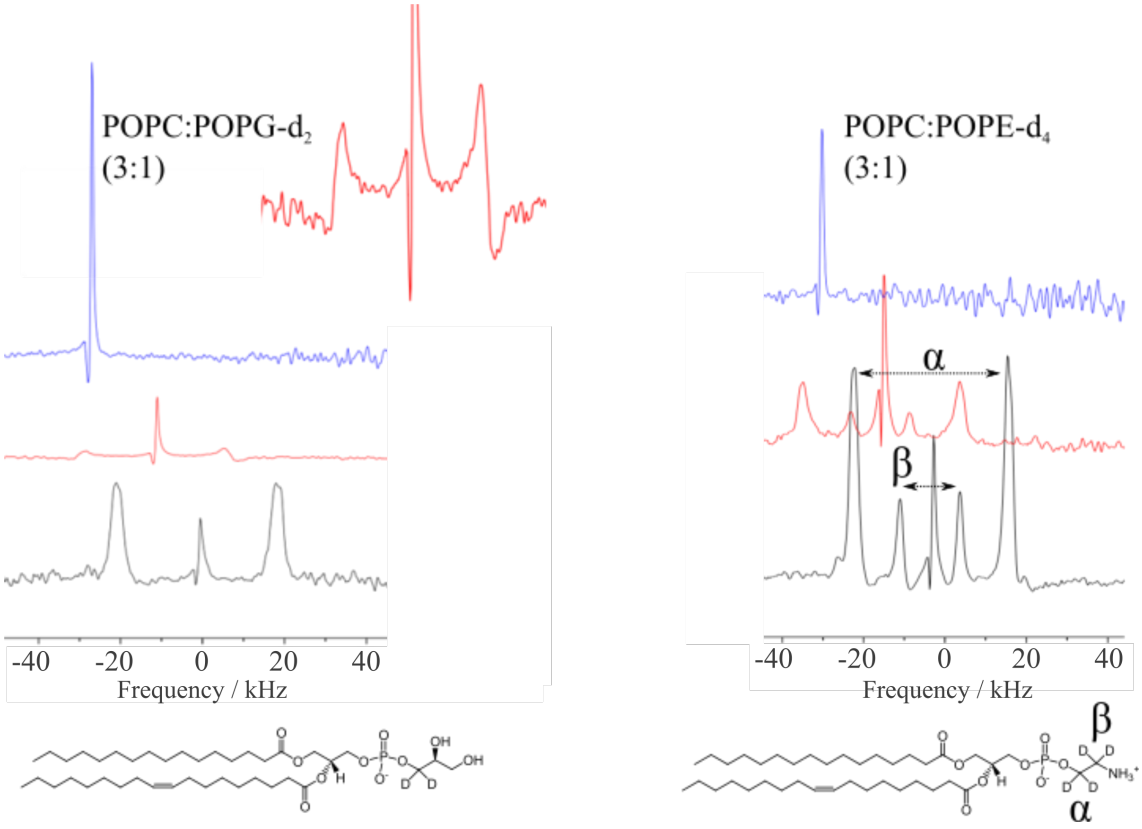

Figure 3.9 Depaked ^{2}H ssNMR spectra of POPC:POPG-d$_2$ (3:1) (*left*) and POPC:POPE-d$_4$ (3:1) (*right*) MLVs in the absence (*black*) and presence of tilamin at 1:100 (*red*) and 1:25 (*blue*). Spectra are offset for clarity, where the isotropic peak always occurs at 0 kHz. 100:1 and lipid-only spectra are normalised with respect to the isotropic line. An inset of the POPG-d$_2$ spectrum shows the quadrupolar splitting magnified for clarity. Experiments were an average of two measurements.

quickly tumbling isotropic vesicles. At 25:1, complete abrogation of the quadrupolar splitting was observed, indicating a complete solubilisation of the MLVs into isotropic vesicles. More modest changes were observed in zwitterionic POPC:POPE-d$_4$ membranes; at P:L 1:100 no changes to the alpha- and beta- splittings, corresponding to the more ordered CD_2 nearest the phosphate group and the adjacent CD_2 segment respectively, were found within error. An increase in the isotropic line area indicated that binding of tilamin induced complete disorder in a small region of the membrane or removal of some lipid to form quickly tumbling isotropic vesicles. The collapse of the quadrupolar splittings at P:L 1:25 indicated that tilamin caused macroscopic changes to the MLV to form small isotropic vesicles.

Qaela

The results of the interaction of qaela with the same membranes are displayed in Figure 3.10.

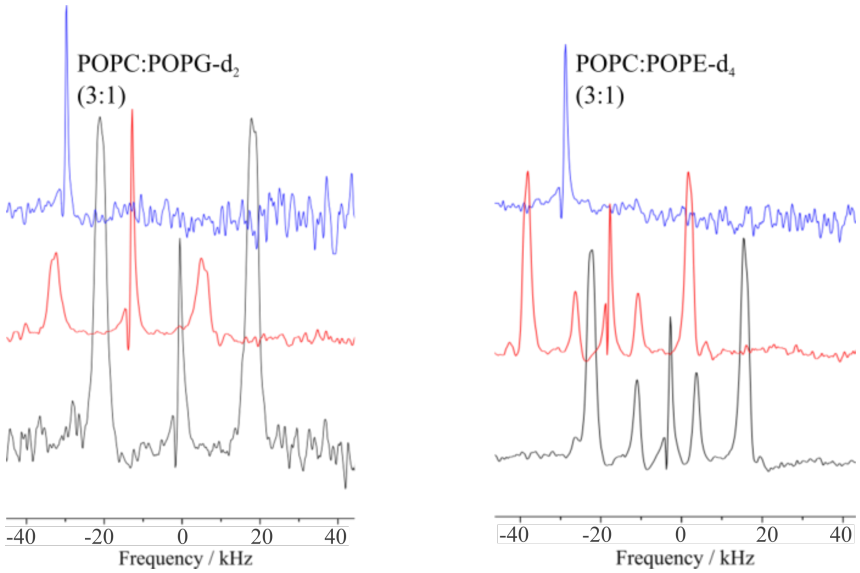

Figure 3.10 Depaked ^{2}H ssNMR spectra of POPC:POPG-d$_2$ (3:1) (*left*) and POPC:POPE-d$_4$ (3:1) (*right*) MLVs in the absence (*black*) and presence of qaela at 1:100 (*red*) and 1:25 (*blue*). Spectra are offset for clarity, where the isotropic peak always occurs at 0 kHz. Spectra are normalised with respect to the isotropic line. Experiments were the average of two measurements.

At P:L ratios of 1:100, no changes were seen in the POPC:POPE-d$_4$ spectrum, indicating little interaction with zwitterionic membranes. Surprisingly, changes were noted in the POPC:POPG-d$_2$ spectrum; a small reduction of the quadrupolar splitting was seen (Table 3.2), with a slight increase in the isotropic peak.

	Lipid Only			P:L 1:100		
	$\Delta\nu_Q(\alpha)$/kHz	$\Delta\nu_Q(\beta)$/kHz	$\Delta\nu_Q$: $\Delta\nu_{iso}$	$\Delta\nu_Q(\alpha)$/kHz	$\Delta\nu_Q(\beta)$kHz	$\Delta\nu_Q$: $\Delta\nu_{iso}$
POPC:POPE-d$_4$ (3:1)	43.7 ± 2	17.1 ± 2	6 : 1	46.3 ± 2	18.1 ± 2	6 : 1
POPC:POPG-d$_2$ (3:1)	45.3 ± 2	-	6 : 1	42.6 ± 2	-	4.5 : 1

Table 3.2 Table summarising the changes in quadrupolar splittings of headgroup-deuterated MLVs in the absence and presence of qaela (1:100), and changes in the ratio of the quadrupolar splitting to the central isotropic peak.

These data could indicate that qaela is binding to the neutral PC component, and causing segregation of PG- lipids due to electrostatic repulsion between the lipids

and the anionic peptide, resulting in lipid demixing. At 25:1, complete collapse of quadrupolar splittings was observed for both vesicles.

Chom

The results of the interaction of chom with the same membranes are displayed in Figure 3.11. At P:L 1:100, chom caused collapse of the quadrupolar splitting for POPC:POPg-d_2 MLVs, implying complete disruption in the lipid headgroup. For POPC:POPE-d_4 MLVs, no change was observed at P:L 1:100, after which the quadrupolar splitting collapsed at P:L 1:25.

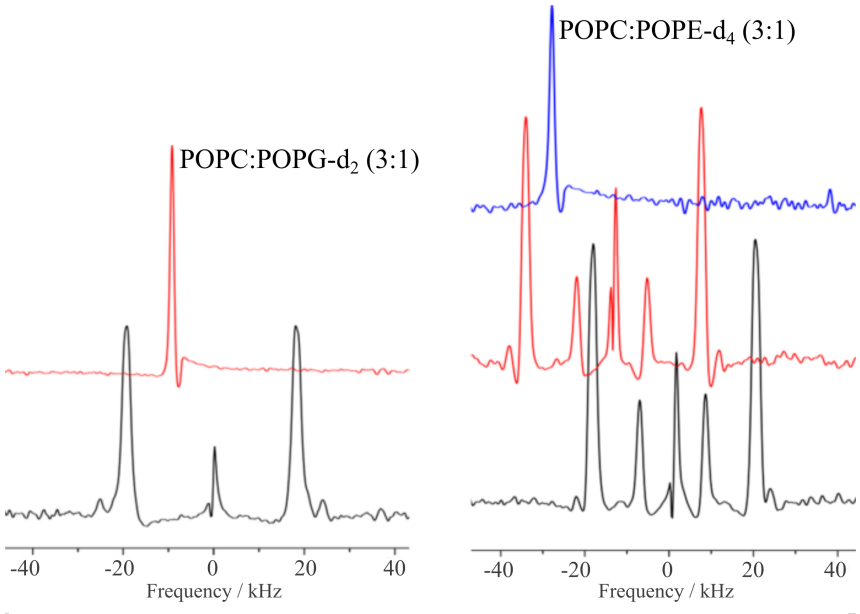

Figure 3.11 Depaked ^{2}H ssNMR spectra of POPC:POPG-d_2 (3:1) (*left*) and POPC:POPE-d_4(3:1) (*right*) MLVs in the absence (*black*) and presence of chom at 1:100 (*red*) and 1:25 (*blue*). 1:25 spectrum for POPC:POPG-d_2 (3:1) was not recorded as the quadrupolar splitting had already collapsed. Spectra are offset for clarity, where the isotropic peak always occurs at 0 kHz. Spectra are normalised with respect to the isotropic line. Experiments were the average of two measurements.

The results suggested that all peptides displayed selectivity for membranes of different lipid composition, and that chom appeared to disrupt headgroup order at lower concentrations than tilamin. Next, the acyl core of the bilayer was examined with tail deuterated lipids.

3.3.4 Changes induced in the acyl region as probed by ^{2}H ssNMR

To investigate the changes induced in the acyl region of model membranes by the AMPs, the ^{2}H spectra MLVs composed of POPCd_{31}, POPC$_{31}$:POPG (3:1) and POPC:POPG$_{31}$ (3:1) in the absence and presence of tilamin, qaela and chom were next obtained.

Tilamin

Figure 3.12 shows the depaked ^{2}H ssNMR spectra for POPC-d_{31}, POPC-d_{31}:POPG (3:1) and POPC:POPG-d_{31} (3:1) MLVs in the absence and presence of tilamin at P:L ratios of 100:1 and 25:1.

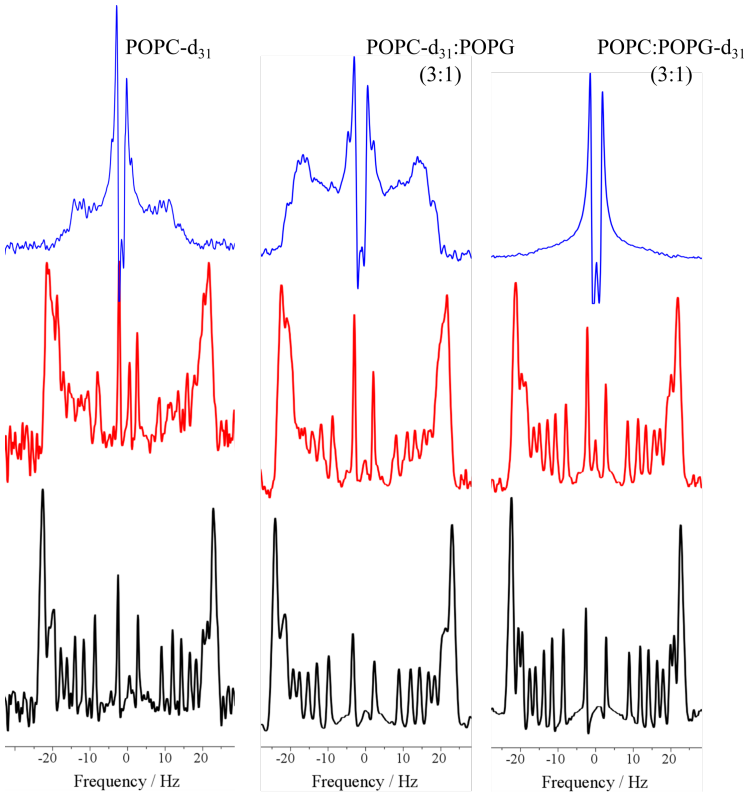

Figure 3.12 Depaked ^{2}H ssNMR spectra of POPC-d_{31} (3:1) (*left*), POPC-d_{31}:POPG (3:1) (*centre*) and POPC:POPG-d_{31} (3:1) (*right*) MLVs in the absence (*black*) and presence of tilamin at 1:100 (*red*) and 1:25 (*blue*).

In the absence of peptide, the ^{2}H spectra were typical of MLV dispersions. The central intense splitting of ≈ 10 kHz was assigned to the terminal methyl groups of the acyl chains that displayed the greatest conformational freedom in the acyl chain. Larger splittings were sequentially assigned to CD_2 segments going towards the headgroup

of the lipid[†]. For the POPC MLVs, not much change was observed in the spectral shape upon the addition of tilamin (P:L 1:100). The resolution of the the peaks was unchanged, indicating little change to the conformational order of the acyl chain. At higher P:L ratios (1:25), significant changes occurred; a large isotropic peak was observed, suggesting that tilamin was causing destruction of the large MLVs into small tumbling isotropic vesicles. However, a narrow, less well-resolved quadrupolar splitting profile was still apparent, implying a population of slowly-tumbling vesicles remained.

When tilamin was added to POPC:POPG (3:1) membranes, different effects were observed in the anionic PG and zwitterionic PC component. At a ratio of P:L 1:100, the quadrupolar splittings of the plateau region, corresponding to CD_2 segments near the headgroup region, became less well-resolved, indicating increased chain flexibility induced by tilamin. At 25:1, the POPG component quadrupolar splittings completely collapsed. The quadrupolar splittings of the POPC component, while becoming even less well-resolved, still persisted. This finding suggested that tilamin was causing lateral phase separation, and causing removal of PG lipids from the MLVs to form small isotropic vesicles, while leaving zwitterionic PC lipids in large MLVs. Indeed, the POPC component of POPC:POPG MLVs was less disrupted than single component POPC membranes, suggesting a strong electrostatic interaction between tilamin and anionic lipids.

Figure 3.13 (overleaf) shows the order parameter profiles obtained for POPC-d_{31}:POPG and POPC:POPG-d_{31} MLVs in the presence of tilamin (P:L 1:100). No significant changes were observed for POPC-d_{31}, indicating little effect by tilamin on lipid mobility in zwitterionic membranes. Hence, at this concentration it is likely the presence of anionic lipid is required for tilamin to adopt the membrane orientation that causes membrane disruption. For POPC:POPG (3:1) membranes, tilamin caused a disorder-

[†]The artefact in the centre of the spectrum between the terminal CD_3 splitting was a result of a slight asymmetry in the pake spectra caused by an instrument issue. The asymmetry caused the depaking script to be inaccurate, but only at this frequency.

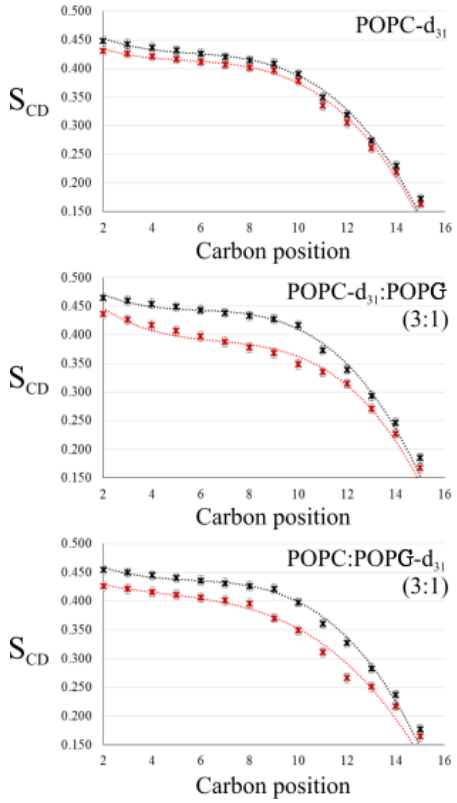

Figure 3.13 Order parameter profile for POPC-d_{31} (*top*), POPC-d_{31}:POPG (3:1) (*middle*) and POPC:POPG-d_{31} (3:1) (*bottom*) in the absence (black crosses) and presence of tilamin (red crosses) at P:L 1:100. Error bars derived from half-width line height of peaks, where was ±2 kHz, corresponding to an error in order parameters of ±0.008.

ing of lipid motion in both the anionic POPG and neutral POPC component. These data suggest that tilamin interacts with and destabilises anionic membranes by binding to the anionic lipids, causing disruption of acyl chain dynamics, but without causing any lateral phase separation. The disordering effect became more pronounced at positions closer to the acyl core; this is consistent with the peptide binding primarily to the headgroup region, causing increased motional freedom further into the core, an effect seen in other carpet-like peptides [117].

Qaela

Figure 3.14 shows the depaked ^{2}H ssNMR spectra for POPC-d_{31}, POPC-d_{31}:POPG (3:1) and POPC:POPG-d_{31} (3:1) MLVs in the absence and presence of qaela at P:L ratios of 100:1 and 25:1.

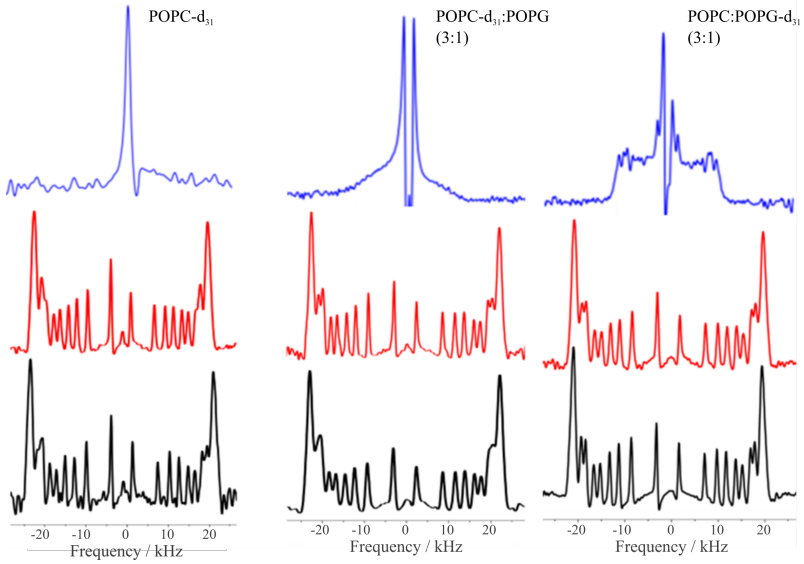

Figure 3.14 Depaked ^{2}H ssNMR spectra of POPC-d_{31} (3:1) (*left*), POPC-d_{31}:POPG (3:1) (*centre*) and POPC:POPG-d_{31} (3:1) (*right*) MLVs in the absence (*black*) and presence of qaela at 1:100 (*red*) and 1:25 (*blue*).

No change was observed at P:L 1:100 with qaela interacting with POPC-d_{31} MLVs. When qaela was added to POPC:POPG (3:1) membranes, different effects were again observed in the anionic PG and zwitterionic PC component. At a ratio of P:L 1:100, the quadrupolar splittings remained well resolved, and qualitatively little change was observed in the spectra, suggesting qaela was not disrupting the membranes. At a ratio of P:L 1:25, an isotropic peak with little underlying order was observed in the neutral PC component, while the PG component retained a reduced splitting pattern. These data suggested that at this concentration, electrostatic repulsion between the anionic peptide and model membrane was not sufficient to prevent disruption of the MLVs and formation of small isotropic vesicles, and that lateral phase separation was occurring. No changes were observed in the order parameter profiles, suggesting little interaction of qaela with the model membranes at this concentration.

Figure 3.15 shows the order parameter profiles obtained for POPC-d_{31}:POPG and POPC:POPG-d_{31} MLVs in the presence of qaela (P:L 1:100).

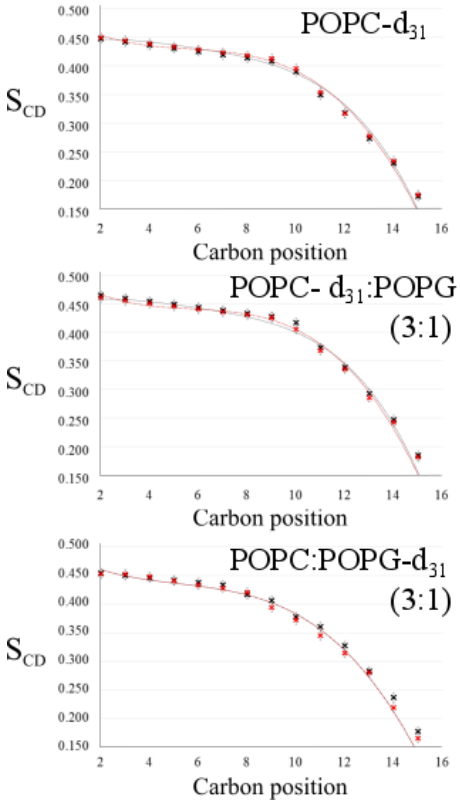

Figure 3.15 Order parameter profile for POPC-d_{31} (*top*), POPC-d_{31}:POPG (3:1) (*middle*) and POPC:POPG-d_{31} (3:1) (*bottom*) in the absence (black crosses) and presence of qaela (red crosses) at P:L 1:100. Error bars derived from half-width line height of peaks, where was ±2 kHz, corresponding to an error in order parameters of ±0.008.

Chom

The effect of chom on acyl-deuterated lipids was next investigated (Figure 3.16). At P:L 1:100, chom caused a slight narrowing of the ^{2}H spectra of POPC-d_{31} and POPC-d_{31}:POPG, however the peaks remained well resolved. A larger effect was observed in the POPC:POPG-d_{31} MLVs; the outermost splittings, corresponding to the plateau region, narrowed significantly, and many of the splittings became less resolved. For all three membranes, there was an increase in the size of the isotropic peak, suggesting the coexistence of small isotropic vesicles. These data suggested that at P:L 1:100,

chom caused lateral phase separation and demixing of the two component membrane of the anionic model membrane, with preferential binding to anionic lipids. At 25 : 1 the quadrupolar splittings for all MLVs collapsed due to chom causing disintegration of the membrane into isotropic vesicles.

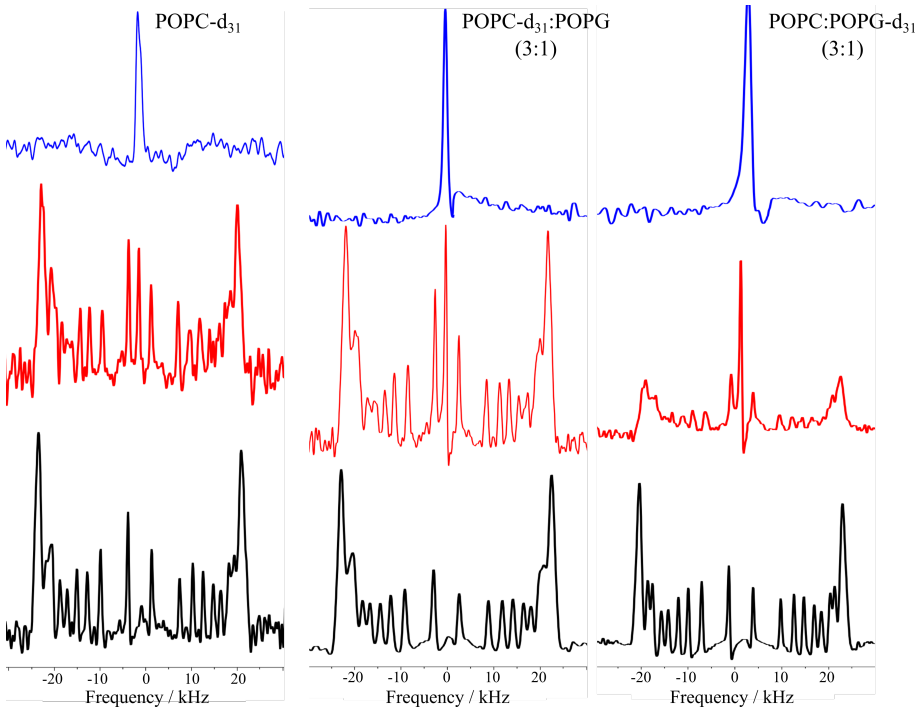

Figure 3.16 Depaked ^{2}H ssNMR spectra of POPC-d_{31} (3:1) (*left*), POPC-d_{31}:POPG (3:1) (*centre*) and POPC:POPG-d_{31} (3:1) (*right*) MLVs in the absence (*black*) and presence of chom at 1:100 (*red*) and 1:25 (*blue*).

Figure 3.17 shows the order parameter profiles obtained for POPC-d_{31}:POPG and POPC:POPG-d_{31} MLVs in the presence of chom (P:L 1:100).

Reductions in S_{CD} of a similar magnitude were found for chom interacting with POPC-d_{31} and POPC-d_{31}:POPG MLVs, indicating perturbation of lipid order. The anionic component of POPC:POPG (3:1) MLVs displayed the greatest change in S_{CD}, confirming that chom was causing lateral phase separation of anionic membranes, with clustering of lipids around the peptide. The changes across the order parameter profile were more uniform than those seen with tilamin; this could be a consequence of residing solely in the headgroup region, causing disruption of the entire bilayer.

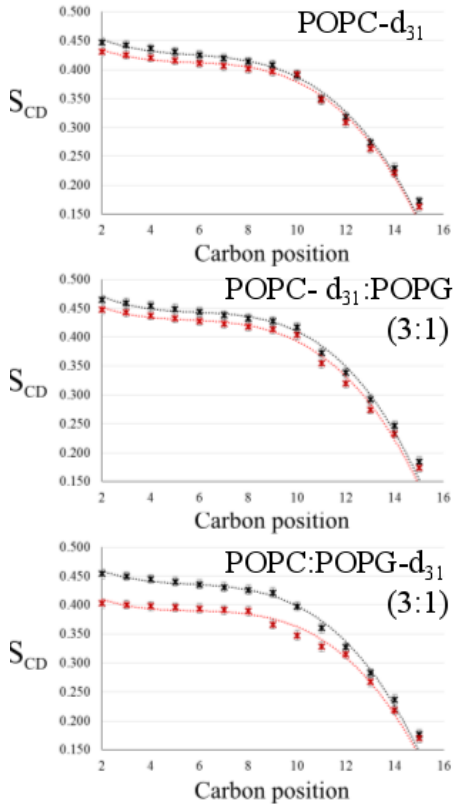

Figure 3.17 Order parameter profile for POPC-d_{31} (*top*), POPC-d_{31}:POPG (3:1) (*middle*) and POPC:POPG-d_{31} (3:1) (*bottom*) in the absence (black crosses) and presence of chom (red crosses) at P:L 1:100. Error bars derived from half-width line height of peaks, where was ±2 kHz, corresponding to an error in order parameters of ±0.008.

Changes in bilayer thickness induced by the AMPs

The average change in order parameter ($\Delta\langle|S|\rangle$) was also used to estimate the membrane thinning (Δd) of both model membranes by the peptides, according to the equation

$$\Delta d = 2L_o\Delta\langle|S|\rangle, \tag{3.2}$$

where L_o is the all trans length of the lipid acyl chain (for PO- type lipids 26.5 Å). Tilamin, chom and qaela were calculated to induce no change in hydrophobic thickness of POPC model membranes, and changes of −0.2 Å±1.3, −1.8 Å±1.3 and 1.2 Å±1.3, respectively, in POPC:POPG (3:1) model membranes. Hence, no significant membrane thinning was observed. Membrane thinning can be a consequence of AMPs inserting

transmembrane, by hydrophobic mismatch between a folded helix length and the hydrophobic thickness of the membrane causing thinning or thickening of the membrane to accommodate the peptide [117]. Therefore, the results give evidence that a transmembrane orientation is not adopted by tilamin or qaela.

^{2}*H NMR of two-component systems*

To assess if the presence of anionic vesicles prevented neutral vesicles from being disrupted by AMPs, ^{2}H ssNMR experiments were carried out on POPC-d_{31} MLVs in the presence of different amounts of unlabelled POPC:POPG (3:1) MLVs and tilamin (P:L 1:25), as shown in Figure 3.18.

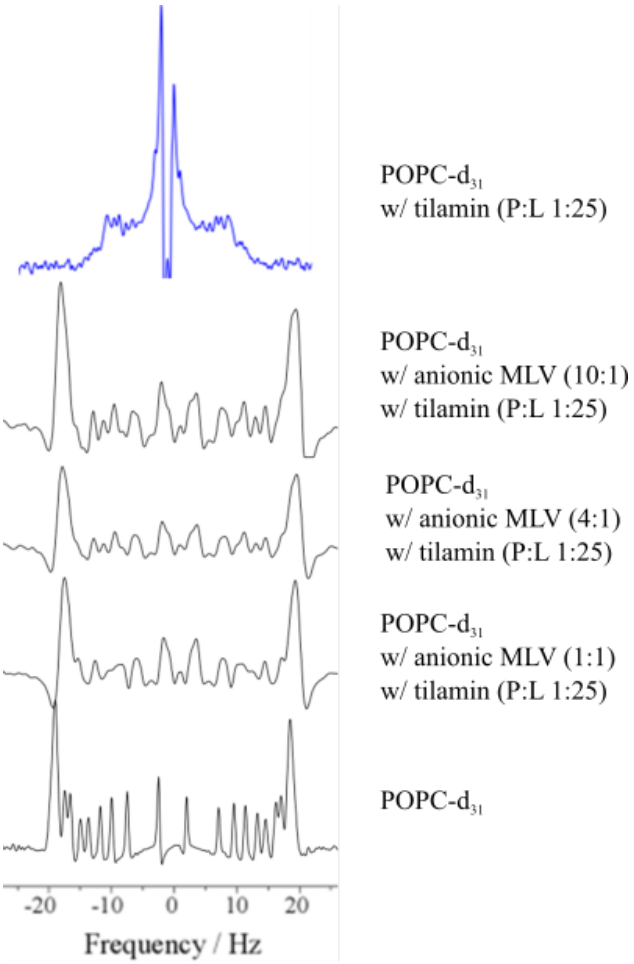

Figure 3.18 ^{2}H NMR spectra of POPC-d_{31} MLVs in the presence of tilamin P:L 1:25, in the presence of unlabelled POPC:POPG 3:1 MLVs. The MLV ratio is zwitterionic:anionic MLVs.

At all concentrations, the quadrupolar splittings for POPC-d_{31} were more poorly resolved, implying some interaction with tilamin causing a reduction in orientational order. However, the presence of anionic membranes did appear to prevent the neutral membranes from undergoing a macroscopic morphological change to small isotropic vesicles, even at a zwitterionic:anionic membrane ratio of 10:1. This gives evidence that the selectivity of AMPs *in vivo* is not solely based on the lipid composition of different cells, but the environment in which the cell resides is also important for non-toxicity.

3.3.5 Dynamic light scattering

To determine if the peptides at P:L ratios of 1:25 were causing morphological changes to the MLVs resulting in formation of small tumbling isotropic vesicles, DLS measurements were carried out to assess the polydispersity and size distribution of particles in the suspensions (Figure 3.19).

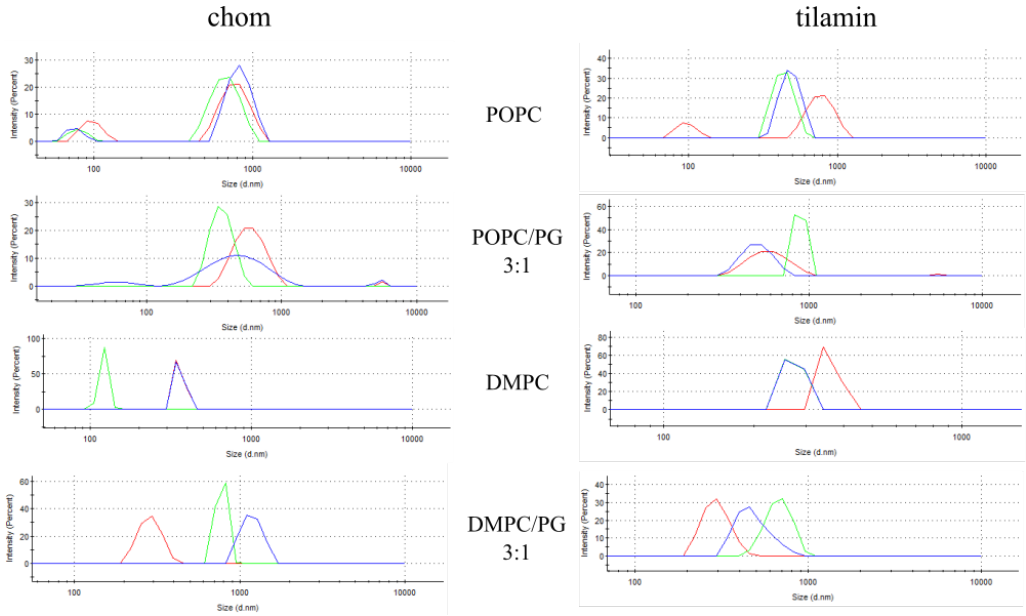

Figure 3.19 Size distribution, as determined by DLS, of MLV dispersions in the absence (*red*) and presence of tilamin (*right*) and chom (*left*) at P:L 1:100 (*blue*) and 1:25 (*green*).

The average diameter of particles in solution (Z-average or Z-ave), and a measure of how monodisperse this population was (polydispersity index, PdI) were calculated and presented in Table 3.3 (overleaf). Generally, the data suggested that significant morphological changes occurred upon interaction of the vesicles with the AMPs, and in all cases these changes became more severe on increasing peptide concentration. For zwitterionic MLVs comprised of -PC lipids, increasing chom/tilamin added caused a reduction in the size of the vesicles. This supports findings from ssNMR that addition of peptide causes formation of small isotropic vesicles. At P:L 1:100 for anionic MLVs, greater decreases in vesicle size were observed, and surprisingly a large increase was observed at P:L 1:25. This suggests that due to the anionic charge of the phosphatidylglycerol headgroup, electrostatic interactions between the cationic peptides cause greater disruption of the MLVs. The increase at higher peptide concentrations could indicate that the cationic AMPs could be clustering together smaller vesicles by electrostatic attractions. This effect is presumably not possible with zwitterionic vesicles so that the smaller structures remained the dominant contribution in the DLS scattering profile.

Both peptides induced morphological changes in a simlar way for DM- vesicles as PO- analogues, giving an indication that the hydrophobic thickness of the bilayer was not linked to the mode of action of the AMPs, a property that is shared by AMPs that insert transmembrane and form pores [216].

		Lipid	P:L 100:1	P:L 25:1
tilamin				
POPC	Z-ave /d.nm	729 ± 74.2	461 ± 89.7	418 ± 57.5
	PdI	0.427 ± 0.135	0.460 ± 0.273	0.589 ± 0.0738
POPC/POPG (3:1)	Z-ave /d.nm	624 ± 69.9	494 ± 40.6	831 ± 296
	PdI	0.509 ± 0.0565	0.326 ± 0.127	0.858 ± 0.0683
DMPC	Z-ave /d.nm	344.3 ± 125	271 ± 86.8	263 ± 65.1
	PdI	0.412 ± 0.200	0.527 ± 0.053	0.355 ± 0.125
DMPC/DMPG (3:1)	Z-ave /d.nm	296 ± 58.8	485 ± 73.1	678 ± 77.4
	PdI	0.387 ± 0.110	0.496 ± 0.094	0.301 ± 0.277
ChoM				
POPC	Z-ave /d.nm	729 ± 74.2	822 ± 63.4	701 ± 60.8
	PdI	0.427 ± 0.135	0.653 ± 0.117	0.705 ± 0.092
POPC/POPG (3:1)	Z-ave /d.nm	624 ± 69.9	414 ± 62.0	364 ± 92.5
	PdI	0.509 ± 0.0565	0.446 ± 0.0238	0.496 ± 0.0553
DMPC	Z-ave /d.nm	344.3 ± 125	345.23 ± 89.3	148 ± 38.1
	PdI	0.412 ± 0.200	0.527 ± 0.053	0.355 ± 0.125
DMPC/DMPG (3:1)	Z-ave /d.nm	296 ± 58.8	1100 ± 104	848 ± 375
	PdI	0.387 ± 0.110	0.414 ± 0.0412	0.757 ± 0.343

Table 3.3 Dynamic light scattering size measurements, showing changes in size of different model membranes in the presence and absence of tilamin and chom.

3.4 Discussion

^{2}H ssNMR experiments performed on headgroup- and acyl chain-deuterated lipids in model membranes revealed greater detail on the nature of the membrane perturbations induced by the AMPs. Measurement of quadrupolar splittings gave a measure of the perturbing influence of the AMPs (Figures **3.9-3.19**); electrostatic interactions between the cationic peptides and anionic lipids appear vital for membrane perturbation, and results were more pronounced for all AMPs interacting with anionic model membranes. Considering the primary structure and charges of the three peptides allows rationalisation of these findings (Figure 3.20).

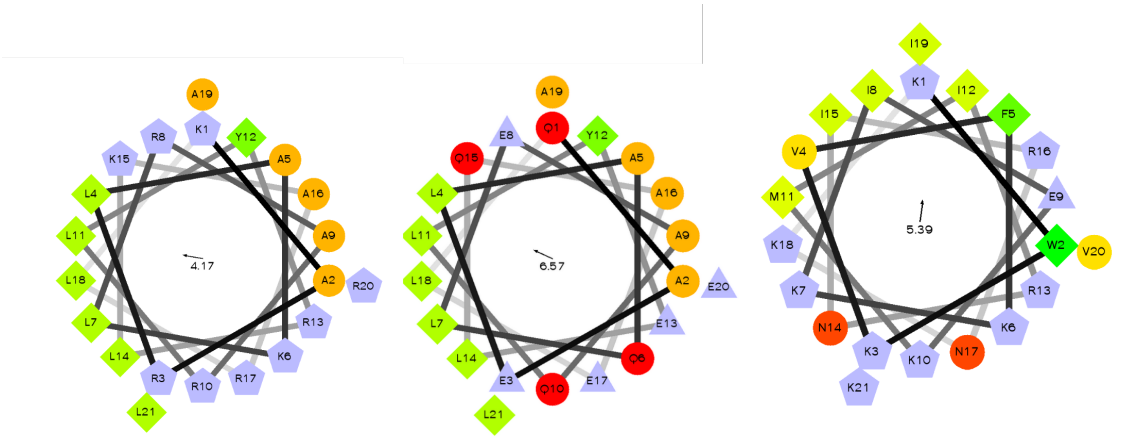

Figure 3.20 The primary sequences and predicted helical structure of tilamin, qaela and chom.

Qaela, despite being anionic, caused significant disruption of model membranes at sufficiently high concentrations. The electrostatic repulsion is presumably overcome at a threshold concentration, where interaction of the hydrophobic acyl core with the hydrophobic residues of the peptide cause destabilisation of the bilayer. Despite no helix formation being observed by CD, perhaps at a critical local concentration, water molecules could provide an interface that permitted folding of the helix. It is noteworthy that MIC experiments showed that qaela displayed no antimicrobial (or hemolytic) activity, which does not seem to be reflected in the ssNMR data. It could

be due to the fact that zwitterionic model membranes are obviously far too simplistic to recreate all of the properties of mammalian membranes. Indeed, all order parameter changes induced by all peptides are far smaller than simply adding cholesterol to membranes [203]. Another explanation is that AMPs are only secreted by mammalian cells in the presence of a bacterial infection; it could be that the presence of anionic membranes attract any AMPs, thereby leaving the less negatively charged mammalian cells unaffected [217]. Evidence for this was provided by the fact the quadrupolar splittings of POPC-d_{31} were preserved in the presence of tilamin (P:L 1:25) when anionic liposomes were also present (Figure 3.18). AMPs are typically excreted by host epithelial cells, which have membranes more inert than other mammalian cell membranes [218]. It can therefore be concluded that while useful for gleaning mechanistic information, simple PC membranes are insufficient to explain the differences in MIC values for tilamin and qaela.

For tilamin and chom, a strong selectivity for PG lipids appeared be the primary factor for membrane disruption, with chom also causing lateral phase separation (Figure 3.17). At 100:1, chom caused collapse of quadrupolar splittings in both the headgroup and acyl region of a POPC:POPG MLVs, where the anionic component was deuterated. This also occurred for tilamin at 25:1. Despite chom being +9 at pH 7.2 compared with tilamin (+10), electrostatic interactions appeared stronger for chom. This could be due to the fact that chom has a larger continuous cationic face of the helix, while tilamin has two smaller cationic faces. Therefore, the more highly charged single face could bind more strongly to anionic membranes, inducing a lytic effect at lower concentrations.

DLS measurements corroborated supposition of the formation of small isotropic vesicles, but due to the inherent polydispersity of MLV suspensions, the errors on all measurements were significant. In addition, light scattering is proportional to r^6 where r is the hydrodynamic radius of the particle. Therefore in DLS, larger MLVs will be weighted far more in the autocorrelation function fitted to the data, potentially mis-

leadingly causing underestimation of the population of isotropic vesicles. The ssNMR data however was further supported by collaborators who obtained fluorescence micrographs of tilamin and chom interacting with POPC:POPG (3:1) giant unilamellar vesicles (GUVs), as shown in Figure 3.21.

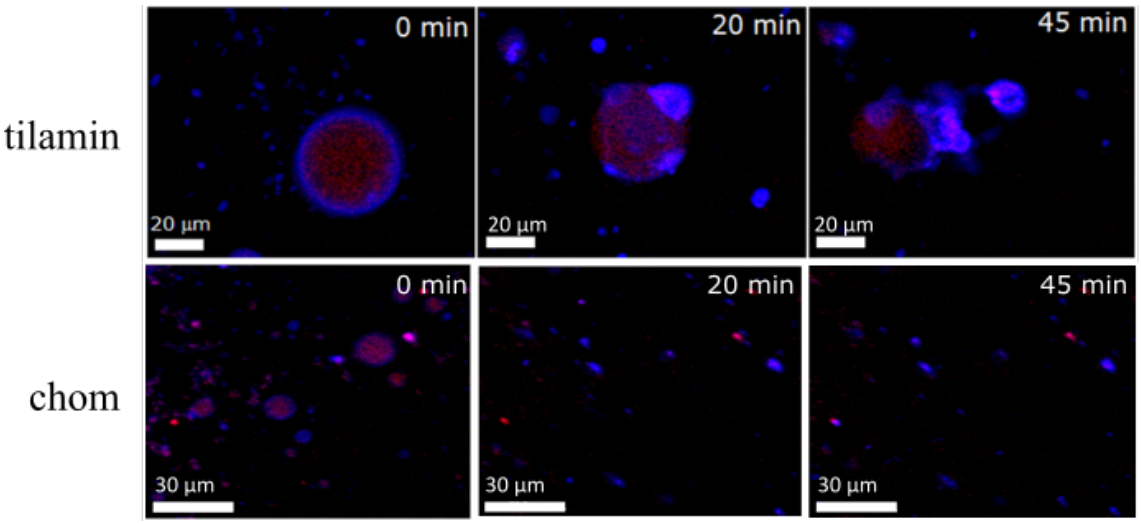

Figure 3.21 Fluorescence micrographs of POPC:POPG (3:1) GUVs treated with tilamin and chom at 10 µM. GUVs were labelled with sulforhodamine B (interior) and CellMask^{TM}(membrane). Experiments performed by B. Lamarre (National Physical Laboratory, Teddington, U.K).

The micrographs on GUVs ($\backsim$ 40 times larger than the MLV dispersions) show the disruption induced by tilamin and chom (P:L 1:100) over 45 min. Data for chom indicated fast disruption of the GUVs, leakage of cell contents and formation of small particles, while for tilamin leakage of cell contents occurred without formation of appreciable visible amounts of small particles, consistent with ssNMR data at the same peptide concentration.

In combination with the QCM results from the previous chapter, a speculative mode of action can be deduced for the three peptides studied. Chom appears to operate *via* the carpet mechanism, with all interactions being observed in the hydrophilic headgroup region of model membranes and supported bilayers. This is supported by uniform decreases in order in the acyl core; by residing in the headgroup region, the

peptide causes more space for the acyl chains to undergo movement, as well as causing positive curvature strain [117]. Above a threshold concentration, all lipid order is abrogated as the membrane is solubilised in a detergent-like manner. This mechanism is summarised in Figure 3.22.

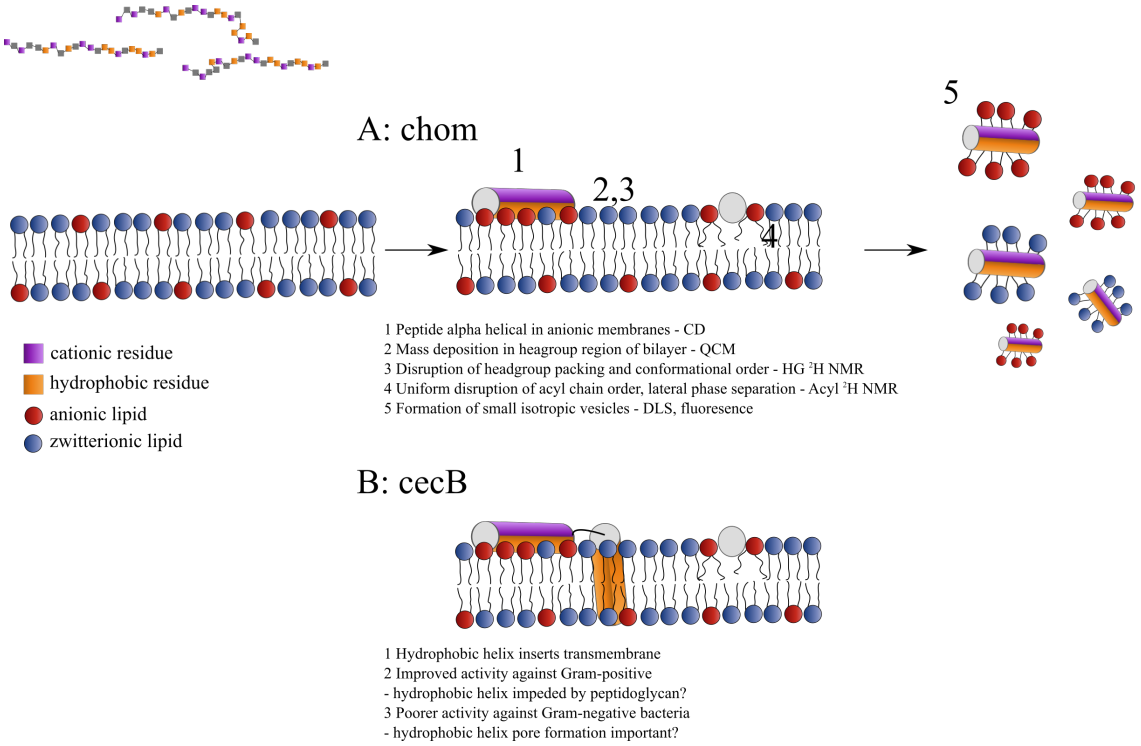

Figure 3.22 Cartoon of the proposed mechanism of action of chom (*A*) and cecB (*B*).

The data suggests that, as hypothesised previously [162], the C-terminal hydrophobic half of native cecB may be dispensible with regards to certain antimicrobial activity; indeed, removal of the hydrophobic helix appeared to improve MIC values against Gram-positive *S. aureus* from > 100 µM to 3.125 µM, while MICs slightly decreased from $\backsim$ 1 µM to 6.25 µM for *E. coli* and *P. auruginosa.* It could be that the hydrophobic helix of cecB makes the peptide too large to traverse the thick peptidoglycan layer of Gram-positive bacteria, while activity against Gram-negative bacteria improves by causing pore formation.

Qaela also appears to cause membrane disruption *via* a carpet mechanism at sufficient concentration, though without any secondary structure induced by the presence of the model membrane, and is summarised in Figure 3.23.

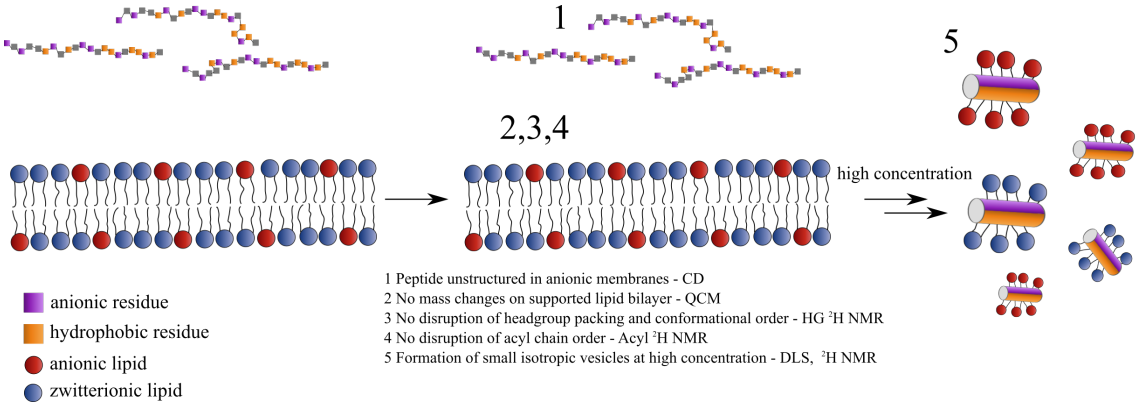

Figure 3.23 Cartoon of the proposed mechanism of action of qaela

A more complicated picture emerges for tilamin; QCM Δf-Δd plots showed that after binding to the surface of an SLB, complicated peptide-lipid interactions at all depths of the bilayer were observed (Figure 2.14). In addition, ssNMR showed interactions with the headgroup of anionic model membranes (Figure 3.9), as well as the hydrophobic core near the interface region (Figure 3.13). Greater perturbations were observed deeper in the acyl core than near the interface region; this suggests that tilamin is inserting more than chom. DLS measurements showed that at P:L 1:25 there was not an overall decrease in the average size distribution of vesicles (Figure 3.3), and fluorescence micrographs also did not show appreciable amounts of small vesicles being formed. These data are consistent with a toroidal pore mechanism, whereby the peptide forms a lipid lined pore. The formation of an isotropic peak could be due to the lipids sampling many angles and in being involved in disordered pores compared with an ordered bilayer. This model is shown in Figure 3.24 (overleaf).

Also shown in Figure 3.24 is a second, novel mode of action that is consistent with the results: monolayer poration [197]. Monolayer poration is a mechanism which is hypothesised to proceed by binding of tilamin to the outer leaflet headgroup, with

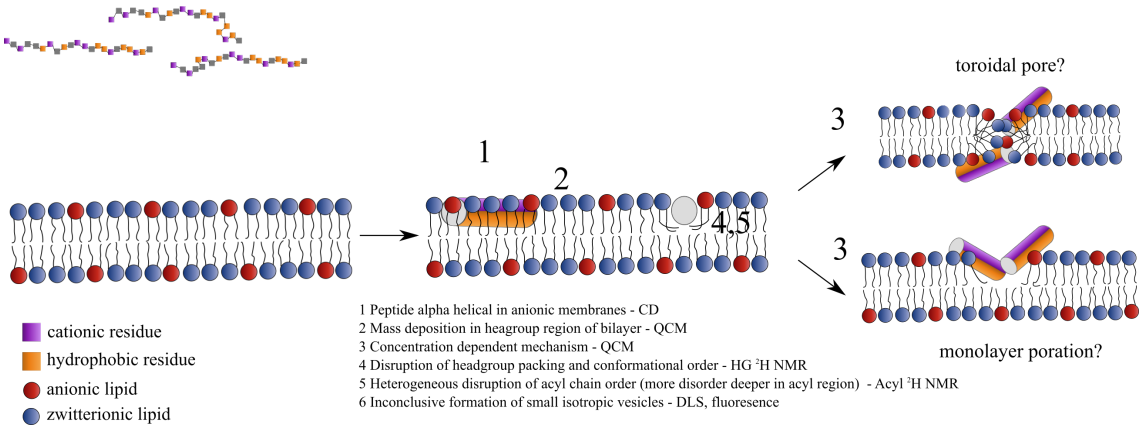

Figure 3.24 Cartoon of the proposed potential mechanisms of action of tilamin.

the peptide orienting at an angle to adapt to membrane curvature. By only forming a monolayer pore or "crater", the inner leaflet acyl chains would be exposed to water, and the resultant destabilisation would cause disintegration of the membrane. This mode of action would not depend on hydrophobic thickness, as observed with DLS data. In addition, the second cationic face of tilamin could allow stabilisation of the tilted conformation by hydrogen-bonding with water, which would simultaneously destabilise the membrane by introducing more water in the peptide-lipid complex. This is a controversial and speculative proposal, but is also consistent with the ssNMR data.

Another interpretation is that the presence of an isotropic peak and a quadrupolar splitting in ^{2}H ssNMR spectra is not due to vesicles of different sizes being present, but two *leaflet specific* peptide-lipid interactions occurring at the bilayer. The outer leaflet may be far more disordered, resulting in an isotropic peak, while if the inner leaflet remains intact, it would be manifested in a quadrupolar splitting remaining. If this were the case, it could also explain the modest changes in order parameter profiles observed for tilamin, if the changes were the ensemble average of two coexisting leaflet states. The mechanism is also consistent with other related, biologically significant phenomena; for example certain neurotoxic prion proteins have been shown to only penetrate half of a mammalian membrane [219].

It is is not possible to separate the two mechanistic scenarios for tilamin with symmetric vesicles and hence it is clear that the conventional model membranes are insufficiently complex to validate the mechanisms proposed. Therefore the next chapter will explore methods of producing more native-like asymmetric model membranes in an attempt to better understand the mode of action of the AMPs, and to further validate the novel monolayer poration mode of action.

Chapter 4

Investigations into Asymmetric Model Membranes

4.1 Introduction

Work in this chapter explores the property of asymmetry that exists both in native lipid membranes, and that may be manifested in peptide-lipid interactions. Methodologies to replicate this in model systems are explored here, and the results are discussed in the context of the findings of the current literature.

The cyclodextrin-mediated approach to produce asymmetric membranes is first explored, and the use of EPR to study peptide-lipid interactions, and the structure of LPS, a vital constituent of the outer cell membrane of gram-negative bacteria, is also discussed.

4.1.1 Cyclodextrin mediates lipid exchanges between vesicles

The cyclodextrins (CDs*), first isolated in 1981 as cellulosine from starch [220], are a large family of cyclic, torus-shaped oligosaccharides, which vary in ring size and side chain identity. They consist of a rigid hydrophobic interior cavity of differing size, flanked by a hydrophilic outer core of hydroxyl groups. Synthetic substitution (typically unspecifically) of certain hydroxyl groups to the corresponding methyl ether, to tune the hydrophilicity of the outer ring and increase overall solubility [221], is also common. The structure of of various CDs are given in Figure 4.1 (overleaf).

By virtue of the amphiphilic properties of this supramolecular species, cyclodextrins have a litany of diverse biochemical applications, including improved the bioavailability of hydrophobic drugs [223], improved separation of isomeric mixtures using

*Due to ambiguity in abbreviations, circular dichroism will not be abbreviated in this chapter

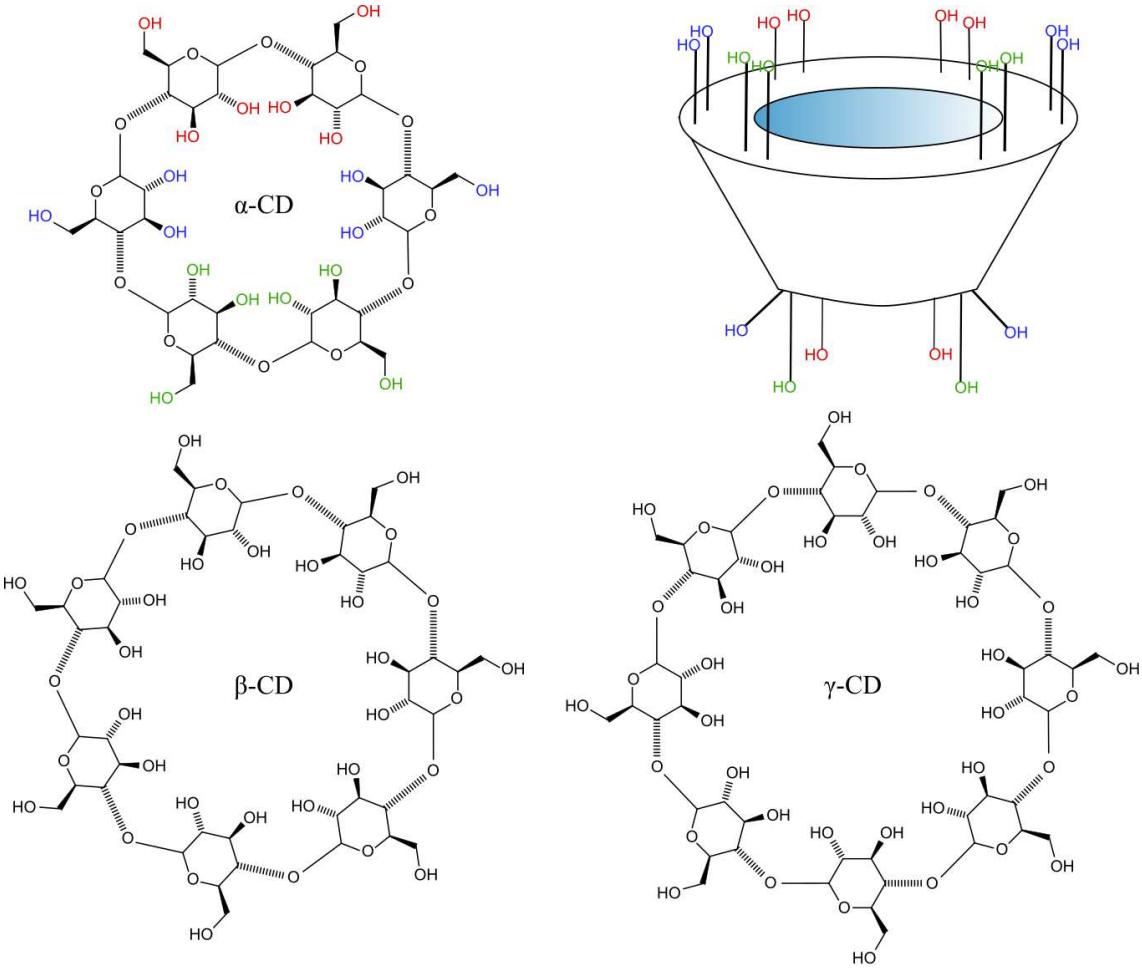

Figure 4.1 Molecular structures of α-, β- and γ-cyclodextrin (adapted from Wikipedia (S. Skowron)).

Cyclodextrin species	Molecular weight (g mol^{-1})	Cavity diameter (Å)	Cone height (Å)
α	972	$4.7-5.3$	7.9 ± 1
β	1135	$6-6.5$	7.9 ± 1
γ	1297	$7.5-8.3$	7.9 ± 1

Table 4.1 The various properties of different cyclodextrins [222].

high performance liquid chromatography [224], as food additives, for removal of odours in commercial air fresheners [225], and selective removal/delivery of cholesterol from/to liposomes and cellular membranes [226, 227].

It is this final property of cyclodextrins, their ability to extract cholesterol and lipids from liposomes (in a similar manner to lipid transfer protein [228]) that was the in-

spiration for the attempt to selectively control leaflet distribution of liposomal lipids, as described below.

Cyclodextrin-enabled asymmetric liposomes

Exploiting the fact that at very high concentrations cyclodextrin can extract phospholipids as well as cholesterol [229], workers from the London group (Stony Brook, USA) devised a protocol to control the lipid distribution between leaflets of a small unilamellar vesicle. The protocol is summarised in Figure 4.2.

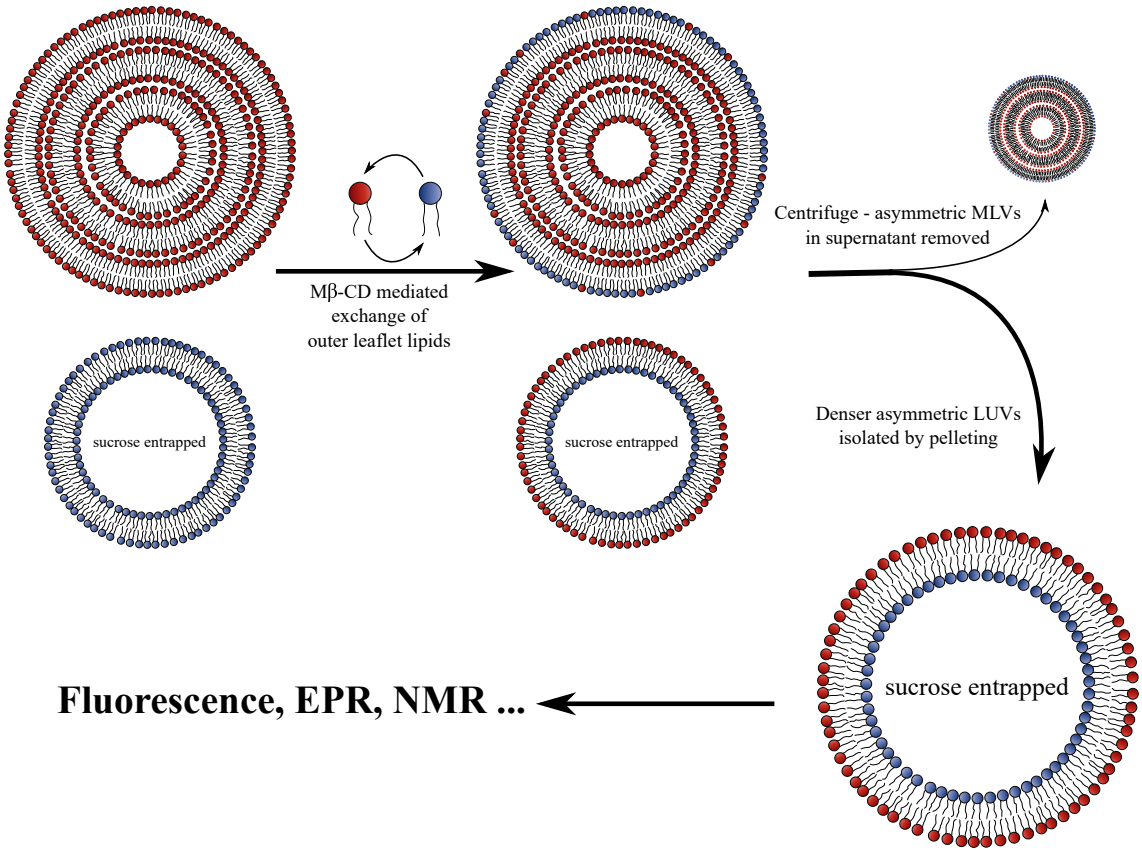

Figure 4.2 Schematic showing the methodology to produce asymmetric vesicles. A more detailed description lies in the text and materials and methods.

Multilamellar vesicles are incubated with Mβ-CD and mixed with large unilamellar vesicles containing sucrose. After an hour of mixing, the outer leaflet lipids of the two vesicles are exchanged. Centrifugation steps pellet the heavier, sucrose-entrapped LUVs, and the supernatant containing excess Mβ-CD and the unpelleted MLVs is discarded.

Investigations into this process has yielded a flexible and robust method for making asymmetric liposomes of different sizes [230, 231], headgroup identity [232], and acyl chain length [233], with various parameters, most importantly CD choice and excess differing between cases. Examples also exist of this methodology being applied to surface-bound lipid bilayers [234] and to investigate the formation of lipid domains in model membranes (sometimes called rafts) [229], interleaflet coupling [235], and flip-flop induced by membrane active proteins and peptides [233].

4.1.2 Analysis of EPR spectra to determine lipid dynamics

The theory behind the principles of EPR for nitroxide spin-labels has been discussed in the main introduction. Here, its application to study the molecular properties of lipid bilayers is discussed.

Calculating lipid order paramters from EPR spectra

Spin-labelled lipids undergo anisotropic motion when constrained within a bilayer, as a result of wobbling of the acyl chains and rapid rotation about the molecular long axis. In the liquid crystal phase these motions occur with a correlation time $\tau < 3 \times 10^{-9}$ s, and as such are in the hyperfine averaging time domain, giving dynamic information about the lipids directly. From an EPR spectrum, two hyperfine splittings, $A_{\parallel}$ and $A_{\perp}$, which describe the angular amplitude of lipid motion, can be measured. These values can be normalised for changes in bilayer polarity to give the effective order parameter, S_{eff}, which is the normalised anisotropy relative to the maximum possible anisotropy which occurs in a rigid crystal with no motion (*i.e.* $0 < S_{\text{eff}} < 1$) [236]:

$$S_{\text{eff}} = \frac{A_{\perp} - A_{\parallel}}{A_{zz} - (\frac{1}{2})(A_{xx} + A_{yy})} \cdot \frac{a'_0}{a_0} \tag{4.1}$$

where A_{zz}, A_{yy}, and A_{xx} are the principal hyperfine splittings of spin label's molecular axes. $\frac{a'_0}{a_0}$ is a normalisation term to account for the dependency of the hyper-

fine splittings upon the polarity of the lipid environment [237], and are related to the principal hyperfine splittings according to equations 4.2 and 4.3. Representative EPR spectra are shown in Figure 4.3.

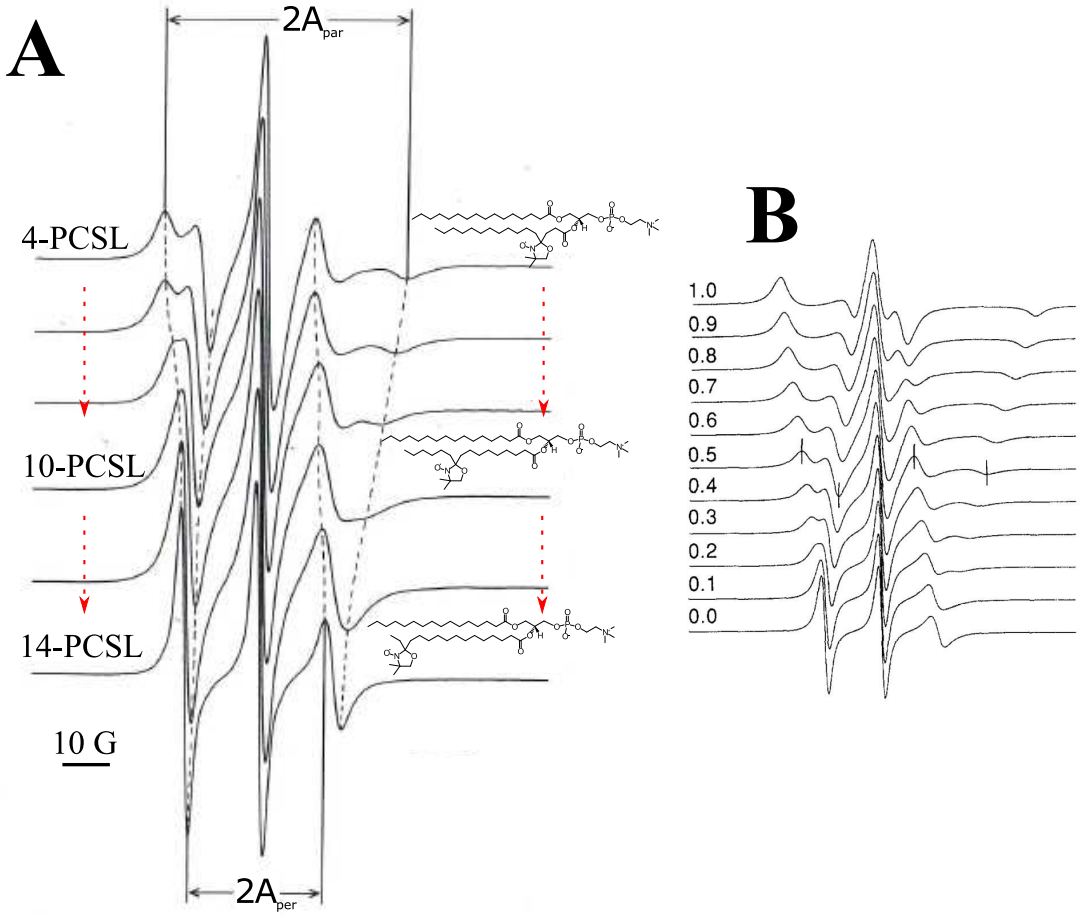

Figure 4.3 ***Left:*** EPR spectra of DPPC lipid bilayers, at 46°C, labelled at different positions along the *sn*-2 acyl chain. The hyperfine splittings $A_{\parallel}$ and $A_{\perp}$ are displayed, from which the order parameter for a particular acyl chain position can be calculated. ***Right:*** Simulated EPR spectra of a nitroxide spin label with order parameters varying between 0 and 1. Figures adapted from Marsh and Watts [236, 238].

By comparison with simulated spectra, it was empirically found that a final correction term to experimentally measured $A_{\perp}$ must be made, which is larger than that directly measured from EPR spectra (Equation 4.4) [239]:

$$a'_0 = (\frac{1}{3})(A_{zz} + A_{yy} + A_{xx}) \tag{4.2}$$

$$a_0 = (\frac{1}{3})(A_\parallel + 2A_\perp) \tag{4.3}$$

$$A_\perp^{act}/G = A_\perp + (1.4)(\frac{1-(A_\parallel - A_\perp)}{A_{zz} - \frac{1}{2}(A_{xx} + A_{yy})} \tag{4.4}$$

Typical CW-EPR experiments probe molecular motions on the 10^{-7}-10^{-9} timescale,[†] and hence are insensitive to the size of vesicle in which the spin label resides. This is advantageous with regard to peptide-lipid interactions since changes in the bilayer order parameters can be determined from smaller, more native-like LUV model membranes compared to MLVs necessary in ssNMR.

Analogous to deuterium order parameters obtained by ssNMR, S_{eff} profiles can be used to detect changes in lipid amplitude of motion at different depths in the hydrophobic core of a membrane, and have been used to examine the effects of cholesterol on membrane fluidity [125], as well as the binding of membrane-active peptides and proteins [240].

With the exception of ^{31}P MAS NMR, the changes observed in ssNMR and EPR are the average of two leaflets, due to an inability to resolve the spectra from each leaflet, giving an averaged interpretation of changes occurring at different depths in one or the other leaflets of the lipid bilayer. Hence, it is of interest to investigate changes resulting from individual leaflets, which is explored in this chapter.

4.1.3 Mimicry of bacterial cell membranes

To gain better mechanistic understanding of the mode of action of an AMP, model cell membranes typically comprise a mixture of glycerophospholipids to replicate some of the properties of bacterial and mammalian cell membranes. Spherical model membranes can accurately simulate properties such as surface charge, ion selectively,

[†]The rotational correlation time $\tau_c = \frac{4}{3}\frac{\pi r^3}{kT}$, where r is the radius of the liposome; even for small unilamellar vesicles ($r < 50$ nm) τ_c is $\backsim 10^{-6}$ s

osmotic swelling and lamellar structures of similar morphologies to their natural counterparts [241]. Different lipids, bearing different overall charge by virtue of different headgroups, can be used to simulate the charge properties of the organelle membranes of different species. For example, mammalian model membranes typically consist of PC lipids, while bacterial model membranes are modelled by either PE:PG (3:2) [242], or, due to the fact that PE lipids do not form stable lamellar-phase bilayers, PC:PG (3:1).

Simple model membranes cannot replicate the immensely complicated function, structure and selectivity of natural cell membranes. For example, an asymmetric distribution of phospholipids and membrane proteins is vital for many cellular processes, and has been investigated for decades [243]. Phosphatidylserine is an anionic lipid found in mammalian cell membranes, that is transported from the inner leaflet of the plasma membrane to the outer leaflet when a cell undergoes apoptosis, changing the surface charge of the membrane and signalling it for destruction [244]. Relatedly, despite the presence of negatively charged phospholipids in mammalian cell membranes, the smaller amount in the outer leaflet, relative to bacterial cell membranes, is thought to be a key difference underpinning the selectivity of antimicrobial peptides [217]. Indeed, in extreme cases, phosphatidylglycerol can comprise up to 90 % of bacterial cell membranes, as in the case of *Staphylococcus epidermidis* [245].

One stark difference between mammalian and bacterial cell membranes is the presence of an outer cell membrane in Gram negative bacteria(discussed in the main introduction). Lipopolysaccharides (LPS) are a structurally diverse family of molecules found in the outer membrane of Gram negative bacteria. It comprises lipid A, bound to a large polysaccharide (Figure 4.4). Found exclusively on the outer leaflet of the outer membrane, LPS is the first point of interaction for an incoming antimicrobial peptide, and performs a great variety of functions [246].
Phospholipids are poor models of LPS in model membranes, and incorporation of LPS into model membranes is desirable to investigate further the mechanism of an

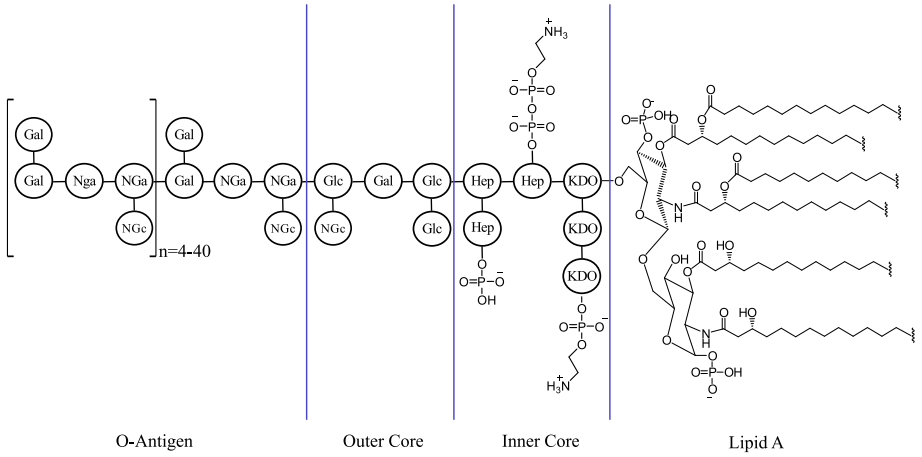

Figure 4.4 Typical structure of lipopolysaccharides. The inner lipid component comprises Lipid A, which is well conserved across bacterial species (with variations in acyl chain length). The inner and outer core region comprise a variety of monosaccharides that vary between species. The O-antigen is a highly variable unit of repeating monosaccharides that differ in sugar identity and length across species. It is absent in certain preparations of LPS (deemed rough-type). KDO: 3-deoxy-α-D-mannooctulosonic acid, Hep: heptulose, NGa: Galactosamine, NGc: Glucosamine. Figure adapted from sigma-aldrich.com.

AMP *in vivo*. Previous approaches suffered from poor incorporation of LPS into model membranes (less than 10% [247]), and uncertainty in how the LPS was oriented [172].

4.1.4 Aims of chapter

Asymmetric peptide-lipid interactions in nature have been underexplored by ssNMR or EPR studies of model membrane systems due to difficultly obtaining liposomes with a leaflet-specific control of lipid distribution. Adapting the work of London *et al* [144, 233, 248], attempts will be made to install selectively an EPR-labelled lipid in one leaflet of a model membrane to investigate for the first time leaflet-specific lipid-peptide interactions with EPR, with a range of antimicrobial and model peptides.

Additionally, this methodology will be employed to mimic a Gram-negative outer cell membrane by selectively incorporating LPS into the outer leaflet of a model membrane, and investigating resulting changes to the susceptibility of a vesicle to cell leakage.

In both cases, assays to determine the leaflet distribution of the installed lipid will be necessary, which will be attempted with fluorescence and EPR techniques.

4.2 Materials and methods

4.2.1 Lipids

Lipid stocks and storage are described in Section 2.2.1. 1-palmitoyl-2-stearoyl-(5/12/14/16-doxyl)-*sn*-glycero-3-phosphocholine (5/12/14/16-PCSL), 1-palmitoyl-2-oleoyl-*sn*-glycero-3-phospho(tempo)choline (HG-PCSL) and Rhodamine-PE (rho-PE) were purchased from Avanti Polar Lipids (Alabaster, AL). Rhodamine-LPS (rho-LPS) was purchased from Nanocs Inc. (Boston, MA), which was extracted from *E. coli* serotype $O26:B6$, which is structurally similar to rough-strain LPS. MβCD was purchased from Sigma Aldrich.

4.2.2 Buffers for fluoresence quenching

Buffer 1-Cl(I): Sodium Phosphate 50 mM, pH 7.2, 27.5% sucrose (w/v), 150 mM KCl(KI)

Buffer 2-Cl(I): Sodium Phosphate 50 mM, pH 7.2, 150 mM KCl(KI)

Buffer 3-Cl(I): Sodium Phosphate 50 mM, pH 7.2, 5 mM $MgCl_2$, 27.5% sucrose (w/v), 150 mM KCl(KI)

Buffer 4-Cl(I): Sodium Phosphate 50 mM, pH 7.2, 5 mM $MgCl_2$, 150 mM KCl(KI)

4.2.3 Peptides

The structures of peptides used in this chapter are given in Table 4.4. Tilamin and chom AMPs were synthesised and purified as described in Section 2.2.2 and stored as 20 mg mL^{-1} stocks in H_2O. Helix-8 peptide (h8p) and WALP-23 was purchased from Peptide Protein Research LTD (Hampshire, UK) and stored in 30 mgmL^{-1} stocks in DMSO.

4.2.4 Dynamic light scattering

DLS experiments were performed as outlined in Section 3.2.3.

4.2.5 Calcein leakage

The vesicles were suspended in self-quenching calcein solution (Calcein (70 mM), TRIS-HCL (10 mM), pH 7.4) to a concentration of 10 mM, and extruded to form 100 nm LUVs. To remove un-entrapped calcein, the LUVs were passed through a size exclusion column (5 mL HiTrap Desalt column (GE Healthcare)), at a flow rate of 2 mL/min and pressure of 0.45 MPa. The faintly yellow LUVs eluted at 1.5 mL, while all strongly-yellow coloured, excess calcein eluted separately after 3 mL. The final concentration of the liposome samples was determined by the lipid concentration assay.

4.2.6 Fluorescence measurements

Fluorescence measurements were performed on a Perkin-Elmer LS-50B fluorimeter (slit width 5 mm). After blanking, samples were excited at 490 nm, and spectra read between 500 nm and 530 nm. LUV samples were diluted to a concentration of 10 μM. Gramicidin D stocks were made in DMSO (10 mg mL^{-1}), while tilamin and chom stocks were made in H_2O (10 mg mL^{-1}). Peptides were then diluted 200-fold in the experimental buffer. Peptides were added to make final lipid:peptide ratios of 1 : 0 (lipid only), 500 : 1, 250 : 1, 100 : 1 and 50 : 1. Fluorescence spectra were then taken again 5 min after addition. After 5 min Triton X-100 (10% v/v in H_2O, 5 μL) was added to the cuvette, and a final fluoresence measurement made to obtain the maximal leakage result. The calcein leakage (%L) was determined, by a standard protocol [171] according to

$$\%L = \frac{F - F_o}{F_T - F_o} \times 100, \tag{4.5}$$

where F is the fluoresence maximum at 520 nm of the sample after peptide is added to the LUV suspension, F_o is the initial fluoresence maximum before peptide addi-

tion, and F_T is the fluoresence after addition of Triton-X100 (maximum fluoresence). All measurements were repeated in triplicate, and plotted as the average with the standard deviation shown.

4.2.7 Asymmetric vesicle Formation

EPR and fluorescence samples

Acceptor vesicle preparation: Adapting a literature protocol [144], acceptor LUVs were formed by first preparing MLVs (2 μmol) of a given composition in chloroform ((chloroform:methanol 3:1 (v/v)) for mixes containing anionic lipids), dried under nitrogen, then *in vacuo* for 1 h. The film was resuspended in 27.5% sucrose (w/v) (for rho-PE quenching, buffer **1-Cl/I**, for rho-LPS quenching buffer **3-Cl/I**, for cw-EPR buffer **1-Cl/I** with neither KCl nor KI was used). The resulting suspension was subjected to five freeze-thaw cycles between liquid N_2 and a temperature above the T_c of the lipids (for POPC/POPG lipids, room temperature was sufficient). The freeze-thawed MLVs were then extruded 11 times through 100 nm polycarbonate filters (Avanti Polar Lipids) to form unilamellar vesicles. The sucrose-entrapped vesicles were diluted with H_2O (9 mL) and centrifuged (2 h, 190,000 g, 10 ℃), using a Beckman Optima XL-100k Ultracentrifuge and SW 41 TI rotor to remove any non-entrapped sucrose. The pelleted vesicles were then resuspended in H_2O (250 mL).

Donor vesicle preparation: Donor MLVs were prepared by mixing the requisite lipid formulation (8 μmol) in chloroform (chloroform : methanol 3:1 (*v*/*v*) for anionic lipids), dried under nitrogen, then *in vacuo* (10^{-5} Torr) for 1 h. The dried lipid film was suspended in 500 μL of H_2O, and left to stand above the T_c of the lipids for 1 h with occasional, gentle vortexing. The MLVs were then incubated with a 0.69 mM solution of MβCD (63 μmol) for 2 h at 1000 rpm and 50 ℃ using a heated vortexer (Eppendorf Thermomixer Comfort).

Asymmetric Vesicle preparation: To the solution of MβCD-solubilised donor MLVs was added the sucrose-entrapped acceptor LUVs, and the resulting suspension mixed (30 min, 1000 rpm, 50 ℃) using a heated vortexer. This mixed suspension was then diluted in 9 mL of 4.5% sucrose solution, and centrifuged (2 h, 190,000g, 10 ℃). The unpelleted MLVs and MβCD were removed in the supernatant, and the exchange LUVs were resuspended in various buffers for various CW-EPR and fluoresence experiments outlined below.

The asymmetric vesicle preparation procedure describes the formation of asymmetric vesicles comprised of POPC. With POPC : POPG(8:1) formulations, the donor MLVs and acceptor LUVs are separated by 13% sucrose solutions. It was not possible to form POPC:POPG (3:1) vesicles, which could have been directly compared to the results from the previous chapter, despite many pelleting conditions being attempted. A phosphate concentration assay was used to determine the yield of pelleted exchange vesicles ten times, and the average of these results was subsequently assumed to apply to all future experiments, due to the narrow range of values obtained (85 – 89% of initial acceptor LUV).

LPS Samples

Symmetric liposomes containing LPS were prepared by mixing POPC with rho-LPS (80 μg μmol^{-1})(ChemQuest Co. Wilmslow, UK) in chloroform, dried under nitrogen, then *in vacuo* for 1 h. The mixture was resuspended in H_2O(1 mL), frozen in liquid N_2, and lyophilised overnight. The resulting powder was then resuspended in buffer **3-Cl/I**, subjected to five free-thaw cycles between liquid N_2 and a temperature above the lipids' T_c (room temperature), and extruded 11 times through 100 nm polycarbonate filters. Fluorescence measurements were carried out as outlined below.

POPC acceptor vesicles were prepared as outlined above, suspended in buffer **3-Cl/I**. 1 mg lipid was used *per* sample.

Donor rho-LPS samples were prepared by lyophilising rho-LPS (800 µg/ µmol acceptor lipid), then resuspension in a 40 µM MβCD solution (500 µL), and incubation for 2 h at 1000 rpm and 50 ℃ using a heated vortexer.

After mixing with the acceptor vesicles for 1 h, they were separated from the donor vesicles and excess MβCD in the same way as above.

4.2.8 Fluorescence measurements

Fluorescence experiments were carried out on a *LS*50*B* Luminescence Spectrometer (Perkin Elmer). The emission spectrum for rho-PE and rho-LPS was obtained from an excitation wavelength of 550 nm, and read between 565 and 620 nm, at a slit length of 5 nm and scan speed of 50 nms^{-1}, in a 500 µL cuvette (path length 2 mm). All measurements were carried out at room temperature.

Quenching

Pelleted asymmetric liposomes prepared contained either 150 mM KCl or KI entrapped by the asymmetry procedure. For rho-PE samples, the samples were resuspended in 200 µL buffer **2Cl/I**, to give four samples - $Cl_{out}|Cl_{in}$, $Cl_{out}|I_{in}$, $I_{out}|Cl_{in}$ and $I_{out}|I_{in}$, where *in*/*out* refers to ion presence inside and outside the asymmetric liposome. For rho-LPS samples, the pelleted samples was resuspended in buffer **4Cl/I** to give the same four samples.

4.2.9 EPR

General

After pelleting of the asymmetric vesicles from the exchange procedure, peptides from a concentrated stock were added to the pellet ($2-20$ µL), and the suspension briefly vortexed (20 s). For asymmetric samples without peptide, an equivalent volume of H_2O (AMPs) or DMSO (h8p and WALP-23) was added. The liposomes were then

loaded into a 0.5 mm glass capillary (Sigma-Aldrich), which were flame-sealed at one end. The capillaries were centrifuged (1,000 g, 1 min).

Spectra were acquired on an X-band CW spectrometer (Bruker EMX, Xenon software) with 9 GHz X-band Super High Sensitivity Probehead (Bruker). All experiments were carried out at room temperature with the exception of the ascorbic acid reduction at 2 ℃ with a liquid nitrogen cryostat. Spectra were acquired with a sweep width of 100 G with the central peak coincident with the centre of field, a modulation amplitude of 1 G, an attenuation of 13 dB, and a sweep time of 30 s. The time constant was set to $\backsim 1/10$ of the conversion time. Receiver gain was set to maximise signal without saturation. Between $10-50$ scans were collected and averaged. Spectra were the average of two separate samples, with a single order parameter quoted, according to literature precedent [238].

Order Parameter Calculation

Hyperfine splittings $A_\perp$ and $A_\parallel$, were obtained from EPR spectra, from which the effective order parameter S_{eff} was calculated according to section 4.1.2. Taking literature values for the principal hyperfine splittings of a spin-labelled diacylglycerophopholipid of $A_{zz} = 32.9$, $A_{yy} = 5.4$ and $A_{xx} = 5.9$ [125], the calculation is reduced to equation 4.6:

$$S_{\text{eff}} = 0.5407 \times \frac{A_\parallel - A_\perp^{act}}{a_0}. \tag{4.6}$$

Ascorbate Acid Reduction

Following a literature procedure [52], pelleted asymmetric liposomes containing TEMPO PC (HG-PCSL) in either leaflet, were cooled to 4 ℃ and resuspended in buffer ***A*** (400 µL). 10 µL of sodium ascorbate (0.35 M) was added to the sample (10 µL of H_2O for controls) and briefly vortexed. The excess ascorbate was removed by size-exclusion chromatography, using two 5 mL HiTrap Desalt Columns (containing G-25 sephadex) (GE Healthcare) in series. Samples were then pelleted a final time and

loaded in the same manner as above. Measurement of the double-integrated EPR spectra of the ascorbate treated samples, relative to the untreated sample control, scaled to the amounts in each sample (calculated by phosphorus concentration assay), gave the % spin-label located in the inner leaflet of the liposome.

4.3 Results

4.3.1 Separation of donor vesicles from acceptor vesicles

Adapting the protocol from the London group [230], modifications had to be made to the pelleting conditions to ensure separation of the donor MLVs from the acceptor LUVs. By using 4.5% sucrose as a pelleting medium, separation of the MLVs from the LUVs was successful, with pelleting of the pink rhodamine PE LUVs and the blue cy5 PE MLVs remaining suspended (Figure 4.5).

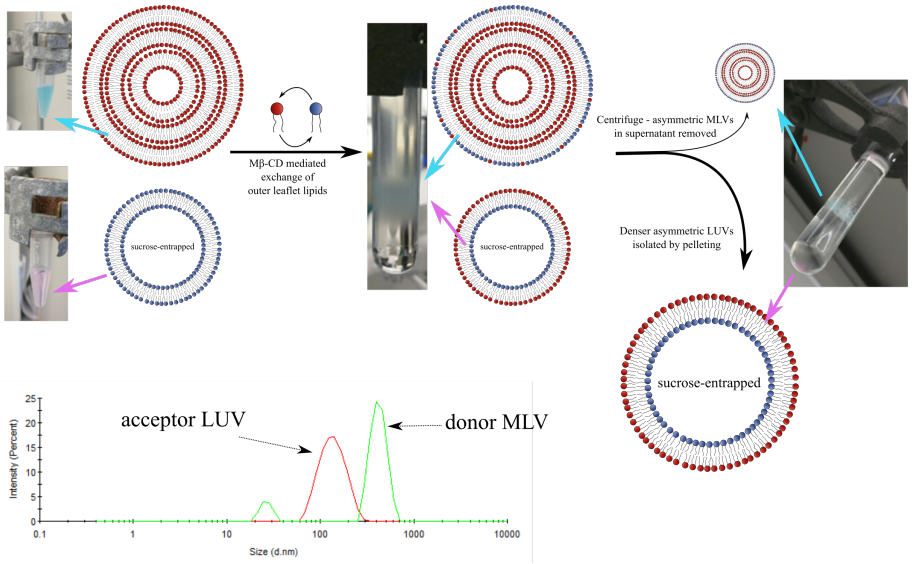

Figure 4.5 Scheme to form asymmetric vesicles. Pink rhodamine-PE labelled LUVs were incubated with blue Cy-5 labelled MLVs, and after centrifuging in 4.5% sucrose complete separation of the two vesicle types occurred as determined by DLS.

Dynamic light scattering measurements on the pelleted sample also revealed a monodisperse population of 120 ± 25 nm LUVs, confirming donor vesicles had not fused with the heavier, acceptor LUVs. Cy-5 PE was included for this experiment to aid in visualisation, but was omitted later. To determine the yield of the exchange process, and the asymmetry of the exchange vesicle (*i.e.* the leaflet distribution of the fluorophore), fluorescence quenching and phosphorus concentration assays were performed next.

4.3.2 Determination of phospholipid yield

Figure 4.6 (*left*) shows the recovery of a symmetric POPC (1% rho-PE) vesicle after the exchange process, as determined by phosphorus concentration assay [249]. A

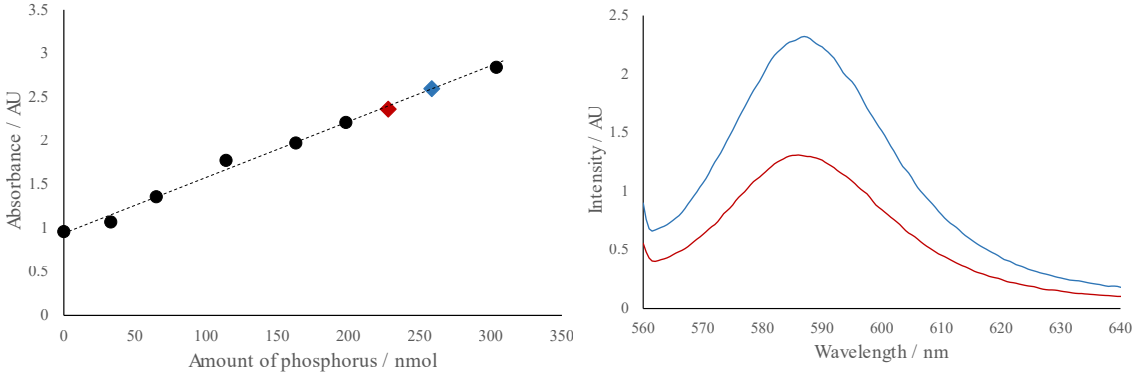

Figure 4.6 (*left*) A phosphorus concentration assay showing the amount of phospholipid before and after outer leaflet exchange. Black circles are phosphorus standards, and the blue/red diamonds are vesicles before/after exchange. Standards were taken in triplicate, vesicles were averaged over ten measurements (error bars too small to be seen). (*right*) Fluorescence spectra taken before and after outer leaflet exchange. The greater reduction in fluorescence intensity compared with phosphorus amount indicates removal of fluorescent lipid from the acceptor vesicle.

post-exchange yield of liposomes was calculated to be 87.6%, implying some loss of material during centrifugation steps, or partial solubilisation of some of the vesicles by the MβCD. This yield was deemed acceptable to allow future EPR measurements to be made. A reduction in fluorescence of 54 ± 5% was observed (Figure 4.6 *right*), indicating that about half of the rhodamine-PE from the acceptor vesicles must have been removed in the exchange process, which is expected.

With the exchange process confirmed to permit recovery of a large unilamellar vesicle, and reduce the rho-PE content of the vesicle, fluorescence quenching experiments to determine the leaflet distribution of the rho-PE label were performed.

4.3.3 Fluorescence-based determination of label distribution in leaflets

The fluorescence of the rhodamine-PE lipid can be quenched in the presence of I^- ions [250], however since I^- is unable to traverse the hydrophobic core of a bilayer,

it will only quench the fluorescence of the leaflet to which it has access. This property makes it suitable for assessing the asymmetrical distribution of a fluorescent label in a liposome. By encapsulating I^- inside a liposome, or having it in bulk solution, leaflets of the liposome can be specifically quenched. Cl^- was used as a control to maintain the same ionic strength without the quenching property. Fig 4.7 shows that the leaflet distribution of rhodamine-PE symmetrically incorporated into a POPC 100 nm LUV and 20 nm SUV can be probed with fluoresence quenching of I^-.

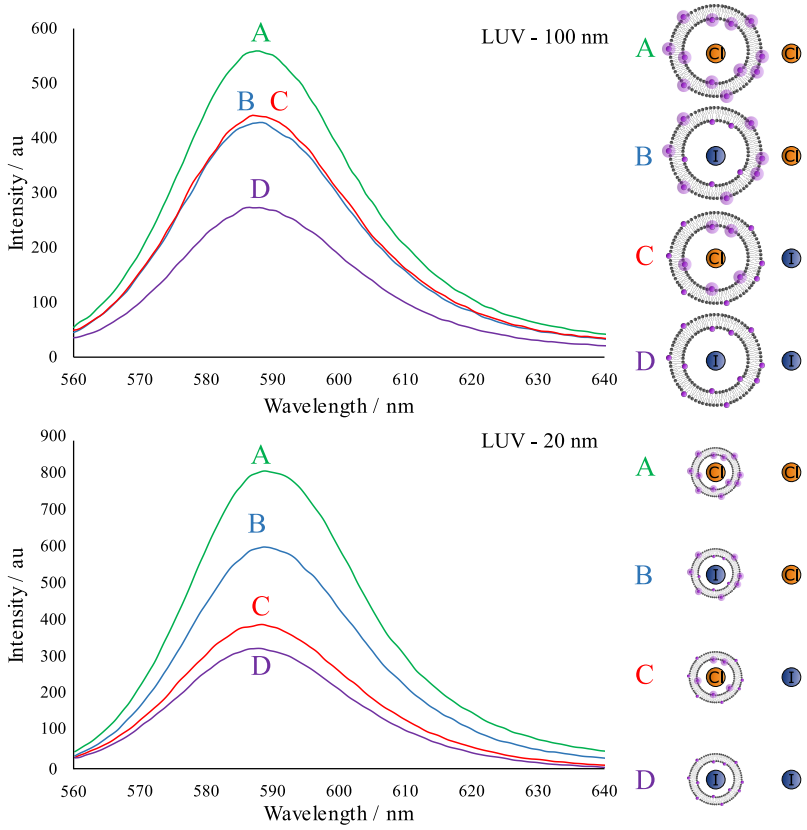

Figure 4.7 Fluorescence spectra showing the leaflet-specific quenching of rhodamine-PE by I^- ions, in a 100 nm (*top*) and 20 nm (*bottom*) unilamellar vesicle (1% rhodamine PE). (*A*) With Cl^- present inside and outside the liposome, the 'all on' state shows maximum fluoresence. (*D*) With I^- inside and outside the vesicle, the 'all off' state shows minimal fluoresence. (*B*) and (*C*) Intermediary fluoresence is displayed when I^- is only present on one side of the liposome, quenching only half the fluorescent lipids. In 100 nm LUVs, the nearly equal lipid amounts on both leaflets are reflected in the same quenching of both leaflets. For SUVs, more lipids reside in the outer leaflet due its greater surface area (which scales with the size of the liposome [251]), and this is reflected in the increase in fluoresence when I^- is only present inside the liposome.

For the LUV, with all labels quenched, a decrease in fluoresence intensity of 51% was observed. When Cl^- was present on the exterior of the liposome (I^- inside), a 21% reduction of quenching was observed, while 23% quenching was observed when I^- was outside (Cl inside). For the SUV, with all labels quenched, a decrease in fluoresence intensity of 41% was observed. When Cl^- was present on the exterior of the liposome (I^- inside), a 75% reduction of quenching was observed, while 50% quenching was observed when I^- was outside (Cl inside). The fact that more quenching was observed when I^- was present on the outside is due to geometric differences in leaflet surface area of the two faces, which is more pronounced with smaller vesicles (it has been calculated that 52% of lipids reside on in the outer leaflet of a 100 nm LUV compared with 64% for a 20 nm SUV [252]). The quenching results are summarised in Table 4.2.

Inner ion	Outer ion	% Intensity reduction 100 nm LUV	20 nm SUV
Cl	Cl	0	0
Cl	I	21 ± 2	75 ± 5
I	Cl	23 ± 3	50 ± 6
I	I	51 ± 3	41 ± 5

Table 4.2 Table summarising the changes in fluorescence intensity of symmetric POPC (1% rhodamine-PE) vesicles in the presence of quenching I^- ions on the inner, outer or both inner and outer leaflets of the liposome.

With a suitable system set up to assess leaflet distribution of lipids, the same experiments were carried out to asymmetrically prepared liposomes, with rhodamine-PE installed specifically in the inner and outer leaflets.

4.3.4 Fluorescence experiments on asymmetric model membranes

To demonstrate that a spectroscopic probe could be selectively incorporated into a specific leaflet of a model membrane, fluoresence quenching was used as a read out. First, an asymmetric 100 nm LUV was prepared with 1% rhodamine-PE selectively

incorporated in the outer leaflet. Figure 4.8 displays the effect of introducing I^- ions to the outer surface of an asymmetric vesicle.

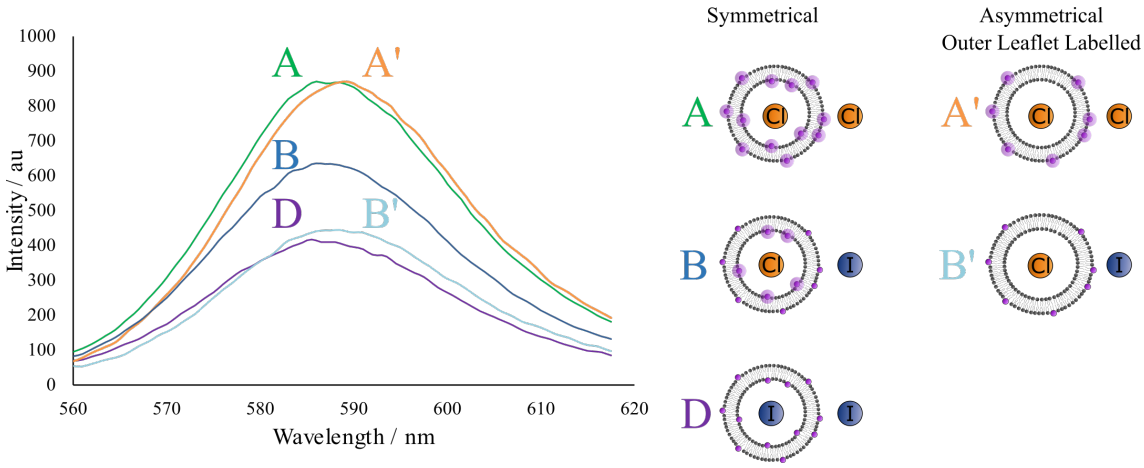

Figure 4.8 Fluorescence spectra showing the quenching by I^- of rhodamine-PE specifically incorporated into the outer leaflet of a POPC LUV, compared to a symmetric control. A reduction of fluoresence intensity of 49 % was observed (*A'*-*B'*), compared to $\backsim$25% for a symmetric control of the outer leaflet (A-B), suggesting all fluorescent label is located in the outer leaflet. The fluoresence of the asymmetric liposomes *A'* and *B'* were normalised in intensity with respect to the symmetric control *A*.

The decrease in fluorescence intensity was not $\backsim$ 25%, as in the case of the symmetric vesicles (Figure 4.7). A reduction of 49% in fluoresence intensity was observed, indicating that > 98% of rhodamine-PE resided in the outer leaflet. In addition, the wavelength of maximum rhodamine fluorescence blue-shifted by 3.8 nm, indicating a change in the environment of the label, which could be caused by all labels residing in the less curvature-strained leaflet. An asymmetric vesicle was then prepared with 1% rhodamine-PE installed in the inner leaflet, displayed in Figure 4.9 (overleaf).

Only partial asymmetry was achieved in the case of inner leaflet labelling: no change in fluoresence intensity upon introduction of I^- to the surface of the liposome would indicate complete asymmetry, however a reduction of 8% was noted, implying 84% of the fluorescent label resided in the inner leaflet. This could indicate either that sterically bulky rhodamine-PE was flipping to the outside of the liposome to relieve curvature strain, or that extraction by MβCD of rhodamine-PE from the acceptor vesicles was less successful due to the larger steric mass of the headgroup. In the former case

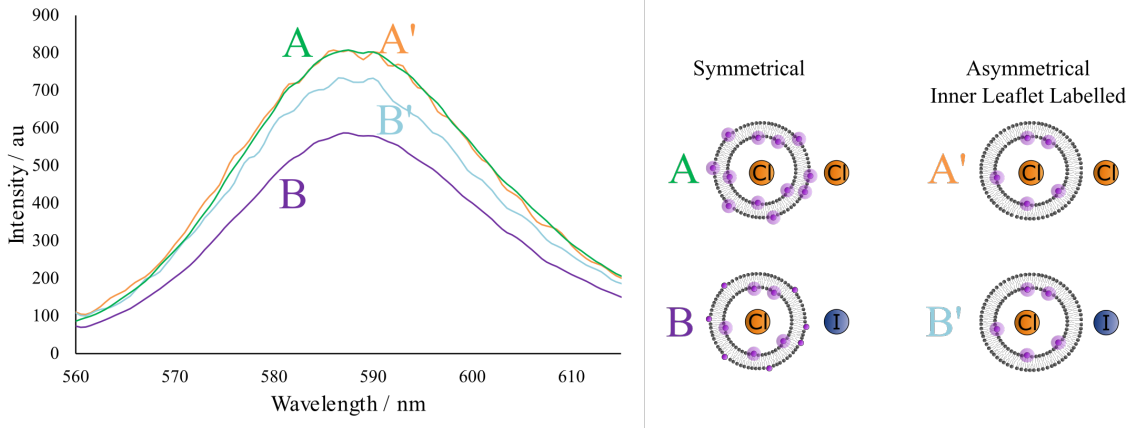

Figure 4.9 Fluorescence spectra showing the quenching by I^- of rhodamine-PE specifically incorporated into the inner leaflet of a POPC LUV, compared to a symmetric control. A reduction of fluorescence intensity of 8 % was observed (*A'*-*B'*), compared to $\backsim$ 25% for a symmetric control of the outer leaflet (*A*-*B*), suggesting 84% of the fluorescent label is located in the inner leaflet. The fluorescence of the asymmetric liposomes *A'* and *B'* were normalised in intensity with respect to the symmetric control *A*.

rhodamine-PE only had to be introduced to the acceptor vesicles for complete asymmetry, whilst in the latter case required all rhodamine-PE from the outer leaflet of the acceptor vesicles to be exchanged by unlabelled POPC from the donor vesicles. The results from both experiments are summarised in Table 4.3.

Inner ion	Outer ion	% Intensity reduction		
		Both leaflets labelled	Inner leaflet labelled	Outer leaflet labelled
Cl	Cl	0	0	0
Cl	I	23 ± 3	8 ± 4	49 ± 2

Table 4.3 Table summarising the changes in fluorescence intensity of asymmetric (and symmetric for comparison) POPC (1% rhodamine-PE) vesicles in the presence of quenching I^- ions on the inner, outer or both inner and outer leaflets of the liposome.

The results confirmed that a spectroscopic label could be introduced to a specific leaflet, producing a spectrum in which leaflet-specific peptide-lipid interactions could be probed, as discussed in the following sections.

4.3.5 Towards a Gram-negative model membrane

Attainment of asymmetric distribution of LPS

To install selectively LPS into the outer leaflet of a model membrane, mimicking Gram-negative bacterial outer membranes, MβCD-mediated exchange was once again exploited. Following the same procedure, fluorescence experiments were carried out to assess the success of this method (Figure 4.10).

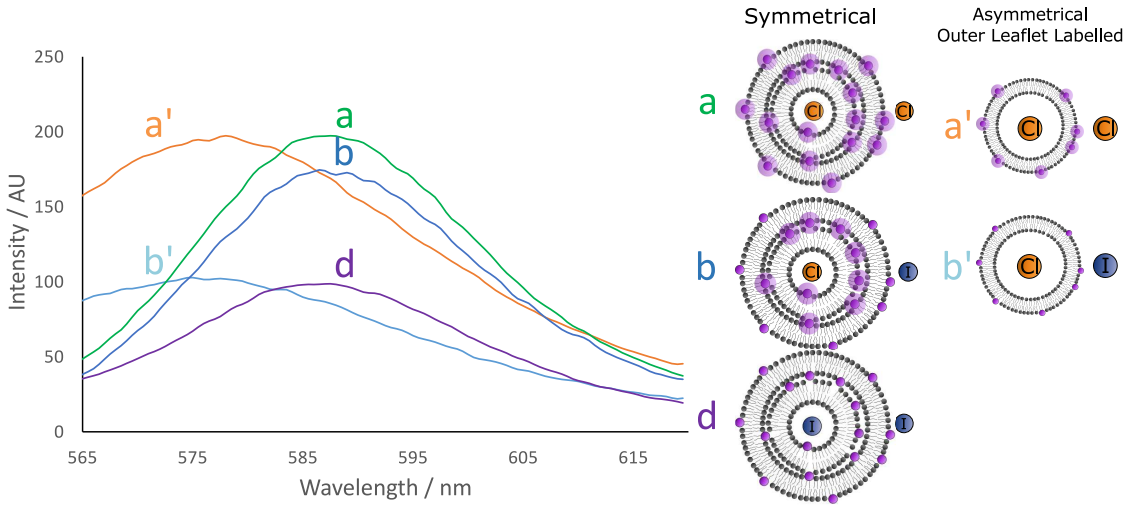

Figure 4.10 Fluorescence spectra showing the quenching by I^- of rhodamine-labelled LPS specifically incorporated into the outer leaflet of a POPC LUV, compared to a symmetric control. A reduction of fluorescence intensity of 48 % is observed (*A'-B'*), compared to 11 % for a symmetric control of the outer leaflet (*A-B*), suggesting all of the fluorescent label is located in the outer leaflet. The fluorescence of the asymmetric liposomes ***A'*** and ***B'*** were normalised with respect to the symmetric control ***A***.

For a control, symmetric MLV, when I^- was present both inside and outside the vesicle, a reduction of 50% fluorescence intensity was observed like before. However, when I^- was only present on the vesicle exterior, a decrease of 11% fluorescence intensity was observed. Since the vesicle is multilamellar, any rho-LPS situated in any but the outermost lamella would not be exposed to quenching $I-$ in solution. When a POPC LUV was prepared with rhodamine-LPS installed asymmetrically in the outer leaflet, a reduction of 48% was noted, indicating all the LPS resided in the outer leaflet.

LUVs were not used as a symmetric control, because when a control LUV of POPC with 20 µg/ µmol was studied, fluoresence data was unobtainable. Despite DLS showing a monodisperse sample of ∽ 100 nm LUVs, no signal was given above baseline noise and was not interpretable. It is unclear why this is, but one explanation could be that when extruded the LPS becomes trapped in some way by the polycarbonate filter. Another remarkable feature was the large blue shift of the asymmetric LPS-containing LUV compared with the MLV control. This may have been due to LPS in MLVs being in a variety of hydrophobic and hydrophilic environments (situated in and inbetween lamellae), and being less curvature-strained than the smaller LUV.

In addition, DLS experiments showed that the fluorescence signal did not originate from any donor MLVs remaining in solution, as shown in Figure 4.11.

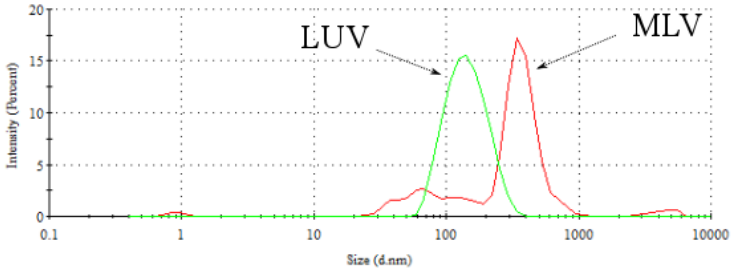

Figure 4.11 Dynamic light scattering profile showing the donor POPC MLVs(*red*) and the acceptor, asymmetric POPC LUVs with LPS selectively incorporated into the outer leaflet (*green*).

Calcein leakage results

To assess if the LPS-liposomes were better model membrane mimics than conventional POPC : POPG liposomes, cell leakage experiments were carried out to see if the presence of LPS affected the ability of AMPs to permeabilise model membranes. It was shown in Chapter 2 that tilamin and chom were broad spectrum, so it was suggested that the presence of LPS should not significantly affect permeabilisation ability, as LPS is only present in the outer membrane of Gram-negative bacteria, and absent in Gram-positive bacteria [253] (Figure 4.12).

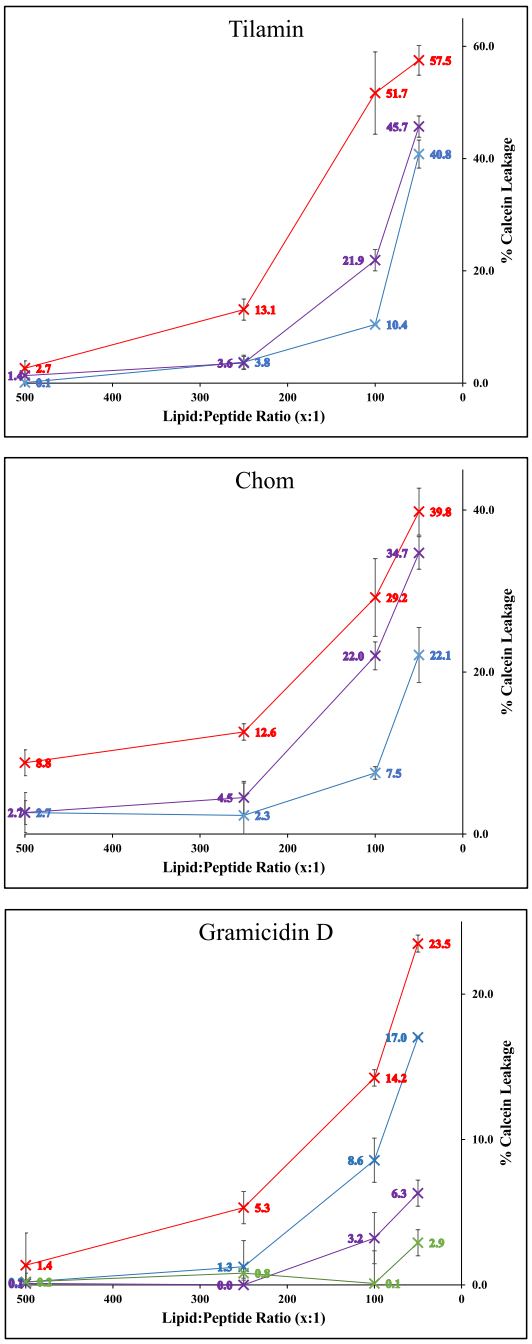

Figure 4.12 Permeation of model membranes by tilamin (*top*), chom (*middle*), and gramD (*bottom*), as monitored by calcein fluoresence. X-POPC:PG(3:1), X-POPC, X-POPC:PG(3:1) with outer leaflet LPS (80 µg/ µmol) and X-POPC:PG(3:1) with "symmetrical" LPS (80 µg/ µmol). Each point is the average of 3 measurements, with the standard deviation shown.

These results were compared with gramicidin D (GramD), a mixture of antimicrobial peptides (Figure 4.13). GramD is selective for Gram-positive bacteria which lack an outer membrane composed of LPS [86], so the ability of GramD to induce cell leakage of Gram-negative model membranes should be more reduced compared to the broad spectrum AMPs. Figure 4.12 shows the calcein leakage induced by chom, tilamin and GramD upon interaction with anionic POPC:PG 8:1 membranes, zwitterionic POPC membranes, and asymmetric anionic PC:PG 8:1 membranes containing LPS.

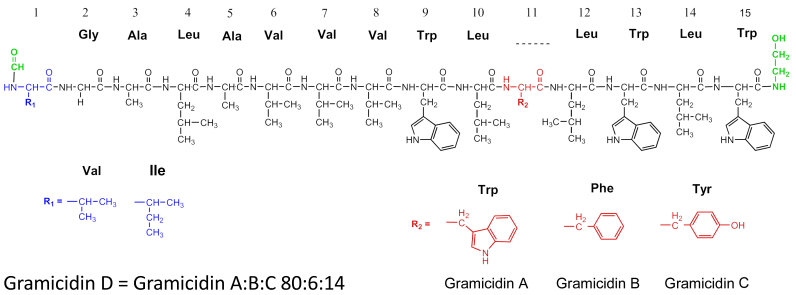

Figure 4.13 The structure of the gramicidins (Grams). GramD is a mixture of GramA, GramB and GramC. The primary sequence comprises alternating D- and L- amino acids.

For tilamin and chom, the presence of LPS reduced calcein leakage at a peptide lipid:ratio of 50:1 by 12% and 5%, respectively. The presence of anionic PG (as well as the anionic LPS) still permitted greater leakage than zwitterionic POPC liposomes, however. In the case of GramD at the same lipid:peptide ratio, a greater reduction of 20% in calcein leakage compared with POPC:POPG membranes was observed. This was a greater decrease from anionic POPC:POPG LUVs than for zwitterionic PC membranes, despite the LUVs still being anionic. This suggests that LPS prevents GramD from inducing cell leakage in gram negative bacteria, explaining its selectivity. Gramicidin forms oligomeric channels in membranes [254], which could be prevented from forming in the presence of LPS. Conversely, for tilamin and chom, if a less structured channel was required for membrane destabilisation, it could explain why LPS had less of an effect in these experiments. In addition, in comparison to a control POPC:PG:LPS vesicle prepared in the conventional way of drying all components

together then rehydrating, a greater reduction of calcein leakage was noted for the asymmetric vesicle, implying the importance of control over LPS leaflet distribution in the creation of better membrane mimetics.

4.3.6 EPR studies on asymmetric peptide-lipid interactions

Peptides used as model systems

To interpret any changes in lipid mobility in one or other bilayer leaflet induced by a surface-bound peptide or transmembrane-embedded peptide, archetypes of both extremes needed to be examined. To study a surface-bound peptide, a residue distribution that produces an amphipathic fold is desired such that the hydrophobic face can make contacts with the hydrophobic core of a lipid membrane, while the hydrophilic face can interact with the bulk water/hydrophilic lipid headgroups. However, binding should not precede any lytic effect or subsequent membrane deformation.

Neurotensin receptor 1 is a G-protein coupled receptor that is important for many disease pathways [255]. Elements of its structure are controversial. In particular, the existence of an eighth helix (common to many other GPCRs [256]), located on the inner leaflet of a eukaryotic cell membrane is debated [257], from crystallographic studies. A peptide consisting of S373-C388 of this protein which covers the putative eighth helix (h8p), was previously shown to be alpha helical in the presence of neutral model membranes (Figure 4.14) [258].

When viewed as a helical wheel projection, h8p forms an amphipathic helix, though with a less severe hydrophobic moment and far lesser overall charge than typical AMPs. The surface binding properties of this peptide sequence, without any noted antimicrobial activity, renders this a suitable "all surface-bound" control peptide.

The family of WALP peptides have used extensively to study the effect of membrane thickness on the angle of insertion of peptides that can span a hydrophobic interior [259–261]. The peptides typically consist of two hydrophilic amino acid caps spanned

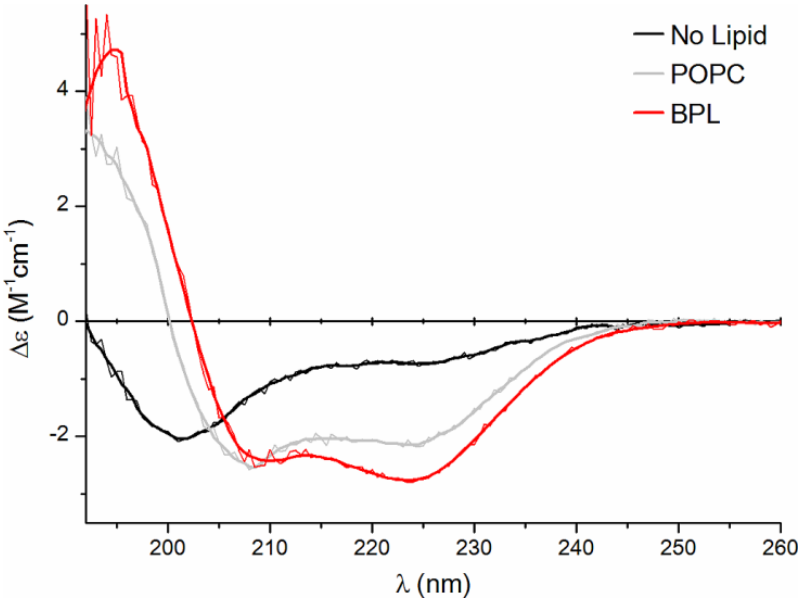

Figure 4.14 Circular dichroism spectrum of h8 peptide (0.1 mg mL^{-1}) in the absence (black) and presence of brain polar lipid (BPL) (red) and POPC liposomes (grey) (P:L 1:5). Spectrum obtained by Dr P. Dijkman (Max Planck Institute of Biophysics).

by a long hydrophobic stretch. The caps interact preferentially with the headgroups of a bilayer, while the hydrophobic middle stretch interacts favourably with the acyl core. WALP-23 has been demonstrated to insert almost completely transmembrane into POPC due to a well matched length of hydrophobic region to the hydrophobic thickness of membranes of this type (25.5 and 26.5 Å, respectively) [179]. This peptide was therefore studied as a "fully transmembrane" control peptide, and the changes in lipid mobility across leaflets were compared to changes induced by tilamin and chom to examine if more subtle interactions could be delineated than previously possible. Table 4.4 summarises the properties of h8p and WALP-23 in comparison to chom and tilamin, with the helical wheels for all four peptides studied overleaf (Figure 4.15).

Peptide	Sequence	Molecular Weight (g mol^{-1})	Charge at pH 7.2	Isoelectric point
tilamin	KARLAKLRARLYRLKARLARL-NH_2	2578.21	+10	12.81
chom	KWKVFKKIEKMIRNIRNKIVK-NH_2	2741.44	+9	12.26
h8p	SANFRQVFLSTLACLC-NH_2	1814.14	1.9	8.8
WALP-23	GWWLALALALALALALALWWA-NH_2	2478.02	0	14

Table 4.4 Table showing the peptides, and molecular properties thereof, used in asymmetric cw-EPR experiments. Properties calculating using the online application pepcalc.com.

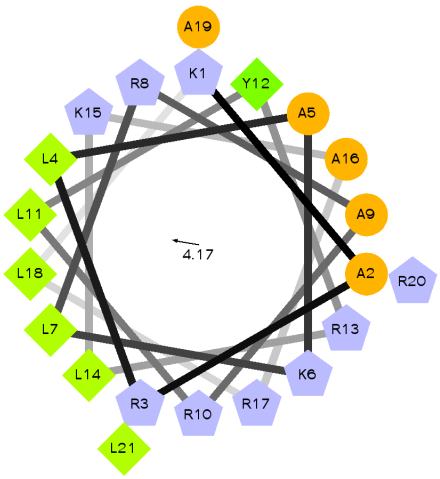

tilamin : KARLAKLRARLYRLKARLARL

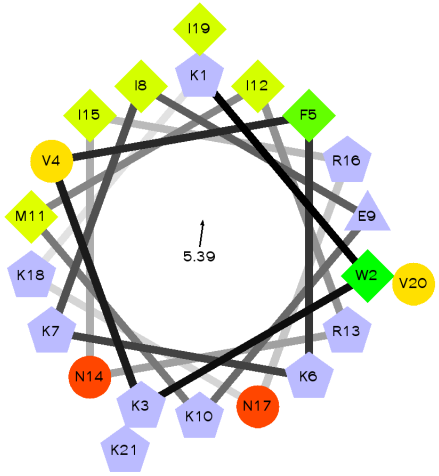

choM : KWKVFKKIEKMIRNIRNKIVK

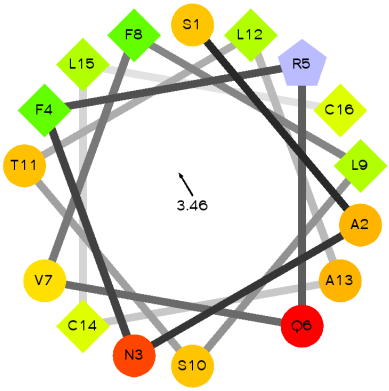

h8p: SANFRQVFLSTLACLC

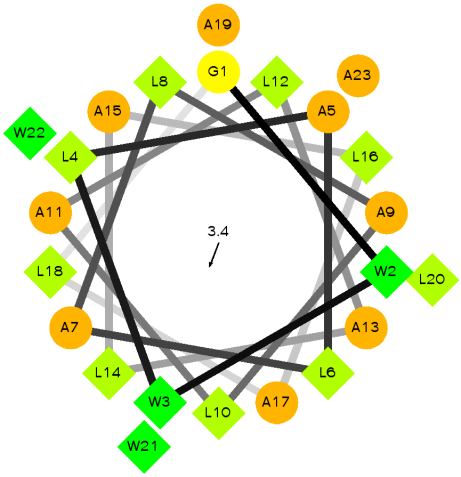

WALP-23 : GWWLALALALALALALALWWA

Figure 4.15 Helical wheel projections of the four peptides studied in this chapter. The hydrophobic middle section of WALP-23, flanked by hydrophilic ends, inserts transmembrane into membranes. Amphipathic helix 8 peptide was predicted to lie on the surface of a membrane. The two AMPs tilamin and chom were expected to fall somewhere inbetween these two extremes. Helical projections created using an online resource [176].

Ascorbate quenching to assess asymmetric spin label distribution

To ascertain if a spin probe could be incorporated into a specific leaflet of a model membrane in an analogous manner to a fluorophore, a quenching experiment with ascorbic acid was performed. In the presence of excess ascorbate, nitroxide and TEMPO spin labels are reduced, abrogating the resulting EPR spectrum. At 0 ℃ the membrane is impermeable to ascorbate ions, and thus only the labels in the outer leaflet are affected [47]. Asymmetric vesicles with a headgroup-labelled lipid residing in only one leaflet were prepared in the same way as in Section 4.3.1. Figure 4.16 shows the result of ascorbate quenching of asymmetric liposomes.

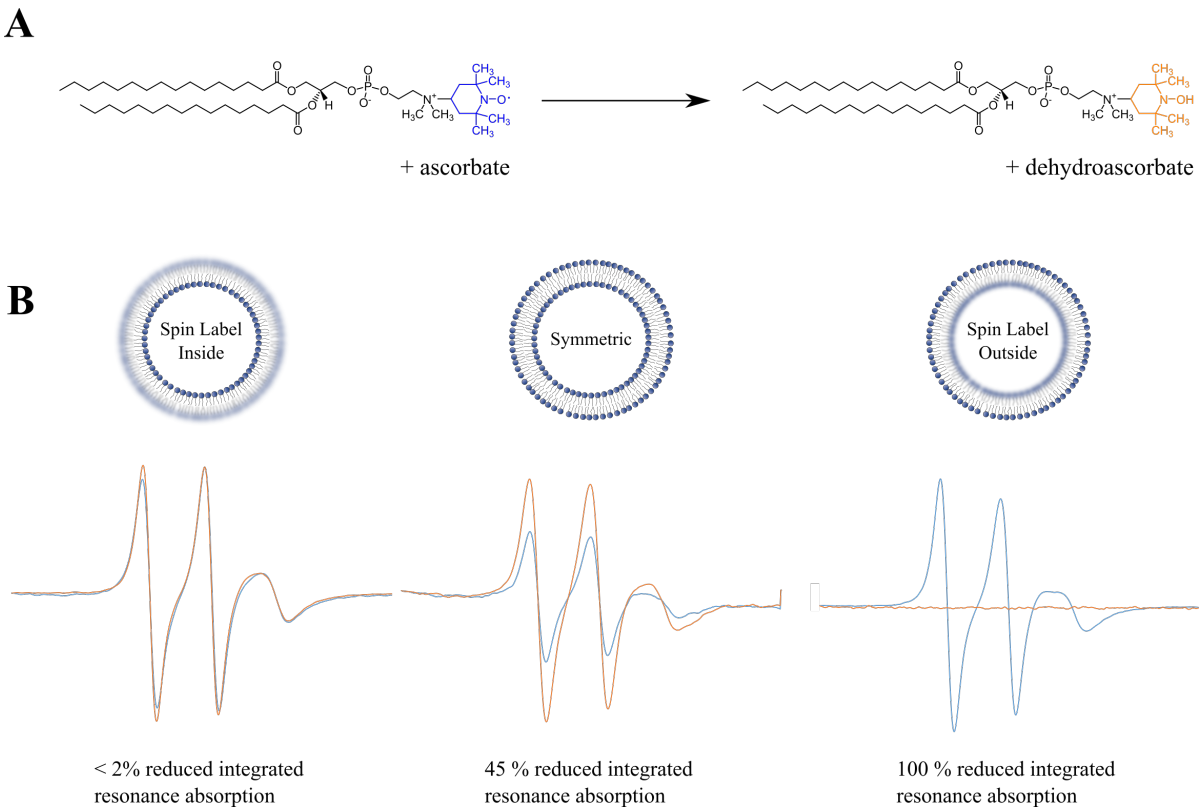

Figure 4.16 A: Reaction scheme of the reduction of TEMPO-DPPC (HG-SL) by ascorbic acid. **B:** EPR spectra of HG-SL before and after addition of 0.35 M ascorbic acid at 0 °C to POPC LUVs with 1.5 % HG-SL. When the spin-labels were on the inner leaflet (*left*) the ascorbate could not permeate the bilayer to cause quenching. When they were all situated on the outer leaflet (*right*) all spin-labels were quenched. Roughly half the spin-labels were quenched in the symmetric control (*centre*).

When liposomes were prepared with HG-SL in the inner leaflet, integrated absorption EPR intensity was more than 98% of the untreated sample, confirming success of the asymmetric liposome preparation. The converse was true when asymmetric liposomes were prepared with HG-SL in the outer leaflet; all spins were quenched. The intermediate case was observed with the symmetric control.

With the success of asymmetric spin-labelled liposome preparations established, peptides were added to attempt to discern leaflet-specific peptide-lipid interactions.

Helix-8

The effect of a peptide bearing the sequence S373-C388 of helix 8 of the NTS1 receptor (h8p) on acyl chain order of POPC model membranes was examined using EPR (Figure 4.17).



Figure 4.17 EPR spectra of symmetrically- and asymmetrically- labelled POPC LUVs (1.5% spin-label), with and without h8p (peptide:lipid MR 1:10). The apparent parameters were calculated from the two hyperfine splittings, $A_{\parallel}$ and $A_{\perp}$, which were read off from the EPR spectra. Pairs of spectra were normalised to each other, as amounts loaded into glass capillaries for measurement differed due to small sample volumes.

Large unilamellar vesicles (100 nm) were formed, with a DOXYL-PC spin label specifically installed in either the outer of inner leaflet of the vesicle, produced *via* MβCD-

mediated lipid exchange [262]. EPR spectra were recorded in the absence and presence of H8 peptide (peptide:lipid MR 1 : 5), and the apparent order parameters S_{app} , derived from the hyperfine splittings of the spectra, were calculated (Table 4.5).

	Symmetric (**+h8p**)	Inner (**+h8p**)	Outer (**h8p**)
5-PCSL	0.528 (**0.560**)	0.537 (**0.542**)	0.517 (**0.594**)
12-PCSL	0.170 (**0.197**)	0.187 (**0.189**)	0.179 (**0.186**)
14-PCSL	0.130 (**0.132**)	0.135 (**0.136**)	0.121 (**0.126**)

Table 4.5 EPR order parameters calculated for asymmetrically-labelled POPC LUVs in the absence and presence of Helix-8 peptide (P:L 1:10).

In the absence of h8p, the inner leaflet spin labels were slightly more ordered than the outer leaflet labels, with the symmetric case having an intermediate value. This may reflect the tighter packing of the inner leaflet due to curvature stress, or an effect of the sucrose inside the vesicle, thus restricting amplitude of motion.

The greatest increase of S_{app}, indicating decreased motional freedom, was observed in the peptide-accessible outer leaflet of the model membrane compared to the peptide-inaccessible inner leaflet. The greatest increase was observed with 5-PCSL, closest to the external headgroup region. A more modest increase was observed at the 12- and 14- position of the outer leaflet. Little change in ordering was observed at the 5-, 12-, and 14- positions of spin labelled lipids residing in the inner leaflet.

These data suggest that the interaction of h8p, composed of S373-C388 from the NTS1 sequence, with uncharged model membranes, is primarily via surface interactions, causing a reduction in lipid mobility close to the headgroup region. The asymmetry of the order parameters across the membrane suggests that in LUVs of this lipid composition, H8 does not insert as a transmembrane peptide. The absence of a significant ordering of the inner leaflet also suggests that the peptide does not cross the membrane to interact with the inner surface of the vesicle.

Interactions of WALP-23 with asymmetric liposomes

The effect of a peptide that inserts transmembrane into POPC membranes was subsequently investigated. To ascertain if WALP-23 interacted with POPC membranes, the fluorescence of the tryptophan amino acids in WALP was monitored in the absence and presence of POPC LUVs (peptide:lipid MR 1:25). The intrinsic fluoresence of tryptophan is sensitive to changes in the polarity of the environment in which it is situated [263]. The maximum wavelength of fluorescence decreases (blue-shift) in more hydrophobic environments, and can thus detect binding of a peptide to a liposome. When POPC LUVs were added to WALP-23 in buffer (P:L 1:25), a decrease of maximum fluorescence wavelength from 355.5 nm to 352 nm was observed, indicating WALP-23 was binding to the LUVs (Figure 4.18).

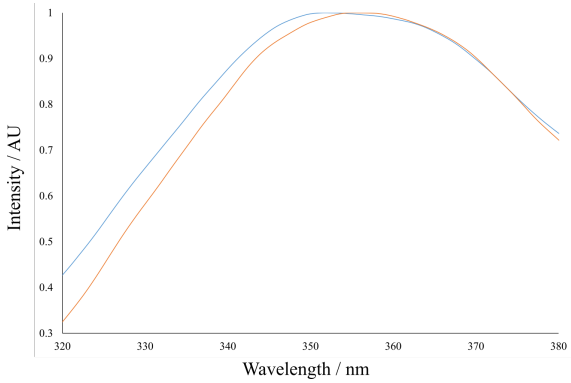

Figure 4.18 Instrinsic tryptophan fluorescence of WALP-23 in the absence and presence of POPC LUVs (P:L 1:25).

The changes induced by WALP-23 on the order parameters of spin-labels in asymmetric vesicles were next explored, as shown in Figure 4.19, and changes in order parameters were derived (Table 4.6).

Despite previous intrinsic fluoresence experiments showing WALP-23 interacting with and presumably inserting transmembrane into POPC LUVs at peptide:lipid ratios of 1:25, no changes of statistical significance were observed at any positions, in either leaflet, or in symmetric liposomes (Figure 4.19). These data suggest that upon insertion into membranes of 26.5 Å hydrophobic thickness [216], the transmembrane

	Symmetric (+**WALP-23**)	Inner (+**WALP-23**)	Outer (+**WALP-23**)
5-PCSL	0.540 (**0.535**)	0.540 (**0.540**)	0.520 (**0.523**)
12-PCSL	0.172 (**0.174**)	0.187 (**0.186**)	0.185 (**0.184**)
14-PCSL	0.130 (**0.134**)	0.126 (**0.128**)	0.125 (**0.125**)

Table 4.6 EPR order parameters calculated for asymmetrically-labelled POPC LUVs in the absence and presence of WALP-23 (P:L 1:25)

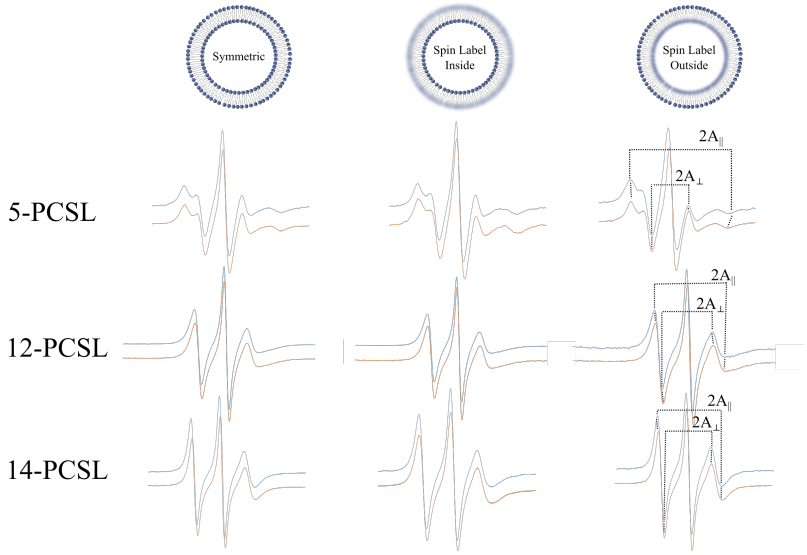

Figure 4.19 EPR spectra of symmetrically- and asymmetrically- labelled POPC LUVs (1.5% spin-label), with and without WALP-23 (peptide:lipid 1:25). The apparent parameters were calculated from the two hyperfine splittings, $A_{\parallel}$ and $A_{\perp}$, which were read off from the EPR spectra. Pairs of spectra were normalised to each other, as amounts loaded into glass capillaries for measurement differed due to small sample volumes.

orientation of WALP-23 peptide had a minimal effect on lipid dynamics. Another possibility is that the peptide was interacting with the hydrophobic cavity of residual cyclodextrin that was not removed in the purification process. However, this was ruled out by intrinsic tryptophan fluoresence of WALP-23 showing no change upon addition of cyclodextrin at peptide:cyclodextrin molar ratios of 1:1, 1:10 and 1:100 (Figure 4.20).

With two extremes of association with lipid membranes examined, tilamin and chom were added to asymmetric vesicles with the aim of obtaining additional information on their interactions with anionic model membranes.

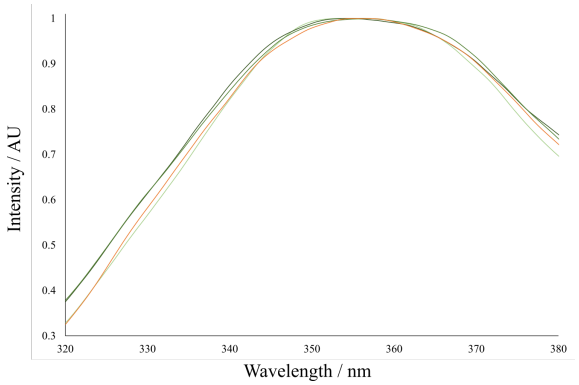

Figure 4.20 Instrinsic tryptophan fluorescence of WALP-23 in the absence (orange) and presence Mβ-CD at P:L molar ratios of 1 : 1 (light green), 1 : 10 (green) and 1 : 100 (dark green).

Interactions with tilamin and chom

To assess leaflet-peptide interactions with asymmetric model membranes, cw-EPR experiments were carried out with tilamin and chom added to POPC : PG (8:1) LUVs. Despite multiple attempts, asymmetric POPC:PG (3 : 1) LUVs could not be formed, precluding direct comparison with previous ssNMR data performed in liposomes of this constitution. It was not possible to separate acceptor LUVs from donor MLVs in any percentage of sucrose solution. The greater anionic character of 3:1 POPC:POPG membranes appeared to make MLVs far more capable of being pelleted. However, in the least dense sucrose solution (22%) that did not pellet the donor MLVs, the acceptor LUVs did not pellet either.

The changes induced by tilamin and chom on the order parameters of spin-labels in asymmetric vesicles are shown in Figure 4.21.

Unequal changes in S_{app} across both leaflets were observed for both tilamin and chom interacting with 8:1 POPC:POPG asymmetric membranes. An ordering effect occurred in the headgroup region (at the 5- position along the acyl chain) of the outer leaflet of the anionic model membrane upon addition of both peptides, while little interaction was seen with the inner leaflet. A more complicated picture emerged at positions closer to the hydrophobic core of the membrane. In the case of tilamin, a

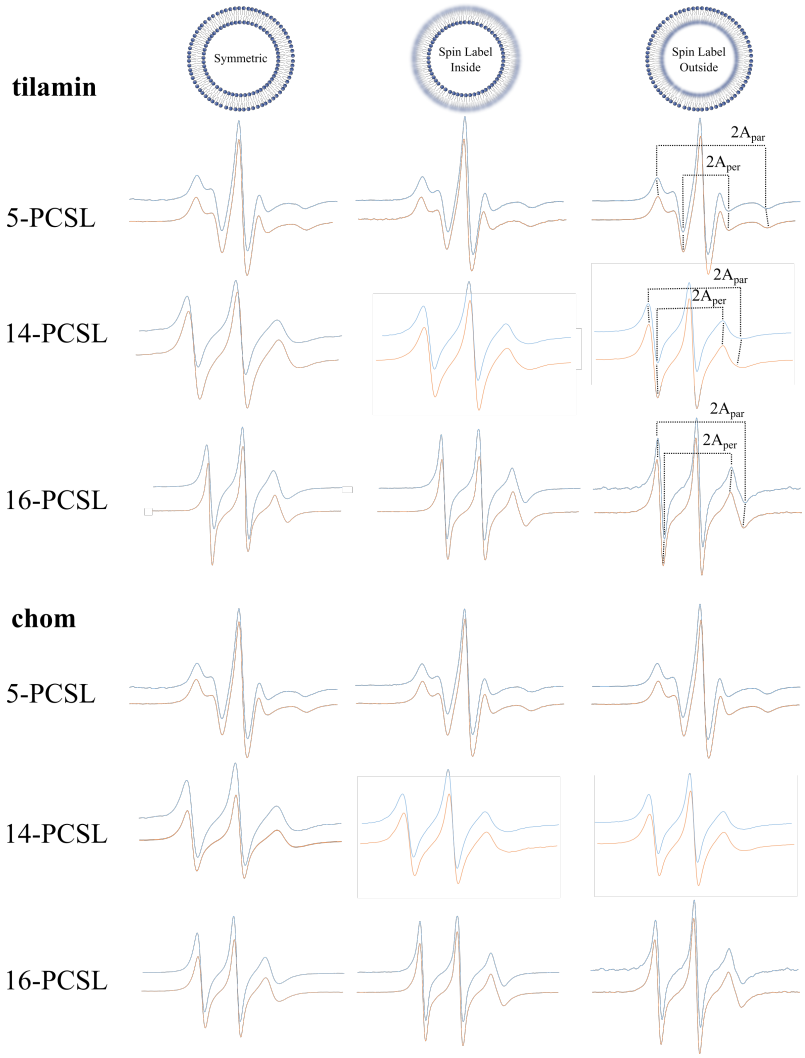

Figure 4.21 EPR spectra of symmetrically- and asymmetrically- labelled POPC LUVs (1.5% spin-label), with (orange) and without (blue) tilamin (top) and chom (bottom) (peptide:lipid 1:25). The apparent parameters were calculated from the two hyperfine splittings, $A_{\parallel}$ and $A_{\perp}$, which were read off from the EPR spectra. Pairs of spectra were normalised to each other, as amounts loaded into glass capillaries for measurement differed due to small sample volumes.

significant disordering effect, indicating increased angular amplitude of motions, was observed at the outer leaflet 14- and 16- acyl position upon addition of tilamin. An identical disordering effect occurred on the inner leaflet 16- position, while the 14- position was unchanged.

For chom, a disordering effect was observed at the outer leaflet 14- and 16- position, while no change occurred at the outer leaflet 16- position, and an ordering effect was

observed at the inner leaflet 16-position (Table 4.7). For the symmetric controls, the magnitude of changes were similar to that of other pore forming peptides, studied with cw-EPR [197].

5-PCSL	Lipid Only	+tilamin (P:L 1:25)	+chom (P:L 1:25)
Symmetric	0.594	0.620	0.616
Inner	0.603	0.601	0.604
Outer	0.578	0.614	0.606
14-PCSL	Lipid Only	+tilamin (P:L 1:25)	+chom (P:L 1:25)
Symmetric	0.248	0.248	0.252
Inner	0.247	0.247	0.266
Outer	0.266	0.254	0.254
16-PCSL	Lipid Only	+tilamin (P:L 1:25)	+chom (P:L 1:25)
Symmetric	0.137	0.134	0.135
Inner	0.135	0.129	0.141
Outer	0.135	0.129	0.135

Table 4.7 EPR order parameters calculated for asymmetrically-labelled POPC:POPG (8:1) LUVs in the absence and presence of AMPs tilamin and chom (P:L 1:25).

In combination with the QCM and ssNMR data, these results indicate that chom interacted with the anionic model membranes in a carpet-like manner. The data also suggests that a transmembrane orientation was not being adopted by either peptide.

From the lack of symmetry across leaflets, a toroidal pore, whereby the peptides tilt into the membrane and cause lipid-lined pores, is also not consistent with these findings in combination with ssNMR and QCM data from the previous chapter.

Ordering effects were seen on the EPR timescale, compared with disordering perturbations observed on the ssNMR timescale (Section 3.3.3). This could be due to broader reordering on the μs timescale, causing lipid acyl chain clustering which restricts amplitude of motion on the ns timescale. The presence of a nitroxide label may also have perturbed the hydrophobic core, an effect not present in ssNMR.

4.4 Discussion

The aims of this chapter were to extend the scope of asymmetric model membranes, to study leaflet specific peptide-lipid interactions, and to form more native like model membranes.

Formation of novel Gram-negative membrane mimetics

The asymmetry protocol allowed installation of a fluorescent molecule into specific leaflets of a model membrane. Quenching of fluorescence by iodide ions provides a fast, reversible and non-destructive way to assess this asymmetry, and is a useful technique to assess leaflet distributions of fluorophores in vesicles, and is very sensitive to size and lamellarity. The asymmetric distribution of LPS also proved to be important, affecting the ability of an antimicrobial agent to induce leakage from a model membrane compared to previously reported methods. The cyclodextrin-mediated asymmetric model membrane formation method allows production of such vesicles, and can be prepared in large quantities, which should render them attractive future candidates as Gram-negative membrane mimics.

The ability to incorporate LPS, a structurally very different molecule to phospholipids, suggests that cyclodextrin is a versatile amphiphile transporter, and that the requirements for lipid transfer appear to be an acyl chain which can be held in the hydrophobic core of the cyclodextrin structure. However, at the same time the precise conditions to obtain asymmetric liposomes seem to vary depending on lipid headgroup identity. It was not possible to form asymmetric POPC:POPG (3:1) LUVs which commonly mimic bacterial membranes. In addition, brain polar lipid extract (BPL) is often used in the study of membrane proteins such as NTS1 due to being directly extracted from native membranes (the lipid composition is given in Table 4.8) [264]. However, attempts to form asymmetric vesicles containing BPL also failed; separation of acceptor LUVs and donor MLVs was again not possible. The large unknown lipid content (referenced as such by Avanti Ltd., Table 4.8) may interfere with lipid extrac-

Lipid Type	PC	PE	PI	PS	PA	Unknown
Wt/wt %	12.6	33.1	4.1	18.5	0.8	30.9

Table 4.8 The lipid composition of brain polar lipid (data obtained from www.avanti.com)

tion by cyclodextrin. Indeed when the lipid composition becomes more complex, it also becomes difficult to fully characterise the lipid make-up of each leaflet.

EPR on asymmetric model membranes to probe the mode of action of antimicrobial peptides

Asymmetric changes in the bilayer apparent order parameter, S_{app}, were observed across model membranes in the presence of h8p, which interacts with the surface of model membranes, while interactions with tilamin and chom were more complex. WALP-23, which inserts transmembrane, did not cause any perturbation on this timescale. Success in separating leaflet-specific effects are an important improvement on conventional model membranes, and may require a reappraisal of conclusions drawn from symmetric systems. However, the reporter system for a transmembrane case may need to be modified, as the lack of effect of WALP-23 induced by WALP, while confirmed by tryptophan fluorescence to be interacting with the membrane, may be unseparable from lack of binding in other cases where fluorescence or CD cannot confirm peptide insertion. In addition, certain antimicrobial peptides are known to induce lipid flip-flop [265], which would abrogate lipid asymmetry, and this must be carefully controlled by quenching experiments.

The findings of this chapter indicate that previous EPR and NMR studies on AMPs with symmetric vesicles give averaged results and changes, thereby not discriminating insights into the bilayer-specific peptide-lipid interactions that predicate bactericidal activity, and the preparation of asymmetric vesicles go some way to address this subtlety of interaction.

The data gave further evidence that chom was acting *via* the carpet mechanism. Further evidence was also provided that tilamin may be perturbing the bilayer *via* a new mode of action: the monolayer poration model, which is described here. The toroidal pore model is less likely in the light of the asymmetric AMP-lipid interactions, as the inner leaflet of the model membranes was unaffected. This supports findings from other researchers; geometric analysis of labelled alanine (GALA) ssNMR experiments [266] performed on tilamin showed that the AMP inserted into membranes with an overall tilt of 70° relative to the membrane normal (Figure 4.22) [197]. Projected onto the membrane normal, for a peptide of helical length 3.5 nm, this would correspond to a depth of insertion of 1.6 nm, which was further corroborated by pores of this depth being observed on DLPC:DLPC (3:1) SLBs by atomic force microscopy (Figure 4.22).

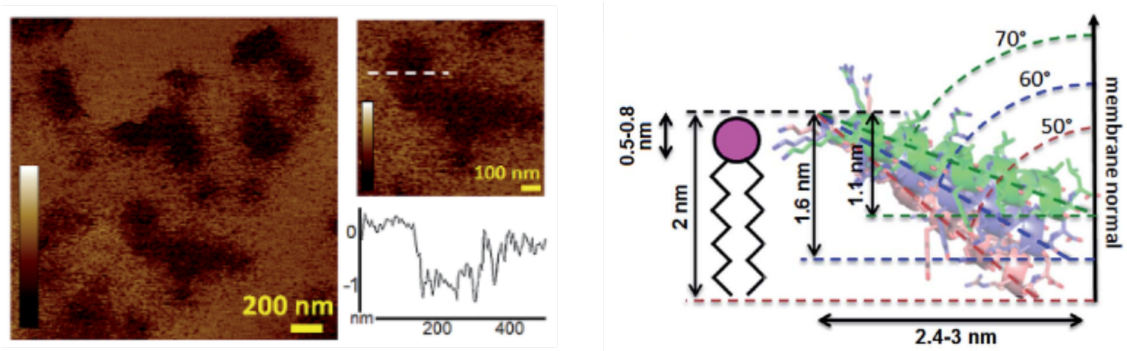

Figure 4.22 AFM images (*left*) on DLPC:DLPG (3:1) SLBs showing pores of 1.6 nm induced by tilamin, and peptide tilt angles for ^{2}H labelled-alanines on tilamin (*right*) of 70^{0} in POPC:POPG (3:1) give further evidence of monolayer poration. AFM images obtained by A.Pyne (University College London), ssNMR GALA analysis performed by M.Pfeil (University of Oxford).

Figure 4.23 summarises the evidence supporting this mechanism from the work in this and preceding chapters, as well as work carried out from collaborators [197].

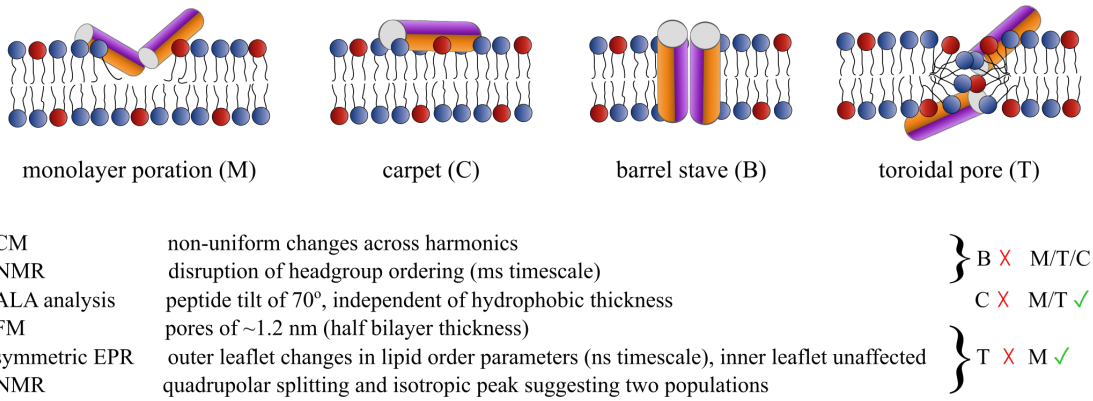

Figure 4.23 Summary of biophysical characterisation of tilamin, which taken in combination suggest a new mode of action.

Implications for biological activity

The monolayer poration mechanism of action has properties that render it an attractive target for future design, and may be adapted in nature by other, uncharacterised AMPs. As opposed to internalisation to effect intracellular targets, monolayer poration can occur on a faster timescale ($\backsim$ 5 min as seen from QCM and calcein leakage) at a site of infection, which would avoid or minimise proteolytic degradation of the AMP. In addition, in contrast to full bilayer-spanning pores, which could be assuaged by lipid flip flop to change surface lipid composition [265] or pore resealing [107], it could be more difficult for a pathogen to adapt to this form of attack.

The techniques used in this thesis were next applied to a related system of membrane active proteins that share many structural features of the AMPs studied thus far: puroindolines.

Chapter 5

Biophysical Investigations into Puroindoline-b

5.1 Introduction

5.1.1 The puroindolines

Wheat is the most widely grown crop in the world, covering the largest amount of the Earth's surface compared to any other crop [267]. Despite being known for gluten-foaming properties, it is primarily categorised by the hardness of the grain (specifically the texture of the wheat endosperm), which dictates the end use in food and agriculture. Soft wheats are used in the productions of cakes and cookies, harder wheats for making bread, and very hard types, such as durum wheat, for producing pasta. The genetic basis for wheat hardness has been found to depend on the *Hardness* gene, located on the short arm of chromosome 5D of the hexaploid genome [268].*

The Hardness gene encodes for two protein isoforms that are present on the surface of soft wheats, puroindoline-a and -b (pinA and pinB), first isolated using TX-114 phase partioning [270]. The pins are basic, ~13 kDa proteins that share ~ 60% homology. IR studies have shown they are comprised of approximately 30% alpha-helices, 30% beta-sheets, and 40% unstructured regions at pH 7 [271], with the protein structure stabilised by four disulfide bonds [272]. Both isoforms share a distinctive tryptophan-rich loop domain (TRD).† Tryptophan typically comprises ~ 1% of protein primary structure, but constitutes 4.3 and 3.4% of total residues of pinA and

*There are also loci of more minor effect, and environmental variables that affect hardness [269], but the *Hardness* gene is the major effect locus.

†The name puroindoline is derived from the greek for wheat, *puros*, and the TRD shared by both proteins.

pinB respectively, in which tryptophan residues are wholly or mainly located within the TRD [273], suggesting they have a role as membrane-bound or -binding proteins [274]. The sequences of the TRD of pinA, pinB and a W44R mutant of pinB are shown in Figure 5.1.‡

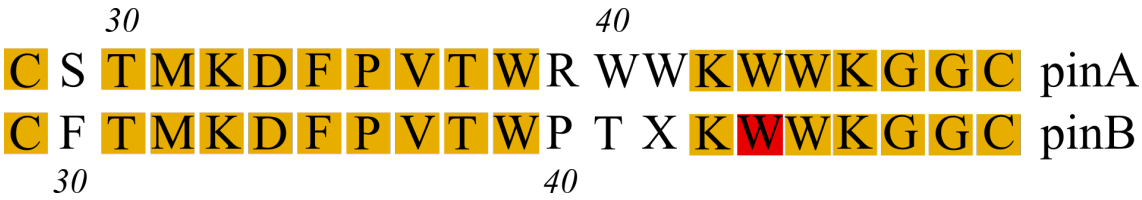

Figure 5.1 The primary sequences of the cysteine-enclosed tryptophan loop of pinA and pinB [271]. X represents a truncation of the sequence. Sequence identities are shown in yellow. A point mutation of W44 (shown in red) to R in the pinB sequence gives pinBs, a mutant studied in this chapter.

The biological function of the pins is currently not well understood, and several roles have been proposed. The pins are thought to serve a function in plant seed defence; transgenic rice that was engineered to express pinB shared elevated resistance to fungal infections compared with hard wheat [275]. Additionally, expression of pinB in durum wheat strains, naturally lacking both puroindoline isoforms, have shown elevated embryo and endosperm resistance to *Penicillium sp.* [276]. Due to the antimicrobial potential of the pins, peptides based on the TRD of pinB and related mutants have also been constructed [145]. The peptides were shown to cause leakage in cell membranes and display bactericidal activity *in vitro*, and were posited from TEM imaging to operate *via* the carpet mechanism [95]. The antimicrobial activity of peptides based off the TRD of pins seems sensitive to single point mutations; an R39G mutation of a pinA peptide displayed a four-fold decrease in the measured MIC [145].

It is also thought that the proteins could control endosperm texture by modulating interactions between starch and wheat protein matrix [277, 278]. Indeed, expression of wild type (WT) pinB§ occurs in soft wheat varieties, while point mutations within

‡The full sequence of pinA and pinB can be found in the appendix.
§When WT pinB is specifically referred to it is designated pinB+.

or near the TRD (G46S and W44R, and L60 respectively) or an absence of the protein have been found in harder wheat varieties [279, 280]. To date, seven separate alleles have been found that code for different mutants of pinB and are associated with differences in wheat hardness [281].

To date, biophysical studies on the mode of insertion of WT and a W44R mutant of pinB (pinBs)[‖] have been restricted to monolayers at the air-water interface [282]. Pressure-area isotherms of binary phospholipid mixtures showed phase separation induced by the proteins [283], which was also observed by Brewster angle microscopy [284]. Fourier-transform infra-red spectroscopy revealed that protein absorption was dependent on the presence of anionic lipid in the monolayer [285]. Surface-pressure measurements showed WT pinB (pinB+) penetrated more deeply into the hydrophobic part of the monolayer than pinBs [285], which was probably promoted by hydrophobic interactions with the additional tryptophan (Figure 5.2), compared to the substitution of arginine in pinBs favouring membrane adsorption.

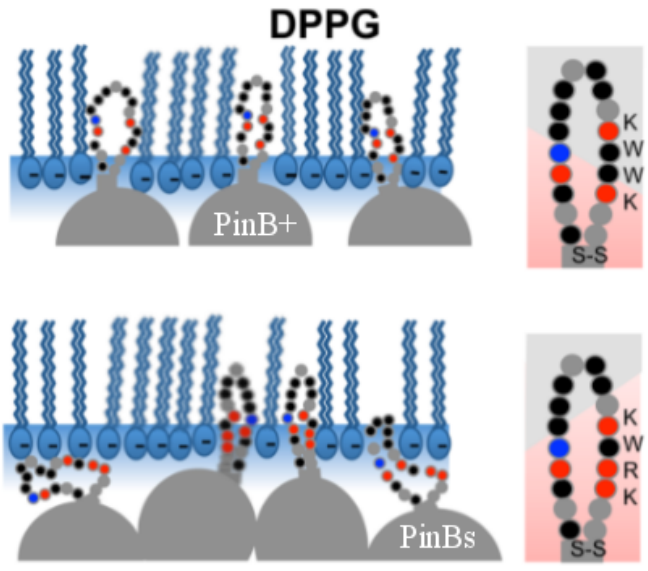

Figure 5.2 Schematic showing the different binding characteristics of pinB and pinBs on a DPPG monolayer. Hydrophobic, cationic and anionic residues are represented respectively by grey, red and blue spheres. Schematic reproduced from [285].

[‖]So named as it is isolated from Soissons wheat [272].

While revealing valuable insight into the lipid specificity and binding behaviour of pinB, the success of monolayers in recreating the properties of natural membranes is debated [286]; floating monolayers necessarily cannot mimic the intrinsic properties of a full lipid bilayer such as internal bilayer pressure, interleaflet coupling or membrane curvature. Therefore there is a need to characterise the pins in more biologically relevant model membranes to better understand their function in nature.

5.1.2 Aims of chapter

The implications of the WT and mutant forms of pinb in controlling wheat endosperm texture and potential antimicrobial defence are of interest due to the similarities with AMPs. The tryptophan rich loop (TRD) appears to be strongly implicated in lipid binding and potential membrane interactions. To date this has only been in explored in relatively simple monolayers that cannot recreate the complexities of real cell membranes.

In order to understand better the interactions of the pinb TRD with more native-like membranes, WT pinB+ and W44-R44 mutant pinBs are investigated with supported lipid bilayers and vesicles, in the gel- and fluid phase. Attempts are made to establish the mode of interaction and lipid-specificity of pinB compared to pinBs, with an aim evaluate the importance of the point mutation in bilayer pertubation, using ssNMR, EPR and NR.

5.2 Materials and methods

5.2.1 Extraction and purification of pinB+ and pinBs

Extraction of crude pinB

Following an established procedure [284], which was adapted from [287] WT pinB (pinB+) and the W44R mutant (pinBs) were extracted from Claire-type wheat and Soissons-grade wheat, respectively.

500 g of wheat was suspended in 2.5 L of PEK buffer (Sodium phosphate 50 mM, EDTA 5 mM, KCl 5 mM, pH 7.6), and stirred mechanically for 1 h at 4 ℃. The resulting suspension was centrifuged (3,500 g, 4 ℃, 10 min), using a Thermo Scientific Sorvall Evolution RC Superspeed centrifuge. The supernatant was discarded, and the pellet solubilised with triton x-114 (4% v/v in 2.5 L PEK buffer) for 1 h. The suspension was centrifuged (13,000 g, 4 ℃, 10 min), the pellet discarded, and the retained supernatant acidified to pH 4.5 with glacial acetic acid (50 mM). To the solution was added carboxy-methyl cellulose (24 g), and the resulting suspension left to stir overnight.

The suspension was centrifuged at 13,000 g, at 4 ℃ for 10 min, and the supernatant discarded. The pellet was washed twice with glacial acetic acid (50 mM) and centrifuged three times at 13,000 g, at 4 ℃ for 10 min. The pellet was resuspended in acetic acid (200 mL, 50 mM, with 1 M NaCl) for 1 h at 4 ℃. The carboxy-methyl cellulose was removed by filtration under vacuum. The filtrate NaCl concentration was increased to 4 M. The suspension was centrifuged (13,000 g, 4 ℃ 10 min). The supernatant, containing purothionins, was discarded. The puroindoline rich pellet was dissolved in 50 mM acetic acid (2 mL), and dialysed for 48 h in 50 mM acetic acid (5 L). The dialysate was then lyophilised overnight to furnish the crude product.

Purification of pinB+ and pinBs

50 mg of protein was dissolved in 1 mL of 3:1 (*v*/*v*) 50 mM ammonium acetate: acetonitrile (pH 5.5) at 37 ºC and aggregates were removed by centrifugation (15,000 g, 5 min, 40 ℃). The proteins were purified *via* cation exchange chromatography using a preparative Mono-S HR 16/10 column (PharmaciaBiotech UK, Buckinghamshire, U.K.) and a BioCad Sprintperfusion chromatography system (Global Medical Instruments, Minneapolis, MN)18. The CMC-bound protein fraction was eluted with a gradient elution of 3:1 (*v*/*v*) 50 mM Ammonium Acetate :Acetonitrile (pH 5.5) to 3:1 (*v*/*v*) 1 M Ammonium Acetate: Acetonitrile (pH 5.5), at a flow rate of 1.8 $mLmin^{-1}$ over 2.5 h.

5.2.2 Solid-state NMR

Headgroup-deuterated lipids were synthesised as described in Section 3.3.1. DMPE-d_4:DMPG (3:2) and DMPE:DMPG-d_2 (3:2) MLVS were prepared as outlined in Section 2.2.1. PinB+ or pinBs from a concentrated stock (> 10 mg mL^{-1}) were added directly to the lipid dispersion. Samples were loaded into a 4 mm NMR MAS rotor by centrifugation (2000 RPM, 1 min) through a 1 mL pipette tip.

Static ssNMR experiments were performed on 800 MHz Infinity plus wide bore spectrometer, equipped with 4 mm HXY probes at 45 ℃. ^{2}H Spectra were acquired at 122.78 using a quadrupole echo sequence with a 4 µs 90° pulse, a 50 µs refocusing delay and a recycle delay of 0.5 s. The spectra were then left-shifted to the echo maximum.

5.2.3 TEMPO Partitioning

Sample loading

MLVs of DPPE:DPPG (3:2) and DPPG were prepared as described in Section 2.2.1 in 20 µL HEPES bufffer (20mM, pH 7.0) at 45 ℃, to a concentration of 40 mg mL^{-1}. PinB+ or pinBs was added from a > 10 mg mL^{-1} stock to give a P:L ratio of 1:100. 2, 2, 6, 6-tetramethyl-piperidine-1-oxyl (TEMPO) was added to the sample (TEMPO:Lipid *mol/mol* 120:1), and the sample centrifuged (100,000 g, 3 h, 20 ℃). The pelleted liposomes and protein were then loaded into a 0.5 mm glass capillary (Sigma-Aldrich), which were flame-sealed from one end. The capillaries were centrifuged (1,000 g, 1 min).

Spectra were acquired on an X-band CW spectrometer (Bruker EMX, Xenon software) with 9 GHz X-band Super High Sensitivity Probehead (Bruker), as described in Section 4.2.9.

Partitioning factor calculation

The TEMPO spectrum is a composite of a contribution from spin-label in the hydrophobic (H) membrane environment, and from the aqueous, polar (P) environment, which can be resolved in the high-field part of the spectrum (Figure 5.3).

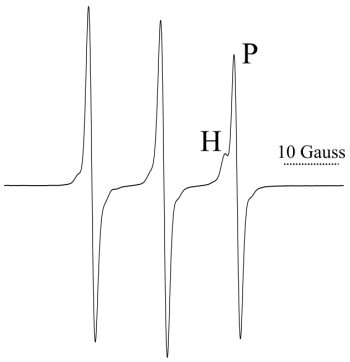

Figure 5.3 TEMPO EPR spectrum in a DMPE:DMPG (3:2) MLV dispersion. The high field component contains contributions from a hydrophobic (H) and polar (P) environment, from which a partioning factor can be calculated as described below.

To a first approximation [288, 289], H is proportional to the amount of TEMPO in a membrane environment, while P is proportional to the amount in an aqueous environment. The partioning factor is then calculated according to

$$f = \frac{H}{H+P}. \tag{5.1}$$

5.2.4 Neutron reflectivity

Bilayer Deposition

Supported bilayers for neutron scattering were composed of inner leaflet - hydrogenous DPPC (referred to in this chapter as hDPPC) or DPPC-d_{62} (referred to in this chapter as dDPPC) and outer leaflet - DMPG-d_2:DMPE-$_4$ (2:3). The inner leaflet was composed of DPPC due to reliable binding to the silicon surface [290]. The bilayer was deposited on the Piranha-cleaned (H_2SO_4:30% H_2O_2 *v/v*) SiO_2 surface of single silicon crystals using a Langmuir-Blodgett (LB) trough (KSV-Nima, Biolin Scientific, Finland), under ambient conditions.

The silicon crystal was submerged in the LB trough, filled with $CaCl_2$ solution (5 mM). The inner hDPPC/dDPPC monolayer was deposited using the Langmuir-Blodgett method [291]. dDPPC/hDPPC (5 mg) was dissolved in $CHCl_3$:MeOH (*v*/*v* 3:1) to a final concentration of (1 mg mL^{-1}). The lipid solution was then deposited onto the clean air-liquid interface of $CaCl_2$ solution and compressed to 31 mNm^{-1}. The submerged silicon crystal was then raised through the air-liquid interface at a speed of 3 mm min^{-1} while the surface pressure was kept constant. The LB trough was cleaned with MeOH, dried then refilled with $CaCl_2$ (5 mM) solution.

The outer leaflet DMPG-d_2:DMPE-$_4$ (2:3) monolayer was deposited using the Langmuir-Schaefer (LS) method [292]. DMPE-d_4:DMPG-d_2 (3:2) was dissolved in $CHCl_3$: MeOH (*v*/*v* 3:1) to a final concentration of (1 mg mL^{-1}). The lipid solution was deposited dropwise onto the clean air-liquid interface of $CaCl_2$ solution (5 mM) and compressed to 31 mNm^{-1}. The silicon crystal, containing the LB-deposited DPPC/dDPPC monolayer, was placed in a holder directly above the air-liquid interface. The angle of the crystal was adjusted to make it parallel with the surface of the air-liquid interface using a purpose-built levelling device. The silicon crystal was then dipped into the interface of the LB trough at a speed of 3 mm min^{-1}, into a purpose-built sample cell. The $CaCl_2$ was removed from the trough and the sample cell, containing the silicon crystal with inner leaflet - dDPPC or hDPPC and outer leaflet - DMPG-d_2:DMPE-$_4$ (2:3), was screw tightened, and mounted onto the NR beam apparatus for measurement.

Neutron reflectometry measurements

Specular NR measurements were performed using INTER and SURF time-of-flight reflectometers at the Rutherford Appleton Laboratory (Oxfordshire, UK), with neutron wavelengths of 0.5 – 6.8 Å and 1 – 16 Å used for SURF and INTER, respectively. The

reflected intensity was measured as a function of (Q_z) according to

$$Q_z = \frac{4\pi sin\Theta}{\lambda}, \tag{5.2}$$

where λ is the wavelength and Θ is the incident angle of the neutron beam. The collimated neutron beam was reflected from the silicon-liquid interface at different glancing angles of incidence, which were 0.35°, 0.65° and 1.5°, and 0.7° and 2.3° for SURF and INTER, respectively.

Purpose-built liquid flow cells for analysis of the silicon-liquid interface were attached to a variable-angle sample stage in the NR instrument, and connected to a liquid chromatography pump (L7100 HPLC pump, Merck, Hitachi), which allowed exchange of isotopic contrast solutions (20 mM pD 7.0 D_2O phosphate buffer, 20 mM pH 7.0 H_2O phosphate buffer, 20 mM pH 7.0/ pD 7.0 silicon-matched water (SMW, 38% D_2O) phosphate buffer) within the sample cell (3 mL total volume). For each solution contrast run, a total of 22.5 mL of a given buffer solution was flowed through the cell at a speed of 1.5 mL min^{-1} to completely exchange contrast buffer between measurements. Each condition was run in duplicate.

Neutron reflectometry data analysis

Reflectivity profiles were obtained for two sample cells measured under three-solvent isotopic contrasts to give six reflectivity profiles, shown in Table 5.1, to permit determination of the structural parameters of individual leaflets of a bilayer [293].
Neutron reflectivity profiles were concurrently analysed using RasCal software [294], a MATLAB-based application, which employed an optical matrix formalism (described in more detail elsewhere [295]) to fit layer models to the interfacial structure. In this way the interface was described as a series of slabs, each with an associated SLD, thickness and roughness. The reflectivity for the model starting point was then calculated and compared to experimental data. A least-squares minimization was im-

Inner Leaflet	Outer Leaflet	Solvent contrast
dDPPC	DMPG-d_2:DMPE-$_4$ (2:3)	20 mM pD 7.0 D_2O phosphate buffer
		20 mM pH 7.0 H_2O phosphate buffer
		20 mM pH 7.0/ pD 7.0 SMW phosphate buffer
hDPPC	DMPG-d_2:DMPE-$_4$ (2:3)	20 mM pD 7.0 D_2O phosphate buffer
		20 mM pH 7.0 H_2O phosphate buffer
		20 mM pH 7.0/ pD 7.0 SMW phosphate buffer

Table 5.1 Lipid composition and solvent contrast conditions for the NR experiments performed.

plemented to adjust the fit parameters to reduce the differences between the model reflectivity and the data. The model requiring the least layers to adequately describe the data was selected. Table 5.2 gives the SLDs for the components used in this study.

Lipid / Solvent / Protein	Neutron scattering length density ρ / 10^{-6} Å^{-2}
D_2O	6.35
SMW	2.07
H_2O	-0.56
Silicon	2.07
SiO_2	0.56
SMW	0.56
h-lipid tails	-0.39
d-lipid tails	7.45
pinB+/Bs in D_2O	3.26
pinB+/Bs in H_2O	1.91

Table 5.2 Summary of scattering length densities for the components studied and the solution subphases. Values obtained from those reported previously (Clifton2013).

The fitted results of reflectivity data obtained from dDPPC bilayers at three different solvent contrasts (100% H_2O phosphate buffer, 100% D_2O phosphate buffer, 62%/38% H_2O/D_2O phosphate buffer) were used to determine the contributions of DPPC, DMPE-d_4:DMPG-d_2 (3:2) and H_2O to the inner and outer acyl regions of the membrane, to assess asymmetry and changes upon protein binding.

Adapting a literature procedure [130], the individual components of a given layer that contribute to the scattering length density of that layer (ρ) can be determined by

$$\rho = (\rho_{lip_I}\phi_{lip_I}) + (\rho_{lip_O}\phi_{lip_O}) + (\rho_{lip_W}\phi_{lip_W}) \tag{5.3}$$

where ρ_{lip_I}, ρ_{lip_O} and ρ_W are the experimentally measured scattering length densities of inner leaflet lipid, outer leaflet lipid and solvent respectively, and $\phi_{lip_{I/O}}/W$ are the respective volume fractions. From exploiting differences in isotopic contrasts, and varying the identity of inner leaflet lipid, it was possible to determine the volume fractions of each component using Equation 5.3 to get[¶]:

$$\phi_W = \frac{\rho_{W1'} - \rho_{W2'}}{\rho_{W1} - \rho_{W2}} \tag{5.4}$$

$$\phi_{lip_I} = \frac{(\rho - (\rho_W\phi_W) - (\rho_{lip_O}(1-\phi_W)))}{\rho_{lip_I} - \rho_{lip_O}} \tag{5.5}$$

$$\phi_{lip_O} = 1 - (\phi_{Lip_I} - \phi_W) \tag{5.6}$$

where $\rho_{W1'}$ and $\rho_{W2'}$ are the scattering length densities of the same lipid composition in two different solvent contrasts, and ρ_{W1} and ρ_{W2} are the respective theoretical scattering length densities of those particular mixes.

5.3 Results

5.3.1 Purification of pinB+ and pinBs

PinB+ and pinBs were extracted following established protocols [272], purified using cation exchange chromatography, with the mass of pinBs confirmed by MALDI mass spectrometry (Figure 5.4 overleaf). Yields of 5 mg and 1 mg of pure protein *per* 130 mg crude extract were recorded for pinBs and pinB+ were obtained, respectively.

[¶]Full explanation of this derivation can be found here [296].

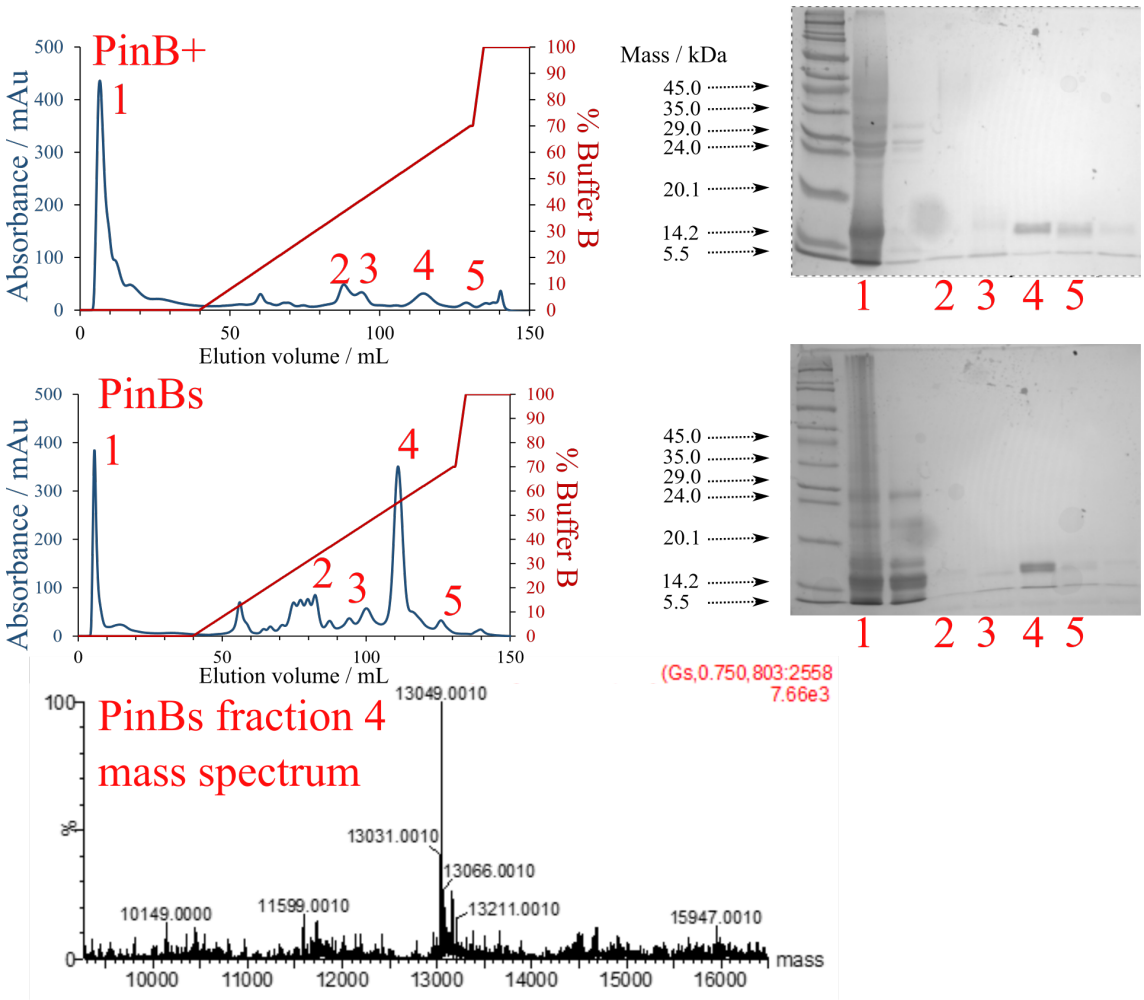

Figure 5.4 Purification of pinBs and pinB+. Elution profiles (*left*) from cation exchange chromatography for pinB+ (*top*) and pinBs (*middle*). Buffer B demarks 3:1 (*v*/*v*) 1 M Ammonium Acetate: Acetonitrile (pH 5.5). SDS-PAGE gels for the pinB fraction (4) are shown (*right*), with the mass for pinBs confirmed by mass spectrometry (*bottom*).

The interactions of the purified proteins with the headgroups of model membranes were first probed using ssNMR.

5.3.2 ssNMR investigations into lipid-protein interactions

The interaction of pinB and pinBs with the headgroup region of model membranes formed of chemically synthesised DMPE-d_4 and DMPG-d_2 was studied by ^{2}H ssNMR.

DMPE:DMPG (3:2) was chosen as a membrane mimick for the bacterial inner membrane.

Attempts were made to study the interaction of the proteins with model membranes in both gel and liquid crystal phases to discern the effect of lipid packing on protein insertion. However at 10 ℃, below the phase transition temperature of a DMPE:DMPG (3:2) MLV (transition temperature 39 ℃, assuming ideal mixing of the lipids), the quadrupolar splitting was broadened to a large degree, making it not possible to measure changes upon addition to protein (Figure 5.5).

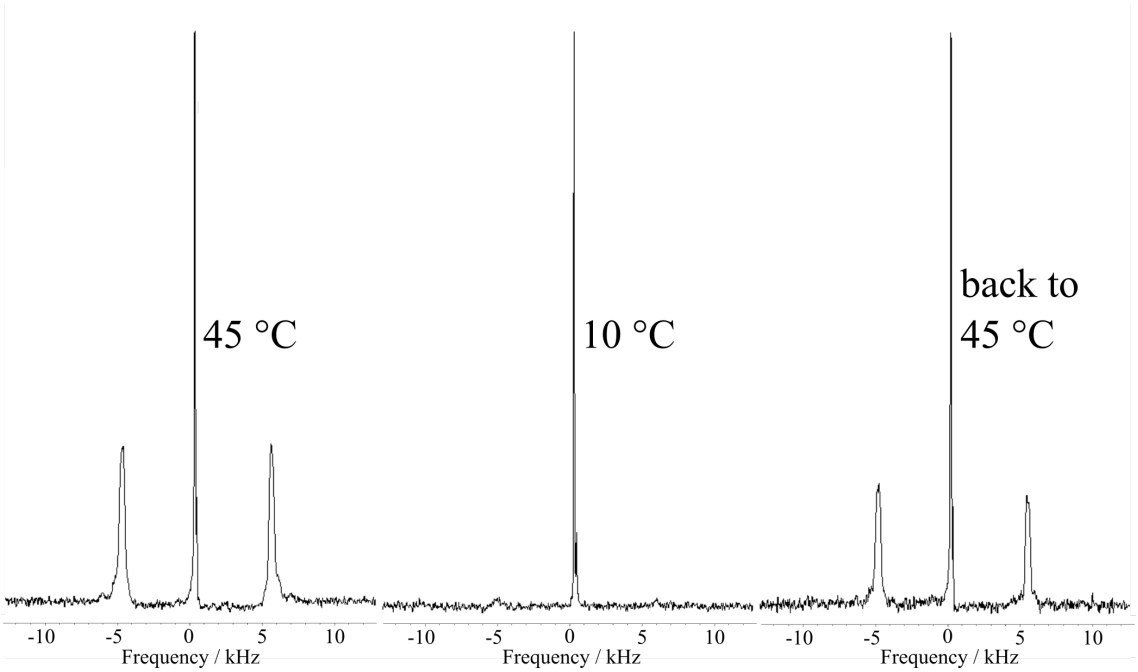

Figure 5.5 The effect of temperature (and lipid phase) on the ^{2}H ssNMR spectra of DMPE:DMPG-d_2 MLVs. The quadrupolar splitting of the DMPG-d_2 lipid was broadened significantly below the phase transition temperature, rendering it not possible to measure changes upon addition of protein.

The changes induced by the proteins were therefore studied at 45 ℃, above the phase transition temperature of the MLVs. The changes in the zwitterionic and anionic components of the MLVs induced by pinB+ and pinBs (P:L 1:100) were investigated, as shown in Figure 5.6 overleaf.

PinBs did not cause any change in the quadrupolar splittings of the zwitterionic DMPE-

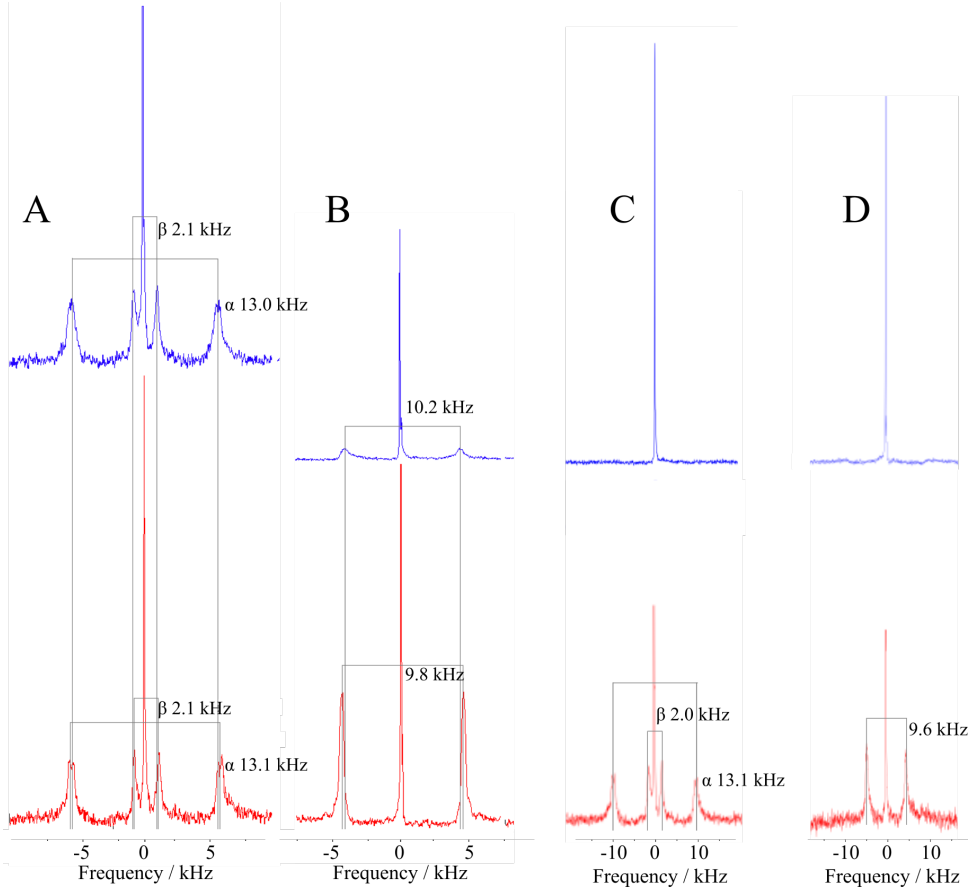

Figure 5.6 ^{2}H ssNMR spectra of DMPE-d_4:DMPG (3:2) (*A* and *C*) and DMPE:DMPG-d_2 (3:2) (*B* and *D*) MLVs in the absence and presence of pinBs (*A* and *B*) and pinB+ (*C* and *D*), at 45 °C. An error of ±2 kHz was assumed for all measurements based on literature precedent [117].

d_4 component. A reduction in the quadrupolar splitting intensity compared to the central isotropic peak was observed in the DMPG-d_2 ssNMR spectrum, suggesting partial disordering, presumably due to electrostatic interactions between the charged TRD. More marked changes were observed with the WT pinB+; the quadrupolar splittings for both components of a DMPE:DMPG (3:2) MLV collapsed to an isotropic peak, implying loss of conformational order of the headgroup region. These data indicated pinB+ interacts more strongly with fluid-phase anionic membranes compared to the point-mutated pinBs. The modest changes in the the ^{2}H ssNMR spectra of MLVs in the presence of pinBs contrasts for measurements performed on lipid monolayers, suggesting that the mode of interaction of the two proteins is sensitive to bilayer structure.

5.3.3 EPR to determine changes in membrane fluidity

TEMPO partitioning experiments were performed between 33 ℃ and 61 ℃ to evaluate membrane fluidity changes upon pinB binding below and above the gel-liquid crystal phase transition temperature (T_m) of DPPE:DPPG (3:2) and DPPG MLVs (54.2 ℃ and 41 ℃, respectively. TEMPO (Figure 1.16) can be present both in the aqueous environment and the hydrophobic interior of the bilayer, which gave two contributions to the high field part of the EPR spectrum, from which a partitioning factor f could be determined. Figure 5.7 shows the changes in TEMPO partitioning in DMPE:DMPG (3:2) MLVs induced by pinB+ and pinBs.

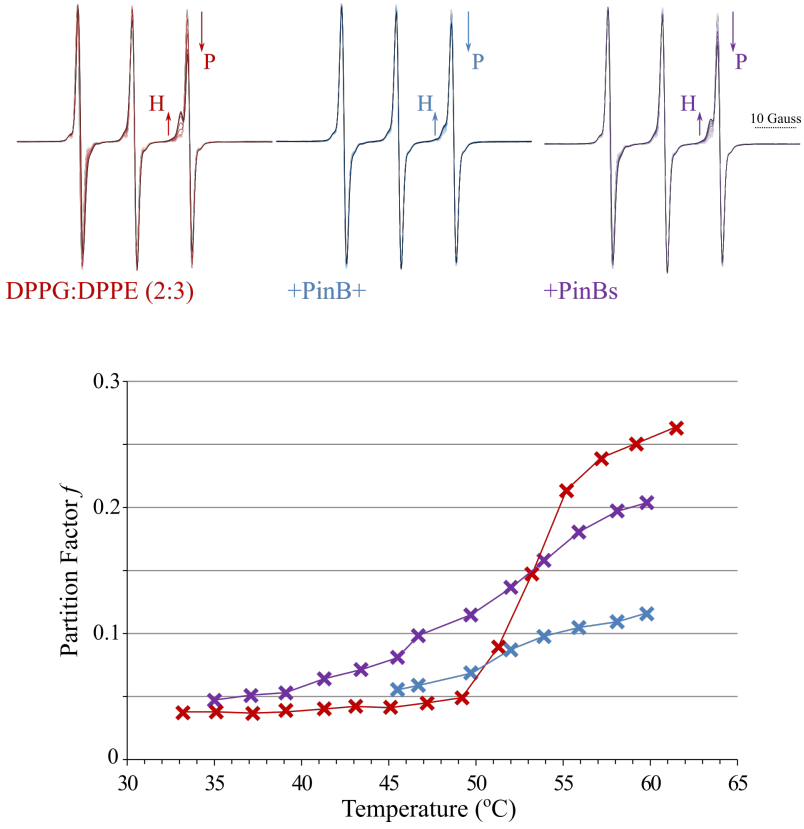

Figure 5.7 TEMPO partitioning in DPPG:DPPE (3:2) MLVs as a function of temperature, in the absence and presence of pinB+ and pinBs (P:L 1:100). The partitioning factor f was calculated from the relative intensities of the hydrophobic (H) and aqueous/polar (P) contributions to the high field part of the TEMPO spectrum.

Generally, all samples displayed an increase in the TEMPO partitioning factor f as temperature increased, as a result of increased membrane fluidity. Little TEMPO par-

tioning was observed below the transition temperature of the MLVs in the absence and presence of protein, due to TEMPO being unable to penetrate the rigid gel-phase bilayer. For the lipid-only sample, a large increase in f was observed at around 53 ℃, as the MLVs transitioned from the gel phase to the more fluid liquid-crystal phase.

The presence of pinB+ and pinBs had an effect on the transition temperature of the MLVs, and the extent of TEMPO partitioning in the liquid-crystal phase; pinBs caused an increase in f from $\backsim$ 40 ℃, and caused a decrease in f relative to the lipid-only sample, while also broadening the transition temperature for the MLVs, indicating the interaction of pinBs reduces the cooperativity of the phase transition [47]. PinB+ had a greater effect on the bilayer fluidity of the MLVs; only a gradual increase in f with temperature was observed, meaning that binding of pinB increased the lateral pressure of the DMPE:DMPG (3:2) MLVs to such an extent that the gel-liquid crystal phase boundary was nearly completely removed. The effect on bilayer fluidity for both proteins, markedly more strongly observed for WT pinB+, is similar to that of cholesterol: whereby insertion into the membrane, and disordering lipid packing in the gel phase cause an increase in fluidity, while ordering of the more chaotic acyl chain motions in the fluid phase causes a decrease in fluidity [125].

The same experiments were performed on pure DPPG bilayers (T_m = 41 ℃) to examine changes in membrane binding by the pinB proteins in a more highly charged model membrane (Figure 5.8).

Similar overall changes were observed for TEMPO partitioning in DPPG MLVs induced by pinBs and pinB+. Both proteins caused an apparent increase in the gel-liquid crystal phase transition of the bilayer, with greater changes induced by pinB+. The extent of the changes was different, however, for both MLVs; both proteins did not cause as much of a change in f compared to DPPE:DPPG (3:2) MLVs. The change in f relative to a lipid-only sample for both cases at 59.3 ℃ was calculated as shown in Table 5.3.

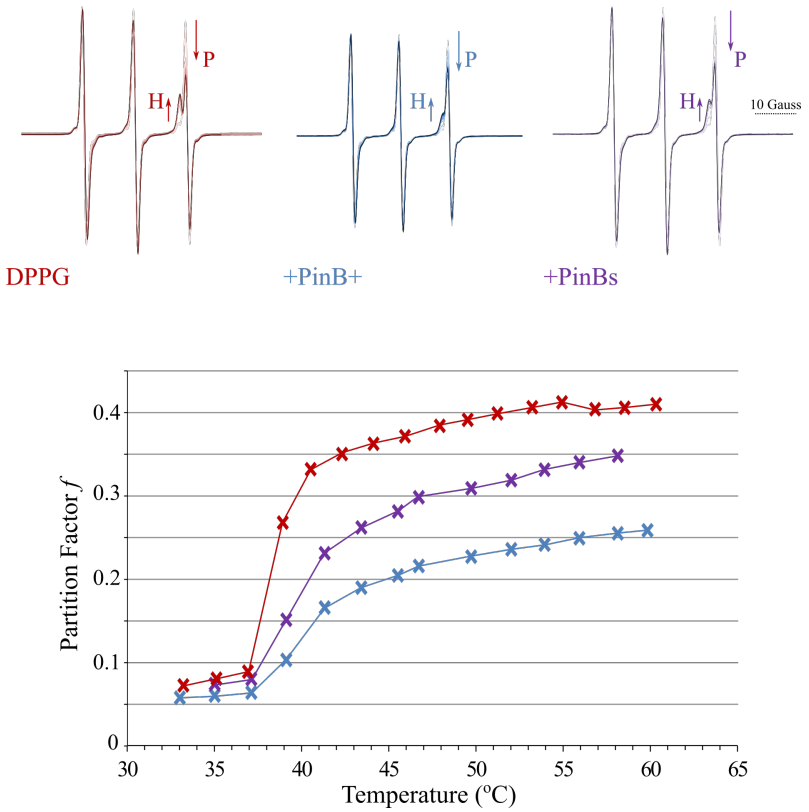

Figure 5.8 TEMPO partitioning in DPPG MLVs as a function of temperature, in the absence and presence of pinB+ and pinBs (P:L 1:100). The partitioning factor f was calculated from the relative intensities of the hydrophobic (H) and aqueous/polar (P) contributions to the high field part of the TEMPO spectrum.

	Lipid-only	+pinB+	+pinBs
DMPG	1.00	0.62	0.85
DMPG:DMPE 3:2	1.00	0.46	0.81

Table 5.3 Table summarising changes in TEMPO partitioning in DPPG and DPPE:DPPG (3:2) MLVs induced pinB+ and pinBs, relative to lipid-only samples ($\frac{f}{f_\circ}$ where $f_\circ$ is the lipid only sample) at 59.3 °C.

The results indicated that pinB+, bearing an additional tryptophan compared to the W44R mutant pinBs, interacts to a greater extent with less anionic membranes. This suggests that the TRD penetrates the headgroup and exerts the bilayer disordering/ordering effect *via* hydrophobic interactions with the acyl core. However for pinBs, with one fewer tryptophan, the results indicate binding is primarily electrostatically driven *via* interaction of anionic lipid headgroups with the more cationic TRD.

It is also of note that below $\backsim$ 30 ℃ neither protein caused any changes in TEMPO partioning. This implies that neither protein interacts greatly with gel-phase lipid membranes or lipid domains within membranes, which has consequences for the role of both proteins *in vivo*; antimicrobial activity may not be membrane-mediated, for instance.

To obtain greater insight into where the proteins were inserting in bilayers, neutron reflectivity experiments on supported lipid bilayers in the absence and presence of pinB+ and pinBs were performed.

5.3.4 Neutron reflectivity

Neutron reflectivity experiments were performed on supported asymmetric bilayers composed of inner leaflet - DPPC, and outer leaflet - DMPE:DMPG (3:2), and changes in interfacial bilayer structure were examined when solutions containing pinB+ and pinBs were flowed across the SLB. All experiments were carried out at 25 ℃, below the phase transition temperature of the lipid mixture, to ensure stable bilayer formation on the silicon block.

Interaction with pinB+

Figure 5.9 shows the neutron reflectivity profiles, model data fits and scattering length density profiles for the asymmetric bilayers before and after pinB+ addition. Fitting of the isotopic contrasts to a five-layer bilayer model (silicon block, inner headgroup, inner tails, outer tails and outer headgroup) revealed the asymmetric structure of the bilayer; the inner leaflet was composed of 77 ± 4% DPPC and 22 ± 4% DMPE:DMPG. Hydration levels of 1±2% indicated some bilayer defects but overall a 99±2% coverage was achieved. The thicknesses of the inner and outer acyl chains were found to be 17.7±0.8 Å and 14.5±0.5 Å, respectively, with an overall bilayer roughness of 4.8±1.9 Å.

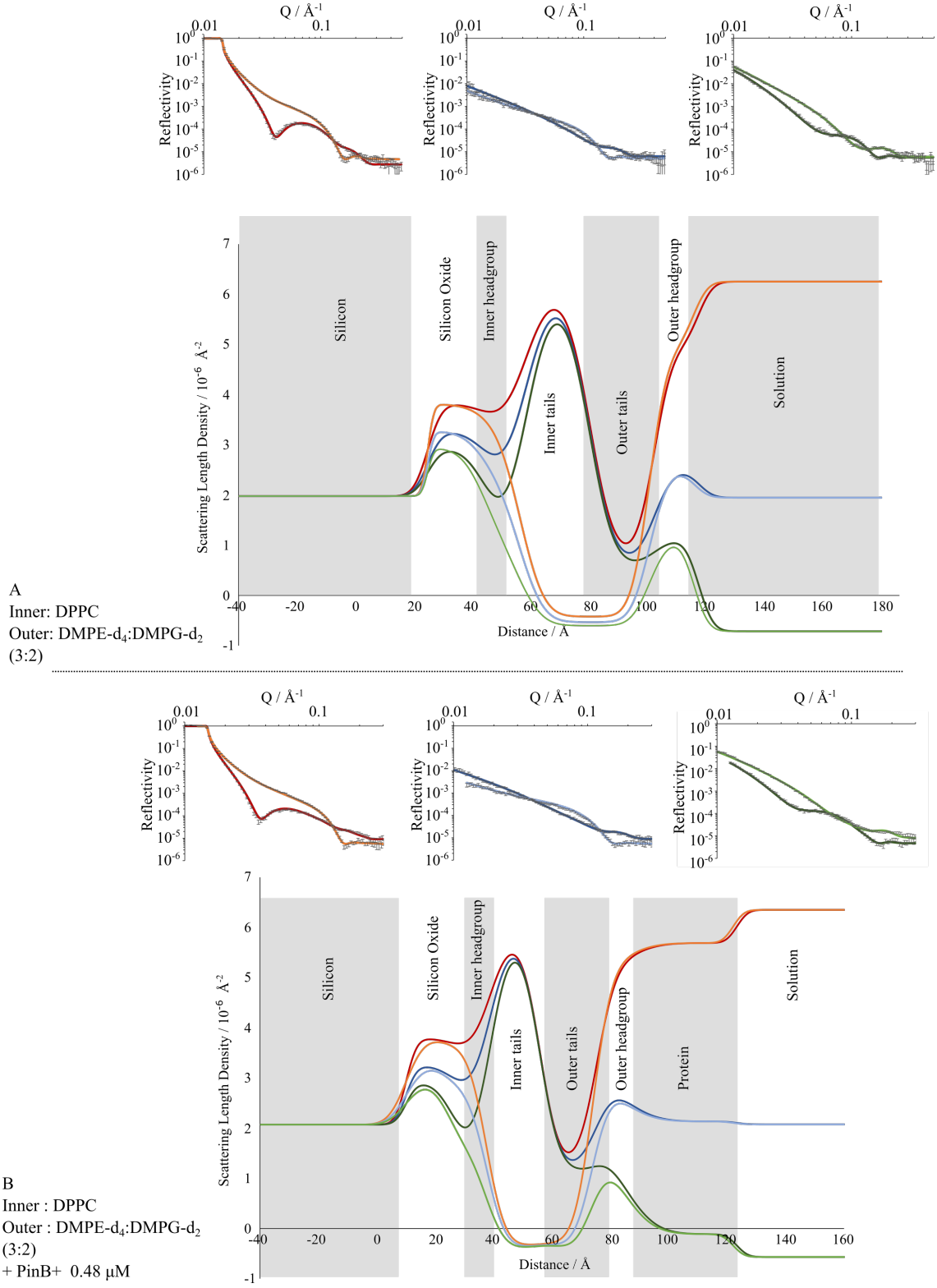

Figure 5.9 Neutron reflectivity profiles, with data model fits (*top*) and the corresponding scattering length density profile (*bottom*) of an inner leaflet - DPPC, and outer leaflet - DPPE:DPPG (3:2) bilayer before (***A***) and after (***B***) pinB+ addition. The isotopic contrasts displayed are inner - dDPPC/hDPPC in D_2O (red/orange), inner - dDPPC/hDPPC in SMW (dark/light blue) and inner - dDPPC/hDPPC in H_2O (dark/light green), all with outer - DMPE-d_4:DMPG-d_2 (3:2).

Addition of pinB+ (0.48μM) caused changes in the interfacial region of the sample cell. Most noticeably the data was now best represented by a six-layer model where a protein layer bound to the outer headgroup region was detected. The protein layer was 40.5 ± 5.4 Å thick, and fairly sparsely spread (evidenced by hydration levels of $80 \pm 5\%$). The overall structure of the bilayer itself was relatively unchanged; within error the thickness of the hydrophobic core was unchanged, but a reduction in the thickness of the outer headgroup region was observed. This suggested that by binding to the headgroup region of the SLB, the headgroup region became disordered and less dense due to increased hydration. However without appropriate contrasts for the headgroup region it was not possible to unambiguously determine this. Additionally, the observation that the asymmetry of the bilayer was unchanged, suggested that the fluidity of the SLB was unchanged upon pinB+ binding. The structural changes to the bilayer are summarised in Table 5.4.

Layer	Thickness (Å)	% DPPC	% DMPE:DMPG (3:2)	% pinB+	% Water	Roughness (Å)
Silicon Oxide	16.5 ± 2.5	N/A	N/A	N/A	13 ± 4	2.9 ± 0.5
	17.4 ± 0.6	N/A	N/A	N/A	11 ± 1	3.0 ± 1.2
Inner Headgroup	8.7 ± 2.0	N/C	N/C	N/C	N/C	
	14.0 ± 3.5	N/A	N/A	N/F	N/A	
Inner Tails	17.7 ± 0.8	77 ± 4	22 ± 4	N/A	1 ± 2	
	17.0 ± 2.2	78 ± 12	21 ± 12	N/F	1 ± 2	4.8 ± 1.9
Outer Tails	14.5 ± 0.5	14 ± 4	85 ± 4	N/A	1 ± 2	5.8 ± 0.6
	19.7 ± 3.0	19 ± 7	80 ± 7	N/F	1 ± 2	
Outer Headgroup	14.5 ± 1.8	N/C	N/C	N/C	N/C	
	7.6 ± 3.0	N/A	N/A	N/F	N/A	
pinB+	N/C	N/A	N/A	N/A	N/A	N/A
	40.5 ± 5.4	N/A	N/A	20 ± 5	80 ± 5	80.0 ± 5

Table 5.4 Structural parameters obtained for an asymmetrically deposited DPPC(inner),DPPE:DPPG (3:2)(outer) bilayer in the absence and presence of pinB+. N/C denotes not calculable, for layers where volume fractions of components were indeterminate due to a lack of suitable contrasts between components. N/F denotes not found, which relates to layers where protein could potentially be embedded but no evidence of such was found. N/A denotes non-applicable. Experiments were performed in duplicate.

Interaction with pinBs

Figure 5.10 shows the neutron reflectivity profiles, model data fits and scattering length density profiles for the asymmetric bilayers before and after pinBs addition. Fitting of the isotopic contrasts to a five-layer bilayer model (silicon block, inner headgroup, inner tails, outer tails and outer headgroup) revealed the asymmetric structure of the bilayer; the inner leaflet was composed of 72 ± 7% DPPC and 25 ± 7% DMPE:DMPG. The thickness, roughness and level of hydration were similar to the bilayer studied previously, and the structural parameters are summarised in Table 5.5.

Upon addition of pinBs (0.48μM), few differences were observed to the interfacial structure. The neutron reflectivity profiles obtained could again be satisfactorily fitted to a five-layer model, without requiring a protein layer. No changes to bilayer thickness, hydration or roughness were found, within error. These data suggested that the pinBs was not interacting at all with the inner - DPPC outer - DMPE-d_4:DMPG-d_2 (3:2) bilayer in the gel phase.

Layer	Thickness (Å)	% DPPC	% DMPE:DMPG (3:2)	% Water	Roughness (Å)
Silicon Oxide	16.3 ± 0.7	N/A	N/A	13 ± 1	3.0 ± 0.8
	15.9 ± 0.4	N/A	N/A	11 ± 2	3.0 ± 1.2
Inner Headgroup	5.0 ± 2.4	N/C	N/C	N/C	
	6.3 ± 3.0	N/A	N/A	N/F	
Inner Tails	19.1 ± 1.0	72 ± 3	25 ± 3	2 ± 2	
	17.0 ± 2.2	66 ± 5	32 ± 5	2 ± 2	2.9 ± 2.1
Outer Tails	19.9 ± 0.6	16 ± 5	82 ± 5	2 ± 2	5.0 ± 0.8
	17.6 ± 2.7	17 ± 8	81 ± 8	2 ± 2	
Outer Headgroup	8.5 ± 1.1	N/C	N/C	N/C	
	8.4 ± 2.6	N/A	N/F	N/A	

Table 5.5 Structural parameters obtained for an asymmetrically deposited DPPC(inner),DPPE:DPPG (3:2)(outer) bilayer in the absence and presence of pinBs. N/C denotes not calculable, for layers where volume fractions of components were indeterminate due to a lack of suitable contrasts between components. N/F denotes not found, which relates to layers where protein could potentially be embedded but no evidence of such was found. N/A denotes non-applicable. Experiments were performed in duplicate.

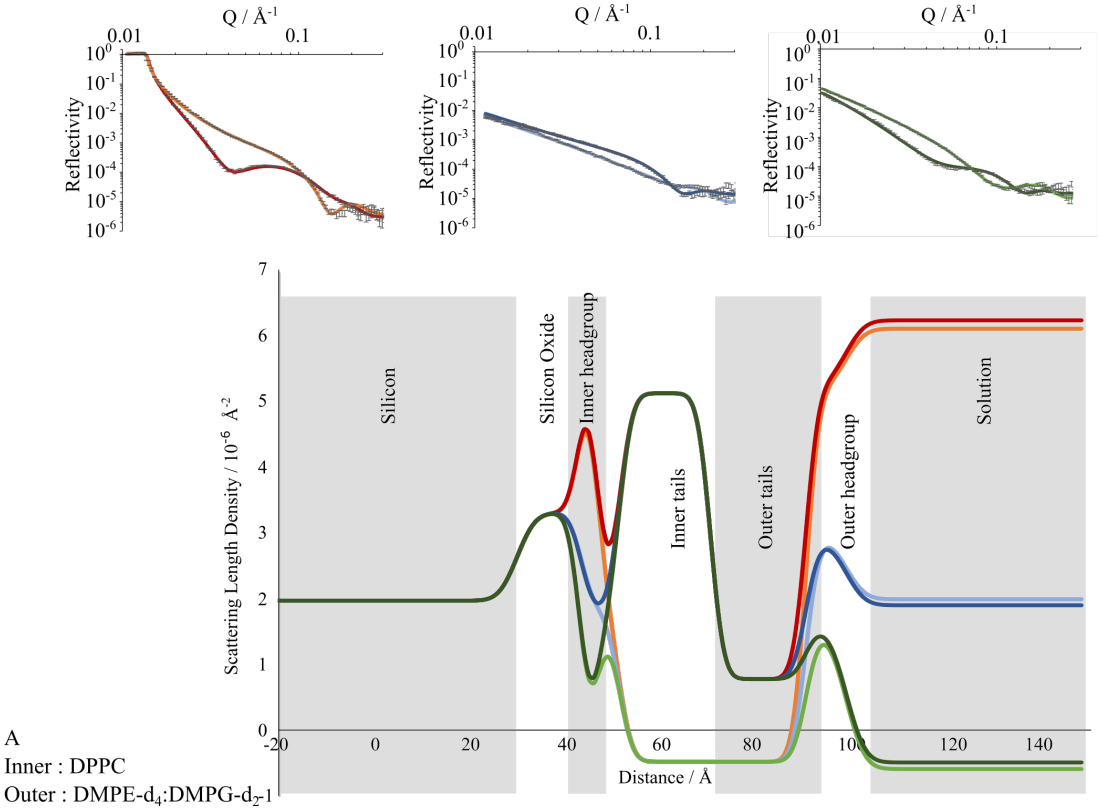

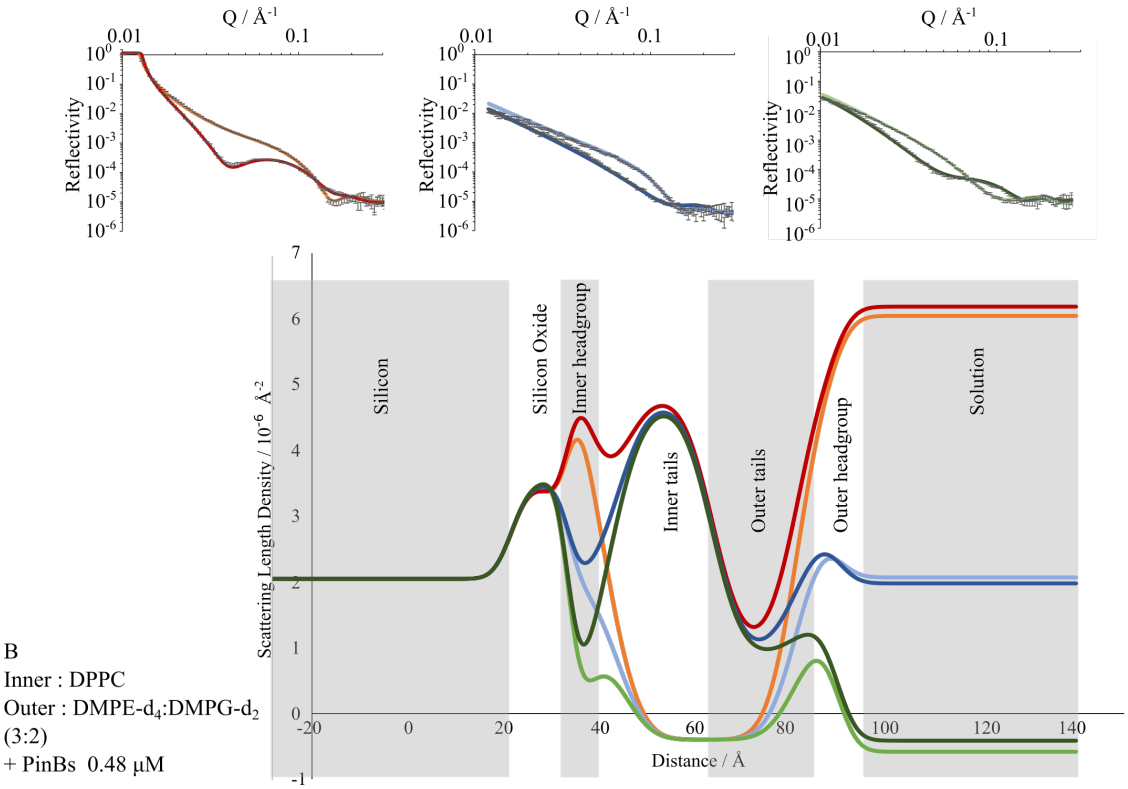

Figure 5.10 Neutron reflectivity profiles, with data model fits (*top*) and the corresponding scattering length density profile (**bottom**) of an inner leaflet - DPPC, and outer leaflet - DPPE:DPPG (3:2) bilayer before (***A***) and after (***B***) pinBs addition. The isotopic contrasts displayed are inner - dDPPC/hDPPC in D_2O (red/orange), inner - dDPPC/hDPPC in SMW (dark/light blue) and inner - dDPPC/hDPPC in H_2O (dark/light green), all with outer - DMPE-d_4:DMPG-d_2 (3:2).

The asymmetry of the bilayer, however, was observed to change; the asymmetry of the inner and outer leaflet lipid composition was scrambled, with the percentage of DPPC in the inner leaflet decreasing from $72 \pm 3\%$ to $66 \pm 5\%$. It is possible the reduction in asymmetry of the bilayer was caused by pinBs, however it appeared more likely the loss of asymmetry was due to the lipids in the bilayer flip-flopping over time, facilitated by defects existing on the surface of the block. The experiments were run in duplicate with similar changes (or lack thereof) being observed each time.

Figure 5.11 summarises and highlights the differences between the two cases; for pinB+ interacting with the bilayers, a clear protein layer can be observed, and the scattering length density of the protein layer in D_2O is lower than that of the lipid-only sample. The lower amount (calculated from the model fits to be $20 \pm 5\%$ less) of D_2O would cause less scattering, as detected.

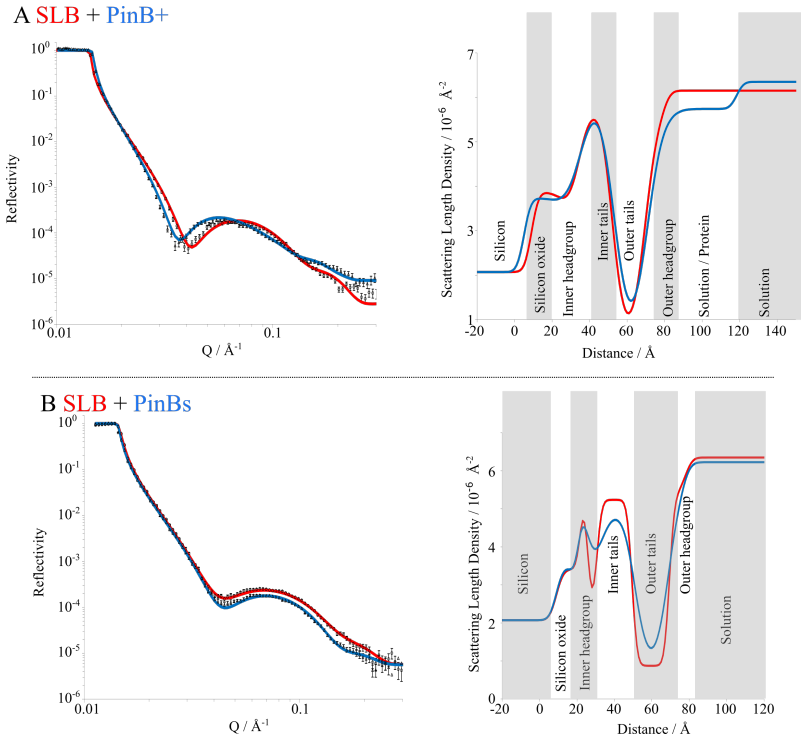

Figure 5.11 Neutron reflectivity profiles, model data fits and scattering length density profiles for dDPPC(inner),DPPE:DPPG (3:2)(outer) bilayer SLBs before and after addition of pinB+ (***A***) and pinBs (***B***), for the D_2O isotropic contrast. The appearance of a protein layer, and loss of membrane asymmetry can be clearly seen in ***A*** and ***B*** respectively.

It was noted that for the lipid-only sample in both cases, certain differences manifested (Figure 5.10 and 5.9) in the bilayer structure; most noticeably, the inner headgroup fit showed less contrast between different solvent contrasts for the PinB+ sample. This could have been due to poorer sample preparation, however the amount of hydration, which can indicate defects of the bilayer for both cases was not significantly different ($1 \pm 1\%$ and $2 \pm 2\%$ for PinB+ and PinBs respectively). Alternatively, the two samples were carried out on two different instruments (CRISP and INTER for PinBs and PinB+, respectively); the poorer neutron flux for CRISP may have resulted in a poorer resolved data set for PinBs, causing a different model to fit the data.

5.4 Discussion

The aim of this chapter was to understand better the interactions of WT pinB+ and a single-point mutant pinBs with native-like model lipid bilayers, and to examine the difference a single W44R mutation in the tryptophan-rich domain made to membrane binding.

After extraction and purification of both pinB+ and pinBs according to literature procedure (Figure 5.4)[272], ssNMR, EPR and NR experiments were performed with lipid dispersions and supported bilayers composed of anionic DMPG/DPPG and zwitterionic DMPE/DPPE. ssNMR experiments revealed that above the phase transition temperature of ^{2}H-labelled DMPE:DMPG (3:2) MLVs, pinB+ caused complete disordering of headgroup conformational order in both the anionic and zwitterionic component of the vesicle (Figure 5.6). The effect of pinBs was more modest; no changes were observed in the DMPE-d_4 component, while small changes were seen in the DMPG-d_2 spectrum. The data suggested that, by virtue of the additional tryptophan in the TRD, pinB+ is better able to interact with the acyl region of the membrane.

TEMPO partitioning experiments revealed complimentary information on the effect of the proteins on the same membranes above and below the phase transition tem-

perature of the lipid mixture. PinB+ (and pinBs to a lesser extent) caused an increase of f below the phase transition temperature, and a decrease above the transition temperature (Figures 5.8 and 5.7). Both proteins appeared to be affecting the membrane fluidity, reducing the cooperativity of the gel-to-liquid crystal transition in a cholesterol-like manner [125]. Again effects were more pronounced for pinB+, however this effect was less obvious in purely anionic DPPG vesicles, again providing more evidence that hydrophobic interactions with the acyl core are important for pinB binding.

Neutron reflectivity experiments on supported bilayers composed of a zwitterionic inner layer DPPC lipids and anionic outer layer DMPE:DMPG (3:2) lipids revealed differences in protein binding compared to work on lipid monolayers [283–285]. PinB+ was found to bind to the headgroup region of the SLB, causing a simultaneous decrease in outer headgroup thickness (Figure 5.4). PinBs did not induce any changes in interfacial structure, and it was assumed that the reduction of asymmetry of the SLB was due to lipid flip-flop over time. Indeed, surface pressure measurements performed have shown that pinBs does not interact with purely zwitterionic PE lipid monolayers [285]; if the DPPC lipids were flip-flopping between leaflets, thereby reducing the surface charge of the bilayer, this could be an explanation for the lack of interaction with pinBs. However, a control of the lifetime of lipid scrambling in the absence was not performed, making it not possible to definitively explain the pinBs behaviour.

With the same lipid mixture, results differ from those taken on lipid monolayers [130, 282, 285], therefore highlighting the importance of more native-like model membranes when elucidating the membrane-active function of proteins. The EPR, ssNMR and NR experiments, performed over a range of temperatures, show that pinB+ and pinBs interact far less with gel-phase lipids; the NR experiments were performed at room temperature, but even at the lowest temperature of 33 °C for the TEMPO experiments, no differences in partitioning were induced by the proteins compared to a

lipid-only sample. These data thus suggest that the mode of interaction of the puroindolines could be *via* preferential interactions with fluid domains of a cell membrane. The tryptophan to arginine mutation point in the TRD significantly alters membrane insertion, which has implications for the role of the puroindolines.

It could also be argued that the pinB proteins may fulfill some different function; a study on antimicrobial peptides based on the TRD of different puroindolines and mutants found that an AMP based on pinB+ and pinBs displayed MICs against *E. coli* of $> 250.0\mu$M, in contrast to 16.0μM for a peptide based on pinA [145]. The lipid compositions used in this study were -PE and -PG lipids, found commonly in many bacterial species and used regularly as a bacterial membrane model [20]. It is therefore possible that pinA is responsible for host defence of a germinating seed against pathogenic bacteria, while pinB may fulfill a more direct role in controlling wheat endosperm texture. The lipid composition of wheat endosperm in fact contains very little PE ($< 1\%$) while the most abundant lipid is lysophosphatidylcholine ($> 65\%$) [297]. It is therefore likely that the interactions of pinB will differ greatly in model membranes mimicking wheat endosperm membranes.

PinA and pinB are encoded by related genes which are physically linked, *i.e.* next to each other, so inherited together. Indeed, together they constitute the hard wheat marker protein mixture Friabilin [298]. It is possible they fulfil orthogonal and complimentary roles, dictated by differences in membrane perturbing properties of the different TRDs.

Chapter 6

Conclusions and Future Work

6.1 Conclusions

Characterisation and elucidation of AMP mode of action reveals a new potential mechanism

The aims of this thesis have been to understand how to alter rationally the primary sequence of antimicrobial templates in order to design novel AMPs with clinical promise that display controllable mechanistic interactions with a range of relevant model membranes, and to study other membrane-active peptides and proteins to understand better the link between primary structure and membrane interactions. A diverse range of established, and in some cases novel, biophysical techniques were employed to achieve these aims.

Two peptides, tilamin and chom, were rationally designed with primary structures based on amhelin and cecropin B, synthetic and naturally occurring AMPs, respectively (Figures 2.2 and 2.4)[155, 195]. They were predicted to fold into amphipathic helices that deviated in the mode of action from their forebears. MIC and hemolysis assays revealed both peptides were broad-spectrum antimicrobial with low μM MICs, with slightly improved potency compared to amhelin and cecB (Table 2.1). A negatively charged non-functional control, qaela, was also synthesised, and showed broad-spectrum inactivity and non-hemolytic activity (Figure 2.3).

To model the biophysical properties such as morphology, thickness and charge of native membranes, simplified phospholipid liposomes were used to understand better the membrane-perturbing influence of the AMPs and if this was correlated with an-

timicrobial activity. In the presence of anionic model membranes mimicking Gram-negative inner membranes and Gram-positive membranes, tilamin and chom adopted amphipathic alpha helix conformations, while remaining unstructured in solution and in the presence of zwitterionic model membranes mimicking mammalian model membranes (Figure 2.9). Qaela remained unstructured in solution and in the presence of all model membranes (Figure 2.9). This gave evidence that adoption of a folded conformation was important for the lytic effect of the AMPs.

Calcein leakage experiments showed that at concentrations similar to the MIC, both functional AMPs induced leakage of calcein from the interior of POPC:POPG liposomes, giving evidence that membrane permeabilisation was important for antimicrobial activity (Figure 2.8). However, in comparison to leakage induced by other AMPs such as magainin and melittin [187, 188], the induced leakage was more modest, giving some indication that membrane activity may not be the sole mechanism of the AMPs.

The qualitative nature of the membrane interactions was probed using quartz crystal microbalance; greater changes at lower harmonics on the chip, corresponding to regions nearer the head group of a supported lipid bilayer, suggested tilamin and chom were not inserting transmembrane but depositing on the surface of a membrane (Figures 2.11-2.14). The magnitude of this effect was dependent on chom concentration, while the QCM-derived Δf-Δd plots for tilamin revealed a change in bilayer interactions above a threshold concentration, suggesting a change in peptide orientation, possibly adopting the antimicrobial conformation. These findings allowed the speculative assignment of a carpet mechanism to chom, while the nature of the mode of action of tilamin remained uncertain. Incorporation of LPS reduced the magnitude of interaction with the SLBs, suggesting a defensive role of LPS for Gram-negative bacteria against AMP attack.

To understand better the effects the AMPs had on model membranes, solid-state NMR experiments were next performed with ^{2}H probes in the acyl region and a headgroup of MLV bilayers reporting on changes in the amplitude of angular motion of the lipid alkyl segments (Figure 3.9-3.16). ssNMR carried out on chemically synthesised headgroup-labelled POPC:POPG-d_2 and POPC:POPE-d_4 vesicles showed that tilamin and chom caused significant perturbation of headgroup dynamics of anionic membranes. Order parameter profiles obtained in the acyl region indicated that chom induced lateral phase separation of the lipid components of an anionic model membrane, and the uniform decreases in order throughout the acyl chain upon peptide binding gave further supporting evidence that the antimicrobial activity of chom is exerted *via* the carpet mechanism (Figure 6.1).

Lipid order parameters in the presence of tilamin were more complex (Figure 3.13), and a toroidal pore mechanism was proposed, along with a new mode of action that caused monoleaflet poration, though it was not possible to resolve the two mechanisms based on data obtained from symmetrical vesicles alone.

Adapting a newly established protocol to control the leaflet distribution of lipids in model membranes, an asymmetrically distributed nitroxide probe revealed for the first time leaflet-specific peptide-lipid interactions using cw-EPR. The leaflet distribution of the spin-probe was ascertained by ascorbic acid quenching experiments, revealing 100% asymmetry in LUVs with spin-probe in the outer leaflet and over 80% asymmetry in LUVs with spin-probe in the inner leaflet (Figure 4.16). Helix-8 peptide (h8p), a sequence based on the eighth helix of the GPCR NTS1 [258] shown to fold into an amphipathic helix in the presence of membranes but with no associated antimicrobial activity, was used as an all-surface bound control (Figure 4.17). WALP-23, a model peptide used to study membrane tilt [261], was used as a transmembrane control (Figure 4.19). The bilayer order parameter profile across both leaflets was shown to be asymmetric for the first time and to display characteristic changes for the two controls. Tilamin showed induced changes in bilayer order parameters

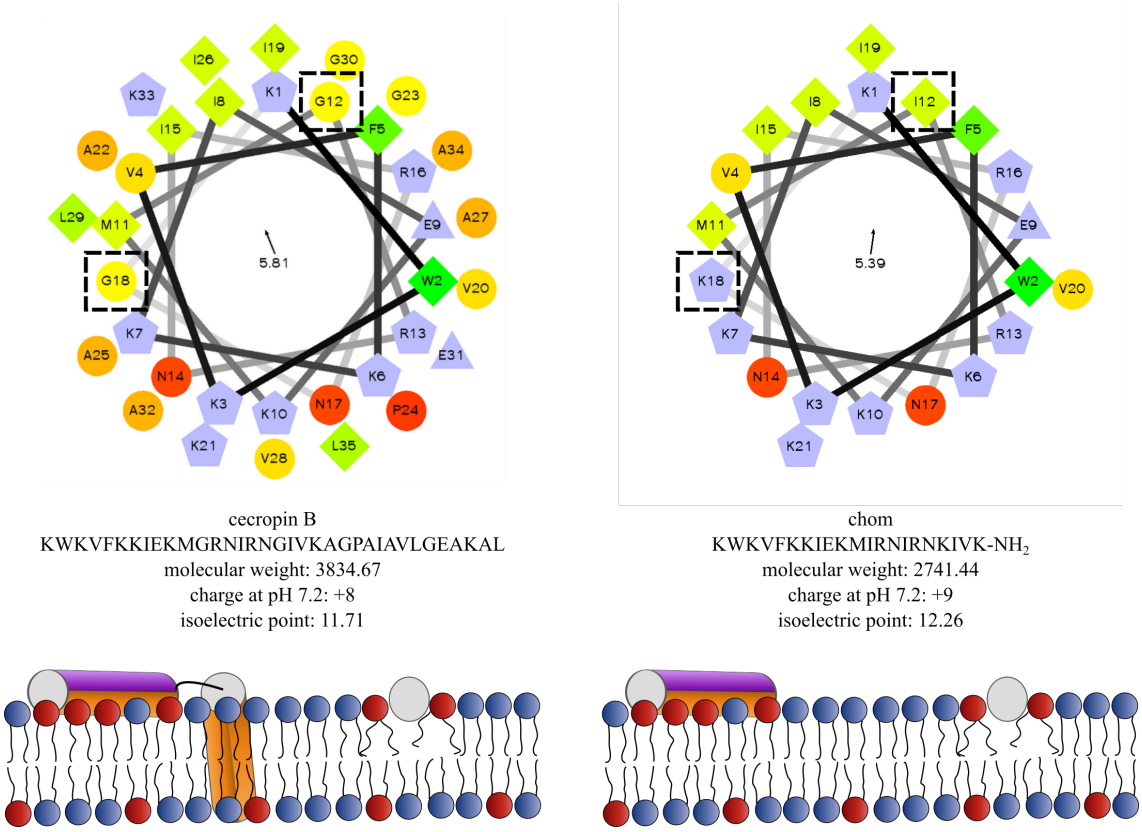

cecropin B
KWKVFKKIEKMGRNIRNGIVKAGPAIAVLGEAKAL
molecular weight: 3834.67
charge at pH 7.2: +8
isoelectric point: 11.71

chom
KWKVFKKIEKMIRNIRNKIVK-NH_2
molecular weight: 2741.44
charge at pH 7.2: +9
isoelectric point: 12.26

Figure 6.1 Rationally altering the primary sequence of cecB to chom predictably changes the mode of action; the amphipathic NH_2-half of cecB(*left*) was shown to bind to the surface of model membranes with the hydrophobic helix inserting into the membrane [162], while chom conformed to the carpet mechanism. The results in this thesis suggest that the lack of hydrophobic helix increases bactericidal activity against Gram-positive bacteria, while slightly adversely affecting the activity against Gram-negative membranes.

that did not match either control peptide, indicating more complex interactions (Figure 4.21). Taken in combination, unique Δf-Δd plots from QCM (Figure 2.14-2.13), heterogeneous changes in order parameter profiles observed with acyl-chain ^{2}H ss-NMR (Figure 3.12), and a lack of interaction with the inner leaflets of anionic model membranes seen by cw-EPR (Figure 4.21) suggest tilamin operates *via* a more complicated mechanism. Supported by tilt angles obtained by GALA analysis of alanine-deuterated tilamin and AFM imaging with collaborators, the results are consistent with a new mechanism; monolayer poration (Figure 6.2).

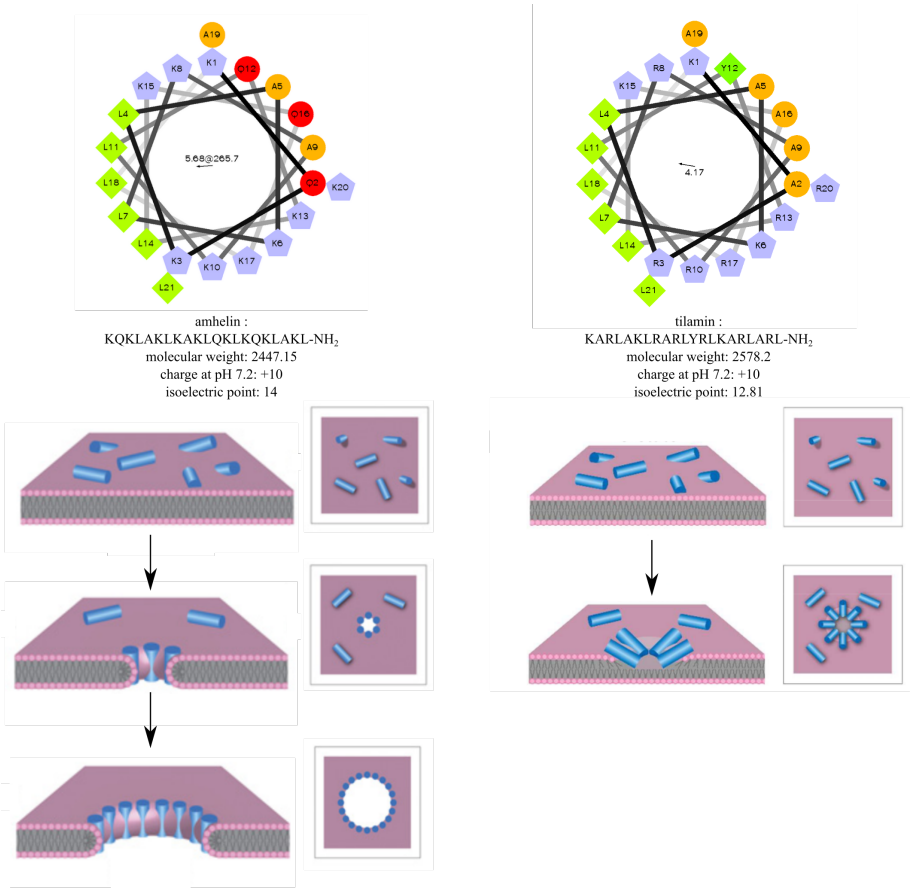

Figure 6.2 Rationally altering the primary sequence of amhelin to tilamin predictably changes the mode of action; amhelin (*left*) was shown to bind to the surface of model membranes, followed by transmembrane insertion, and pore formation and expansion [155]. The results in this thesis give evidence for a new mechanism action of tilamin (*right*); monolayer poration, where after insertion, transient, single-leaflet pores can form on the surface of a membrane [197]. Dashed boxes highlight additional modifications to the chom sequence from cecB.

The methodology to produce asymmetric vesicles was extended, in an attempt to form more native-like model membranes. LPS, a key constituent of the outer membrane of Gram-negative model membranes, was asymmetrically incorporated into LUVs, which was confirmed by a fluorescence quenching assay. The incorporation of LPS had a pronounced effect on the cell permeabilising ability of AMPs; the ability of chom and tilamin to cause cell leakage was reduced in the presence of LPS, however the greatest effect was observed for a Gram-positive selective peptide, Gramicidin D. This suggested that formation of this more native-like model membrane could help

delineate which membrane components are important for the antimicrobial activity of different AMPs.

The anionic non-functional AMP qaela was a useful control; key differences in peptide-lipid interactions were observed using QCM and ssNMR, compared with the positively charged, "functional" analogue tilamin. Despite electrostatics playing an important role in peptide-lipid binding, qaela still induced large structural perturbations even on anionic model membranes, as seen by ssNMR (Figure 3.14). This underlines the importance of considering hydrophobic interactions in the model of antimicrobial activity.

In spite of the ssNMR observations, qaela was shown with MIC and hemolysis experiments to be inactive (Figure 2.1), with over ten-fold MIC and hemolytic values compared with tilamin. This raises a broader question on the importance of the biophysical interactions of the AMPs with model membranes. It is obvious that there is not a strong link between membrane permeabilisation and perturbation of lipid dynamics, and *in vitro* antimicrobial activity.

A valid response to this argument is that *in vivo* MIC and hemolysis assays suffer from several drawbacks themselves; MICs are typically performed at bacterial cell concentrations of $1 \times 10^5 - 1 \times 10^6$ cells/mL, while hemolysis assays are performed at hematocrit values of 5%. For a typical volume of 86 fL per erythrocyte [217] this corresponds to a concentration of 6×10^8 cells/mL. In addition, erythrocytes ($\backsim 7$ μm) are larger than bacterial cells ($\backsim 1$ μm), and as such it is obvious that a greater peptide concentration will be needed to achieve the same lytic effect. Indeed, when correcting for this, it was found that magainin caused lysis of Chinese hamster ovary (CHO)-K1 cells at the MIC of 10 μM [136].

It is therefore clear that much research is still required to establish the link between the interaction of AMPs with model membranes and the resulting antimicrobial activity and selectivity.

Membrane morphology affects the binding and insertion of puroindolines

Wild-type PinB (pinB+), a membrane-active protein with proposed antimicrobial activity, and a single point W44R mutant (PinBs) were also studied using EPR, ssNMR and NR, in model lipid bilayers for the first time. Both proteins differed in their interactions with anionic PE:PG membranes in contrast to monolayer studies; ssNMR revealed pinB+ binded to the membranes *via* interaction of lipid headgroups, causing a loss of conformation order and hydrogen-bonding between headgroups (Figure 5.6). Changes in TEMPO partitioning revealed that both proteins do not cause changes in bilayer fluidity at temperatures more than $\backsim$ 10 ℃ below the phase transition temperature of the bilayer (Figures 5.7 and 5.8). At temperatures near the transition temperature, both proteins cause a reduction in the cooperativity of the phase transition in a cholesterol-like manner [125], with the changes in membrane fluidity induced by pinB+ being greater. Finally NR experiments on gel-phase asymmetric supported lipid bilayers show that pinB+ forms a protein layer upon interaction with the membrane (Figure 5.9), while pinBs appears not to interact.

It can be concluded that the single-point W44R mutation, occurring in the TRD of the pins, markedly alters the membrane binding characteristics. Wheat strains expressing pinBs are harder than the WT analogues [299], for which the biophysical data provides good evidence the cause of this is membrane-mediated due to the large changes in interactions observed. It is also concluded that the pinB proteins may perform this role in tandem with the purported antimicrobial activity of pinA; a study on antimicrobial peptides based on the TRD of different puroindolines and mutants found that an AMP based on pinB+ and pinBs displayed MICs against *E. coli* of > 250.0 μM, in contrast to 16.0 μM for a peptide based on pinA [145]. Since pinA and pinB are often expressed together in a complex known as Friabilin [298], it is possible they fulfil orthogonal and complimentary roles, which may be understood better upon study using wheat-membrane mimetics.

Despite being a diverse family of over 2500 members [60], only relatively few AMPs have been fully characterised. Employing a wide range of biophysical techniques, this thesis described the rigorous characterisation of two potent broad spectrum AMPs, tilamin and chom, as well as a negative control peptide, qaela. It has been shown that rational changes to the primary structure of a peptide can result in changes in membrane orientation in a controllable way. The design features, as well as consideration of the structural features of membrane-active peptides such as the puroindoline family, should inform future design of better antimicrobials.

It has also been shown that the link between biophysical characterisation and clinical potential must be bridged more completely in the future, and more sophisticated model membranes are required. Conventional symmetric model membranes composed of simple mixtures of phospholipids are, in the author's opinion, at the limit of utility in terms of describing the mode of action of AMPs at real cell membranes. This work has provided novel ways of creating more complex model membranes and probing leaflet-specific changes occurring during peptide-lipid interactions.

6.2 Future work

Further characterisation of AMP-cell interactions, and improvements to AMP design

This thesis has highlighted the fact that membrane disruption, while unequivocally involved in interactions of AMPs with bacteria, incompletely describes how AMPs kill living cells. Therefore the effect on other components of a cell, such as membrane proteins, cholesterol, ergesterol and LPS should be investigated more thoroughly to obtain a more holistic picture on how the AMPs elicit antimicrobial activity. Recent examples have been reported of AMPs causing binding to DNA [95], and inhibiting cell wall synthesis analogous to conventional antibiotics [300], and should aid in characterising these complicated molecules. Relatively underexplored compared

to the focus of AMP action on membranes, effects such as these should be examined with the AMPs studied here to understand better the mode of action.

The structural design principles discussed in this thesis (Section 2.3.1) which lead to a desired amphipathic molecular conformation, could also be applied to non-proteinogenic structures. The structures could retain the favourable membrane interactions of tilamin and chom, but display improved resistance to hydrolysis, making them better drug candidates for the future. Chemical methods of hydrocarbon-stapling α-α disubstituted peptides *via* olefin tethers have shown increased resistance to hydrolysis and reinforced secondary structure [301]. In addition, synthetic peptidomimetics that allow spatial projection of residues in a similar way to helical peptides, while having a non-amide backbone are also promising extensions of antimicrobial peptides [302–304]. These approaches and improvements to peptide design are already showing great promise; bralicidin, a synthetic amphipathic polymer based on defensin has successfully completed phase 2b clinical trials and is the first in its class of approved drugs that work *via* membrane perturbation [305].

Further elucidation of PinB-cell interactions

The work performed on pinB+ and pinBs interactions with model lipid bilayers again highlighted the importance of using native-like model membranes when investigating the nature of protein-lipid interactions. To understand further how the pins influence wheat endosperm texture, model membranes mimicking wheat cells should be studied; an *N*-acyl PE:PC:lyso-PC (1:1:1) lipid mixtures approximates that found from wheat flour [306], and differences in interactions with the pins compared to bacterial model membranes should reveal useful structural information on these proteins. In addition, attempts to crystallise the pins should be performed to ascertain the structure of the TRD during interactions with cell membranes.

Development of more native like model membranes

To expedite the discovery of AMP-based therapeutics and improve general understanding of the function of membrane-active proteins, the use of more realistic model membranes to understand the mechanism of action should become more prevalent. In addition to the work presented in this thesis, other interesting approaches are being taken. Asymmetric floating bilayers, comprised of an inner thiolipid monolayer, above which sits an asymmetric bilayer composed of inner leaflet phospholipid and outer leaflet LPS, have been formulated with membrane proteins embedded. They simulate accurately both the inner and outer membrane of Gram-negative bacteria (Figure 6.3)[140].

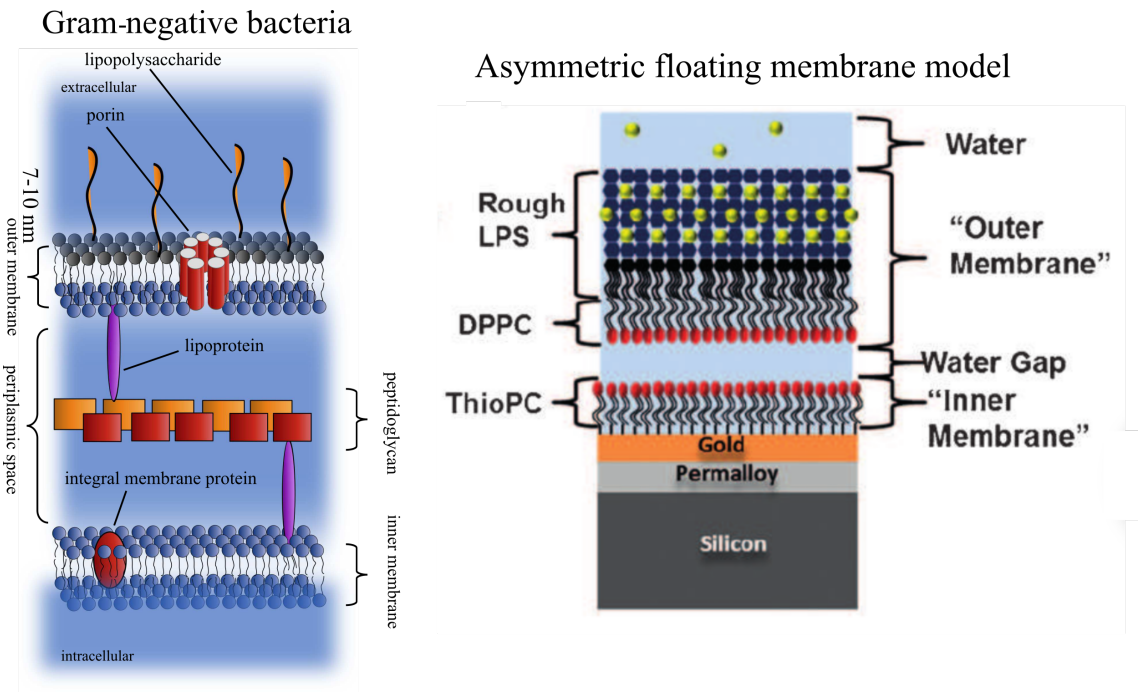

Figure 6.3 New approaches to modelling natural bacterial membranes; Gram-negative bacterial membranes (schematically pictured, left) have been accurately modelled by free floating asymmetric bilayers [140].

With the ability to form asymmetric bilayers in vesicles and polymers that can bias the formation of bilamellar vesicles [307], this could be recreated in vesicles that allow study from a battery of biophysical techniques that do not depend on substrate support, and redress the issues that limit the utility of conventional phospholipid

membranes discussed in the thesis. Another promising source of model membrane systems can be seen with Lipodisqs (LQ). LQs are nanoparticles of 10 nm, in which a phospholipid core is constrained into a disc-like shape by a copolymer of styrene and maleic anhydride (SMA) (Figure 6.4).

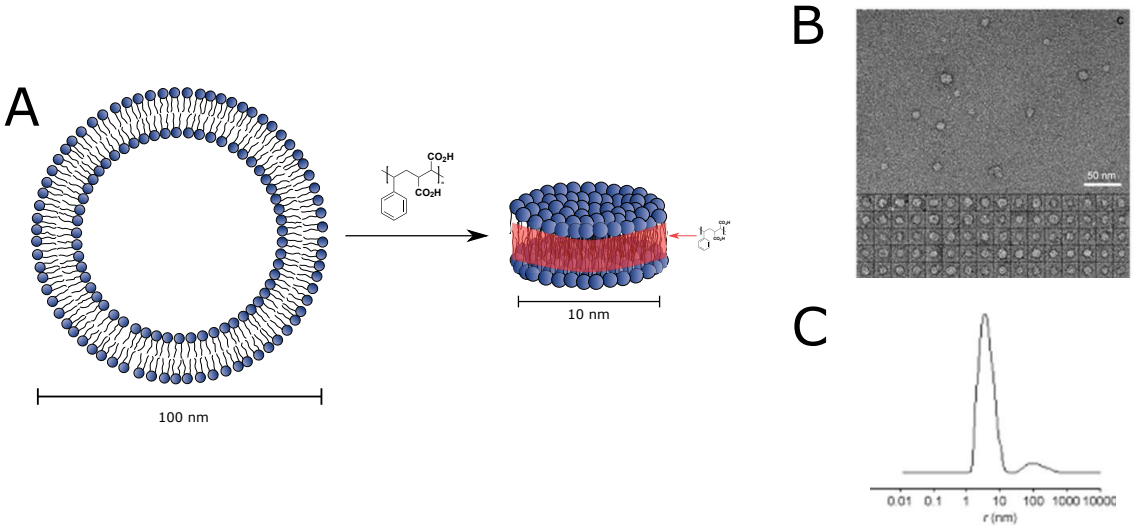

Figure 6.4 Schematic depiction of formation of "coin shaped" lipodisqs from liposomes, effected by SMA (**A**). The sizes of the nanoparticles from electron microscopy (**B**) and dynamic light scattering (**C**) are also shown. ***B*** and ***C*** taken from [308].

The amphipathic SMA polymer forms a hypercoil around the acyl region of phospholipids and hence around the hydrophobic core of the bilayer, leaving the hydrophilic lipid headgroups exposed to bulk solvent. Originally devised as a hydrophobic platform to study and characterise the structures of membrane proteins [308, 309], their small size makes them amenable to a range of biophysical techniques. It has been shown recently that the SMA polymer is able to extract lipodisqs from native membranes, forming nanoparticles with lipid compositions that reflect accurately the lipid composition of the cell membranes from which they are extracted [310, 311]. These systems should be applied to AMP research to improve upon simplistic phospholipid model membranes and gain a greater understanding of their mode of action. What is not understood is the nature of assembly of native membranes upon addition of SMA; to preserve native function it is desirable that any inherent asymmetry is retained in the resultant lipodisq. By using the methods to produce asymmetry described in this

thesis, it should be possible to determine the mode of formation of these interesting model membranes.

Preliminary work on this system using Förster resonance energy transfer (FRET) pairs to elucidate interleaflet effects and asymmetry lifetimes have yielded promising results and should be fully characterised in the near future, yielding a biologically relevant lipid environment to understand better AMPs and other membrane-active peptides and proteins, and help answer some of the most pertinent questions threatening the future of mankind.

References

[1]Editorials, “The antibiotic alarm”, Nature, 141 (2013).

[2]J Davies and D Davies, “Origins and evolution of antibiotic resistance”, Microbiology and Molecular Biology Reviews **74**, 417–433 (2010).

[3]J. I. M. O. Neill, “Tackling drug-resistant infections globally: final report and recommendations. The review on antimicrobial resistance.”, Government Report (2016).

[4]C. Nathan and F. M. Goldberg, “Outlook: the profit problem in antibiotic R&D.”, Nature reviews. Drug discovery **4**, 887–891 (2005).

[5]J. O. . Neill, “Antimicrobial Resistance: Tackling a crisis for the health and wealth of nations”, Government Report (2014).

[6]C. Cain, “Rediscovering antibiotics”, SciBX: Science-Business eXchange **5**, 1–3 (2012).

[7]D. a. Phoenix, S. R. Dennison, and F. Harris, “Antimicrobial Peptides : Their History , Evolution , and Functional Promiscuity”, Antimicrobial peptides, 1–37 (2013).

[8]W. K. Derickson, “Lipid storage and utilization in reptiles”, Integrative and Comparative Biology **16**, 711–723 (1976).

[9]M. P. Wymann and R. Schneiter, “Lipid signalling in disease.”, Nature reviews. Molecular cell biology **9**, 162–76 (2008).

[10]M. Sud, E. Fahy, D. Cotter, A. Brown, E. A. Dennis, C. K. Glass, A. H. Merrill, R. C. Murphy, C. R. H. Raetz, D. W. Russell, and S. Subramaniam, “LMSD: LIPID MAPS structure database”, Nucleic Acids Research **35**, 527–532 (2007).

[11]S. J. Singer and G. L. Nicolson, “The fluid mosaic model of the structure of cell membranes.”, Science (New York, N.Y.) **175**, 720–31 (1972).

[12]L. Brown, J. M. Wolf, R. Prados-Rosales, and A. Casadevall, “Through the wall: extracellular vesicles in Gram-positive bacteria, mycobacteria and fungi.”, Nature reviews. Microbiology **13**, 620–30 (2015).

[13]J. R. Brender, A. J. McHenry, and A. Ramamoorthy, “Does cholesterol play a role in the bacterial selectivity of antimicrobial peptides?”, Frontiers in Immunology **3**, 1–4 (2012).

[14]E. Fahy, M. Sud, D. Cotter, and S. Subramaniam, “LIPID MAPS online tools for lipid research”, Nucleic Acids Research **35**, 606–612 (2007).

[15]*LIPID MAPS Structure Database (LMSD)*.

[16]A. Ltd, *What is the meaning of "sn" in the lipid name?*

[17]P. L. Yeagle, W. C. Hutton, C. H. Huang, and R. B. Martin, “Headgroup conformation and lipid–cholesterol association in phosphatidylcholine vesicles: a 31P(1H) nuclear Overhauser effect study.”, Proceedings of the National Academy of Sciences of the United States of America **72**, 3477–81 (1975).

[18]O. Geiger, I. M. L??pez-Lara, and C. Sohlenkamp, “Phosphatidylcholine biosynthesis and function in bacteria”, Biochimica et Biophysica Acta - Molecular and Cell Biology of Lipids **1831**, 503–513 (2013).

[19]K. Malinska, J. Malinsky, M. Opekarova, and W. Tanner, “Distribution of Can1p into stable domains reflects lateral protein segregation within the plasma membrane of living S. cerevisiae cells.”, Journal of cell science **117**, 6031–6041 (2004).

[20]M. R. Yeaman and N. Y. Yount, “Mechanisms of antimicrobial peptide action and resistance.”, Pharmacological reviews **55**, 27–55 (2003).

[21]N. B. Gilula, R. R. Eger, and D. B. Rifkin, “Plasma membrane alteration associated with malignant transformation in culture.”, Proceedings of the National Academy of Sciences of the United States of America **72**, 3594–8 (1975).

[22]N. J. Russell, “The Regulation of Membrane Fluidity in Bacteria by Acyl Chain Length Changes”, Biomembrane **12**, 329–347 (1984).

[23]D. Marsh, *Handbook of lipid bilayers*, Taylor & Francis Group (2013), p. 385.

[24]M. Zasloff, "Antimicrobial peptides of multicellular organisms", Nature **415**, 389–395 (2002).

[25]S.-H. Lee, X. W. Meng, K. S. Flatten, D. A. Loegering, and S. H. Kaufmann, "Phosphatidylserine exposure during apoptosis reflects bidirectional trafficking between plasma membrane and cytoplasm.", Cell death and differentiation **20**, 64–76 (2013).

[26]F. Ghahremanfard, M. Mirmohammadkhani, B. Shahnazari, G. Gholami, and J. Mehdizadeh, "The valuable role of measuring serum lipid profile in cancer progression", Oman Medical Journal **30**, 353–357 (2015).

[27]T. R. Skrbic and J. N. Cumings, "FATTY ACIDS OF LECITHIN IN SUBCELLULAR FRACTIONS DURING MATURATION OF BRAIN", **17**, 85–90 (1970).

[28]G. S. Getz, W Bartley, F Stirpe, B. M. Notton, Renshaw, and A, "The lipid composition of rat liver.", The Biochemical journal **80**, 176–81 (1961).

[29]K. Miyamoto, L. E. O. M. Stephanides, and J. Bernsohn, "Fatty acids of glycerophosphatides in developing chick embryonic brain and liver", **7** (1966).

[30]T. Kobayashi, M. Nishijima, Y. Tamori, S. Nojima, Y. Seyama, and T. Yamakawa, "No Title", Biochimica et biophysica acta **620**, 356 (1980).

[31]J. M. dos Santos Mota, J. A. den Kamp, H. M. Verheij, and L. L. van Deenen, "Phospholipids of Streptococcus faecalis.", Journal of Bacteriology **104**, 611–619 (1970).

[32]B. Poolman, A. J. M. Driessen, and W. N. Konings, "Regulation of arginine-ornithine exchange and the arginine deiminase pathway in Streptococcus lactis", Journal of Bacteriology **169**, 5597–5604 (1987).

[33]D. Marquardt, B. Geier, and G. Pabst, "Asymmetric lipid membranes: Towards more realistic model systems", Membranes **5**, 180–196 (2015).

[34]H. Träuble and H. Eibl, "Electrostatic effects on lipid phase transitions: membrane structure and ionic environment", Proceedings of the National Academy of Sciences of the United States of America **71**, 214–219 (1974).

[35]S. J. Marrink, J. Risselada, and A. E. Mark, "Simulation of gel phase formation and melting in lipid bilayers using a coarse grained model", Chemistry and Physics of Lipids **135**, 223–244 (2005).

[36]H. Schindler, *Introduction to Biological Membranes*, Vol. 3, 10 (1980), p. XXII.

[37]M. R. Rintoul, R. D. Morero, and F. G. Dupuy, "The antimicrobial peptide microcin J25 stabilizes the gel phase of bacterial model membranes", Colloids and Surfaces B: Biointerfaces **129**, 183–190 (2015).

[38]T. J. LaRocca, P. Pathak, S. Chiantia, A. Toledo, J. R. Silvius, J. L. Benach, and E. London, "Proving Lipid Rafts Exist: Membrane Domains in the Prokaryote Borrelia burgdorferi Have the Same Properties as Eukaryotic Lipid Rafts", PLoS Pathogens **9** (2013) 10.1371/journal.ppat.1003353.

[39]M. Orwick-Rydmark, J. E. Lovett, A. Graziadei, L. Lindholm, M. R. Hicks, and A. Watts, "Detergent-free incorporation of a seven-transmembrane receptor protein into nanosized bilayer lipodisq particles for functional and biophysical studies", Nano Letters **12**, 4687–4692 (2012).

[40]H. Smith, "Sperm motility and MSP.", WormBook : the online review of C. elegans biology, 1–8 (2006).

[41]M. Bretscher, "Asymmetrical lipid bilayer structure for biological membranes", Nature **236**, 11–12 (1972).

[42]J. a. Virtanen, K. H. Cheng, and P Somerharju, "Phospholipid composition of the mammalian red cell membrane can be rationalized by a superlattice model.", Proceedings of the National Academy of Sciences of the United States of America **95**, 4964–4969 (1998).

[43]W. T. Kong QY, Wu X, Li J, Peng WX, Ye R, Lindholm B, "Loss of phospholipids asymmetry in red blood cells contributes to anemia in uremic patients.", Adv Perit Dial. **17**, 58–60 (2001).

[44]P. F. Devaux, A. Herrmann, N. Ohlwein, and M. M. Kozlov, "How lipid flippases can modulate membrane structure", Biochimica et Biophysica Acta - Biomembranes **1778**, 1591–1600 (2008).

[45]E. M. Bevers, P. Comfurius, D. W. C. Dekkers, and R. F. A. Zwaal, *Lipid translocation across the plasma membrane of mammalian cells*, 1999.

[46]S. K. Sahu, S. N. Gummadi, N. Manoj, and G. K. Aradhyam, "Phospholipid scramblases: An overview", Archives of Biochemistry and Biophysics **462**, 103–114 (2007).

[47]D Marsh, A Watts, and P. F. Knowles, "Evidence for phase boundary lipid. Permeability of Tempo-choline into dimyristoylphosphatidylcholine vesicles at the phase transition", Biochemistry **15**, 3570–3578 (1976).

[48]S. Vehring, L. Pakkiri, A. Schröer, N. Alder-Baerens, A. Herrmann, A. K. Menon, and T. Pomorski, "Flip-flop of fluorescently labeled phospholipids in proteoliposomes reconstituted with Saccharomyces cerevisiae microsomal proteins", Eukaryotic Cell **6**, 1625–1634 (2007).

[49]F.-X. Contreras, L. Sánchez-Magraner, A. Alonso, and F. M. Goñi, "Transbilayer (flip-flop) lipid motion and lipid scrambling in membranes", FEBS Letters **584**, 1779–1786 (2010).

[50]B. D. Kruijff and E. J. J van Zoelen, "No Title", Biochimica et biophysica acta **511**, 105 (1978).

[51]W. C. Wimley and T. E. Thompson, "Exchange and flip-flop of dimyristoylphosphatidylcholine in liquid-crystalline, gel, and two-component, two-phase large unilamellar vesicles.", Biochemistry **29**, 1296–303 (1990).

[52]R. D. Kornberg and H. M. McConnell, "Inside-outside transitions of phospholipids in vesicle membranes.", Biochemistry **10**, 1111–1120 (1971).

[53]M. Nakano, M. Fukuda, T. Kudo, N. Matsuzaki, T. Azuma, K. Sekine, H. Endo, and T. Handa, "Flip-flop of phospholipids in vesicles: kinetic analysis with time-resolved

small-angle neutron scattering", Journal of Physical Chemistry B **113**, 6745–6748 (2009).

[54]T. E. Redelmeier, M. J. Hope, and P. R. Cullis, "On the mechanism of transbilayer transport of phosphatidylglycerol in response to transmembrane pH gradients.", Biochemistry **29**, 3046–53 (1990).

[55]A. J. Verkleij, R. F. A. Zwaal, B. Roelofsen, P. Comfurius, D. Kastelijn, and L. L. M. van Deenen, "The asymmetric distribution of phospholipids in the human red cell membrane. A combined study using phospholipases and freeze-etch electron microscopy", BBA - Biomembranes **323**, 178–193 (1973).

[56]R. J. Dubos, "Studies on a bactericidal agent extracted from a soil Bacillus: I. Preparation of the agent. Its acticity in vitro", The Journal of experimental medicine **70**, 1–10 (1939).

[57]R. Ezekowitz, A. B., and J. Hoffmann, "Innate immunity in insects", Current opinion in immunology, 1–2 (1996).

[58]H.-L. Lu, J. B. Wang, M. A. Brown, C. Euerle, and R. J. St Leger, "Identification of Drosophila Mutants Affecting Defense to an Entomopathogenic Fungus.", Scientific reports **5**, 12350 (2015).

[59]M. H. Braff, A. Di Nardo, and R. L. Gallo, "Keratinocytes store the antimicrobial peptide cathelicidin in lamellar bodies", Journal of Investigative Dermatology **124**, 394–400 (2005).

[60]G. Wang, X. Li, and Z. Wang, "APD3: the antimicrobial peptide database as a tool for research and education.", Nucleic acids research **44**, D1087–D1093 (2016).

[61]G. Wang, X. Li, and Z. Wang, "APD2: The updated antimicrobial peptide database and its application in peptide design", Nucleic Acids Research **37**, 933–937 (2009).

[62]L. Stuart and T. Harris, "Bactericidal and fungicidal properties of a crystalline protein isolated from unbleached wheat flour.", Cereal Chemistry **19**, 288–300 (1942).

[63]D. Hawksworth, P. Kirk, B. Sutton, and D. Pegler, *Ainsworth & Bisby's dictionary of the fungi*, 1996.

[64]E Habermann and Z Jentsch, "Melittin is the first polypeptide whose biological effects can be understood on the basis of its primary structure. Elucidation of structure and correlation with activity:" Physiology Chem **348**, 37 (1967).

[65]A Csordas and H Michl, "No Title", Monatsh. Chem. **101**, 182–189 (1970).

[66]D. Hultmark, A. Engstrom, H. Bennich, R. Kapur, and H. G. Boman, "Insect immunity: Isolation and structure of Cecropin D and four minor antibacterial components from Cecropia pupae", European Journal of Biochemistry **127**, 207–217 (1982).

[67]T. Ganz, M. E. Selsted, D. Szklarek, S. S. Harwig, K. Daher, D. F. Bainton, and R. I. Lehrer, "Defensins. Natural peptide antibiotics of human neutrophils", Journal of Clinical Investigation **76**, 1427–1435 (1985).

[68]S. Chatterjee, S. Chatterjee, S. J. Lad, M. R. Phansalkar, R. H. Rupp, and B. N. Ganguli, "Mersacidin, a new antibiotic from Bacillus - Fermentation, isolation, purification and chemical characterization", The Journal of Antibiotics **45**, 832–838 (1992).

[69]H. N. Ulrich, U. S. Sudheendra, and A. Ramamoorthy, "LL-37, the only human member of the cathelicidin family of antimicrobial peptides", Biochimica et Biophysica Acta - Biomembranes **1758**, 1408–1425 (2006).

[70]J Krijgsveld, S. a. Zaat, J Meeldijk, P. a. van Veelen, G Fang, B Poolman, E Brandt, J. E. Ehlert, a. J. Kuijpers, G. H. Engbers, J Feijen, and J Dankert, "Thrombocidins, microbicidal proteins from human blood platelets, are C-terminal deletion products of CXC chemokines.", The Journal of biological chemistry **275**, 20374–20381 (2000).

[71]L. L. Ling, T. Schneider, A. J. Peoples, A. L. Spoering, I. Engels, B. P. Conlon, A. Mueller, D. E. Hughes, S. Epstein, M. Jones, L. Lazarides, V. a. Steadman, D. R. Cohen, C. R. Felix, K. A. Fetterman, W. P. Millett, A. G. Nitti, A. M. Zullo, C. Chen, and K. Lewis, "A new antibiotic kills pathogens without detectable resistance", Nature **517**, 455–459 (2015).

[72]A. Tossi, L. Sandri, and A. Giangaspero, "Amphipathic, alpha-helical antimicrobial peptides.", Biopolymers **55**, 4–30 (2000).

[73]B Bechinger, M Zasloff, and S. J. Opella, "Structure and orientation of the antibiotic peptide magainin in membranes by solid-state nuclear magnetic resonance spectroscopy.", Protein science : a publication of the Protein Society **2**, 2077–2084 (1993).

[74]Z. Wang and G. Wang, "APD: the Antimicrobial Peptide Database.", Nucleic acids research **32**, D590–2 (2004).

[75]A. C. Conibear and D. J. Craik, "The chemistry and biology of theta defensins", Angewandte Chemie - International Edition **53**, 10613–10623 (2014).

[76]N. L. Daly, Y. K. Chen, K. J. Rosengren, U. C. Marx, M. L. Phillips, A. J. Waring, W. Wang, R. I. Lehrer, and D. J. Craik, "Retrocyclin-2: Structural analysis of a potent Anti-HIV ??-defensin", Biochemistry **46**, 9920–9928 (2007).

[77]K Kavanagh and S Dowd, "Histatins: antimicrobial peptides with therapeutic potential", J Pharm Pharmacol **56**, 285–289 (2004).

[78]C. H. Hsu, C. Chen, M. L. Jou, A. Y. L. Lee, Y. C. Lin, Y. P. Yu, W. T. Huang, and S. H. Wu, "Structural and DNA-binding studies on the bovine antimicrobial peptide, indolicidin: Evidence for multiple conformations involved in binding to membranes and DNA", Nucleic Acids Research **33**, 4053–4064 (2005).

[79]Z. Jiang, A. I. Vasil, J. D. Hale, R. E. W. Hancock, M. L. Vasil, and R. S. Hodges, "NIH Public Access", October **90**, 369–383 (2009).

[80]Y. Chen, M. T. Guarnieri, A. I. Vasil, M. L. Vasil, C. T. Mant, and R. S. Hodges, "Role of peptide hydrophobicity in the mechanism of action of α-helical antimicrobial peptides", Antimicrobial Agents and Chemotherapy **51**, 1398–1406 (2007).

[81]B. M. Burkhart, R. M. Gassman, D. A. Langs, W. A. Pangborn, W. L. Duax, and V. Pletnev, "Gramicidin D conformation, dynamics and membrane ion transport", Biopolymers - Peptide Science Section **51**, 129–144 (1999).

[82]N. Kessler, H. Schuhmann, S. Morneweg, U. Linne, and M. A. Marahiel, "The Linear Pentadecapeptide Gramicidin Is Assembled by Four Multimodular Nonribosomal Peptide Synthetases That Comprise 16 Modules with 56 Catalytic Domains", Journal of Biological Chemistry **279**, 7413–7419 (2004).

[83]H. Rindfleisch and H. Kleinkauf, "Biosynthesis of alamethicin", FEBS Letters **62**, 276–280 (1976).

[84]E. a. Porter, X Wang, H. S. Lee, B Weisblum, and S. H. Gellman, "Non-haemolytic beta-amino-acid oligomers.", Nature **404**, 565 (2000).

[85]G. Carmona, A. Rodriguez, D. Juarez, G. Corzo, and E. Villegas, "Improved protease stability of the antimicrobial peptide pin2 substituted with d-Amino acids", Protein Journal **32**, 456–466 (2013).

[86]A. A. Bahar and D. Ren, "Antimicrobial peptides", Pharmaceuticals **6**, 1543–1575 (2013).

[87]M.-D. Seo, H.-S. Won, J.-H. Kim, T. Mishig-Ochir, and B.-J. Lee, "Antimicrobial Peptides for Therapeutic Applications: A Review", Molecules **17**, 12276–12286 (2012).

[88]A. Rozek, C. L. Friedrich, and R. E. W. Hancock, "Structure of the Bovine Antimicrobial Peptide Indolicidin Bound to Dodecylphosphocoline and Sodium Dodecyl Sulfate Micelles", Biochemistry **39**, 15765–15774 (2000).

[89]M Bak, R. P. Bywater, M Hohwy, J. K. Thomsen, K Adelhorst, H. J. Jakobsen, O. W. Sørensen, and N. C. Nielsen, "Conformation of alamethicin in oriented phospho-

lipid bilayers determined by (15)N solid-state nuclear magnetic resonance.", Biophysical journal **81**, 1684–98 (2001).

[90]M. S. Sansom, "Alamethicin and related peptaibols–model ion channels.", European biophysics journal : EBJ **22**, 105–24 (1993).

[91]D. Sengupta, H. Leontiadou, A. E. Mark, and S. J. Marrink, "Toroidal pores formed by antimicrobial peptides show significant disorder", Biochimica et Biophysica Acta - Biomembranes **1778**, 2308–2317 (2008).

[92]H. Margus, K. Padari, and M. Pooga, "Cell-penetrating Peptides as Versatile Vehicles for Oligonucleotide Delivery", Molecular Therapy **20**, 525–533 (2012).

[93]Y.-Q. Xiong, A. S. Bayer, and M. R. Yeaman, "Inhibition of intracellular macromolecular synthesis in Staphylococcus aureus by thrombin-induced platelet microbicidal proteins.", The Journal of infectious diseases **185**, 348–356 (2002).

[94]D. Jantz and J. M. Berg, "Probing the DNA-binding affinity and specificity of designed zinc finger proteins", Biophysical Journal **98**, 852–860 (2010).

[95]E. F. Haney and R. E. W. Hancock, "Peptide design for antimicrobial and immunomodulatory applications", Biopolymers **100**, 572–583 (2013).

[96]N. Mookherjee and R. E. W. Hancock, *Cationic host defence peptides: Innate immune regulatory peptides as a novel approach for treating infections*, 2007.

[97]M. Chromek, Z. Slamová, P. Bergman, L. Kovács, L. Podracká, I. Ehrén, T. Hökfelt, G. H. Gudmundsson, R. L. Gallo, B. Agerberth, and A. Brauner, "The antimicrobial peptide cathelicidin protects the urinary tract against invasive bacterial infection.", Nature medicine **12**, 636–641 (2006).

[98]Y. Campbell, M. L. Fantacone, and A. F. Gombart, "Regulation of antimicrobial peptide gene expression by nutrients and by-products of microbial metabolism", European Journal of Nutrition **51**, 899–907 (2012).

[99]X. Ding, J. Boney-montoya, B. M. Owen, A. L. Bookout, C. Coate, D. J. Mangelsdorf, and S. A. Kliewer, "NIH Public Access", **16**, 387–393 (2013).

[100]B. Sperandio, B. Regnault, J. Guo, Z. Zhang, S. L. Stanley, P. J. Sansonetti, and T. Pédron, "Virulent Shigella flexneri subverts the host innate immune response through manipulation of antimicrobial peptide gene expression.", The Journal of experimental medicine **205**, 1121–32 (2008).

[101]M. G. Ryadnov, G. V. Mukamolova, A. S. Hawrani, J. Spencer, and R. Platt, "RE coil: An antimicrobial peptide regulator", Angewandte Chemie - International Edition **48**, 9676–9679 (2009).

[102]L. Ryan, B. Lamarre, T. Diu, J. Ravi, P. J. Judge, A. Temple, M. Carr, E. Cerasoli, B. Su, H. F. Jenkinson, G. Martyna, J. Crain, A. Watts, and M. G. Ryadnov, "Anti-antimicrobial peptides: Folding-mediated host defense antagonists", Journal of Biological Chemistry **288**, 20162–20172 (2013).

[103]G. A. McCubbin, S. Praporski, S. Piantavigna, D. Knappe, R. Hoffmann, J. H. Bowie, F. Separovic, and L. L. Martin, "QCM-D fingerprinting of membrane-active peptides", European Biophysics Journal **40**, 437–446 (2011).

[104]M. Rodahl, F. H????k, A. Krozer, P. Brzezinski, and B. Kasemo, "Quartz crystal microbalance setup for frequency and Q-factor measurements in gaseous and liquid environments", Review of Scientific Instruments **66**, 3924–3930 (1995).

[105]N. J. Cho, C. W. Frank, B Kasemo, and F Hook, "Quartz crystal microbalance with dissipation monitoring of supported lipid bilayers on various substrates", Nature Protocols **5**, 1096–1106 (2010).

[106]G. Sauerbrey, "Verwendung von Schwingquarzen zur Wägung dünner Schichten und zur Mikrowägung", Zeitschrift für Physik **155**, 206 (1964).

[107]M.-T. Lee, W.-C. Hung, F.-Y. Chen, and H. W. Huang, "Mechanism and kinetics of pore formation in membranes by water-soluble amphipathic peptides.", Proceedings of the National Academy of Sciences of the United States of America **105**, 5087–5092 (2008).

[108]M. V. Voinova, M. Rodahl, M. Jonson, and B. Kasemo, "Viscoelastic Acoustic Response of Layered Polymer Films at Fluid-Solid Interfaces: Continuum Mechanics Approach", Physica Scripta **59**, 391–396 (1999).

[109]A. Mechler, S. Praporski, K. Atmuri, M. Boland, F. Separovic, and L. L. Martin, "Specific and selective peptide-membrane interactions revealed using quartz crystal microbalance.", Biophysical journal **93**, 3907–16 (2007).

[110]M. Rodahl and B. Kasemo, "Frequency and dissipation-factor responses to localized liquid deposits on a QCM electrode", Sensors and Actuators B: Chemical **37**, 111–116 (1996).

[111]M. Rodahl, F. Höök, C. Fredriksson, C. A. Keller, A. Krozer, P. Brzezinski, M. Voinova, and B. Kasemo, "Simultaneous frequency and dissipation factor QCM measurements of biomolecular adsorption and cell adhesion", Faraday Discussions **107**, 229–246 (1997).

[112]H. A. Rydberg, A. Kunze, N. Carlsson, N. Altgärde, S. Svedhem, and B. Nordén, "Peptide-membrane interactions of arginine-tryptophan peptides probed using quartz crystal microbalance with dissipation monitoring", European Biophysics Journal **43**, 241–253 (2014).

[113]H Raghuraman and A. Chattopadhyay, "Interaction of melittin with membrane cholesterol: a fluorescence approach.", Biophysical journal **87**, 2419–32 (2004).

[114]P. J. Hore, *Nuclear Magnetic Resonance* (1994).

[115]H. Rattle, *An NMR primer for life scientists* (1996).

[116]D. G. Hamilton and R. H. Crabtree, "an {Nmr} Method for Distinguishing Classical From Nonclassical Structures in Transition-Metal Polyhydrides", J. Am. Chem. Soc. **110**, 4126 (1988).

[117]E. S. Salnikov, A. J. Mason, and B. Bechinger, "Membrane order perturbation in the presence of antimicrobial peptides by 2 H solid-state NMR spectroscopy", Biochimie **91**, 734–743 (2009).

[118]P. M. Macdonald and J. Seelig, "Phospholipids and proteins in biological membranes. 2H NMR as a method to study structure, dynamics, and interactions", American Chemical Society **20**, 221–228 (1987).

[119]A. Drechsler, G. Anderluh, R. S. Norton, and F. Separovic, "Solid-state NMR study of membrane interactions of the pore-forming cytolysin, equinatoxin II", Biochimica et Biophysica Acta - Biomembranes **1798**, 244–251 (2010).

[120]A. S. Ulrich, T. W. Poile, and A. Watts, "Deuterium NMR to study the surface of phospholipid bilayers", Bull Magn Tes **12**, 80–83 (1990).

[121]Bruker, *EMX User's Manual* (1998).

[122]G. R. Eaton, S. S. Eaton, D. P. Barr, and R. T. Weber, *Quantitative EPR: A practitioners guide* (2010), pp. 1–185.

[123]K. Schmidt-Rohr and H. Spiess, *Multidimensional Solid-State NMR and Polymers* (1994), pp. 466–478.

[124]K. Matsuo and K. Gekko, *Lipid-Protein Interactions*, Vol. 974 (2013), pp. 297–328.

[125]D. Kurad, G. Jeschke, and D. Marsh, "Lateral ordering of lipid chains in cholesterol-containing membranes: high-field spin-label EPR.", Biophysical journal **86**, 264–271 (2004).

[126]J Seelig, "Deuterium Magnetic Resonance: Theory and Application to Lipid Membranes", Q. Rev. Biophys. **10**, 353–418 (1977).

[127]A. Daillant, Jean and Gibaud, *X-ray and Neutron Reflectivity*, Vol. 770 (2009), pp. 133–182.

[128]X.-l. Zhou, S.-h. Chen, and N. E. W. York, "THEORETICAL FOUNDATION OF X-RAY AND NEUTRON REFLECTOMETRY of X-ray and neutron reflectometry", Physics Reports **257**, 223–348 (1995).

[129]J. Penfold, R. M. Richardson, A. Zarbakhsh, J. R. P. Webster, D. G. Bucknall, A. R. Rennie, R. a. L. Jones, T. Cosgrove, R. K. Thomas, J. S. Higgins, P. D. I. Fletcher, E. Dickinson, S. J. Roser, I. A. McLure, A. R. Hillman, R. W. Richards, E. J. Staples, A. N. Burgess, E. A. Simister, and J. W. White, "Recent advances in the study of chemical surfaces and interfaces by specular neutron reflection", Journal of the Chemical Society, Faraday Transactions **93**, 3899–3917 (1997).

[130]L. Clifton, M. Skoda, E. Daulton, a.V. Hughes, a.P. Le Brun, J. Lakey, and S. Holt, "Asymmetric phospholipid: lipopolysaccharide bilayers; a Gram-negative bacterial outer membrane mimic.", Journal of the Royal Society, Interface / the Royal Society **10**, 20130810 (2013).

[131]J. R. Lu and R. K. Thomas, "Neutron reflection from wet interfaces", Journal of the Chemical Society, Faraday Transactions **94**, 995–1018 (1998).

[132]D. Guard-friar, C.-h. Cben, and A. S. Engle, "Deuterium Isotope Effect on the stability of molecules: phospholipids", Journal of physical chemistry **89**, 1810–1813 (1985).

[133]C Chen, F Tow, and D. Berns, "Solvent Isotope Effect on the Differences in Structure and Stability between Normal and Deuterated Proteins", Biopolymers **23**, 887 (1984).

[134]M. D. Lad, F. Birembaut, L. a. Clifton, R. a. Frazier, J. R. P. Webster, and R. J. Green, "Antimicrobial peptide-lipid binding interactions and binding selectivity.", Biophysical journal **92**, 3575–3586 (2007).

[135]L Yang, T. a. Harroun, T. M. Weiss, L Ding, and H. W. Huang, "Barrel-stave model or toroidal model? A case study on melittin pores.", Biophysical journal **81**, 1475–1485 (2001).

[136]Y. Imura, N. Choda, and K. Matsuzaki, "Magainin 2 in action: distinct modes of membrane permeabilization in living bacterial and mammalian cells.", Biophysical journal **95**, 5757–5765 (2008).

[137]B. C. S. Chia, J. A. Carver, T. D. Mulhern, and J. H. Bowie, "Maculatin 1.1, an antimicrobial peptide from the Australian tree frog, Litoria genimaculata. Solution structure and biological activity", European Journal of Biochemistry **267**, 1894–1908 (2000).

[138]D. I. Fernandez, A. P. Le Brun, T. H. Lee, P. Bansal, M. I. Aguilar, M. James, and F. Separovic, "Structural effects of the antimicrobial peptide maculatin 1.1 on supported lipid bilayers", in European biophysics journal, Vol. 42, 1 (2013), pp. 47–59.

[139]T. J. Beveridge, *Structures of gram-negative cell walls and their derived membrane vesicles*, 1999.

[140]L. A. Clifton, M. W. A. Skoda, A. P. Le Brun, F. Ciesielski, I. Kuzmenko, S. A. Holt, and J. H. Lakey, "Effect of divalent cation removal on the structure of gram-negative bacterial outer membrane models", Langmuir **31**, 404–412 (2015).

[312]Malvern and M Instruments, "Dynamic Light Scattering : An Introduction in 30 Minutes", Technical Note MRK656-01, 1–8 (2011).

[141]L. Whitmore and B. A. Wallace, "DICHROWEB, an online server for protein secondary structure analyses from circular dichroism spectroscopic data", Nucleic Acids Research **32**, 668–673 (2004).

[142]N. Greenfield, "Using circular dichroism spectra to estimate protein secondary structure", Nat Protoc. **1**, 2876–2890 (2007).

[143]C. Avitabile, L. D. D'Andrea, and A. Romanelli, "Circular Dichroism studies on the interactions of antimicrobial peptides with bacterial cells.", Scientific reports **4**, 4293 (2014).

[144]H.-T. Cheng and E. London, "Preparation and Properties of Asymmetric Large Unilamellar Vesicles: Interleaflet Coupling in Asymmetric Vesicles Is Dependent on Temperature but Not Curvature", Biophysj **100**, 2671–2678 (2011).

[145]R. L. Alfred, E. A. Palombo, J. F. Panozzo, and M. Bhave, "The Antimicrobial Domains of Wheat Puroindolines Are Cell-Penetrating Peptides with Possible Intra-

cellular Mechanisms of Action", PLoS ONE **8** (2013) 10.1371/journal.pone.0075488.

[146]C Pabo, *Molecular technology. Designing proteins and peptides.* 1983.

[147]K Yue and K. a. Dill, "Inverse protein folding problem: designing polymer sequences.", Proceedings of the National Academy of Sciences of the United States of America **89**, 4163–4167 (1992).

[148]C. Mas-Moruno, F. Rechenmacher, and H. Kessler, "Cilengitide: the first anti-angiogenic small molecule drug candidate design, synthesis and clinical evaluation.", Anti-cancer agents in medicinal chemistry **10**, 753–768 (2010).

[149]M. G. Ryadnov, *Prescriptive peptide design* (2012), pp. 190–237.

[150]C. D. Fjell, J. A. Hiss, R. E. W. Hancock, and G. Schneider, "Designing antimicrobial peptides: form follows function.", Nature reviews. Drug discovery **11**, 37–51 (2012).

[151]M. K. P. Jayatunga, S. Thompson, and A. D. Hamilton, "α-Helix mimetics: Outwards and upwards", Bioorganic and Medicinal Chemistry Letters **24**, 717–724 (2014).

[152]M. Ryadnov, "Peptide alpha-helices for synthetic nanostructures.", Biochemical Society Transactions **35**, 487–91 (2007).

[153]J. Rossmeisl, I. Kristensen, M. Gregersen, K. W. Jacobsen, and J. K. Nørskov, "β-Sheet Preferences from First Principles", Journal of the American Chemical Society **125**, 16383–16386 (2003).

[154]C. N. Pace and J. M. Scholtz, "A helix propensity scale based on experimental studies of peptides and proteins.", Biophysical journal **75**, 422–427 (1998).

[155]P. D. Rakowska, H. Jiang, S. Ray, A. Pyne, B. Lamarre, M. Carr, P. J. Judge, J. Ravi, U. I. M. Gerling, B. Koksch, G. J. Martyna, B. W. Hoogenboom, A. Watts, J. Crain, C. R. M. Grovenor, and M. G. Ryadnov, "Nanoscale imaging reveals laterally expanding antimicrobial pores in lipid bilayers", PNAS **110**, 8918–8923 (2013).

[156]B. Lamarre, J. Ravi, and M. G. Ryadnov, “GeT peptides: a single-domain approach to gene delivery.”, Chemical communications (Cambridge, England) **47**, 9045–7 (2011).

[157]J. A. Killian, “Hydrophobic mismatch between proteins and lipids in membranes”, Biochimica et Biophysica Acta - Reviews on Biomembranes **1376**, 401–415 (1998).

[158]D Hultmark, a Engström, K Andersson, H Steiner, H Bennich, and H. G. Boman, “Insect immunity. Attacins, a family of antibacterial proteins from Hyalophora cecropia.”, The EMBO journal **2**, 571–576 (1983).

[159]H. Boman, “Cell-Free Immunity In Insects”, Annual Review of Microbiology **41**, 103–126 (1987).

[160]T. D. Lockey and D. D. Ourth, “Formation of pores in Escherichia coli cell membranes by a cecropin isolated from hemolymph of Heliothis virescens larvae.”, European journal of biochemistry / FEBS **236**, 263–71 (1996).

[161]J. M. Wu, P. S. Jan, H. C. Yu, H. Y. Haung, H. J. Fang, Y. I. Chang, J. W. Cheng, and H. M. Chen, “Structure and function of a custom anticancer peptide, CB1a”, Peptides **30**, 839–848 (2009).

[162]D. W. Hoskin and A. Ramamoorthy, *Studies on anticancer activities of antimicrobial peptides*, 2008.

[163]E Gazit, I. R. Miller, P. C. Biggin, M. S. Sansom, and Y Shai, “Structure and orientation of the mammalian antibacterial peptide cecropin P1 within phospholipid membranes.”, Journal of molecular biology **258**, 860–70 (1996).

[164]E Gazit, W. J. Lee, P. T. Brey, and Y Shai, “Mode of action of the antibacterial cecropin B2: a spectrofluorometric study.”, Biochemistry **33**, 10681–10692 (1994).

[165]E Gazit, a Boman, H. G. Boman, and Y Shai, “Interaction of the mammalian antibacterial peptide cecropin P1 with phospholipid vesicles.”, Biochemistry **34**, 11479–11488 (1995).

[166]M. J. Hope, M. B. Bally, G. Webb, and P. R. Cullis, "Production of large unilamellar vesicles by a rapid extrusion procedure. Characterization of size distribution, trapped volume and ability to maintain a membrane potential", BBA - Biomembranes **812**, 55–65 (1985).

[167]R. B. Merrifield, "Solid Phase Peptide Synthesis. I. The Synthesis of", Journal of the American Chemical Society **85**, 2149 (1963).

[168]D. F. Swinehart, "The Beer-Lambert Law", Journal of Chemical Education **39**, 333 (1962).

[169]S. C. Gill and P. H. von Hippel, "Calculation of protein extinction coefficients from amino acid sequence data", Analytical Biochemistry **182**, 319–326 (1989).

[170]I. Wiegand, K. Hilpert, and R. E. W. Hancock, "Agar and broth dilution methods to determine the minimal inhibitory concentration (MIC) of antimicrobial substances.", Nature protocols **3**, 163–75 (2008).

[171]H.-T. Chou, H.-W. Wen, T.-Y. Kuo, C.-C. Lin, and W.-J. Chen, "Interaction of cationic antimicrobial peptides with phospholipid vesicles and their antibacterial activity.", Peptides **31**, 1811–1820 (2010).

[172]J Dijkstra, J. L. Ryan, and F. C. Szoka, "A procedure for the efficient incorporation of wild-type lipopolysaccharide into liposomes for use in immunological studies.", Journal of immunological methods **114**, 197–205 (1988).

[173]P Koehl and M Levitt, "Structure-based conformational preferences of amino acids.", Proceedings of the National Academy of Sciences of the United States of America **96**, 12524–12529 (1999).

[174]X. Liu, R. Cao, S. Wang, J. Jia, and H. Fei, "Amphipathicity determines different cytotoxic mechanisms of lysine- or arginine-rich cationic hydrophobic peptides in cancer cells", Journal of Medicinal Chemistry, acs.jmedchem.5b02016 (2016).

[175]M. Dathe, T. Wieprecht, H. Nikolenko, L. Handel, W. L. Maloy, D. L. MacDonald, M. Beyermann, and M. Bienert, "Hydrophobicity, hydrophobic moment and angle subtended by charged residues modulate antibacterial and haemolytic activity of amphipathic helical peptides", FEBS Letters **403**, 208–212 (1997).

[176]D. Armstrong and R. Zidovetski, *Http://rzlab.ucr.edu/scripts/wheel/wheel.html*, 2001.

[177]M. F. Perutz, B. J. Pope, D. Owen, E. E. Wanker, and E. Scherzinger, "Aggregation of proteins with expanded glutamine and alanine repeats of the glutamine-rich and asparagine-rich domains of Sup35 and of the amyloid β-peptide of amyloid plaques", Proceedings of the National Academy of Sciences of the United States of America **99**, 5596–5600 (2002).

[178]L. Li, I. Vorobyov, and T. W. Allen, "The different interactions of lysine and arginine side chains with lipid membranes", Journal of Physical Chemistry B **117**, 11906–11920 (2013).

[179]M. R. R. de Planque and J. A. Killian*, "Protein–lipid interactions studied with designed transmembrane peptides: role of hydrophobic matching and interfacial anchoring (Review)", Molecular Membrane Biology **20**, 271–284 (2003).

[180]S. C. Chan, W. L. Yau, W Wang, D. K. Smith, F. S. Sheu, and H. M. Chen, "Microscopic observations of the different morphological changes caused by anti-bacterial peptides on Klebsiella pneumoniae and HL-60 leukemia cells.", Journal of peptide science : an official publication of the European Peptide Society **4**, 413–425 (1998).

[181]S. Kim, T.-J. Jeon, A. Oberai, D. Yang, J. J. Schmidt, and J. U. Bowie, "Transmembrane glycine zippers: physiological and pathological roles in membrane proteins.", Proceedings of the National Academy of Sciences of the United States of America **102**, 14278–83 (2005).

[182]K. Hall, T.-H. Lee, A. I. Mechler, M. J. Swann, and M.-I. Aguilar, "Real-time Measurement of Membrane Conformational States Induced by Antimicrobial Peptides: Balance Between Recovery and Lysis.", Scientific reports **4**, 5479 (2014).

[183]M. Mihajlovic and T. Lazaridis, "Charge distribution and imperfect amphipathicity affect pore formation by antimicrobial peptides", Biochimica et Biophysica Acta - Biomembranes **1818**, 1274–1283 (2012).

[184]Y. He and T. Lazaridis, "Activity Determinants of Helical Antimicrobial Peptides: A Large-Scale Computational Study", PLoS ONE **8** (2013) 10.1371/journal.pone.0066440.

[185]T. Arai and T. Ito, "Antimicrobial Activity of", Journal of bacteriology **93**, 59–64 (1967).

[186]J. Pogliano, N. Pogliano, and J. A. Silverman, "Daptomycin-mediated reorganization of membrane architecture causes mislocalization of essential cell division proteins", Journal of Bacteriology **194**, 4494–4504 (2012).

[187]K. Matsuzaki, M. Harada, T. Handa, S. Funakoshi, N. Fujii, H. Yajima, and K. Miyajima, "Magainin 1-induced leakage of entrapped calcein out of negatively-charged lipid vesicles", BBA - Biomembranes **981**, 130–134 (1989).

[188]T. Benachir and M. Lafleur, "Study of vesicle leakage induced by melittin", BBA - Biomembranes **1235**, 452–460 (1995).

[189]K. F. Wang, R. Nagarajan, and T. A. Camesano, "Differentiating antimicrobial peptides interacting with lipid bilayer: Molecular signatures derived from quartz crystal microbalance with dissipation monitoring", Biophysical Chemistry **196**, 53–57 (2015).

[190]J. R. Silvius, "Thermotropic phase transitions of pure lipids in model membranes and their modifications by membrane proteins", in *Lipid-protein interactions* (1982).

[191]K. L. Weirich, J. N. Israelachvili, and D. K. Fygenson, "Bilayer edges catalyze supported lipid bilayer formation", Biophysical Journal **98**, 85–92 (2010).

[192]S. B. Nielsen and D. E. Otzen, "Quartz crystal microbalances as tools for probing protein-membrane interactions", Methods in Molecular Biology **974**, 1–21 (2013).

[193]K. F. Wang, R. Nagarajan, and T. A. Camesano, "Antimicrobial peptide alamethicin insertion into lipid bilayer: A QCM-D exploration", Colloids and Surfaces B: Biointerfaces **116**, 472–481 (2014).

[194]T. M. Ferreira, F. Coreta-Gomes, O. H. S. Ollila, M. J. Moreno, W. L. C. Vaz, and D. Topgaard, "Cholesterol and POPC segmental order parameters in lipid membranes: solid state 1H-13C NMR and MD simulation studies.", Physical chemistry chemical physics : PCCP **15**, 1976–89 (2013).

[195]S. J. Kang, H. Y. Ji, and B. J. Lee, "Anticancer activity of undecapeptide analogues derived from antimicrobial peptide, Brevinin-1EMa", Archives of Pharmacal Research **35**, 791–799 (2012).

[196]W. Wang, D. K. Smith, K. Moulding, and H. M. Chen, "The dependence of membrane permeability by the antibacterial peptide cecropin B and its analogs, CB-1 and CB-3, on liposomes of different composition", Journal of Biological Chemistry **273**, 27438–27448 (1998).

[197]A. Pyne, M.-P. Pfeil, I. Bennett, J. Ravi, P. Iavicoli, B. Lamarre, A. Roethke, S. Ray, H. Jiang, A. Bella, B. Reisinger, D. Yin, B. Little, J. Munoz-Garcia, E. Cerasoli, P. Judge, N. Faruqui, L. Calzolai, A. Henrion, G. Martyna, C. Grovenor, J. Crain, B. Hogenboom, A. Watts, and M. Ryadnov, "Engineering monolayer poration for rapid exfoliation of microbial membranes", Chem. Sci. (2016) 10.1039/C6SC02925F.

[313]S. Amos, L. Vermeer, P. Ferguson, J. Kozlowska, M. Davy, T. Bui, A. Drake, C. Lorenz, and A. Mason, "Antimicrobial peptide potency is facilitated by greater conformational flexibility when binding to gram-negative bacterial inner membranes", Scientific Reports **6** (2016) 10.1038/srep37639.

[198]J. Vörös, "The density and refractive index of adsorbing protein layers.", Biophysical journal **87**, 553–61 (2004).

[199]M. V. Voinova, M. Jonson, and B. Kasemo, "'Missing mass' effect in biosensor's QCM applications", Biosensors and Bioelectronics **17**, 835–841 (2002).

[200]G. Dunér, E. Thormann, and A. Dedinaite, "Quartz Crystal Microbalance with Dissipation (QCM-D) studies of the viscoelastic response from a continuously growing grafted polyelectrolyte layer", Journal of Colloid and Interface Science **408**, 229–234 (2013).

[201]K. F. Wang, R. Nagarajan, C. M. Mello, and T. A. Camesano, "Correction to " Characterization of Supported Lipid Bilayer Disruption by Chrysophsin 3 Using QCM-D "", Journal of Physical Chemistry B, 410498 (2013).

[202]H. Eibl, "Synthesis of glycerophospholipids", Chemistry and Physics of Lipids **26**, 405–429 (1980).

[203]F. Sixl and A. Watts, "Headgroup interactions in mixed phospholipid bilayers", Proceedings of the National Academy of Sciences **80**, 1613–1615 (1983).

[204]D. R. Kodali, A. Tercyak, D. A. Fahey, and D. M. Small, "Acyl migration in 1,2-dipalmitoyl-sn-glycerol", Chemistry and Physics of Lipids **52**, 163–170 (1990).

[205]M. a. Sani, D. K. Weber, F Delaglio, F Separovic, and J. D. Gehman, "A practical implementation of de-Pake-ing via weighted Fourier transformation", PeerJ **1**, e30 (2013).

[206]A. A. Duralski, P. J. R. Spooner, and A. Watts, "Synthesis of optically active polyunsaturated diacylglycerols", Tetrahedron Letters **30**, 3585–3588 (1989).

[207]A. A. Duralski, P. J. R. Spooner, S. E. Rankin, and A. Watts, "Synthesis of isotopically labelled cardiolipins", Tetrahedron Letters **39**, 1607–1610 (1998).

[208]G. Sabitha, R. S. Babu, M. Rajkumar, R. Srividya, and J. S. Yadav, "A highly efficient, mild, and selective cleavage of ??-methoxyethoxymethyl (MEM) ethers by cerium(III) chloride in acetonitrile", Organic Letters **3**, 1149–1151 (2001).

[209]D Buchnea, "Detritylation by silicic acid boric acid column chromatography", Lipids **9**, 55–57 (1974).

[210]N. A. Bragina and V. V. Chupin, "Methods of synthesis of deuterium labelled lipids", Uspekhi Khimii **66**, 1077–1090 (1997).

[211]G. E. Pake, “Nuclear Resonance Absorption in Hydrated Crystals: Fine Structure of the Proton Line”, The Journal of Chemical Physics **16**, 327–336 (1948).

[212]A. Pines, D. J. Ruben, S. Vega, and M. Mehring, “New approach to high-resolution proton NMR in solids: Deuterium spin decoupling by multiple-quantum transitions”, Physical Review Letters **36**, 110–113 (1976).

[213]F. Delaglio, S. Grzesiek, G. W. Vuister, G. Zhu, J. Pfeifer, and A. Bax, “NMRPipe: A multidimensional spectral processing system based on UNIX pipes”, Journal of Biomolecular NMR **6**, 277–293 (1995).

[214]B. Bechinger, “Rationalizing the membrane interactions of cationic amphipathic antimicrobial peptides by their molecular shape”, Current Opinion in Colloid and Interface Science **14**, 349–355 (2009).

[215]M Lafleur, B Fine, E Sternin, P. R. Cullis, and M Bloom, “Smoothed orientational order profiles of lipid bilayers by 2H-nuclear magnetic resonance.”, Biophys. J. **56**, 1037–1041 (1989).

[216]A. Grau-Campistany, E. Strandberg, P. Wadhwani, J. Reichert, J. Bürck, F. Rabanal, and A. S. Ulrich, “Hydrophobic mismatch demonstrated for membranolytic peptides, and their use as molecular rulers to measure bilayer thickness in native cells”, Scientific Reports **5**, 9388 (2015).

[217]K. Matsuzaki, “Control of cell selectivity of antimicrobial peptides”, Biochimica et Biophysica Acta (BBA) - Biomembranes **1788**, 1687–1692 (2009).

[218]R Bals, “Epithelial antimicrobial peptides in host defense against infection.”, Respiratory research **1**, 141–150 (2000).

[219]J. Zhong, W. Zheng, L. Huang, Y. Hong, L. Wang, Y. Qiu, and Y. Sha, “PrP106-126 amide causes the semi-penetrated poration in the supported lipid bilayers”, Biochimica et Biophysica Acta - Biomembranes **1768**, 1420–1429 (2007).

[220]A Villiers, “Blanchiment du coton 1 l’eau oxygeneb”, Compt. Rend. Acad. Sci. Paris, 112 (1891).

[221]Y. Gan, Y. Zhang, C. Xiao, C. Zhou, and Y. Zhao, "A novel preparation of methyl-beta-cyclodextrin from dimethyl carbonate and beta-cyclodextrin", Carbohydrate Research **346**, 389–392 (2011).

[222]W. Saenger, J. Jacob, K. Gessler, T. Steiner, D. Hoffmann, H. Sanbe, K. Koizumi, S. M. Smith, and T. Takaha, "Structures of the Common Cyclodextrins and Their Larger AnaloguesBeyond the Doughnut", Chemical Reviews **98**, 1787–1802 (1998).

[223]B. Mccormack and G. Gregoriadis, "Comparative studies of the fate of free and liposome-entrapped hydroxypropyl-B-cyclodextrin/ drug complexes after intravenous injection into rats: implications in drug delivery", Biochimica et Biophysica Acta (BBA) **1291**, 237–244 (1996).

[224]A. Berthod, S. S. C. Chang, J. P. S. Kullman, and D. W. Armstrong, "Practice and mechanism of HPLC oligosaccharide separation with a cyclodextrin bonded phase", Talanta **47**, 1001–1012 (1998).

[225]*https://en.wikipedia.org/wiki/Febreze*.

[226]R Leventis and J. R. Silvius, "Use of cyclodextrins to monitor transbilayer movement and differential lipid affinities of cholesterol.", Biophysical journal **81**, 2257–2267 (2001).

[227]S. K. Rodal, G. Skretting, Ø. Garred, F. Vilhardt, B. V. Deurs, and K. Sandvig, "Extraction of Cholesterol with Methyl- -Cyclodextrin Perturbs Formation of Clathrin-coated Endocytic Vesicles", **10**, 961–974 (1999).

[228]V Kainu, M Hermansson, and P Somerharju, "Introduction of phospholipids to cultured cells with cyclodextrin", J. Lipid Res. **51**, 3533–3541 (2010).

[229]H.-T. Cheng, Megha, and E. London, "Preparation and properties of asymmetric vesicles that mimic cell membranes: effect upon lipid raft formation and transmembrane helix orientation.", The Journal of biological chemistry **284**, 6079–92 (2009).

[230]H.-T. Cheng and E. London, "Preparation and Properties of Asymmetric Large Unilamellar Vesicles: Interleaflet Coupling in Asymmetric Vesicles Is Dependent on Temperature but Not Curvature", Biophysical Journal **100**, 2671–2678 (2011).

[231]S. Chiantia, P. Schwille, A. S. Klymchenko, and E. London, "Asymmetric GUVs prepared by M??CD-mediated lipid exchange: An FCS study", Biophysical Journal **100**, L1–L3 (2011).

[232]M. Son and E. London, "The Dependence of Lipid Asymmetry upon Phosphatidylcholine Acyl Chain Structure", The Journal of Lipid Research **54**, 223–231 (2012).

[233]Z. Huang and E. London, "Effect of cyclodextrin and membrane lipid structure upon cyclodextrin-lipid interaction", Langmuir **29**, 14631–14638 (2013).

[234]M. S. Jablin, M. Flasiński, M. Dubey, D. R. Ratnaweera, M. Broniatowski, P. Dynarowicz-Łatka, and J. Majewski, "Effects of β-cyclodextrin on the structure of sphingomyelin/cholesterol model membranes", Biophysical Journal **99**, 1475–1481 (2010).

[235]F. A. Heberle, D. Marquardt, M. Doktorova, B. Geier, R. F. Standaert, P. Heftberger, B. Kollmitzer, J. D. Nickels, R. A. Dick, G. W. Feigenson, J. Katsaras, E. London, and G. Pabst, "Sub-nanometer Structure of an Asymmetric Model Membrane: Interleaflet Coupling Influences Domain Properties", Langmuir, acs.langmuir.5b04562 (2016).

[236]A. Watts and D. Marsh, "ESR spin label studies of liposomes", in *Liposomes: from physical structure to therapeutic application* (1981), pp. 139–188.

[237]W. L. Hubbell and H. M. McConnell, "Molecular motion in spin-labeled phospholipids and membranes.", Journal of the American Chemical Society **93**, 314–326 (1971).

[238]K. Schorn and D. Marsh, "Extracting order parameters from powder EPR lineshapes for spin-labelled lipids in membranes", Spectrochimica Acta Part A: Molecular and Biomolecular Spectroscopy **53**, 2235–2240 (1997).

[239]B. Gaffney, *Spin Labelling: Theory and Applications* (1976), pp. 55–132.

[240]I. Visco, S. Chiantia, and P. Schwille, "Asymmetric supported lipid bilayer formation via methyl-beta-cyclodextrin mediated lipid exchange: Influence of asymmetry on lipid dynamics and phase behavior", Langmuir **30**, 7475–7484 (2014).

[241]G Sessa and G Weissmann, "Phospholipid spherules (liposomes) as a model for biological membranes.", Journal of lipid research **9**, 310–318 (1968).

[242]K. Murzyn, T. Róg, and M. Pasenkiewicz-Gierula, "Phosphatidylethanolamine-phosphatidylglyc bilayer as a model of the inner bacterial membrane.", Biophysical journal **88**, 1091–103 (2005).

[243]J. a. Op den Kamp, "Lipid asymmetry in membranes.", Annual review of biochemistry **48**, 47–71 (1979).

[244]D. L. Bratton, V. A. Fadok, D. A. Richter, J. M. Kailey, L. A. Guthrie, and P. M. Henson, "Appearance of Phosphatidylserine on Apoptotic Cells Requires Calcium-mediated Nonspecific Flip-Flop and Is Enhanced by Loss of the Aminophospholipid Translocase *", **272**, 26159–26165 (1997).

[245]M. P.Komarat, "The lipid composition of a halotolerant species of Staphylococcus epidermidis", Biochimica et Biophysica Acta (BBA) - Biomembranes **398**, 464–484 (1975).

[246]R. C. and W. C., "Lipopolysaccharide Endotoxins", October, 1–57 (2002).

[247]A. D. Bangham and R. W. Horne, "Negative staining of phospholipids and their structural modification by surface-active agents as observed in the electron microscope.", Journal of Molecular Biology **8**, 660–668 (1964).

[248]S. Chiantia, A. S. Klymchenko, and E. London, "A novel leaflet-selective fluorescence labeling technique reveals differences between inner and outer leaflets at high bilayer curvature", Biochimica et Biophysica Acta - Biomembranes **1818**, 1284–1290 (2012).

[249]M. C. Shaw, "Microdetermination of phosphorus in proteins", Analytical Biochemistry **44**, 288–291 (1971).

[250]J. M. Leenhouts and B. D. Kruijff, "Membrane potential-driven translocation of a lipid-conjugated rhodamine", Biochimica et biophysica acta **1237**, 121–126 (1995).

[251]D. Marquardt, B. Geier, and G. Pabst, *Asymmetric lipid membranes: Towards more realistic model systems*, 2015.

[252]N. Ku??erka, M. P. Nieh, and J. Katsaras, "Fluid phase lipid areas and bilayer thicknesses of commonly used phosphatidylcholines as a function of temperature", Biochimica et Biophysica Acta - Biomembranes **1808**, 2761–2771 (2011).

[253]T. J. Silhavy, D. Kahne, and S. Walker, "The bacterial cell envelope.", Cold Spring Harbor perspectives in biology **2**, 1–16 (2010).

[254]D. A. Kelkar and A. Chattopadhyay, "The gramicidin ion channel: a model membrane protein.", Biochimica et Biophysica Acta-Biomembranes **1768**, 2011–2025 (2007).

[255]J. H. Bolivar, J. C. Muñoz-García, T. Castro-Dopico, P. M. Dijkman, P. J. Stansfeld, and A. Watts, "Interaction of lipids with the neurotensin receptor 1", Biochimica et Biophysica Acta - Biomembranes **1858**, 1278–1287 (2016).

[256]C. Zhang, Y. Srinivasan, D. H. Arlow, J. J. Fung, D. Palmer, Y. Zheng, H. F. Green, A. Pandey, R. O. Dror, D. E. Shaw, W. I. Weis, S. R. Coughlin, and B. K. Kobilka, "High-resolution crystal structure of human protease-activated receptor 1.", Nature **492**, 387–92 (2012).

[257]J. White, N Noinaj, Y Shibata, J Love, B Kloss, F Xu, J Gvozenovic-Jeremic, P Shah, J Shiloach, C. Tate, and R Grisshammer, "Structure of the agonist-bound neurotensin receptor", Nature **409**, 508–513 (2012).

[258]P. M. Dijkman, "DPhil Thesis; publication in preparation", PhD thesis ().

[259]E. Strandberg, S. Özdirekcan, D. T. Rijkers, P. C. van der Wel, R. E. Koeppe, R. M. Liskamp, and J. Antoinette Killian, "Tilt Angles of Transmembrane Model Peptides in Oriented and Non-Oriented Lipid Bilayers as Determined by 2H Solid-State NMR", Biophysical Journal **86**, 3709–3721 (2004).

[260]J. M. Rankenberg, V. V. Vostrikov, D. V. Greathouse, C. V. Grant, S. J. Opella, and R. E. Koeppe, "Properties of membrane-incorporated WALP peptides that are anchored on only one end", Biochemistry **51**, 10066–10074 (2012).

[261]A. Holt, L. Rougier, V. Réat, F. Jolibois, O. Saurel, J. Czaplicki, J. Antoinette Killian, and A. Milon, "Order parameters of a transmembrane helix in a fluid bilayer: Case study of a WALP peptide", Biophysical Journal **98**, 1864–1872 (2010).

[262]Q. Lin and E. London, "Preparation of artificial plasma membrane mimicking vesicles with lipid asymmetry.", PloS one **9**, e87903 (2014).

[263]B. Christiaens, S. Symoens, S. Vanderheyden, Y. Engelborghs, A. Joliot, A. Prochiantz, J. Vandekerckhove, M. Rosseneu, and B. Vanloo, "Tryptophan fluorescence study of the interaction of penetratin peptides with model membranes", European Journal of Biochemistry **269**, 2918–2926 (2002).

[264]P. J. Harding, H. Attrill, J. Boehringer, S. Ross, G. H. Wadhams, E. Smith, J. P. Armitage, and A. Watts, "Constitutive dimerization of the G-Protein coupled receptor, neurotensin receptor 1, reconstituted into phospholipid bilayers", Biophysical Journal **96**, 964–973 (2009).

[265]K. Matsuzaki, O. Murase, N. Fujii, and K. Miyajima, "An antimicrobial peptide, magainin 2, induced rapid flip-flop of phospholipids coupled with pore formation and peptide translocation", Biochemistry **35**, 11361–11368 (1996).

[266]P van der Wel Strandberg, E., Killian, J.A. and Koeppe, R.E., "Geometry and Intrinsic tilt of Tryptophane-Anchored Transmembrane a-Helix determined by 2H NMR", Biophys.J. **83** (2002).

[267]H. E. Mason and D. Spaner, "Competitive ability of wheat in conventional and organic management systems: A review of the literature", Canadian Journal of Plant Science **86**, 333–343 (2006).

[268]D. Li, "Fluorescence Resonance Energy Transfer (FRET)", IUPAC Compendium of Chemical Terminology, 737–737 (2008).

[269]K.-M. Turnbull and S. Rahman, "Endosperm Texture in Wheat", Journal of Cereal Science **36**, 327–337 (2002).

[270]J. E. Blochet, C. Chevalier, E. Forest, E. Pebay-Peyroula, M. F. Gautier, P. Joudrier, M. Pézolet, and D. Marion, "Complete amino acid sequence of puroindoline, a new basic and cystine-rich protein with a unique tryptophan-rich domain, isolated from wheat endosperm by Triton X-114 phase partitioning", FEBS Letters **329**, 336–340 (1993).

[271]T. Le Bihan, J.-É. Blochet, A. Désormeaux, D. Marion, and M. Pézolet, "Determination of the secondary structure and conformation of puroindolines by Infrared and Raman spectroscopy.", Biochemistry **35**, 12712–12722 (1996).

[272]L. Day, D. G. Bhandari, P. Greenwell, S. A. Leonard, and J. D. Schofield, "Characterization of wheat puroindoline proteins", FEBS Journal **273**, 5358–5373 (2006).

[273]C. Morris and G. Greenblatt, *Isolation and characterization of multiple forms of friabilin*, 1994.

[274]A. J. De Jesus and T. W. Allen, "The determinants of hydrophobic mismatch response for transmembrane helices", Biochimica et Biophysica Acta - Biomembranes **1828**, 851–863 (2013).

[275]P. R. Wiley, P. Tosi, A. Evrard, A. Lovegrove, H. D. Jones, and P. R. Shewry, "Promoter analysis and immunolocalisation show that puroindoline genes are exclusively expressed in starchy endosperm cells of wheat grain", Plant Molecular Biology **64**, 125–136 (2007).

[276]M. J. Giroux, T. Sripo, S. Gerhardt, and J. Sherwood, "Puroindolines: Their Role in Grain Hardness and Plant Defence", Biotechnology and Genetic Engineering Reviews **20**, 277–290 (2003).

[277]L Dubreil, V Vié, S Beaufils, D Marion, and a Renault, "Aggregation of puroindoline in phospholipid monolayers spread at the air-liquid interface.", Biophysical journal **85**, 2650–2660 (2003).

[278]M. Bhave and C. F. Morris, "Molecular genetics of puroindolines and related genes: Allelic diversity in wheat and other grasses", Plant Molecular Biology **66**, 205–219 (2008).

[279]M. J. Giroux and C. F. Morris, "A glycine to serine change in puroindoline b is associated with wheat grain hardness and low levels of starch-surface friabilin", Theoretical and Applied Genetics **95**, 857–864 (1997).

[280]J. M. Martin, R. C. Frohberg, C. F. Morris, L. E. Talbert, and M. J. Giroux, "Milling and bread-baking traits associated with puroindoline sequence type in hard red spring wheat", Crop Science **41**, 228–234 (2001).

[281]C. F. Morris, "Puroindolines: The molecular genetic basis of wheat grain hardness", Plant Molecular Biology **48**, 633–647 (2002).

[282]L. A. Clifton, R. J. Green, and R. A. Frazier, "Puroindoline-b mutations control the lipid binding interactions in mixed puroindoline-a:puroindoline-b systems", Biochemistry **46**, 13929–13937 (2007).

[283]L. A. Clifton, R. J. Green, A. V. Hughes, and R. A. Frazier, "Interfacial structure of wild-type and mutant forms of puroindoline-b bound to DPPG monolayers", Journal of Physical Chemistry B **112**, 15907–15913 (2008).

[284]L. A. Clifton, M. D. Lad, R. J. Green, and R. A. Frazier, "Single amino acid substitutions in puroindoline-b mutants influence lipid binding properties", Biochemistry **46**, 2260–2266 (2007).

[285]M. R. Sanders, L. A. Clifton, R. A. Frazier, and R. J. Green, "The role of lipid composition on the interaction between a tryptophan-rich protein and model bacterial membranes.", Langmuir : the ACS journal of surfaces and colloids (2016) 10.1021/acs.langmuir.5b04628.

[286]A. Czogalla, M. Grzybek, W. Jones, and Ü. Coskun, "Validity and applicability of membrane model systems for studying interactions of peripheral membrane pro-

teins with lipids", Biochimica et Biophysica Acta - Molecular and Cell Biology of Lipids **1841**, 1049–1059 (2014).

[287]M. Kooijman, R. Orsel, M. Hessing, R. Hamer, and A. Bekkers, "Spectroscopic Characterisation of the Lipid-binding Properties of Wheat Puroindolines", Journal of Cereal Science **26**, 145–159 (1997).

[288]E. J Schimshack and H. M. McConnell, "Lateral phase separation in phospholipid membranes", Biochemistry **12**, 2351–2360 (1973).

[289]J. E. Watts and R. L. Luff, "The importance of the radical mules operation and tail length for the control of breech strike in scouring Merino sheep", Aust Vet J **7**, 356–357 (54).

[290]C. M. Hollinshead, M. M. Hanna, D. J. Barlow, V. De Biasi, D. G. Bucknall, P. Camilleri, A. J. Hutt, M. J. Lawrence, J. R. Lu, and T. J. Su, "Neutron reflection from a dimyristoylphosphatidylcholine monolayer adsorbed on a hydrophobised silicon support", Biochimica et Biophysica Acta - Biomembranes **1511**, 49–59 (2001).

[291]A. V. Hughes, J. R. Howse, A. Dabkowska, R. A. L. Jones, M. J. Lawrence, and S. J. Roser, "Floating lipid bilayers deposited on chemically grafted phosphatidylcholine surfaces", Langmuir **24**, 1989–1999 (2008).

[292]L. K. Tamm and H. M. McConnell, "Supported phospholipid bilayers.", Biophysical journal **47**, 105–13 (1985).

[293]H. P. Wacklin, "Composition and asymmetry in supported membranes formed by vesicle fusion", Langmuir **27**, 7698–7707 (2011).

[294]a.V. Hughes, "Rascal Sourceforge",

[295]M Born and E Wolf, *Principles of optics* (Oxford, UK, 1970).

[296]L. A. Clifton, C. Neylon, and J. H. Lakey, *Examining Protein-Lipid Complexes Using Neutron Scattering* (2013), pp. 119–150.

[297]W. R. Morrison, *Wheat Lipids Composition*, 1978.

[298]M. J. Giroux and C. F. Morris, "Wheat grain hardness results from highly conserved mutations in the friabilin components puroindoline a and b", Proceedings of the National Academy of Sciences **95**, 6262–6266 (1998).

[299]T. M. Ikeda, N. Ohnishi, T. Nagamine, S. Oda, T. Hisatomi, and H. Yano, "Identification of new puroindoline genotypes and their relationship to flour texture among wheat cultivars", Journal of Cereal Science **41**, 1–6 (2005).

[300]V. Sass, T. Schneider, M. Wilmes, C. Körner, A. Tossi, N. Novikova, O. Shamova, and H. G. Sahl, "Human β-defensin 3 inhibits cell wall biosynthesis in staphylococci", Infection and Immunity **78**, 2793–2800 (2010).

[301]L. D. Walensky and G. H. Bird, "Hydrocarbon-stapled peptides: Principles, practice, and progress", Journal of Medicinal Chemistry **57**, 6275–6288 (2014).

[302]H. Peacock, J. Luo, T. Yamashita, J. Luccarelli, S. Thompson, and A. D. Hamilton, "Non-covalent SO interactions control conformation in a scaffold that disrupts islet amyloid polypeptide fibrillation", Chem. Sci. **00**, 1–5 (2016).

[303]Y. Niu, H. Wu, Y. Li, Y. Hu, S. Padhee, Q. Lin, C. Cao, and J. Cai, "AApeptides as a new class of antimicrobial agents", Org. Biomol. Chem. **11**, 4283–4280 (2013).

[304]S. J. Lam, N. M. O'Brien-Simpson, N. Pantarat, A. Sulistio, E. H. H. Wong, Y.-Y. Chen, J. C. Lenzo, J. A. Holden, A. Blencowe, E. C. Reynolds, and G. G. Qiao, "Combating multidrug-resistant Gram-negative bacteria with structurally nanoengineered antimicrobial peptide polymers", Nature Microbiology **1**, 16162 (2016).

[305]R. P. Kowalski, E. G. Romanowski, K. A. Yates, and F. S. Mah, "An Independent Evaluation of a Novel Peptide Mimetic, Brilacidin (PMX30063), for Ocular Anti-infective.", Journal of ocular pharmacology and therapeutics **32**, 23–27 (2016).

[306]B. T. A. Macmurray and W. R. Morrison, "COMPOSITION OF WHEAT-FLOUR LIPIDS", J. Sci. Fd Agrici. Fd Agric **21** (1970).

[307]J. H. Lee, V. Agarwal, A. Bose, G. F. Payne, and S. R. Raghavan, "Transition from unilamellar to bilamellar vesicles induced by an amphiphilic biopolymer", Physical Review Letters **96**, 2–5 (2006).

[308]M. C. Orwick, P. J. Judge, J. Procek, L. Lindholm, A. Graziadei, A. Engel, G. Gr??bner, and A. Watts, "Detergent-free formation and physicochemical characterization of nanosized lipid-polymer complexes: Lipodisq", Angewandte Chemie - International Edition **51**, 4653–4657 (2012).

[309]M. C. Orwick, P. J. Judge, J. Procek, L. Lindholm, A. Graziadei, A. Engel, G. Gr??bner, and A. Watts, "Detergent-free formation and physicochemical characterization of nanosized lipid-polymer complexes: Lipodisq", Angewandte Chemie - International Edition **51**, 4653–4657 (2012).

[310]S. C. Lee, T. J. Knowles, V. L. G. Postis, M. Jamshad, R. A. Parslow, Y.-p. Lin, A. Goldman, P. Sridhar, M. Overduin, S. P. Muench, and T. R. Dafforn, "A method for detergent-free isolation of membrane proteins in their local lipid environment", Nature Protocols **11**, 1149–1162 (2016).

[311]V. Postis, S. Rawson, J. K. Mitchell, S. C. Lee, R. A. Parslow, T. R. Dafforn, S. A. Baldwin, and S. P. Muench, "The use of SMALPs as a novel membrane protein scaffold for structure study by negative stain electron microscopy", Biochimica et Biophysica Acta - Biomembranes **1848**, 496–501 (2015).

Appendices

Appendix A

^{2}H-Labelled Phospholipid Synthesis

Experimental data and reaction procedures to produce POPG-d_2, POPE-d_4, DMPG-d_2 and DMPE-d_4 used in Chapter 3 and 5 are presented below.

(*S*)-4-(((2-methoxyethoxy)methoxy)methyl)-2,2-dimethyl-1,3-dioxolane (2-1)

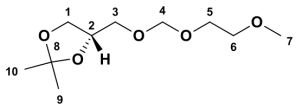

According to a literature procedure [A1], 1,2-isopropylidene-sn-glycerol (15 g, 113 mmol) was dissolved in dry DCM (150 mL) under nitrogen at 0°C. *N,N*-Diisopropylethylamine (30 ml, 170 mmol) was added to the solution and left to stir for 5 min. 2-methoxyethoxymethyl chloride (19.5 ml, 170 mmol) was added dropwise and the mixture was left to stir overnight. Ammonium chloride (150 ml) was added and the solution was left to stir for 5 min. The reaction mixture was poured into a separating funnel, the organic phase removed and the aqueous phase extracted with chloroform (3 x 200 ml). The combined organic layers were dried ($MgSO_4$) and the solvent removed *in vacuo*. The residue was purified by flash column chromatography (2 : 1 PE: Et_2O) to yield compound **2-1** (15.6 g, 64.0 mmol, 57 %) as a colourless oil: $[\alpha]_D^{20}$ +18.00 (*c* 3.0, $CHCl_3$); δ_H (500MHz, $CDCl_3$) 4.75 (2H, s, H4), 4.29 (1H, m, H2), 4.06 (1H, dd, *J* 6.4,8.3, H1), 3.68-3.73 (3H, m, H1, H5), 3.60 (2H, d, *J* 5.6, H3), 3.55 (2H, m, H6), 3.38 (3H, s, H7), 1.42, 1.35 (6H, s, H9, H10); δ_C (125MHz, $CDCl_3$) 109.5 (C8), 96.0 (C4), 74.7 (C2), 71.6 (C6), 68.9 (C3), 66.9 (C5), 66.6 (C1), 59.0 (C7), 26.8, 25.4 (C9, C10); υ_{max} 2912, 2813, 1650, 1053; HRMS (ESI) found 243.1207, $C_{10}H_{20}NaO_5$ $[M+Na]^+$ requires 243.1203.

(*S*)-5-(2-methoxyethoxy)-2-methylpentane-1,2-diol (2-2)

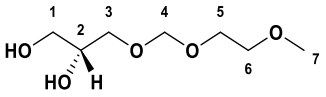

Modifying a literature procedure [A1], **2-1** (30 g, 123 mmol) was dissolved in 1 % aqueous acetic acid (445 ml) and the solution was left to stir for 1 h at 60 °C. The solvent was removed *in vacuo*, and the residue was purified by flash column chromatography (100 : 1 Et_2O : MeOH) to yield diol **2-2** (20.0 g, 112 mmol, 91 %) as a colourless oil: $[\alpha]_D^{20}$ - 2.2 (*c* 2.75, $CHCl_3$); δ_H (500MHz, $CDCl_3$) 4.73 (2H, s, H4), 3.86 (1H, m, H2), 3.71 (2H, m, H5), 3.69-3.57 (4H, m, H1, H3), 3.56 (2H, m, H6), 3.38 (3H, s, H7); δ_C (125MHz, $CDCl_3$) 95.9 (C4), 71.7 (C6), 70.8 (C2), 70.1 (C3), 67.1 (C5), 63.6 (C1), 59.0 (C7); υ_{max} 3404, 2929, 2881, 1035; HRMS (ESI) found 203.0897, $C_7H_{16}NaO_5$ $[M+Na]^+$ requires 203.0890.

(*S*)-2-hydroxy-3-((2-methoxyethoxy)methoxy)propyl palmitate (2-3)

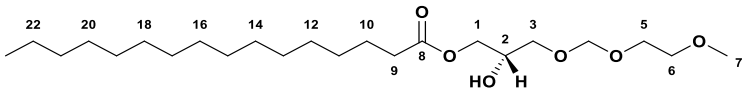

Modifying a literature procedure [A2], DMAP (10.4 g, 83.2 mmol) was added to a solution of diol **2** (10.0 g, 55.5 mmol) in DCM (280.0 ml), and cooled to -10 °C using an ice bath with 66 % NH_4Cl *wt/wt*). Palmitoyl chloride (19.6 ml, 65.0 mmol) was added dropwise and the solution was left to stir overnight. The solvent was removed *in vacuo*, Et_2O (200.0 ml) was added, and the solution filtered. The solvent was again removed *in vacuo*, and the residue was purified by flash column chromatography (2 : 1 PE : Et_2O) to yield compound **2-3** (14.0 g, 33.3 mmol, 60 %) as a colourless oil: $[\alpha]_D^{20}$ – 1.92 (*c* 1.04, $CHCl_3$); δ_H (500MHz, $CDCl_3$) 4.72 (2H, s, H4), 4.12 (2H, m, H1), 3.98 (1H, m, H2), 3.70 (2H, m, H5), 3.66 (1H, dd, *J* 3.8, 10.6, H3), 3.59 (1H, dd, *J* 6.3, 10.6, H3), 3.54 (2H, t, *J* 4.6, H6), 3.37 (3H, s, H7) 2.31 (2H, t, *J* 7.5, H9), 1.60 (2H, m, H10), 1.30-1.17 (24H, m, H11-22), 0.85 (3H, t, *J* 6.8, H23); δ_C (125MHz, $CDCl_3$) 174.2

(C8) 96.4 (C4), 72.0 (C6), 70.4 (C3), 69.2 (C2), 67.5 (C5), 65.5 (C1), 59.3 (C7), 34.5 (C9), 32.3 (C21), 30.4- 29.5 (C11-20), 25.3 (C10), 23.0 (C22), 14.5 (C23); υ_{max} 3447, 2922, 2853, 1737, 1045; HRMS (ESI) found 441.3187, $C_{23}H_{46}NaO_6$ [M+Na]+ requires 441.3170.

(*S*)-3-((2-methoxyethoxy)methoxy)propane-1,2-diyl dipalmitate (2-4)

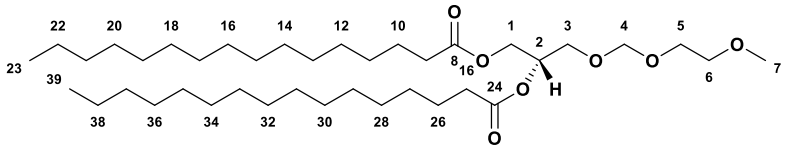

Molecule **2-4** was isolated as a side product of the above reaction (4.06 g, 5.98 mmol, 25 %) as a colourless oil: $[\alpha]_D^{20}$ +2.00 (*c* 1.0, $CHCl_3$); δ_H (400MHz, $CDCl_3$) 5.16 (1H, m, H2), 4.65 (2H, s, H4), 4.26 (1H, dd, *J* 3.9, 11.9, H1), 4.09 (1H, dd, *J* 6.4, 11.9, H1), 3.61 (4H, m, H3, H5), 3.48 (2H, m, H6), 3.32 (3H, s, H7) 2.24 (4H, m, H9, H25), 1.55 (4H, m, H10, H26), 1.24-1.14 (48H, m, H11-22, H27-38), 0.88 (6H, m, H23, H39); δ_C (100MHz, $CDCl_3$) 173.4 (C8), 173.1 (C24), 95.6 (C4), 71.7 (C6), 70.0 (C2), 67.0 (C5), 66.0 (C3), 62.6 (C1), 59.1 (C7), 34.3, 34.1 (C9, C25), 31.2 (C21, C37), 29.7-29.1 (C11-20, C27-36), 25.0 (C10, C26), 22.7 (C22, C38) 14.1 (C23, C39); υ_{max} 2956, 2850, 1739, 1468, 1049; HRMS (ESI) found 656.5605, $C_{39}H_{76}NaO_7$ [M+Na]+ requires 656.5591.

(*S*)-12-oxo-2,5,7,11-tetraoxaheptacosan-9-yl oleate (2-5)

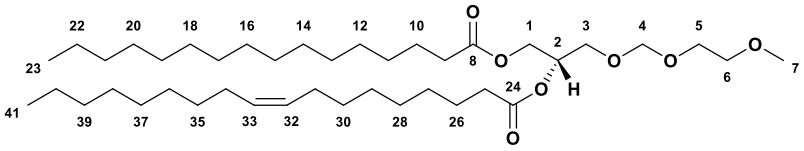

Modifying a literature procedure [A3], DMAP (4.3 g, 35.9 mmol) was added to a solution of **2-3** (10.0 g, 23.9 mmol) in DCM (100.0 ml). Oleoyl chloride (10.0 ml, 31.0 mmol) was added dropwise and the solution was left to stir overnight. The solvent was removed *in vacuo*, Et_2O (100.0 ml) was added, and the solution filtered. The solvent was again removed *in vacuo*, and

the residue was purified by flash column chromatography (3 : 1 PE : Et_2O) to yield compound **2-5** (12.2 g, 18.0 mmol, 75 %) as a yellow oil: $[\alpha]_D^{20}$ +1.26 (*c* 1.04, $CHCl_3$); δ_H (500MHz, $CDCl_3$) 5.34 (2H, m, H32,H33), 5.22 (1H, m, H2), 4.72 (2H, s, H4), 4.33 (1H, dd, *J* 3.8, 12.0, H1), 4.16 (1H, dd, *J* 6.3, 12.0, H1), 3.68 (4H, m, H3, H5), 3.55 (2H, m, H6), 3.39 (3H, s, H7) 2.31 (4H, m, H9, H25), 2.01 (4H, m, H31, H34) 1.61 (4H, m, H10, H26), 1.36-1.21 (44H, m, H11-22, H27-30, H35-40), 0.88 (6H, m, H23, H41); δ_C (125MHz, $CDCl_3$) 173.4 (C8), 173.0 (C24), 130.0, 129.7 (C32, C33), 95.6 (C4), 71.6 (C6), 70.0 (C2), 67.0 (C5), 65.9 (C3), 62.5 (C1), 59.0 (C7), 34.3, 34.0 (C9, C25), 31.9, 29.7- 29.0, 22.7 (C11-22, C27-30, C35-40), 27.2 (C31, C34) 24.9 (C10, C26), 14.1 (C23, C41); υ_{max} 2923, 2854, 1742, 1465, 1046, 723; HRMS (ESI) found 705.5662, $C_{41}H_{78}NaO_7$ [M+Na]+ requires 705.5640.

(*S*)-3-((2-methoxyethoxy)methoxy)propane-1,2-diyl ditetradecanoate (6)

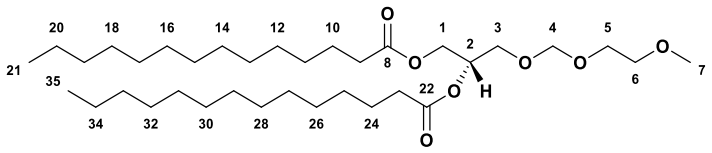

DMAP (12.9 g, 71.7 mmol) was added to a solution of diol **2-2** (10.0 g, 23.9 mmol) in DCM (100.0 ml). Myristoyl chloride (16.9 ml, 62.1 mmol) was added dropwise and the solution was left to stir overnight. The solvent was removed *in vacuo*, Et_2O (100.0 ml) was added, and the solution filtered. The solvent was again removed *in vacuo*, and the residue was purified by flash column chromatography (3 : 1 PE : Et_2O) to yield compound **2-6** (6.45 g, 10.8 mmol, 45 %) as a colourless oil: $[\alpha]_D^{20}$ +2.10 (*c* 1.04, $CHCl_3$); δ_H (500MHz, $CDCl_3$) 5.22 (1H, m, H2), 4.72 (2H, s, H4), 4.33 (1H, dd, *J* 3.9, 11.1, H1), 4.16 (1H, dd, *J* 6.6, 11.9, H1), 3.69 (4H, m, H3, H5), 3.55 (2H, m, H6), 3.40 (3H, s, H7) 2.36-2.29 (4H, m, H9, H23), 1.61 (4H, m, H10,

H24), 1.36-1.21 (40H, m, H11-20, H25-34), 0.88 (6H, m, H21, H35); δ_C (125MHz, $CDCl_3$) 173.4 (C8), 173.1 (C22), 95.6 (C4), 71.6 (C6), 70.0 (C2), 66.9 (C5), 65.9 (C3), 62.5 (C1), 59.0 (C7), 34.3, 34.1 (C9, C23), 29.7- 29.0 (C11-19, C25-33), 24.9 (C10, C24), 22.7 (C20, C34) 14.1 (C21, C35); υ_{max} 2923, 2854, 1742, 1466, 1046; HRMS (ESI) found 623.4864, $C_{35}H_{68}NaO_7$ [M+Na]+ requires 623.4857.

(*S*)-3-hydroxypropane-1,2-diyl ditetradecanoate (2-7)

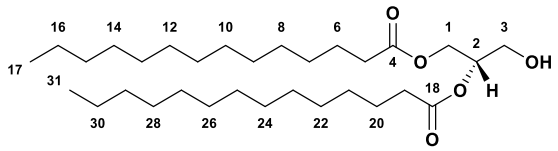

$TiCl_4$ (30.0 ml, 1M in DCM, 30.0 mmol) was added dropwise to a solution of **2-6** (10.0 g, 16.7 mmol) in DCM (332 ml) under nitrogen at 0 °C. The solution was left to stir for 2 h and consumption of starting material was monitored by TLC. NH_4Cl was added dropwise until a white precipitate formed, and the mixture was filtered through Celite^{TM}. The organic layer was then washed with H_2O (100 ml) and brine (100 ml). The solvent was removed *in vacuo* and the residue was purified by flash column chromatography (3 : 1 PE : Et_2O) to yield compound **2-7** (3.42 g, 6.68 mmol, 40 %) as a white solid: $[\alpha]_D^{20}$ -1.80 (*c* 1.2, $CHCl_3$); δ_H (500MHz, $CDCl_3$) 5.09 (1H, q, *J* 5.0, H2), 4.32 (1H, dd, *J* 4.4, 12.0, H1), 4.23 (1H, dd, *J* 6.0, 11.7, H1), 3.73 (2H, d, *J* 4.3, H3) 2.34, 2.32 (4H, d, *J* 5.6, H5, H19), 1.61 (4H, m, H6, H20), 1.33-1.21 (40H, m, H7-16, H21-30), 0.88 (6H, m, H17, H31); δ_C (125MHz, $CDCl_3$) 173.8 (C4), 173.4 (C18), 72.1 (C2), 62.0 (C1), 61.5 (C3), 34.3, 34.1 (C5, C19), 31.9 (C15, C29) 29.7- 29.1 (C7-14, C21-28), 24.9 (C6, C20), 22.7 (C16, C30) 14.1 (C17, C31); υ_{max} 2955, 2853, 1738, 1466, 1049; HRMS (ESI) found 535.4319, $C_{31}H_{60}NaO_5$ [M+Na]+ requires 535.4333.

(*S*)-12-oxo-2,5,7,11-tetraoxaheptacosan-9-yl oleate (2-8)

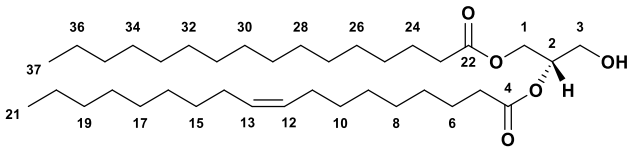

Following the same procedure for compound **2-7**, compound **2-5** (10.0 g, 14.7 mmol) gave **2-8** (3.05 g, 5.13 mmol, 35 %) as a viscous yellow oil: $[\alpha]_D^{20}$ -1.64 (*c* 1.1, $CHCl_3$); δ_H (300MHz, $CDCl_3$) 5.35 (2H, m, H12, H13), 5.08 (1H, q, *J* 5.0, H2), 4.32 (1H, dd, *J* 4.5, 12.0, H1), 4.22 (1H, dd, *J* 5.7, 12.0, H1), 3.73 (2H, d, *J* 5.5, H3), 2.33 (4H, m, H5, H23), 2.00 (4H, m, H11, H14), 1.62 (4H, m, H6, H24), 1.39-1.17 (44H, m, H7-10, H15-20, H25-36), 0.88 (6H, m, H21, H37);δ_C (75MHz, $CDCl_3$) 173.9 (C22), 173.6 (C4), 130.2, 129.8 (C12, C13), 72.3 (C2), 62.2 (C1), 61.7 (C3), 34.5, 34.3 (C5, C23), 32.1, 29.9- 29.3, 22.8 (C7-10, C15-20, C25-36), 27.4 (C11, C14) 25.9 (C6, C24), 14.3 (C21, C37); υ_{max} 2923, 2853, 1742, 1465, 1096, 722; HRMS (ESI) found 617.5222, $C_{37}H_{70}NaO_5$ [M+Na]+ requires 617.5121.

Solketal-d_2 (2-9)

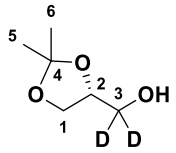

A solution of methyl (*R*)-2,2-dimethyl-1,3-dioxolane-4-carboxylate (10.0 g, 62.4 mmol) in Et_2O (110.0 ml) was added dropwise to a stirred solution of $LiAlD_4$ (2.62 g, 69.1 mmol) in Et_2O (174 ml) at 0 °C under nitrogen. The solution was left to stir for 15 min, then heated to reflux for 1 h. The mixture was cooled again to 0 °C, and H_2O (3.48 ml), aqueous NaOH (3.48 ml), and H_2O (10.4) were added dropwise. The resulting mixture was filtered through Celite,™ dried (Mg_2SO_4), and the solvent removed *in vacuo*. The residue was purified by distillation to afford the title compound **2-9** (8.22 g, 62.4 mmol, 100 %) as a colourless oil: $[\alpha]_D^{20}$ - 23.0 (*c*

0.97, EtOH); δ_H (400MHz, $CDCl_3$) 4.25 (1H, t, *J* 6.6, H2), 4.05 (1H, dd, *J* 6.6, 8.2, H1), 3.81 (1H, dd, *J* 6.5, 8.1, H1), 1.46, 1.39 (6H, s, H5,H6); δ_C (100MHz, $CDCl_3$) 109.4 (C4), 76.0 (C2), 65.7 (C1), 62.3 (t, *J* 21.9, C3), 27.2, 26.7 (C5, C6); υ_{max}, 3420, 3012, 1325 1110; HRMS (ESI) found 135.0958, $C_6H_{10}D_2O_3$ [M+Na]+ requires 135.0946

Ethanolamine-d$_4$ (2-10)

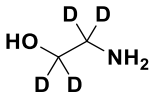

Ethanolamine was refluxed in D_2O over a bed of Raney nickel, with the D2O replace every two hours until consumption of ethanolamine as detected by 1H NMR. The crude product was purified by fractional distillation to furnish **2-10** as a colourless oil. HRMS (ESI) found 65.1075}, $C_6H_{10}D_2O_3$ [M+Na]+ requires 65.1075.

POPG-d$_2$ (2-11)

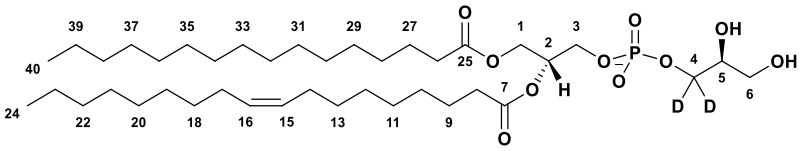

According to a literature procedure,[28] a solution of **2-8** (1.50 g, 2.53 mmol) and NEt_3 (0.379 g, 3.79 mmol) in THF (15 ml) was added dropwise to $POCl_3$ (0.455 g, 3.03 mmol) under nitrogen at 0 °C. The temperature was raised to room temperature for one hour. A solution of compound **2-9** (0.405 g, 3.03 mmol) and NEt_3 (0.758 g, 7.58 mmol) in THF (10.1 ml) was then added dropwise to the previous solution, and left to stir at 45 °C for one hour. The reaction was filtered, $NaCO_3$ (12.7 ml of a 1M solution) added to the filtrate and the resulting solution left to stir for 6 h. Acetone (23.0 ml) was added to the organic phase and the resulting precipitate filtered. The filtrate was evaporated to dryness and dissolved in 70 % aqueous acetic acid (23.5 ml) and left to stir for 1 h. The mixture was then extracted with $CHCl_3$ (3 x 25.0 ml) and the

solvent removed *in vacuo*. The residue was purified by flash column chromatography (200 : 15 : 1 › 100 : 15 : 1 › 65 : 15 : 1 $CHCl_3$: MeOH : NH_4OH) to yield compound **2-11** (0.460 g, 0.633 mmol, 25 %) as a colourless oil: δ_H (500MHz, $CDCl_3$) 5.33 (2H, m, H15, H16), 5.20 (1H, m, H2), 4.37 (1H, dd, *J* 2.9, 11.7, H1), 4.14 (1H, dd, *J* 6.9, 12.1, H1), 3.92 (2H, m, H3), 3.83 (1H, m, H5), 3.70 (2H, m, H6), 2.31, 2.28 (4H, m, H14, H17), 2.00 (4H, m, H8, H26), 1.58 (4H, m, H9, H27), 1.35-1.21 (44H, m, H10-13, H18-23, H28-39), 0.88 (6H, m, H24, H40); δ_C (125MHz, $CDCl_3$) 173.7 (C25), 173.4 (C7), 130.0, 129.6 (C15, C16), 70.8 (C5), 70.2 (C2), 66.4 (br, C4), 63.6 (C3), 62.7, 62.6 (C1,6), 34.2, 34.1 (C14, C17), 31.9 (C22, C38), 29.7- 29.1, 18.3 (C9-12, C19-22, C27-37), 27.2 (C8, C26) 24.9 (C13, C18), 22.7 (C23, C39), 14.1 (C24, C40); υ_{max} 3396, 2954, 2517, 1700, 1080, 740; HRMS (ESI) found 749.5305, $C_{40}H_{74}D_2NaO_{10}P$ [M+Na]+ requires 749.5307.

DMPG-d_2 (2-12)

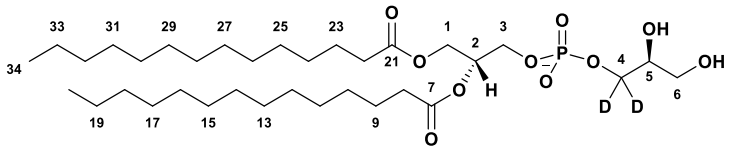

Following the same procedure for compound **2-11**, compound **2-7** (3.0 g, 5.86 mmol) gave **2-12** (0.860 g, 1.29 mmol, 22 %) as a white solid: δ_H (500MHz, $CDCl_3$) 5.17 (2H, m, H2), 4.37 (1H, dd, *J* 3.2, 12.0, H1), 4.11 (1H, dd, *J* 6.9, 12.1, H1), 3.91 (2H, t, *J* 5.8, H3), 3.83 (1H, t, *J* 4.8, H5), 3.56 (2H, m, H6), 2.25 (4H, m, H8, H22), 1.54 (4H, m, H9, H23), 1.29-1.17 (40H, m, H10-19, H24-33), 0.82 (6H, m, H20, H34); δ_C (125MHz, $CDCl_3$) 173.8 (C21), 173.4 (C7), 70.8 (C5), 70.3 (C2), 66.0 (br, C4), 63.6 (C3), 62.5 (C1,6), 34.3, 34.1 (C8, C22), 31.9, 29.7-29.2, 24.9 (C10-19, C24-33), 22.7 (C9, C23), 14.0 (C20, C34); υ_{max} 3450, 2520, 1688, 1100; HRMS (ESI) found 689.4341, $C_{34}H_{63}D_2NaO_{10}P$ [M+Na]+ requires 689.4344.

POPE-d_4 (2-13)

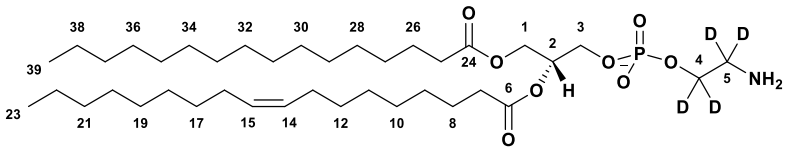

According to a literature procedure,[28] a solution of **2-8** (0.700 g, 1.34 mmol) and NEt_3 (0.20 mg, 2.35 mmol) in THF (8.2 ml) was added dropwise to $POCl_3$ (0.25 g, 1.64 mmol) under nitrogen at 0 °C. The temperature was raised to room temperature for one hour. A solution of compound **2-10** (0.095 g, 1.44 mmol) and NEt_3 (0.525 g, 5.24 mmol) in THF (3.0 ml) was then added dropwise to the previous solution, and left to stir at 45 °C for one hour. The reaction was filtered, $NaCO_3$ (6.0 ml of a 1M solution) added to the filtrate and the resulting solution left to stir for 6 h. Acetone (12.0 ml) was added to the organic phase and the resulting precipitate filtered. The filtrate was evaporated to dryness and dissolved in 20 % aqueous acetic acid (6.8 ml) and propan-2-ol (13.6 ml) left to stir for 1 h. The mixture was then extracted with $CHCl_3$ (3 x 12.0 ml) and the solvent removed *in vacuo*. The residue was purified by flash column chromatography (65 : 15 : 1 $CHCl_3$: MeOH : NH_4OH) to yield compound **2-13** (0.477 g, 0.643 mmol, 48 %) as a white powder: δ_H (500MHz, $CDCl_3$) 5.32 (2 H, m, H14, H15), 5.20 (1 H, m, H2), 4.36 (1 H, dd, *J*=12.2, 3.4 Hz, H1), 4.13 (1 H, dd, *J*=12.0, 6.9 Hz, H1), 3.94 (2 H, m, H3), 2.29 (4 H, m, H7, H25), 1.99 (4 H, m, H13, H16), 1.56 (4 H, m, H8, H26), 1.32-1.21 (46 H, m, H9-12, H17-22, H26-38), 0.86 (6 H, t, *J*=7.0 Hz, H23, H39); δ_C (125MHz, $CDCl_3$) 173.6 (C24), 173.2 (C7), 130.0 (C14), 129.6 (C15), 70.1 (C2), 63.8 (C3), 62.5 (C1), 61.3 (br, C4), 39.8 (br, C5), 34.2 (C7), 34.0 (C25), 31.9, 29.7-29.1, 22.6 (C7, C9-12, C17-22, C25, C27-38), 27.2 (C13, C16), 24.9 (C8, C26), 14.1 (C23, C39); HRMS (ESI) found 743.5360, $C_{39}H_{71}D_4NO_8P$ [M+Na]+ requires 743.5400 (main peak).

DMPE-d_4 (2-14)

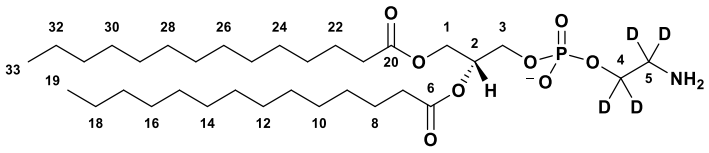

Following the same procedure for compound **2-13**, compound **2-9** (0.700 g, 1.23 mmol) gave **2-14** (0.455 g, 0.688 mmol, 56 %) as a white solid: δ_H (500 MHz, CDCl3) δ ppm 5.18 (1H, m, H2), 4.34 (1H, dd, *J*=12.1, 3.2 Hz, H1), 4.12 (1 H, dd, *J*=12.1, 6.9 Hz, H1), 3.92 (2 H, t, *J*=5.9 Hz, H3), 2.21 - 2.32 (4 H, m, H7, H21), 1.50 - 1.62 (4 H, m, H8, H22), 1.19 - 1.29 (40 H, H9-18, H23-32), 0.85 (6 H, t, *J*=7.0 Hz, H19, H33); δ_C (125MHz, $CDCl_3$) 173.7 (C26), 173.4 (C6), 70.2 (C2), 63.7 (C3), 62.5 (C1), 61.3 (br, C4) 34.0 (C21, C7), 31.3 (br, C5) 31.9, 29.6-29.1, 22.6 (C9-C18, C23-32), 24.8 (C8, C22), 22.6 (C), 14.0 (C19, C33); HRMS (ESI) found 661.4613, $C_{33}H_{61}D_4NNaO_8P$ [M+Na]+ requires 661.4591 (main peak).

References:

[A1] A. Duralski, P. Spooner and A.Watts, “Synthesis of optically active polyunsaturated diacylglycerols.”, Tetrahedron Letters, **30**, 3585-3588, 1989.

[A2] S. Furumoto, R. Iwata, T. Ido, “Synthesis of 1-*O*-(8-[18F]fluorooctanoyl)-2-*O*-palmitoyl-*rac*-glycerol for imaging intracellular signal transduction.”, Journal of Labelled Compounds and Radiopharmaceuticals, **43**, 1159-1172, 2000.

[A3] A. Duralski, P. Spooner, S. Rankin and A.Watts, “Synthesis of isotopically labelled cardiolipis.”, Tetrahedron Letters, **39**, 1607-1610, 1998.

Appendix B

Full Sequence of PinA, PinB+ and PinBs

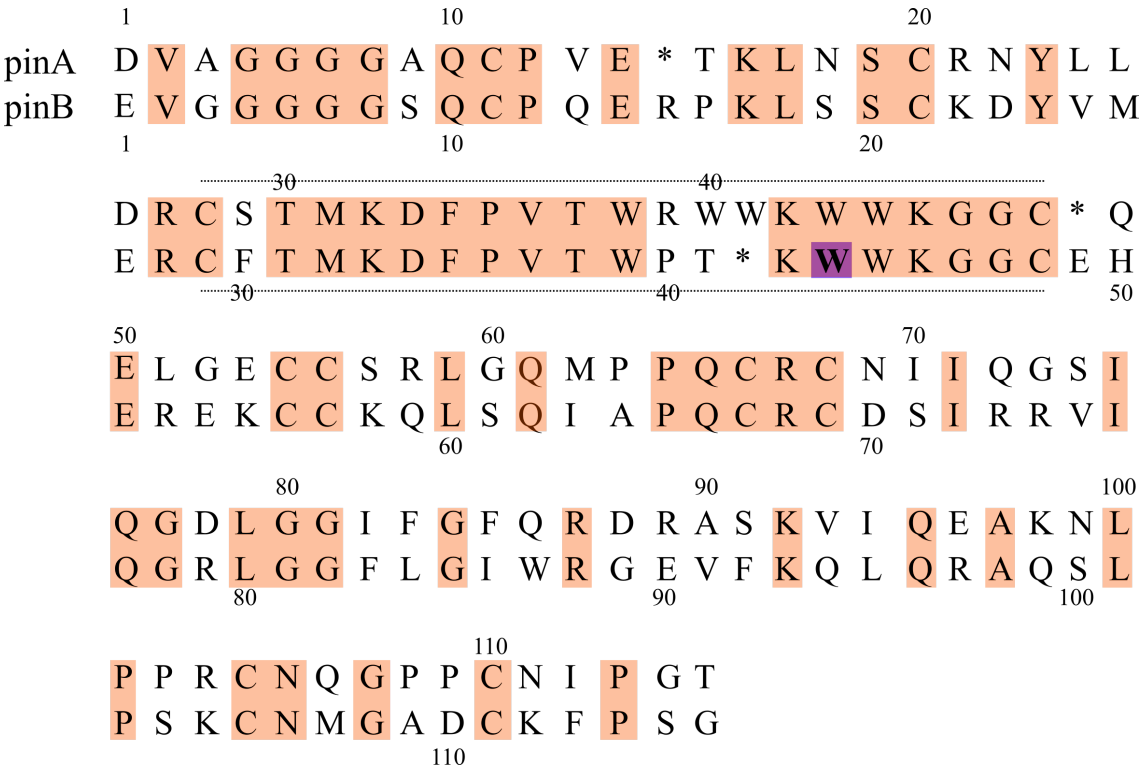

Figure B.1 The full amino acid sequence alignment for pinA and pinB wild-type (pinB+) is shown below. Yellow boxes indicate conserved residues, and the cystein-enclosed, tryptophan-rich domain between residues 28 and 48 is highlighted. A point mutation of W44R (the pinBs sequence) is also highlighted, in purple. Figure adapted from [A4].

References

[A4] T. Le Bihan, J.E Blochet, A. Désomrmeaux, D. Marion, M Pézolet M, "Determination of the secondary structure and conformation of puroindolines by infrared and Raman spectroscopy.", Biochemistry, **35**, 12712-22, 1996